

AFRL-SR-BL-TR-00-

REPORT DOCUMENTATION PAGE

Public reporting burden for this collection of information is estimated to average 1 hour per response, including the reviewing and maintaining the data needed, and completing and reviewing the collection of information. Send comments regarding this burden estimate or any other aspect of this collection of information, including suggestions for reducing this burden, to Washington Headquarters Services, Directorate for Information Operations and Reports, 1215 Jefferson Davis Highway, Suite 1204, Arlington, VA 22202-4302, and to the Office of Management and Budget, Paperwork Reduction Project (0704-0188), Washington, DC 20503.

1. AGENCY USE ONLY (Leave blank)		2. REPORT DATE November 22, 2000	3. REPORT TYPE AND DATES COVERED Final Report, 04/01/97 - 12/31/99
4. TITLE AND SUBTITLE Development of Robust Boundary Layer Controllers			5. FUNDING NUMBERS G: F49620-97-1-0276
6. AUTHORS Jason L. Speyer and John Kim			
7. PERFORMING ORGANIZATION NAME(S) AND ADDRESS(ES) Mechanical and Aerospace Engineering Department 48-121 Engineering IV, Box 951597 University of California, Los Angeles Los Angeles, CA 90095-1597			8. PERFORMING ORGANIZATION REPORT NUMBER
9. SPONSORING/MONITORING AGENCY NAME(S) AND ADDRESS(ES) AFOSR/NA 801 N. Randolph Street, Room 732 Arlington, VA 22203-1977			10. SPONSORING/MONITORING AGENCY REPORT NUMBER
11. SUPPLEMENTARY NOTES The views, opinions and/or findings contained in this report are those of the author(s) and should not be construed as an official Department of the Air Force position, policy or decision, unless so designated by other documentation.			
12a. DISTRIBUTION/AVAILABILITY STATEMENT Approved for public release; distribution unlimited			12b. DISTRIBUTION CODE UL
13. ABSTRACT (Maximum 200 words) The problem of controlling turbulent boundary layers was studied using techniques employed in control system analysis and design. During the last three years, the linearized Navier-Stokes equations were modified to include a boundary input of blowing/suction along the wall. By a Galerkin method, the modified linearized Navier-Stokes equations were converted into a temporal control theoretical model, to which modern control synthesis can be applied. The resulting state space model allows a multivariable feedback design combining an array of sensors with an array of actuators along the wall. Based on this spectral decomposition, a parallel architecture for the implementation of temporal controllers allows significant decrease in computational bandwidth. For each wavenumber linear-quadratic-Gaussian multi-variable synthesis and model reduction techniques are used to derive robust feedback controllers. Controller performance was tested on a direct numerical simulation of a fully developed turbulent channel flow. Controller performance for the nonlinear flow was surprisingly good, suggesting that linear systems can be used as a basis for developing controllers for near-wall turbulence. Controllers are being developed on the basis of the three dimensional linearized Navier-Stokes equations. Both spanwise and streamwise shear sensors are considered. By a Galerkin method, a temporal state space model is determined where, for every wave number pair, a 500 state system is obtained with two inputs and four outputs. Model reduction techniques are used to reduce the state space drastically, and wave number pairs that produce the largest shear stress amplification for uncertainty induced at the wall are investigated.			
14. SUBJECT TERMS robust feedback flow control, control of turbulence, model reduction, shear flows, skin friction, drag reduction			15. NUMBER OF PAGES 153
			16. PRICE CODE
17. SECURITY CLASSIFICATION OF REPORT Unclassified	18. SECURITY CLASSIFICATION OF THIS PAGE Unclassified	19. SECURITY CLASSIFICATION OF ABSTRACT Unclassified	20. LIMITATION OF ABSTRACT UL

NSN 7540-01-280-5500

Computer Generated

STANDARD FORM 298 (Rev 2-89)
Prescribed by ANSI Std Z39-18
298-102

20001205 080

DTIC QUALITY INSPECTED 4

DEVELOPMENT OF ROBUST BOUNDARY LAYER CONTROLLERS

Final Report

Air Force Office of Scientific Research

F49620-97-1-0276

Period of Performance: 04/01/1997 — 12/31/1999

Jason L. Speyer and John Kim, Principal Investigators
Department of Mechanical and Aerospace Engineering
University of California, Los Angeles
Los Angeles, CA 90095-1597

The problem of controlling turbulent boundary layers was studied using techniques employed in control system analysis and design. During the last three years, the linearized Navier-Stokes equations were modified to include a boundary input of blowing/suction along the wall. By a Galerkin method, the modified linearized Navier-Stokes equations were converted into a temporal control theoretical model, to which modern control synthesis can be applied. The resulting state space model allows a multivariable feedback design combining an array of sensors with an array of actuators along the wall. Based on this spectral decomposition, a parallel architecture for the implementation of temporal controllers allows significant decrease in computational bandwidth. For each wavenumber linear-quadratic-Gaussian multi-variable synthesis and model reduction techniques are used to derive robust feedback controllers. Controller performance was tested on a direct numerical simulation of a fully developed turbulent channel flow. Controller performance for the nonlinear flow was surprisingly good, suggesting that linear systems can be used as a basis for developing controllers for near-wall turbulence. Controllers are being developed on the basis of the three dimensional linearized Navier-Stokes equations. Both spanwise and streamwise shear sensors are considered. By a Galerkin method, a temporal state space model is determined where, for every wave number pair, a 500 state system is obtained with two inputs and four outputs. Model reduction techniques are used to reduce the state space drastically, and wave number pairs that produce the largest shear stress amplification for uncertainty induced at the wall are investigated.

Table of Contents

Abstract	i
1. Introduction	1
2. Progress Over the Grant Period	1
3. References	5
APPENDIX A: Robust Reduced-Order Controller of Laminar Boundary Layer Transitions	
APPENDIX B: Finite-dimensional Optimal Control of Poiseuille Flow	
APPENDIX C: Skin-Friction Drag Reduction via Robust Reduced-Order Linear Feedback Control	
APPENDIX D: Robust Reduced-Order Control of Turbulent Channel Flows via Distributed Sensors and Actuators	
APPENDIX E: Application of Robust Reduced-Order Controller to Turbulent Flow for Drag Reduction	
APPENDIX F: State-Space Formulation and Controller Design for Three-Dimensional Channel Flows	
APPENDIX G: Robust Feedback Control of Rayleigh-Bénard Convection	

1 Introduction

The potential benefits of controlling flows that occur in common engineering applications are significant. Applications include drag reduction for aircraft, high maneuverability for military aircraft, jet noise reduction, and enhanced mixing and better fuel efficiency for internal combustion engines. Because of its importance as well as its genuine intellectual challenge, flow control has attracted much attention from many able fluid dynamicists. These attempts, however, have not been very satisfactory.

Most of the flow control research, however, has been ad-hoc based on the investigator's physical intuition. Some progress has been made from such attempts, especially since the discovery of the coherent turbulence structures that exist in the near-wall region of turbulent boundary layers. Choi et al. [1], for example, report an active control scheme, which was designed to reduce the strength of the near-wall streamwise vortices. This active control scheme, which was based on the physical observations that there are strong correlations between the near-wall streamwise vortices and the high skin-friction region, is reported to reduce the viscous drag by as much as 25%.

Although some progress has been made through similar ad-hoc attempts, it is our belief that much more progress can be made if we can utilize modern control theories for flow control. A few examples of applications of modern control theories to flow control have appeared in the literature recently. The foundations of optimal control theory as applied to the equations governing fluid flow were developed and its application to flow control was reported by Choi et al. [2], Moin and Bewley [3], and Lee et al. [4].

Unlike previous researchers, our group considered a system theory approach to transition control, which revealed a rich structure of modes whose input-output properties were characterized in terms of their observability and controllability [5]. These dynamical systems were obtained by a Galerkin projection applied to the two-dimensional linearized Navier-Stokes equations. Two important aspects were recognized. Only modes which were controllable and observable at the wall could be used by the controller and that the near-wall turbulence structure alone was sufficient to control for viscous drag prediction. In [5] only a simple integral controller on the shear stress measurement was used and only applied to, at most, a few wave numbers. However, it was shown to control a two-dimensional finite-amplitude disturbance responsible for the secondary instability, thus suggesting that nonlinear effects could be handled by a linear controller. Efforts on improved dynamic response by using linear-quadratic-Gaussian (LQG) optimal control synthesis showed that the required control energy could be reduced over that of the simple integral compensator [6]. The LQG controller was designed on a reduced state space obtained from the Galerkin projection method.

2 Progress Over the Grant Period

Over the last three years, these results for a single wavenumber have been significantly modified. First, it was recognized that even for a single wavenumber, there are two controls and two outputs [7]. The original work [5] considered only a single input/single output system.

The dynamic system in [5] contained a derivative of the control. By a simple transformation, this was removed [7]. The spatial decomposition produces a controllable system only with respect to the control at that wavenumber. Therefore, a parallel architecture of compensators in wave space can be constructed [7, Appendix A]. Each compensator is based on the dynamic system formed from the Galerkin projection associated with the Chebyshev expansion for each wavenumber. The resulting state space is quite large and a much smaller state space is required for controller development. This smaller state space, obtained by a form of balanced realization [7,8, Appendix A and B], is used for LQG design where the uncertainty is assumed to be emanating from the wall and is modeled as an input with the same input matrix as the control [7,8, Appendix A and B]. For the two-dimensional controller where the system is minimal phase, good loop transfer recovery is obtained producing good stability margins for robust control [7,8].

The parallel structured controller of [7] for multiple wave numbers was first applied to the more realistic linearized Navier-Stokes equations to test controller performance. The full order system had 8,000 states and the controller only required 640, where 32 controllers of the order 20 operated in parallel. The result is that the reduced order controller suppressed up to 90% of the wall shear stress in a two-dimensional channel flow. Given this success, the controller was embedded in a direct simulation of Navier-Stokes equations for controlling skin-frictional drag in a two-dimensional channel flow [9, Appendix C]. Although controlling skin-friction drag in two dimensions cannot be readily extrapolated to the three-dimensional turbulence case, the testing of the controller in a nonlinear two-dimensional environment has produced valuable insight into the capability of linear controllers. Applying the linear controller (10% of the order of the full system) to the bottom wall of a two-dimensional turbulent periodic channel flow at a Reynolds number of 1,500 dramatic drag reduction of up to 60% with respect to the turbulent flow was obtained. This motivated the application of an array of two-dimensional controllers placed parallel to each other at 32 spanwise locations in a three-dimensional channel. Streamwise shear stress measurements are only shared within each two-dimensional controller at the same spanwise locations. Therefore, no information from different spanwise locations was shared. A 10% decrease in drag reduction occurred [10, Appendix D]. However, since no measurements were shared in the spanwise direction, the resulting shear stress varies significantly in the spanwise direction, at a wavenumber corresponding to the wall-layer streaky structures (Fig. 1). By additional blowing and suction proportional to the spanwise variation of the streamwise-averaged wall shear stress, the shear stress oscillations in the spanwise direction was removed (Fig. 2) and the drag reduction was about 16%. These results are reported in detail in [11, Appendix E].

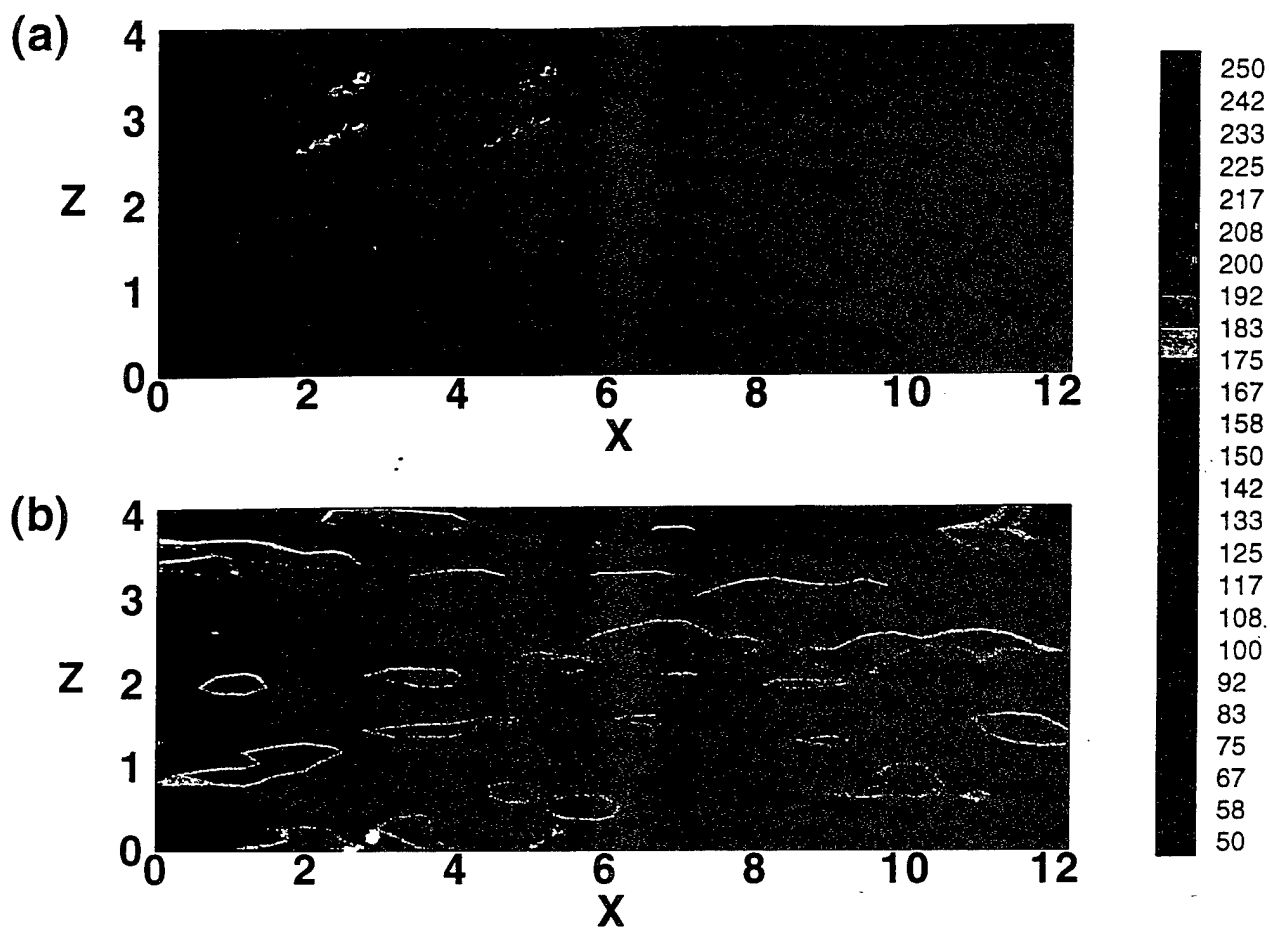


**Figure 1. Contours of the wall-shear stress, $\partial u / \partial y|_w$:
(a) channel with 2d controller; (b) uncontrolled.**

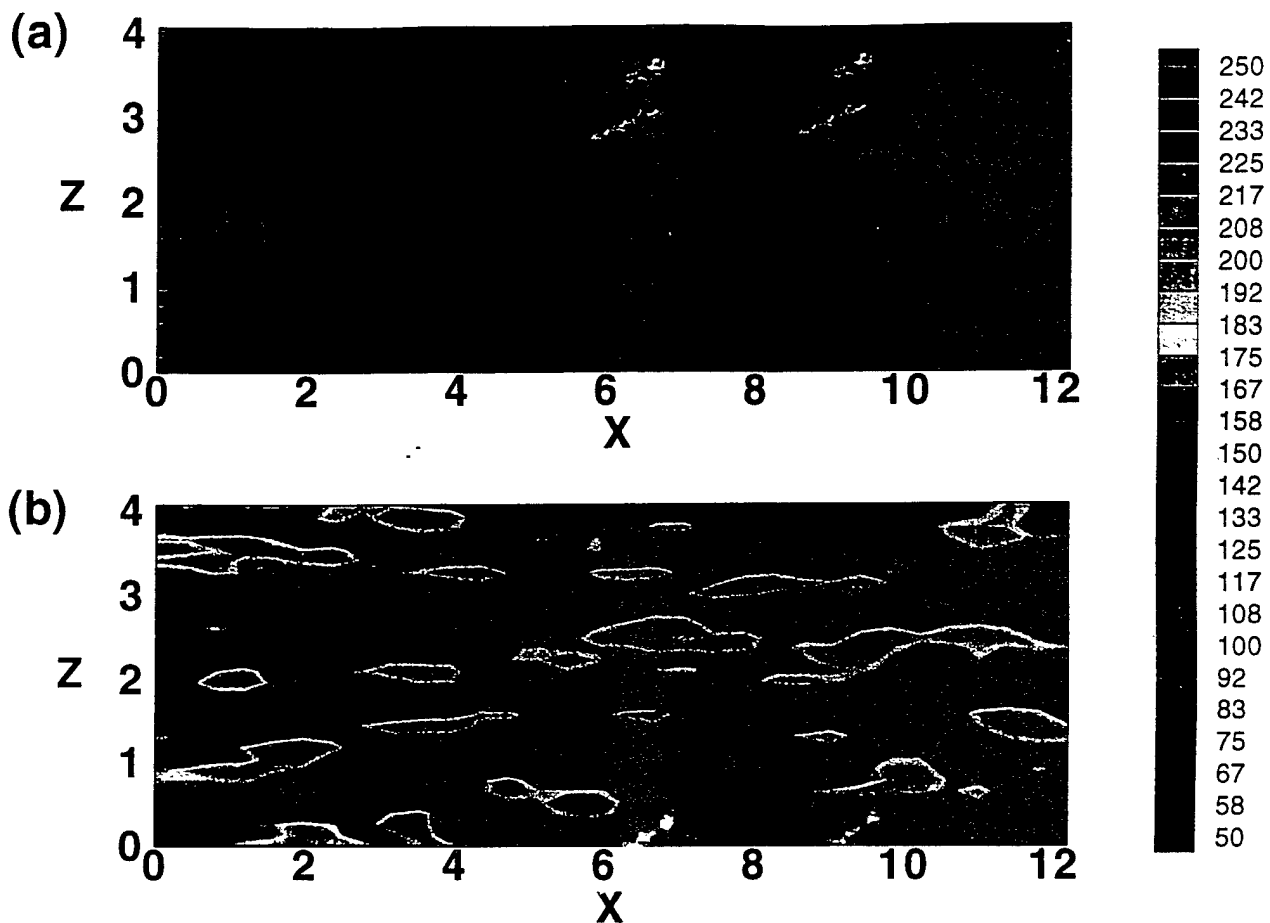


Figure 2. Contours of the wall-shear stress, $\partial u / \partial y|_w$:
(a) channel with 2d controller plus ad-hoc controller;
(b) uncontrolled.

Given the success with the two-dimensional controller, the three-dimensional controller is being developed. Here, we consider the linearized three-dimensional Navier-Stokes equations as the system dynamics where the control is applied through wall-transpiration on a two-dimensional surface and both spanwise and streamwise shear stress distributed over the wall are used as measurements. The linearized governing equations are discretized through a Fourier transform which decomposes the system controls and outputs into a set of independent systems, controls, and outputs for each streamwise and spanwise wavenumber pair. The cost criterion, total wall-shear stress, also decomposes into a sum of components of wall-shear stress for each wavenumber pair. Again, reduced order controllers for each wavenumber pair can be implemented in parallel [12, Appendix F]. The dynamic structure now contains both the Orr-Sommerfield and Squire modes and the important coupling between them. The question about energy amplification associated with the linear dynamic system can now be addressed. Observability and controllability resolution allows the construction of reduced-order controllers. For each streamwise and spanwise wavenumber pair, a reduced-order controller has been designed and its performance evaluated in the presence of the full dynamic system [12].

Besides boundary layer control, our linear controller design approach, based on approximation of the physical system, is applicable to other processes. For example, in [13, Appendix G] the Rayleigh-Bénard problem of delaying the onset of convection in terms of increasing the temperature difference across an infinite layer of fluid heated from below is stabilized where the critical Rayleigh number is elevated significantly above that of the uncontrolled system. These results have application of material processing, solidification, semiconductor melts, welding, evaporative coating and crystal growth.

3 References

1. Choi, H., Moin, P., and Kim, J., "Active Turbulence Control for Drag Reduction in Wall-Bounded Flows," *J. Fluid Mech.*, Vol. 262, p. 75, 1994.
2. Choi, H., Teman, R., Moin, P., and Kim, J., "Feedback Control for Unsteady Flow and its Application to the Stochastic Burgers Equation," *J. Fluid Mech.*, Vol. 253, p. 509, 1993.
3. Lee, C., Kim, J., and Choi, H., "Suboptimal Control of Turbulent Channel Flow for Drag Reduction," *J. Fluid Mech.*, Vol. 358, pp. 245–258, 1998.
4. Moin, P. and Bewley, T., "Application of Control Theory to Turbulence," Proc. 12th Australian Fluid Mechanics Conference, p. 109, December 10–15, Sydney, 1995.
5. Joshi, S.S., Speyer, J.L., and Kim, J., "A Systems Theory Approach to the Feedback Stabilization of Infinitesimal and Finite-Amplitude Disturbances in Plane Poiseuille Flow," *J. Fluid Mech.*, Vol. 332, p. 157, 1997.
6. Joshi, S.S., Speyer, J.L., and Kim, J., "Modelling and Control of Two-Dimensional Poiseuille Flow," Proc. 34th Conf. on Decision and Control, pp. 921–927, Dec. 1995.

7. Cortelezzi, L. and Speyer, J.L., "Robust Reduced-Order Controller of Laminar Boundary Layer Transitions," *Phys. Rev. E*, Vol. 58, No. 2, pp. 1906-1910, Aug. 1998.
8. Joshi, S.S., Speyer, J.L., and Kim, J., "Finite-Dimensional Optimal Control of Poiseuille Flow," *AIAA J. of Guidance, Control and Dynamics*, Vol. 22, No. 2, pp. 340-348, March-April 1999.
9. Cortelezzi, L., Lee, K.H., Kim, J., and Speyer, J.L., "Skin-Friction Drag Reduction via Robust Reduced-Order Linear Feedback Control," *Int'l. J. Comp. Fluid Dyn.*, Vol. 11, No. 1-2, pp. 79-92, 1998.
10. Cortelezzi, L., Lee, K.H., Kim, J., and Speyer, J.L., "Reduced-Order Control of Turbulent Channel Flows via Distributed Sensors and Actuators," *Proc. IEEE Conf. on Decision and Control*, pp. 1906-1911, Dec. 1998.
11. Lee, K.H., Cortelezzi, L., Kim, J., and Speyer, J.L., "Application of Reduced-Order Controller to Turbulent Flow for Drag Reduction," submitted to *Phys. Fluids*, 2000.
12. Kang, S.M., Ryder, V., Cortelezzi, L., and Speyer, J.L., "State-Space Formulation and Controller Design for Three-Dimensional Channel Flows," *Proc. of the American Controls Conf.*, June 1999.
13. Or, A.C., Cortelezzi, L., and Speyer, J.L., "Robust Feedback Control of Rayleigh-Bénard Convection," submitted *J. Fluid Mech.*

APPENDIX A

Robust Reduced-Order Controller of Laminar Boundary Layer Transitions

L. Cortelezzi and J.L. Speyer

APPENDIX B

Finite Dimensional Optimal Control of Poiseuille Flow

S.S. Joshi, J.L. Speyer, J. Kim

APPENDIX C

Skin-Friction Drag Reduction via Robust Reduced-Order Linear Feedback Control

L. Cortelezzi, K.H. Lee, J. Kim, J.L. Speyer

APPENDIX D

*Robust Reduced-Order control of Turbulent Channel Flows
via Distributed Sensors and Actuators*

L. Cortelezzi, J.L. Speyer, K.H. Lee, J. Kim

APPENDIX E

Application of Robust Reduced-Order Controller to Turbulent Flows for Drag Reduction

K.H. Lee, L. Cortelezzi, J. Kim, J.L. Speyer

APPENDIX F

State-Space Formulation and Controller Design for a Three-Dimensional Channel Flow

S.M. Kang, V. Ryder, L. Cortelezzi, J.L. Speyer

APPENDIX G

Robust Feedback Control of Rayleigh Bénard Convection

A.C. Or, L. Cortelezzi, J.L. Speyer

APPENDIX A

Robust Reduced-Order Controller of Laminar Boundary Layer Transitions

L. Cortelezzi and J.L. Speyer

Robust reduced-order controller of laminar boundary layer transitions

L. Cortelezzi and J. L. Speyer

Department of Mechanical and Aerospace Engineering, University of California, Los Angeles, California 90095-1597

(Received 2 February 1998)

A framework to derive optimal and robust reduced-order controllers of fluid mechanics and plasma physics flows using linear-quadratic-Gaussian design, or, in modern terms, \mathcal{H}_2 design, is presented. As a test case, two-dimensional channel flow is considered. A reduced model is derived, and a controller is designed based upon this model. Initial conditions creating transient growth of wall-shear stress are constructed. The controller is tested on a 32 wave number simulation. A wall-shear stress reduction, up to 90%, is obtained. The potential transferability of the controller to engineering applications is discussed. [S1063-651X(98)06408-8]

PACS number(s): 47.62.+q, 47.27.Cn, 47.27.Rc, 47.27.Vf

The reduction of drag produced by skin friction, or, in other words, the reduction of wall-shear stresses (WSS's) generated by near-wall turbulence have received wide attention. "The skin friction constitutes about 50%, 90%, and 100% of the total drag on commercial aircraft, underwater vehicles, and pipelines, respectively" [1]. Two are the near-wall flows of interest: boundary layers that change from laminar to turbulent regimes, and boundary layers that are inherently turbulent. Correspondingly, efforts to reduce skin friction fall into two broad categories: transition inhibition and turbulence suppression. References [1-4] are recent reviews summarizing achievements and open questions in boundary layer control.

Boundary layer control has been attempted with some success. References [5-23] are articles published in the past four years. It is becoming widely accepted that even better results can be obtained by using controllers able to analyze distributed measurements and coordinate distributed actuators. However, very little has been done [24-26] to exploit the tools recently developed in the control community [27,28]. In particular, linear-quadratic-Gaussian (LQG) design, or, in modern terms, \mathcal{H}_2 design, combined with model reduction techniques for multiinput-multioutput (MIMO) systems, has never been used in fluid mechanics nor plasma physics.

Using a case study, this paper introduces the reader to a framework for deriving optimal and robust reduced-order controllers for flows of interest in fluid mechanics and plasma physics. As a case study, we show that MIMO LQG (\mathcal{H}_2) design can be successfully applied to suppress up to 90% of the WSS in a two-dimensional transitional channel flow. The framework can be easily applied to control problems described over simple domains (rectangles, circles and ellipsis, cubes, cylinders, tori, etc.) by linear partial differential equations with nonhomogeneous boundary conditions. The spectral decomposition depends on the geometry of the problem and, consequently, appropriate base functions should be selected. Once the spectral decomposition is in order, the framework can be applied step by step. In the case when there is more than one partial differential equation, the state space equations for the full problem are obtained by stacking the ordinary differential equations generated by the Galerkin projection of each partial differential equation. This

paper also addresses the potential transferability of the controller to engineering applications.

We consider two-dimensional incompressible Poiseuille flow in a periodic channel of length Lh and height $2h$. The undisturbed velocity field has a parabolic profile with center-line velocity U_c : see Fig. 1. Since we are interested in controlling the transition of the boundary layer from laminar to turbulent regimes, we consider a small perturbation of flow quantities. The reader should be aware that with the term "transition," we identify the disruption of the laminar regime in a fully developed boundary layer due to the growth of spatially localized near-wall perturbations. The linearized Navier-Stokes equations are written in terms of the perturbation stream-function ψ ,

$$(\partial_t + U \partial_x) \Delta \psi - U'' \psi_x = \text{Re}^{-1} \Delta \Delta \psi, \quad (1)$$

to satisfy continuity identically. The problem is made dimensionless by using h as a characteristic length and h/U_c as a characteristic time. The Reynolds number is $\text{Re} = U_c h / \nu$.

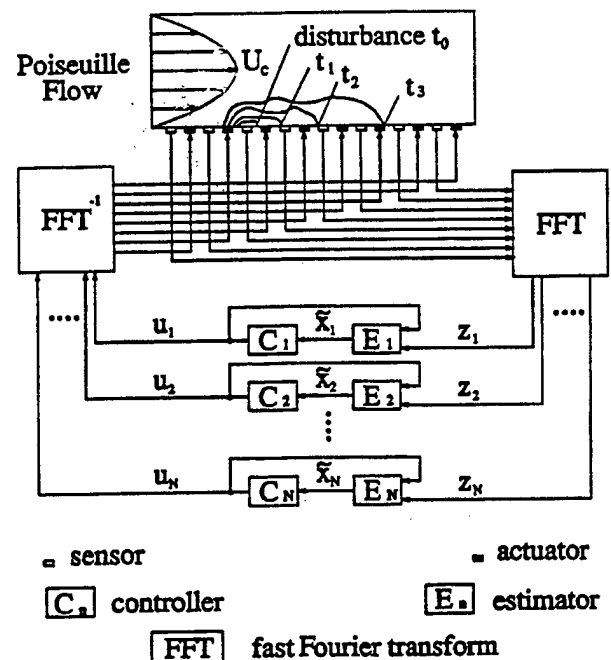


FIG. 1. Controller architecture.

To suppress perturbations evolving within the bottom boundary layer, we apply blowing and suction at the bottom wall (see Fig. 1). For simplicity we assume that the actuators are uniformly distributed. Perturbations in the top boundary layer are left free to evolve. The corresponding boundary conditions are

$$\psi_x|_{y=-1} = -v_w(x, t), \quad \psi_y|_{y=\pm 1} = \psi|_{y=1} = 0, \quad (2)$$

where the control function v_w prescribes the amount of blowing and suction at the bottom wall. We impose that the mass of fluid injected equals the mass of fluid removed.

To detect and measure the deviations of the boundary layer from the laminar regime, we measure the gradient of the streamwise velocity component at given points $x = x_i$ along the bottom wall (see Fig. 1),

$$z(x_i, t) = \psi_{yy}|_{y=-1}. \quad (3)$$

In other words, we measure the first term of the WSS, $\tau_{yx} = \text{Re}^{-1}(\psi_{yy} - \psi_{xx})|_{y=-1}$. The second term of the WSS is zero in the uncontrolled case, and is known in the controlled case.

We define an optimal performance index J , or cost function, to design a controller for the LQG (\mathcal{H}_2) problem. Since we are interested in suppressing the WSS, we define

$$J = \lim_{t_f \rightarrow \infty} \int_t^{t_f} \int_0^L (\psi_{yy}^2 + \psi_{xx}^2)|_{y=-1} dx dt. \quad (4)$$

The integrand represents the cost of the WSS being different from zero. Moreover, the integrand implicitly accounts for the cost of implementing the control itself. There are two reasons to minimize the cost of the controller: In any engineering application the energy available to drive the controller is limited, and a large control action may drive the system away from the region where the linear model is valid.

To reduce Eqs. (1)–(3) to a set of first-order ordinary differential equations, we make a few transformations loosely based on Refs. [24] and [26]. We write the stream function as $\psi = \phi + \chi$ to embed the actuator into the evolution equation, and to make the boundary conditions homogeneous. Substituting $\psi = \phi + \chi$ into Eq. (1), we obtain a forced equation for the Poiseuille flow

$$\begin{aligned} (\partial_t + U\partial_x)\Delta\phi - U''\phi_x &= \text{Re}^{-1}\Delta\Delta\phi \\ &\quad - (\partial_t + U\partial_x)\Delta\chi + U''\chi_x \\ &\quad + \text{Re}^{-1}\Delta\Delta\chi, \end{aligned} \quad (5)$$

with homogeneous boundary conditions $\phi|_{y=\pm 1} = \phi_y|_{y=\pm 1} = 0$. The forcing function χ satisfies the nonhomogeneous boundary conditions (2), i.e., $\chi_x|_{y=-1} = -v_w(x, t)$, $\chi|_{y=1} = \chi_y|_{y=\pm 1} = 0$. We also substitute $\psi = \phi + \chi$ into Eqs. (3) and (4). The measurement equation (3) becomes

$$z(x_i, t) = (\phi_{yy} + \chi_{yy})|_{x=x_i, y=-1}, \quad (6)$$

while the cost function (4) takes the following form:

$$J = \lim_{t_f \rightarrow \infty} \int_t^{t_f} \int_0^L [(\phi_{yy} + \chi_{yy})^2 + \chi_{xx}^2]|_{y=-1} dx dt. \quad (7)$$

Subsequently, flow quantities are spectrally decomposed by using circular functions in the streamwise direction and Chebyshev polynomials in the vertical direction. We expand ϕ and χ as follows:

$$\phi = \sum_{n=1}^N \sum_{m=0}^M [a_{nm}(t)\cos(\alpha_n x) + b_{nm}(t)\sin(\alpha_n x)]C_m(y), \quad (8)$$

$$\chi = \sum_{n=1}^N [p_n(t)\cos(\alpha_n x) + q_n(t)\sin(\alpha_n x)]D(y), \quad (9)$$

where $\alpha_n = 2\pi n/L$. Functions C_m and D are combinations of Chebyshev polynomials constructed to satisfy the boundary conditions, i.e., $C_m(\pm 1) = C'_m(\pm 1) = D(1) = D'(\pm 1) = 0$ and $D(-1) = 1$. We also expand the measurement function z as follows:

$$z = \sum_{n=1}^N [c_n(t)\cos(\alpha_n x) + d_n(t)\sin(\alpha_n x)]. \quad (10)$$

Substituting expansions (8), (9), and (10) into equations (5) and (6) and using Galerkin's projection, we obtain

$$\frac{dy}{dt} = Ay + B_1 u + B_2 \frac{du}{dt}, \quad z = Cy + D_3 u. \quad (11)$$

To transform the above equations into standard state-space form, we define a new vector $x = y + B_2 u$, and two new matrices $B = B_1 + AB_2$, $D = D_3 + CB_2$. Finally, we obtain the state-space equations

$$\frac{dx}{dt} = Ax + Bu, \quad z = Cx + Du, \quad (12)$$

with initial condition $x(0) = x_0$, where x is the internal state vector, u is the control vector, and z is the measurement vector. Matrices A , B , and C contain the dynamics of the Poiseuille flow, actuators, and sensors, respectively. Matrix D contains the direct coupling between sensors and actuators. The cost function (7) becomes

$$J = \lim_{t_f \rightarrow \infty} \int_t^{t_f} [z^T z + u^T W^T W u] dt, \quad (13)$$

where the superscript T denotes transpose. The matrix W is obtained by spectrally decomposing the last term in the cost function (7).

The advantage of the present formulation is that the whole problem decouples with respect to the wave number. All matrices in Eqs. (12) and (13) are block diagonal. The block diagonal structure of the matrix A was first recognized in Ref. [24]. The above state-space system is consequently equivalent to N state-space subsystems, one for each wave number. For a given wave number r the state-space equations are

$$\frac{dx_r}{dt} = A_r x_r + B_r u_r, \quad z_r = C_r x_r + D_r u_r, \quad (14)$$

with initial condition $x_r(0) = x_{r0}$. Vectors x_r , u_r , and z_r have the following structure: $x_r = [a_{r0}, \dots, a_{rM}, b_{r0}, \dots, b_{rM}]^T$, $u_r = [p_r, q_r]^T$, $z_r = [c_r, d_r]^T$. The cost function also decouples with respect to the wave number, and we obtain N optimal performance indexes. For a given wave number r , the cost function is defined as follows:

$$J_r = \lim_{t_f \rightarrow \infty} \int_t^{t_f} [z_r^T z_r + u_r^T W_r^T W_r u_r] dt. \quad (15)$$

Consequently, the design of an optimal and robust controller for system (12) with Eq. (13) has been reduced to the independent design of N optimal and robust controllers, one for each wave number, for the subsystems (14) with Eq. (15).

The challenge of the present study is to reduce the size of the controller. The controller of the full system would have $2N(M+1)$ states. A controller with thousands of states is of no interest in engineering applications, because of the amount of hardware and computer power necessary to compute a real-time control law. We derive a lower order controller in two steps: First we construct a lower order model of Eq. (14), and subsequently we design an optimal and robust controller for the reduced-order model. To obtain a lower order model, we transform Eq. (14) into Jordan canonical form. The matrices \hat{A}_r , \hat{B}_r , \hat{C}_r , and \hat{D}_r that describe the dynamics of the reduced-order model are obtained from the matrices in Jordan canonical form by retaining rows and columns corresponding to equally well controllable or observable states. Hat denotes the quantities associated with the reduced-order model.

The design of an optimal and robust controller for the LQG (\mathcal{H}_2) problem is divided in two parts: the linear quadratic regulator (LQR) and the minimum variance estimator (Kalman-Bucy filter) [27,28]. The LQR provides an optimal control law in terms of the internal state vector. In general, however, the internal state vector is not directly measurable. The Kalman-Bucy filter provides an optimal estimate of the internal state vector in terms of the measurement vector z_r . The result of the LQG (\mathcal{H}_2) design of an optimal and robust controller based on the reduced-order model of Eq. (14) is summarized by the following equations:

$$u_r = -\hat{K}_r \tilde{x}_r, \quad (16)$$

$$\frac{d\tilde{x}_r}{dt} = \hat{A}_r \tilde{x}_r + \hat{B}_r u_r + \hat{L}_r [z_r - \hat{C}_r \tilde{x}_r - \hat{D}_r u_r], \quad (17)$$

with initial conditions $\tilde{x}_r(0) = 0$. Equation (16) is the control law. The gains matrix \hat{K}_r is obtained by minimizing the optimal performance index

$$\hat{J}_r = \lim_{t_f \rightarrow \infty} \int_t^{t_f} [\tilde{z}_r^T \tilde{z}_r + u_r^T W_r^T W_r u_r] dt, \quad (18)$$

where $\tilde{z}_r = \hat{C}_r \tilde{x}_r - \hat{D}_r u_r$. Equation (17) is the minimum variance estimator. The matrix \hat{L}_r is obtained by minimizing the variance of the estimated state vector \tilde{x}_r with respect to the internal state vector \hat{x}_r , assuming that the reduced model of Eq. (14) is affected by additive Gaussian white noise. In

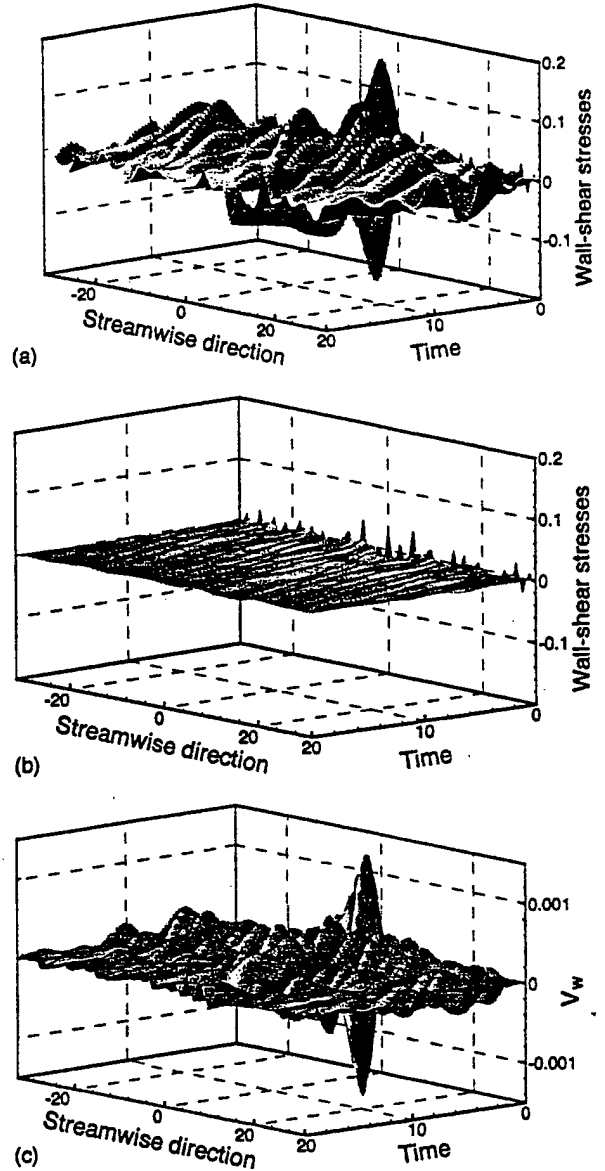


FIG. 2. Temporal evolution of wall-shear stress along the bottom wall of the channel: uncontrolled case (a); controlled case (b). Temporal evolution of blowing and suction along the bottom wall of the channel (c).

this study, however, the power spectral densities of the additive noise are used as design parameters to produce robust controllers. The initial condition $\tilde{x}_r(0) = 0$ implies that the estimator starts with no information about \hat{x}_r .

Figure 1 links with simplicity the mathematical formulation to its computational implementation, by summarizing in a block diagram the control strategy described above. The controller can be programmed in a computer routine whose input is an array containing the gradients of the streamwise velocity component, and whose output is an array containing the blowing and suction at the wall. The gradient of the streamwise velocity component, ψ_{yy} , is converted by a fast Fourier transform (FFT) into z_r 's. Each pair of estimator (17) and controller (16) blocks is integrated in time by, for example, a third-order low-storage Runge-Kutta scheme. Parallel computation produces u_r 's. An inverse FFT converts u_r 's into the actuating signal u_w . This routine can be embed-

ded in any Navier-Stokes solver able to handle time-dependent boundary conditions for the control of more realistic two-dimensional transitional boundary layers [29].

Figure 1 also provides the basic architecture for the potential implementation of the present controller in practical engineering applications. The gradient of the streamwise velocity component, ψ_{yy} , can be measured by microelectromechanical-systems (MEMS) hot film sensors [30]. Analog to digital converters (A/D) and digital signal processors (DSP's) convert the measured gradients into z_r 's. Each pair of estimator (17) and control (16) blocks is replaced by a microprocessor, and a parallel computation produces u_r 's. A DSP and a digital to analog converter (D/A) produce the actuating signal. Finally, MEMS technology will provide the necessary hardware. Note that a variety of actuators can mimic small amplitude blowing and suction at the wall: porous walls, micropumps, deformable walls, and thermal actuators [30].

We use a combination of unsteady modes and transient growth to create a worse scenario test case. We choose the Reynolds number and channel length in order to have at least a few unstable modes. The nonorthogonality of the eigenfunctions associated with Eq. (1) permits us to construct initial conditions leading to transient growth; see Ref. [3] for references. We obtain initial conditions specifically able to generate transient growth of the WSS, instead of internal energy, by modifying a technique proposed in Ref. [31]. Although transient growth will be eventually subdued by the viscous effects, it permits testing the capability of the controller in suppressing disturbances that can trigger nonlinear effect and transition to turbulence.

We design a controller for two-dimensional Poiseuille flow in a periodic channel of length $L=20\pi$ at $Re=10\,000$. The wave numbers $n=8,9$, and 10 are unstable. We use a grid resolution of $N=32$ and $M=124$. The order of the full system is 8000. Using the model reduction technique previously described, we create a reduced model of order 640. This reduced model maximizes the ratio between performance and the number of states. We derive 32 controllers of order 20, one for each wave number. Controllers operate in parallel. Figure 2(a) shows the temporal evolution of the

WSS along the bottom wall of the channel for the uncontrolled case. The WSS presents a rich structure because of the transient growth of 32 stable and unstable wave numbers. Figures 2(b) and 2(c) show the temporal evolution of the controlled WSS and of the blowing and suction along the bottom wall of the channel. Although the estimator starts with no information about the internal state of the system, the controller reduces the initial WSS in the first few time steps. Subsequently, the amplitude of blowing and suction rises to suppress the effects of transient growth. Eventually, blowing and suction decreases as the transient growth subdues. The controlled WSS shows only some low amplitude ripples during the entire simulation. The comparison of the Figs. 2(a) and 2(b) shows up to 90% WSS reduction. The remaining unsuppressed WSS is due to the modes that cannot be controlled. The performance of the controller can be improved at the price of increasing its order.

In conclusion, we presented a framework for the application of LQG (\mathcal{H}_2) design and model reduction to flows of interest in fluid mechanics and plasma physics. As a case study, this framework has been used to design an optimal and robust reduced-order controller able to suppress up to 90% of the WSS in a two-dimensional transitional channel flow. This controller can be programmed in a computer routine whose inputs are the gradients of the streamwise velocity component, and whose outputs are the blowing and suction at the wall. This routine, suited for parallel computing, can be embedded in any Navier-Stokes solver for the control of more realistic two-dimensional transitional boundary layers [29]. We also presented a hardware architecture for the potential implementation of the controller in engineering applications. Extensions of LQG (\mathcal{H}_2) design and applications of \mathcal{H}_∞ design [27,28] to three-dimensional Poiseuille flow and two- and three-dimensional Blasius boundary layers are in progress.

The authors thank Dr. J. Burns, Dr. S. Joshi, Dr. R.E. Kelly, Dr. J. Kim, and Dr. R.T. MCloskey for enlightening discussions. This work was supported by AFOSR Grant No. F49620-97-1-0276 and by NASA Grant No. NCC 2-374 Pr 41.

-
- [1] M. Gad-el-Hak, *AIAA J.* 32, 1753 (1994).
 - [2] V. J. Modi, *J. Fluids Struct.* 11, 627 (1997).
 - [3] H. L. Reed, W. S. Saric, and D. Arnal, *Annu. Rev. Fluid Mech.* 28, 389 (1996).
 - [4] R. W. Barnwell and M. Y. Hussaini *Natural Laminar Flow and Laminar Flow Control* (Springer-Verlag, New York, 1992).
 - [5] P. Koumoutsakos, *Phys. Fluids* 9, 3808 (1997).
 - [6] R. Rathnasingham and K. S. Breuer, *Phys. Fluids* 9, 1867 (1997).
 - [7] C. Lee, J. Kim, D. Babcock, and R. Goodman, *Phys. Fluids* 9, 1740 (1997).
 - [8] C. H. Crawford and G. E. Karniadakis, *Phys. Fluids* 9, 788 (1997).
 - [9] T. Kato, Y. Fukunishi, and R. Kobayashi, *JSME Int. J. Ser. B* Fluids Thermal Eng. 40, 536 (1997).
 - [10] P. A. Nelson, M. C. M. Wright, and J. L. Rioual, *AIAA J.* 35, 85 (1997).
 - [11] H. A. Carlson and J. L. Lumley, *J. Fluid Mech.* 329, 341 (1996).
 - [12] B. F. Farrell and P. J. Ioannou, *Phys. Fluids* 8, 1257 (1996).
 - [13] R. D. Joslin, G. Eriebacher, and M. V. Hussaini, *J. Fluids Eng. Trans. ASME* 118, 494 (1996).
 - [14] T. Lee, M. Fisher, and W. H. Schwarz, *J. Fluid Mech.* 288, 37 (1995).
 - [15] P. Hackenberg, J. L. Rioual, O. R. Tutty, and P. A. Nelson, *Appl. Sci. Res.* 54, 293 (1995).
 - [16] U. Rist and H. Fasel, *J. Fluid Mech.* 298, 211 (1995).
 - [17] S. Hubbard and N. Riley, *Int. J. Heat Mass Transf.* 38, 3209 (1995).

- [18] R. D. Joslin *et al.*, AIAA J. **33**, 1521 (1995).
- [19] H. H. Hu and H. H. Bau, Proc. R. Soc. London, Ser. A **447**, 299 (1994).
- [20] J. Jimenez, Phys. Fluids **6**, 944 (1994).
- [21] M. M. Elrefae, Eng. Anal. Boundary Elements **14**, 239 (1994).
- [22] A. H. M. Kwong and A. P. Dowling, AIAA J. **32**, 2409 (1994).
- [23] H. Choi, P. Moin, and J. Kim, J. Fluid Mech. **262**, 75 (1994).
- [24] S. S. Joshi, J. L. Speyer, and J. Kim, J. Fluid Mech. **332**, 157 (1997).
- [25] S. N. Singh and P. R. Bandyopadhyay, J. Fluids Eng. Trans. ASME **119**, 852 (1997).
- [26] S. S. Joshi, J. L. Speyer, and J. Kim, *Proceedings of the 34th IEEE Conference on Decision and Control, New Orleans, LA, December 1995* (IEEE, New York, 1995), p. 921.
- [27] K. Zhou, J. C. Doyle, and K. Glover, *Robust and Optimal Control* (Prentice Hall, Englewood Cliffs, NJ, 1996).
- [28] I. Rhee and J. L. Speyer, IEEE Trans. Autom. Control. **36**, 1021 (1996).
- [29] L. Cortelezzi, K. H. Lee, J. Kim, and J. L. Speyer, Int. J. Comput. Fluid Dyn. (to be published).
- [30] C. M. Ho and Y. C. Tai, J. Fluids Eng. Trans. AMSE **118**, 437 (1996).
- [31] B. F. Farrell, Phys. Fluids **31**, 2093 (1988).

APPENDIX B

Finite Dimensional Optimal Control of Poiseuille Flow

S.S. Joshi, J.L. Speyer, J. Kim

Finite Dimensional Optimal Control of Poiseuille Flow

Sanjay S. Joshi

Jet Propulsion Laboratory, California Institute of Technology, Pasadena, California 91101
and

Jason L. Speyer and John Kim

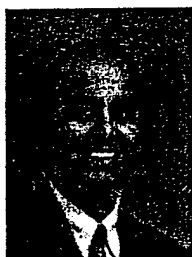
University of California, Los Angeles, Los Angeles, California 90095

In this paper we consider linear stabilization of plane, Poiseuille flow using linear quadratic Gaussian optimal control theory. It is shown that we may significantly increase the dissipation rate of perturbation energy, while reducing the required control energy, as compared with that reported using simple, integral compensator control schemes. Poiseuille flow is described by the infinite dimensional Navier–Stokes equations. Because it is impossible to implement infinite dimensional controllers, we implement high but finite order controllers. We show that this procedure in theory can lead to destabilization of unmodeled dynamics. We then show that this may be avoided using distributed control or, dually, distributed sensing. A problem in high plant order linear quadratic Gaussian controller design is numerical instability in the synthesis equations. We show a linear quadratic Gaussian design that uses an extremely low-order plant model. This low-order controller produces results essentially equivalent to the high-order controller.

Nomenclature

A, B, C, D = state-space representation of system
 E_u = control energy
 H = channel half-height
 $J(u)$ = cost functional
 j = $\sqrt{-1}$

K_e, \bar{K}_e = estimator gain
 L = nondimensional channel length
 P, \bar{P} = solution of controller Riccati equation
 P_e, \bar{P}_e = covariance of estimator error
 $P^*(x, y, t)$ = primary pressure field solution
 $\hat{p}(x, y, t)$ = small perturbation of pressure



Sanjay S. Joshi received his B.S. degree in Electrical Engineering from Cornell University, Ithaca, New York, in 1990 and his Ph.D. degree in Electrical Engineering from the University of California, Los Angeles, in 1996. Since 1991 he has been a Member of the Technical Staff at the Jet Propulsion Laboratory, California Institute of Technology, in the Guidance and Control Analysis Staff. Currently, he is a researcher and a technical lead in the NASA Origins Program in space-based interferometry focusing on multidisciplinary modeling and control of complex optomechanical instruments. His research interests include multidisciplinary modeling/control/design, failure detection and isolation, spacecraft autonomy, and distributed control and sensing. He has worked on applications in aerospace systems including interplanetary spacecraft systems and fluid dynamic systems. He is a Member of AIAA.



Jason L. Speyer received his S.B. degree in Aeronautics and Astronautics from Massachusetts Institute of Technology in 1960 and his Ph.D. degree in Applied Mathematics from Harvard University in 1968. His industrial experience includes research at Boeing, Raytheon, Analytic Mechanics Associates, and the Charles Stark Draper Laboratory. He was the Harry H. Power Professor in Aerospace Engineering at the University of Texas, Austin, and is currently Professor in the Department of Mechanical and Aerospace Engineering at the University of California, Los Angeles. He spent research leaves as a Lady Davis Professor at the Technion–Israel Institute of Technology, Haifa, Israel, in 1983 and was the 1990 Jerome Hunsaker Visiting Professor of Aeronautics and Astronautics at the Massachusetts Institute of Technology. In 1985 he received the Mechanics and Control of Flight Award and in 1995 held the Dryden Lectureship in Research. He also has served on the U.S. Air Force Scientific Advisory Board. He is a Fellow of AIAA.



John Kim received his Ph.D. in Mechanical Engineering from the Department of Mechanical Engineering at Stanford University in 1978. He joined the Department of Mechanical and Aerospace Engineering at the University of California, Los Angeles, in 1993 as Rockwell International Professor in Engineering. Before 1993 he was with NASA Ames Research Center, where he conducted research in the areas of turbulence and transition physics as Chief of the Turbulence and Transition Physics Branch. He has pioneered the development of numerical simulations as a reliable tool for studying transitional and turbulent flows. His current research interest includes turbulence control through various means, application of systems control theory being one of them. He currently serves as the Editor of *Physics of Fluids*. He is an Associate Fellow of AIAA.

Q_e, W_e	= power spectral density matrices of process and measurement noises
$q(t)l(x)f(y)$	= boundary input function
R, Λ	= state and control weighting matrices
Re	= Reynolds number $U_c H/\nu$
s	= complex frequency
U_c	= centerline velocity
$U^*(y)$	= primary Poiseuille flow solution for velocity in x direction
$u(t), \bar{u}(t)$	= scalar input function
$\hat{u}(x, y, t), \hat{v}(x, y, t)$	= small perturbation of flow velocity in x and y directions
$V^*(x, y, t)$	= primary velocity of flow in y direction
$v(t), w(t)$	= Gaussian, white process and measurement noises
x, y	= channel coordinates in streamwise and wall-normal directions
$x(t), \bar{x}(t)$	= state vector
$\hat{x}(t)$	= estimate of state vector
z	= streamwise component of shear
α, α_0	= wave number, fundamental wave number
γ	= degree of closed-loop stability
$\delta()$	= delta function
ν	= kinematic viscosity
ϕ	= modified stream function
ψ	= stream function
$[a, b]$	= a^*b
$[a(x), b(x)]_x$	= inner product of a and b defined as $\frac{1}{L} \int_{-L/2}^{L/2} a(x)b(x) dx$
$()_u, ()_m$	= unmodeled and modeled components
$()^*$	= conjugate transpose
$ \cdot $	= absolute value
\triangleq	= defined as

I. Introduction

FEEDBACK control of plane Poiseuille flow was introduced in Hu and Bau¹ and Joshi et al.² Hu and Bau¹ approached the problem as a modified Orr-Sommerfeld solution problem. Joshi et al.² introduced a control-theoretic framework to the problem. It was shown that the governing Navier-Stokes equations can be converted to control-theoretic transfer function and state-space models using a numerical discretization method.² Using the transfer function models, it was shown that plane Poiseuille flow (channel flow) can be stabilized using a simple, constant gain feedback, integral compensator controller.² By choosing proper sensor locations, Joshi et al.² were able to achieve a stable, closed-loop system that was extremely robust to changing Reynolds numbers. The subject of this paper is the description of an optimal controller by moving away from classical transfer function control design to state space methods. In the transfer function design used thus far,² the system was stabilized, but the stable system still had closed-loop eigenvalues very near the imaginary s axis. This resulted in slow dissipation of perturbation energy. The present design provides an optimal, stabilizing controller that achieves a significantly faster dissipation rate of perturbation energy, while reducing required control energy.

Unlike the simple integral feedback control of Joshi et al.,² optimal controllers are complicated systems in themselves.³ This adds considerably to the complexity of the overall closed-loop system. In fact, many beneficial qualities have been proven only when the controller is of the same dimension as that of the plant. In the flow case, this brings a special problem because the plant is of infinite dimension. Theoretically, the controller must also be of infinite dimension. This is impractical for many reasons. First, it is impossible to physically implement an infinite dimensional controller. Second, the use of even very high-order finite dimensional plants for controller design leads to numerical problems in the optimal control synthesis equations. We will design an optimal controller using a finite order model of the infinite dimensional plant. However, applying reduced-order controllers to full-order plants has the risk of making unmodeled, stable parts of the plant unstable. Therefore, controllers must be designed to ensure this does not happen.

This paper is organized as follows. In Sec. II, the linear channel flow problem, state-variable control models, and the single-wave-number flow model are reviewed. This section is essentially a review of Ref. 2. In Secs. III and IV, a linear quadratic Gaussian (LQG) controller design is introduced, and ways in which closed-loop eigenvalues can be made stable to a prescribed degree are shown. Section V explains how the unavoidable unmodeled dynamics of any reduced-order model of an infinite dimensional plant can lead to closed-loop instability in LQG design. Distributed actuation and distributed sensing are shown to be dual solutions to the stability problem. Section VI demonstrates the performance of high-order optimal controllers. Section VII presents an extremely low-order controller design that achieves comparable performance to the high-order optimal controller design. Section VIII presents conclusions.

II. Linear Channel Flow Control Problem

A. Dynamic Equations

We consider the same plant as in Ref. 2, i.e., two-dimensional, plane, Poiseuille flow between two parallel, stationary plates (Fig. 1). Let the channel be of finite length and finite height, with the centerline at zero. The flow in the channel is described by the Navier-Stokes equations. Poiseuille flow is an exact solution to the nonlinear, incompressible Navier-Stokes equations given flow driven by an externally imposed pressure gradient through two stationary walls. It is given as $U^*(x, y, t) = U(y) = 1 - y^2$, $V^*(x, y, t) = 0$, and $P^*(x, y, t) = -2x/Re$. Given the primary Poiseuille flow, consider small perturbations in the velocities of $\hat{u}(x, y, t)$ in the horizontal direction, $\hat{v}(x, y, t)$ in the vertical direction, and $\hat{p}(x, y, t)$ in the pressure field. The linearized, incompressible Navier-Stokes equations may be formed by substituting the primary flow and small perturbations into the nonlinear, incompressible Navier-Stokes equations and disregarding the second-order terms involving the perturbations:

$$\frac{\partial \hat{u}(x, y, t)}{\partial t} + U(y) \frac{\partial \hat{u}(x, y, t)}{\partial x} + \frac{dU(y)}{dy} \hat{v}(x, y, t) = -\frac{\partial \hat{p}(x, y, t)}{\partial x} + \frac{1}{Re} \nabla^2 \hat{u}(x, y, t) \quad (1)$$

$$\frac{\partial \hat{v}(x, y, t)}{\partial t} + U(y) \frac{\partial \hat{v}(x, y, t)}{\partial x} = -\frac{\partial \hat{p}(x, y, t)}{\partial y} + \frac{1}{Re} \nabla^2 \hat{v}(x, y, t) \quad (2)$$

$$\frac{\partial \hat{u}(x, y, t)}{\partial x} + \frac{\partial \hat{v}(x, y, t)}{\partial y} = 0 \quad (3)$$

where the flow variables are nondimensionalized by the channel half-height and the centerline velocity. By introducing a stream function, $\psi(x, y, t)$, where

$$\hat{u}(x, y, t) \triangleq \frac{\partial \psi(x, y, t)}{\partial y} \quad (4)$$

and

$$\hat{v}(x, y, t) \triangleq -\frac{\partial \psi(x, y, t)}{\partial x} \quad (5)$$

Eqs. (1-3) may be combined into a single equation:

$$\frac{\partial}{\partial t} \frac{\partial^2 \psi}{\partial x^2} + \frac{\partial}{\partial t} \frac{\partial^2 \psi}{\partial y^2} = -U(y) \frac{\partial^3 \psi}{\partial x^3} - U(y) \frac{\partial}{\partial x} \frac{\partial^2 \psi}{\partial y^2} + \frac{d^2 U(y)}{dy^2} \frac{\partial \psi}{\partial x} + \frac{1}{Re} \nabla^2 (\nabla^2 \psi) \quad (6)$$

Assume periodic boundary conditions in the streamwise x direction. For channel flow, with rigid plates at $y = -1$ and 1 , the no-slip boundary conditions become

$$\psi(x, y = -1, t) = 0 \quad (7)$$

$$\frac{\partial \psi}{\partial y}(x, y = -1, t) = 0 \quad (8)$$

$$\psi(x, y = 1, t) = 0 \quad (9)$$

$$\frac{\partial \psi}{\partial y}(x, y = 1, t) = 0 \quad (10)$$

With an initial condition,

$$\psi(x, y, t = 0) = g(x, y) \quad (11)$$

the boundary value problem is completely formed. Equations (6–11) represent the starting point for construction of a feedback control system. These equations do not include any control terms and they do not describe any sensing of flowfield variables.

B. Boundary Input

We consider the case of blowing/suction at the lower wall of the channel. The boundary conditions are now modified from before to include boundary input, represented as the known separable function $q(t)l(x)f(y)$,

$$\psi(x, y = -1, t) = q(t)l(x)f(y = -1) \quad (12)$$

$$\frac{\partial \psi}{\partial y}(x, y = -1, t) = q(t)l(x)\frac{\partial f(y = -1)}{\partial y} = 0 \quad (13)$$

$$\psi(x, y = 1, t) = 0 \quad (14)$$

$$\frac{\partial \psi}{\partial y}(x, y = 1, t) = q(t)l(x)\frac{\partial f(y = 1)}{\partial y} = 0 \quad (15)$$

Note that these conditions constrain the function $f(y)$ such that $f(y = -1) \neq 0$, $[\partial f(y = -1)]/\partial y = 0$, $f(y = 1) = 0$, and $[\partial f(y = 1)]/\partial y = 0$. Many functions may be appropriate. One such function is

$$f(y) = \frac{1}{2}y^4 + \frac{1}{4}y^3 - y^2 - \frac{3}{4}y + 1 \quad (16)$$

To relate boundary conditions on ψ to blowing/suction in the wall-normal direction, we use Eq. (5) to relate $\hat{v}(x, y, t)$ and $\psi(x, y, t)$. Then Eq. (12) becomes

$$\hat{v}(x, y = -1, t) = -q(t)\frac{\partial l(x)}{\partial x}f(y = -1) \quad (17)$$

Note that $\hat{v}(x, y, t)$ is related to the derivative of $l(x)$.

The homogeneous equation (6) and the inhomogeneous boundary condition (12) can be converted into an inhomogeneous equation with homogeneous boundary conditions by introducing

$$\phi(x, y, t) \triangleq \psi(x, y, t) - q(t)f(y)l(x) \quad (18)$$

Then by substituting Eq. (18) into Eq. (6), we obtain

$$\begin{aligned} \frac{\partial}{\partial t} \frac{\partial^2 \phi}{\partial x^2} + \frac{\partial}{\partial t} \frac{\partial^2 \phi}{\partial y^2} = & -U(y)\frac{\partial^3 \phi}{\partial x^3} - U(y)\frac{\partial}{\partial x} \frac{\partial^2 \phi}{\partial y^2} \\ & + \frac{d^2 U(y)}{dy^2} \frac{\partial \phi}{\partial x} + \frac{1}{Re} \frac{\partial^4 \phi}{\partial x^4} + 2 \frac{1}{Re} \frac{\partial^2}{\partial x^2} \frac{\partial^2 \phi}{\partial y^2} + \frac{1}{Re} \frac{\partial^4 \phi}{\partial y^4} \\ & - \frac{\partial q(t)}{\partial t} \frac{\partial^2 l(x)}{\partial x^2} f(y) - \frac{\partial q(t)}{\partial t} l(x) \frac{\partial^2 f(y)}{\partial y^2} \\ & - q(t) \frac{\partial^3 l(x)}{\partial x^3} U(y) f(y) - q(t) \frac{\partial l(x)}{\partial x} U(y) \frac{\partial^2 f(y)}{\partial y^2} \\ & + q(t) \frac{\partial l(x)}{\partial x} \frac{d^2 U(y)}{dy^2} f(y) + \frac{1}{Re} q(t) \frac{\partial^4 l(x)}{\partial x^4} f(y) \\ & + 2 \frac{1}{Re} q(t) \frac{\partial^2 l(x)}{\partial x^2} \frac{\partial^2 f(y)}{\partial y^2} + \frac{1}{Re} q(t) l(x) \frac{\partial^4 f(y)}{\partial y^4} \end{aligned} \quad (19)$$

The boundary conditions in terms of ϕ are now $\phi(y = -1) = 0$, $[\partial \phi(y = -1)]/\partial y = 0$, $\phi(y = 1) = 0$, and $[\partial \phi(y = 1)]/\partial y = 0$. The first two lines of Eq. (19) are the original dynamical equation, Eq. (6), and the next four lines are all known input terms.

C. Boundary Output

We use the streamwise component of shear at a single boundary point, $z(x_i, y = -1, t)$, as our boundary output, which is given by $z(x_i, y = -1, t) = [\partial \hat{u}(x_i, y = -1, t)]/\partial y$. By expressing $\hat{u}(x_i, y = -1, t)$ in terms of the stream function (4), $z(x_i, y = -1, t) = [\partial^2 \psi(x_i, y = -1, t)]/\partial y^2$, and by observing Eq. (18),

$$\begin{aligned} z(x_i, y = -1, t) &= \frac{\partial^2 \psi(x_i, y = -1, t)}{\partial y^2} \\ &= \frac{\partial^2 \phi(x_i, y = -1, t)}{\partial y^2} + q(t) \frac{\partial^2 f(y = -1)}{\partial y^2} l(x_i) \end{aligned} \quad (20)$$

D. State-Space Formulation

As described in Ref. 2, the linear partial differential flow equation (19) can be converted to a set of linear ordinary differential equations by use of a Galerkin method. Approximate the solution of Eq. (19) as

$$\phi(x, y, t) = \sum_{n=-N}^N \sum_{m=0}^M a_{nm}(t) P_n(x) \Gamma_m(y) \quad (21)$$

and then use appropriate inner products to obtain a first-order system of equations.⁴ In Eq. (21), the various $\Gamma_m(y)$ are formed from Chebyshev polynomials⁴ and

$$P_n(x) \triangleq e^{jn\alpha_0 x}, \quad \alpha_0 = 2\pi/L, \quad -L/2 \leq x \leq L/2 \quad (22)$$

where the value $(n\alpha_0)$ is called the wave number α of the system, whereas α_0 is called the fundamental wave number. Note that only integral multiples of the fundamental wave number are represented in the solution (21). This comes about because periodic boundary conditions in the x direction can only be satisfied by integral numbers of the fundamental wave number.

The resulting ordinary differential equations are then expressed in state-space form by defining the state as a vector of coefficients $a_{nm}(t)$ from Eq. (21). The result is the standard state-space representation

$$\frac{dx(t)}{dt} = Ax(t) + Bu(t) \quad (23)$$

$$z(t) = Cx(t) + Du(t) \quad (24)$$

In our case, $D = 0$.

E. Single-Wave-Number Model

We consider the periodic channel model shown in Fig. 1 with boundary blowing/suction and boundary shear measurement. The Reynolds number considered is $Re = 1 \times 10^4$. The total length of the channel is $L = 4\pi$ leading to the fundamental wave number $\alpha_0 = 0.5$. Recall that only integral multiples of this fundamental wave number may exist in the periodic channel. For the single wave number model, only one wave number is included in the model, corresponding to $\alpha = n\alpha_0 = 1.00$. This wave number is selected because it is the only wave number that leads to unstable modes for this channel geometry.⁴ Input is distributed along the entire bottom plate with a sinusoidal weighting function, $l(x) = \sin(x)$. This type of distributed input has very favorable properties. It will be shown in

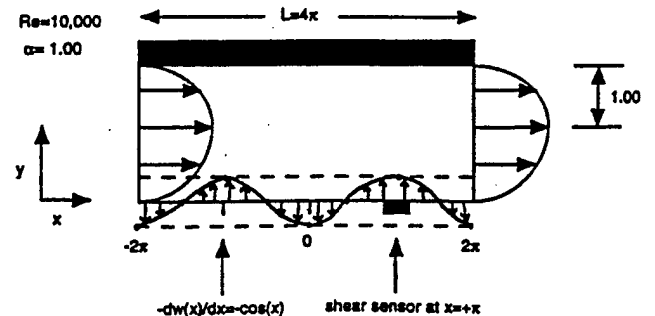


Fig. 1 System model for Poiseuille channel flow.

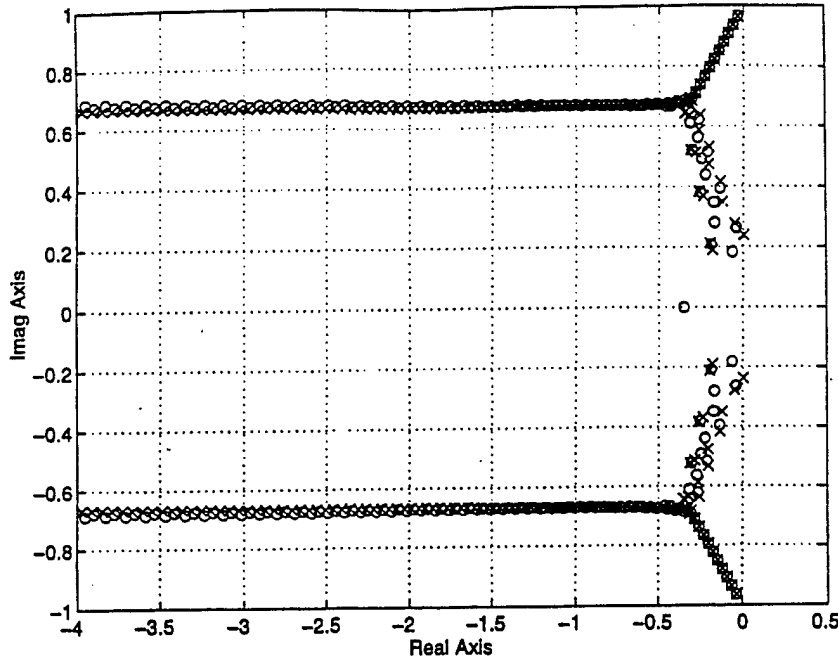


Fig. 2 Pole (x)/zero (o) configuration, channel model: $Re = 1 \times 10^4$, shear sensor at π , $l(x) = \sin(x)$, $L = 4\pi$, and $\alpha = 1.0$.

Sec. V that a distributed input of this type leads to a system in which all modes are uncontrollable except those associated with the wave number of $l(x)$. In this case, the wave number of $l(x) = \sin(1.0x)$ is $\alpha = 1.0$. Therefore, all modes resulting from all wave numbers other than 1.0 are uncontrollable. This will allow us to consider only those poles and zeros associated with $\alpha = 1.0$ because the control will affect these modes only. Note that the physical blowing/suction is described by the equation $\hat{v}(x, y, t) = -q(t)[\partial l(x)/\partial x]f(y = -1) = -q(t)\cos(x)f(y = -1)$, Eq. (17). The $f(y)$ function in the input is chosen as in Eq. (16). To visualize the control theoretic model, the A , B , and C matrices of the state-space model are transformed to transfer function form. Figure 2 shows the locations of the poles and zeros in the s plane for the channel flow system of Fig. 1. The numerical verification of these poles and zeros was described in Ref. 2.

III. Linear Quadratic Optimal Control Design with Prescribed Degree of Stability

To achieve a prescribed degree of stability³ with an optimal controller, consider the exponential cost functional

$$J(u) \triangleq \lim_{T \rightarrow \infty} \frac{1}{T} \int_0^T e^{2\gamma t} \{ [R\dot{x}(t), \dot{x}(t)] + [\Lambda u(t), u(t)] \} dt \quad (25)$$

where the matrix R is semipositive definite, Λ is positive definite and defined a priori, and γ is a positive scalar. We may show (see Ref. 5) that we may convert this problem into a quadratic form and solve for a controller that prescribes all eigenvalues of the closed-loop system to be to the left of $s = -\gamma$. Rewrite the cost functional as

$$J(u) = \lim_{T \rightarrow \infty} \frac{1}{T} \int_0^T [R\dot{x}(t), \dot{x}(t)] + [\Lambda e^{\gamma t} u(t), e^{\gamma t} u(t)] dt \quad (26)$$

Define $\bar{x}(t) \triangleq e^{\gamma t} x(t)$ and $\bar{u}(t) \triangleq e^{\gamma t} u(t)$. Then

$$J(\bar{u}) = \lim_{T \rightarrow \infty} \frac{1}{T} \int_0^T [R\dot{\bar{x}}, \dot{\bar{x}}] + [\Lambda \bar{u}, \bar{u}] dt \quad (27)$$

Note

$$\frac{d\bar{x}(t)}{dt} = \frac{d}{dt}[e^{\gamma t} x(t)] = \gamma e^{\gamma t} x(t) + e^{\gamma t} \frac{dx(t)}{dt} \quad (28)$$

By substituting for $dx(t)/dt$,

$$\frac{d\bar{x}}{dt} = (A + I\gamma)\bar{x} + B\bar{u} \quad (29)$$

Let $\bar{A} \triangleq A + I\gamma$. Then the optimal control is given by $\bar{u}_{opt}(t) = -\Lambda^{-1}B^* \bar{P} \bar{x}(t)$ and

$$u_{opt}(t) = -\Lambda^{-1}B^* \bar{P} x(t) \quad (30)$$

where \bar{P} is obtained by solving the Riccati equation

$$\bar{P}\bar{A} + \bar{A}^* \bar{P} - \bar{P}B\Lambda^{-1}B^* \bar{P} + R = 0 \quad (31)$$

The new closed-loop system dynamics matrix becomes

$$A - B\Lambda^{-1}B^* \bar{P} \quad (32)$$

whose eigenvalues are all to the left of $s = -\gamma$. It can be shown (see Ref. 4) that, if (A, B) is controllable and (A, R) is observable, then $(A + \gamma I, B)$ is controllable and there exists a positive definite solution \bar{P} of the matrix Riccati equation (31) for $R \geq 0$.

In theory, for full-order plant models, there is no restriction on the value of γ . In practice, however, for controllers built using reduced-order plant models, γ is limited by robustness of the controller when applied to the full-order system.

IV. Optimal Estimator Design with Prescribed Degree of Stability

In the previous section, we derived an optimal controller. As can be seen from Eq. (30), the control is always represented in terms of the current state $x(t)$. These states, however, are not available to us in the channel problem. Instead, we have access to shear measurements at only one or several locations along the boundary. Therefore, we must construct an observer to estimate the state $x(t)$ from the measured shear outputs $z(t)$. To see how this is done, consider a noisy version of the state-space model shown earlier:

$$\frac{dx(t)}{dt} = Ax(t) + Bu(t) + v(t) \quad (33)$$

$$z(t) = Cx(t) + w(t) \quad (34)$$

$$x_0 \triangleq x(t=0) \quad (35)$$

where (A, B) is again assumed controllable and (A, C) is assumed observable.

Assumption 1: The noise processes $v(t)$ and $w(t)$ are white, Gaussian, of zero mean, and independent of each other and have known covariances. The matrices P_0 , Q_e , and W_e are positive definite:

$$E[v(t)v^*(\tau)] = Q_e \delta(t - \tau), \quad E[v(t)] = 0 \quad (36)$$

$$E[w(t)w^*(\tau)] = W_e \delta(t - \tau), \quad E[w(t)] = 0 \quad (37)$$

$$E[x(t_0)] \triangleq m \quad (38)$$

$$E\{[x(t_0) - m][x(t_0) - m]^*\} \triangleq P_0 \quad (39)$$

where $E(\cdot)$ is an expectation operator.

It may be shown that a steady-state estimator may be constructed that minimizes the error covariance between the actual state $x(t)$ and the estimated state $\hat{x}(Z_t)$, where $Z_t = [z(l) : -\infty < l \leq t]$, i.e., the measurement history

$$\min_{\hat{x}(Z_t)} E\{[x(t) - \hat{x}(Z_t)][x(t) - \hat{x}(Z_t)]^*\} \quad (40)$$

It can be shown that the optimal estimate, in the sense of Eq. (40), is given by the conditional expectation $\hat{x}(t) \triangleq \hat{x}(Z_t) = E[x(t)/Z_t]$, where $E(\cdot/Z_t)$ is the conditional mean operator. In the linear case with Gaussian noises, the structure of the estimator is

$$\frac{d\hat{x}(t)}{dt} = A\hat{x}(t) + Bu(t) + K_e[C\hat{x}(t) - z(t)] \quad (41)$$

where

$$K_e = -P_e C^* W_e^{-1} \quad (42)$$

and P_e is calculated from a matrix Riccati equation,

$$P_e A^* + A P_e - P_e C^* W_e^{-1} C P_e + Q_e = 0 \quad (43)$$

Note that the stability of Eq. (41) depends on the stability of $(A - P_e C^* W_e^{-1} C)$. The assumptions that $W_e, Q_e > 0$ and (A, C) observable assure $\exists P_e > 0$ such that Eq. (43) is satisfied.

By considering a slightly different estimator Riccati equation, we may constrain the closed-loop estimator poles to be stable to a prescribed degree. It can be shown (see Ref. 4) that, if (A, C) is observable, then $(A + \gamma I, C)$ is observable, and there exists a positive-definite solution of the matrix Riccati equation:

$$\overline{P}_e(A + \gamma I)^* + (A + \gamma I)\overline{P}_e - \overline{P}_e C^* W_e^{-1} C \overline{P}_e + Q_e = 0 \quad (44)$$

for $Q_e > 0$, where γ is a real, positive scalar. Then all eigenvalues of $(A - \overline{P}_e C^* W_e^{-1} C)$ are all to the left of $s = -\gamma$. The new estimator gain is given as

$$\overline{K}_e = -\overline{P}_e C^* W_e^{-1} \quad (45)$$

The goal of LQG design is to combine the results of deterministic linear quadratic control theory and stochastic estimation theory to form an overall control system. As we have seen, our system equations become stochastic with the addition of noise terms. Therefore, in our controller design, we may no longer minimize a deterministic cost functional. Rather, we now minimize the expected value of the cost functional:

$$E(J) = E\left\{\lim_{T \rightarrow \infty} \frac{1}{T} \int_0^T [Rx(t), x(t)] + [\Lambda u(t), u(t)] dt\right\} \quad (46)$$

where $x(t)$ is now a stochastic process. It can be shown that the optimal control is now expressed in terms of the estimated state, $u_{\text{opt}}(t) = -\Lambda^{-1} B^* \bar{P} \hat{x}(t)$. The complete LQG solution is then

Plant:

$$\frac{dx(t)}{dt} = Ax(t) + Bu(t) + v(t) \quad (47)$$

Observation:

$$z(t) = Cx(t) + w(t) \quad (48)$$

Initial condition:

$$x_0 \triangleq x(t=0) \quad (49)$$

Estimator:

$$\frac{d\hat{x}(t)}{dt} = A\hat{x}(t) + Bu(t) + \overline{K}_e[C\hat{x}(t) - z(t)] \quad (50)$$

Feedback:

$$u_{\text{opt}}(t) = -\Lambda^{-1} B^* \bar{P} \hat{x}(t) \quad (51)$$

where \bar{P} is the positive-definite solution of Eq. (31) and \overline{K}_e is given in Eq. (45).

We may show that the overall estimator/controller system is stable by stacking the state, $x(t)$, and the error, $e(t) \triangleq \hat{x} - x$, into one vector and studying the dynamics of the new system:

$$\begin{bmatrix} \frac{dx(t)}{dt} \\ \frac{de(t)}{dt} \end{bmatrix} = \begin{bmatrix} (A - B\Lambda^{-1}B^*\bar{P}) & -B\Lambda^{-1}B^*\bar{P} \\ 0 & (A - \overline{P}_e C^* W_e^{-1} C) \end{bmatrix} \begin{bmatrix} x(t) \\ e(t) \end{bmatrix} + \begin{bmatrix} v(t) \\ -\overline{K}_e w(t) - v(t) \end{bmatrix} \quad (52)$$

The stability of the system is determined by the eigenvalues of the dynamical matrix. Clearly, the eigenvalues are composed of the eigenvalues of the closed-loop controller, $(A - B\Lambda^{-1}B^*\bar{P})$, and the eigenvalues of the closed-loop estimator, $(A - \overline{P}_e C^* W_e^{-1} C)$. We have already proven that both of these matrices are stable (under appropriate assumptions). Therefore, the overall control system is stable also. This is known as the separation principle in LQG control.

V. Effects of Unmodeled Wave Number Dynamics on the LQG Problem

We have already seen that the separation principle in LQG control allows us to show that if the controller and estimator are both stable, then the overall system is stable. We will see in this section that this principle breaks down in the presence of unmodeled dynamics.

Any finite dimensional model is a reduced-order model for the infinite dimensional channel flow problem. In terms of poles and zeros studied earlier, more poles and zeros exist in the system than are accounted for in the model and the subsequent controller design. It is easy to imagine that an unmodeled pole could be drawn to the unstable half of the s plane by a reduced-order controller. As a result, even though the designed controller may stabilize the reduced-order plant, it may not stabilize the actual infinite dimensional plant. Consider the following partition of the state-space model with noise terms added:

$$\frac{dx}{dt} = \begin{bmatrix} \frac{dx_m}{dt} \\ \frac{dx_u}{dt} \end{bmatrix} = \begin{bmatrix} A_m & 0 \\ 0 & A_u \end{bmatrix} \begin{bmatrix} x_m \\ x_u \end{bmatrix} + \begin{bmatrix} B_m \\ B_u \end{bmatrix} u(t) + \begin{bmatrix} v_m(t) \\ v_u(t) \end{bmatrix} \quad (53)$$

$$z = [C_m \quad C_u]x + w(t) \quad (54)$$

The process noise v and the measurement noise w are assumed to be Gaussian, independent, zero mean, white noise processes as in Eqs. (36) and (37). The unmodeled part is meant to denote only the dynamics of wave numbers left out of the reduced-order model, represented by $(|n| > N)$ in Eq. (21). The term A_u is assumed stable. Both A_u and A_m are of infinite dimension²— A_u because of the infinite number of wave numbers left out of the reduced-order model and A_m because of the infinite number of poles for each of the finite number of modeled wave numbers, represented by $(m > M)$ in Eq. (21).

Because we only know the modeled part of the system, we design an LQG controller/observer based on that part. Minimize the expected value of a cost functional J ,

$$E(J) = E\left\{\lim_{T \rightarrow \infty} \frac{1}{T} \int_0^T [Rx_m(t), x_m(t)] + [\Lambda u(t), u(t)] dt\right\} \quad (55)$$

where R is any semi-positive-definite matrix and Λ is any positive-definite matrix. The optimal control is of the form

$$u_{\text{opt}}(t) = -\Lambda^{-1} B_m^* \bar{P} \hat{x}_m(t) \quad (56)$$

where $\hat{x}_m(t)$ is the estimate of the modeled state and the matrix \bar{P} is calculated by solving the algebraic Riccati equation,

$$A_m^* \bar{P} + \bar{P} A_m - \bar{P} B_m \Lambda^{-1} B_m^* \bar{P} + R = 0 \quad (57)$$

with the same assumptions as in Eqs. (47–51) for the modeled parts.

Because we cannot obtain direct measurements of the current state $x_m(t)$, we construct an observer as described in Sec. IV:

$$\frac{d\hat{x}_m(t)}{dt} = A_m \hat{x}_m(t) + B_m u(t) + \bar{K}_e [C_m \hat{x}_m(t) - z(t)] \quad (58)$$

where the estimator gain $\bar{K}_e = -\bar{P}_e C_m^* W_e^{-1}$ requires the solution of another matrix Riccati equation,

$$\bar{P}_e A_m^* + A_m \bar{P}_e - \bar{P}_e C_m^* W_e^{-1} C_m \bar{P}_e + Q_e = 0 \quad (59)$$

Define the error between the estimated, modeled state, $\hat{x}_m(t)$, and the actual state, $x_m(t)$, as $e_m(t)$. Then as in Ref. 6

$$\begin{aligned} \frac{de_m(t)}{dt} &\triangleq \frac{d\hat{x}_m(t)}{dt} - \frac{dx_m(t)}{dt} \\ &= [A_m - \bar{P}_e C_m^* W_e^{-1} C_m] e_m(t) + \bar{P}_e C_m^* W_e^{-1} C_u x_u(t) \\ &\quad + \bar{P}_e C_m^* W_e^{-1} w - v_m \end{aligned} \quad (60)$$

where the unmodeled state acts as a forcing term.

To study the entire controller/observer system, stack the modeled state, the modeled error, and the unmodeled state, and consider the dynamics of the stacked system:

$$\begin{bmatrix} \frac{dx_m}{dt} \\ \frac{de_m}{dt} \\ \frac{dx_u}{dt} \end{bmatrix} = \begin{bmatrix} (A_m - B_m \Lambda^{-1} B_m^* \bar{P}) & -B_m \Lambda^{-1} B_m^* \bar{P} & 0 \\ 0 & (A_m - \bar{P}_e C_m^* W_e^{-1} C_m) & \bar{P}_e C_m^* W_e^{-1} C_u \\ -B_u \Lambda^{-1} B_m^* \bar{P} & -B_u \Lambda^{-1} B_m^* \bar{P} & A_u \end{bmatrix} \begin{bmatrix} x_m \\ e_m \\ x_u \end{bmatrix} + \begin{bmatrix} v_m \\ -\bar{K}_e w - v_m \\ v_u \end{bmatrix} \quad (61)$$

From the LQG theory presented in Sec. III, $(A_m - B_m \Lambda^{-1} B_m^* \bar{P})$ and $(A_m - \bar{P}_e C_m^* W_e^{-1} C_m)$ are stable. However, from Eq. (61), the overall system may not be stable due to the unmodeled actuator influence B_u and sensor influence C_u matrices. Therefore, we have seen that in the LQG framework we cannot ensure overall stability unless the unmodeled parts of the system are accounted for.

There are two ways to ensure system (61) is stable. One way is to ensure $B_u = 0$, i.e., make sure the unmodeled dynamics are uncontrollable with respect to the actuator. The other way is to ensure $C_u = 0$, i.e., make sure the unmodeled dynamics are unobservable with respect to the sensor. Controllability and observability for the plane Poiseuille flow problem were introduced in Ref. 2. We now explore how we may achieve these conditions:

A. Point Actuation vs Distributed Actuation

One way to guarantee that the overall system (61) is stable is to ensure that all modes associated with unmodeled wave numbers are uncontrollable with respect to the input by making $B_u = 0$. In the fully developed channel flow system, this would account for the wave numbers left out of the reduced-order model. If

$$l(x) \triangleq \text{Real} \left(\sum_{n=-N}^N e^{jn\alpha_0 x} \right) \quad (62)$$

where the n range corresponds to the modeled wave numbers only, then the projection of $l(x)$ onto unmodeled wave numbers is zero due to the orthogonality of Fourier components. As a result, $B_u = 0$

and the stability of unmodeled dynamics is retained. Note that because $l(x) \neq 0$ for all but a finite number of points in the x direction, this type of scheme is a distributed actuation scheme. Therefore, by moving from a physically easier to implement point actuator to a more difficult distributed actuator, we have retained stability of the unmodeled dynamics. Physically, a distributed actuator is obtained by a large number of independently programmable actuators placed along the lower wall. If distributed actuation is infeasible or undesirable, we must look to the dual problem of sensing to gain stability.

B. Point Sensing vs Distributed Sensing

It is seen from Eq. (61) that if $B_u \neq 0$, stability may still be maintained if $C_u = 0$. This corresponds to making all unmodeled wave number dynamics unobservable with respect to the shear sensor. Placing a single shear sensor at a point along the lower channel wall results in a measurement that includes the effects of all wave numbers, both modeled and unmodeled. Clearly, $C_u \neq 0$, and stability is not guaranteed. This corresponds to the point forcing case in the dual problem of actuation. By using a distributed sensing scheme, however, we may form a new measurement that includes only the effects of the modeled wave numbers. This is done by projecting a distributed shear function, $z(x, y = -1, t)$, onto the modeled wave numbers. The distributed shear function, $z(x, y = -1, t)$ is physically created by measuring the shear at all points along the lower channel wall. Then a new projected shear measurement, denoted $\bar{z}(t)$, is defined as

$$\bar{z}(t) \triangleq \text{Real} \left\{ \left[z(x, y = -1, t), \sum_{n=-N}^N e^{jn\alpha_0 x} \right]_x \right\} \quad (63)$$

where again the n range corresponds to modeled wave numbers only. Note that, just as in the actuator case, we have implemented

a more physically complicated series of sensors to achieve overall stability.

There is a subtle difference between making the channel system unmodeled dynamics unobservable as opposed to uncontrollable. By making unmodeled dynamics uncontrollable, linear stability is maintained (under appropriate conditions) because the unmodeled dynamics cannot be affected by the input. By making unmodeled dynamics unobservable, however, linear stability is also maintained (under appropriate conditions), but unmodeled dynamics may be affected by the input. These affected dynamics could produce transients that cause the linear model to become invalid.²

In terms of modeling, we need not include either unobservable or uncontrollable modes in our plant models. Therefore, distributed actuation or sensing allows models to be created using only a finite number of wave numbers. Note, however, that even a single wave number model contains an infinite number of modes shown by the infinite number of poles extending out into the left-hand s plane, as shown in Fig. 2 (see also Ref. 4).

VI. Control Design Using Finite Large-Order Models

As we have seen in Sec. V, we may reduce the problem of including an infinite number of wave numbers in a reduced-order model to a problem of including a finite number of wave numbers by using distributed actuation or sensing. However, even with a model containing only a finite number of wave numbers, the problem is still infinite dimensional because of the infinite number of poles

extending into the left-hand s plane for each wave number. Furthermore, we do not know the exact position of poles far into the left-hand s plane due to the finite number of basis functions used in the y direction.⁴ Still, these poles must be accounted for in the control design. The fact that uncertain poles appear only at higher frequencies in the bandwidth will be advantageous. It will allow a robust controller to be designed that rolls off at high frequencies.

For disturbance rejection, it can be shown (see Ref. 5) that high loop gain is preferable. On the other hand, for good output noise suppression, the loop gain should be low at all frequencies in which the noise enters.⁵ It is generally assumed that noise is most destructive at higher frequencies. As a result, control design focuses on high loop gain at low frequencies where disturbance rejection is most important and low loop gain at high frequencies where noise is more of a problem. Therefore, an ideal controller will cause loop gain to roll off at high frequencies.

In addition to noise at high frequencies, the other major problem at high frequencies is unmodeled dynamics. We have already pointed out that there are two types of unmodeled dynamics in the channel flow problem. The first type is unmodeled dynamics of unmodeled wave numbers. We accounted for these dynamics through distributed control or distributed sensing. The second type is unmodeled dynamics at high frequencies for modeled wave numbers. This type of unmodeled dynamics has yet to be considered and is common to most infinite dimensional systems. To account for these dynamics, controllers are designed that give low loop gain at the high frequencies of the open-loop controller/plant series where unmodeled dynamics exist in order not to stimulate modes at those frequencies. Roll-off has also been given a more analytic framework by considering multiplicative, unstructured uncertainty.⁷

We consider the one-wave-number model shown in Fig. 1 with $Re = 1 \times 10^4$. Only $\alpha = 1.0$ is included in the model. All other wave numbers are uncontrollable due to the distributed input of $l(x) = \sin(x)$ as shown in Sec. V.A. A single point sensor is located at π . The length of the channel is 4π leading to a fundamental wave number of $\alpha_0 = \frac{1}{2}$.

We now design an LQG controller and compare closed-loop response with that of the simple, integral controller introduced in Ref. 2. The integral control method is shown in Fig. 3, and the LQG control method is shown in Fig. 4. Two criteria will be used in comparing controllers: 1) output (shear) settling time and 2) required control energy. Control energy will be defined as

$$E_u \triangleq \sqrt{\int_0^T |u(t)|^2 dt} \quad (64)$$

where T is a finite upper bound.

We consider two models in evaluating the resulting LQG controller: one model of order 252 (validation model) and the other model of order 140 (reduced-order model). The validation model is constructed by including all poles and zeros to the right of $s = -4$ (refer to Fig. 2). The reduced-order model includes all observable and controllable poles and zeros to the right of $s = -2$ (refer to Fig. 2). The reduced-order model was created by using the minreal function within the MATLABTM control toolbox² with the parameter value $\text{tol} = 1e-3$. Table 1 lists all models considered in this study. The `lqr` and `lqe2` functions of the MATLAB control toolbox were used to create an LQG controller using the reduced-order model. The A matrix supplied to each of these MATLAB functions was modified to $(A + I\gamma)$ to achieve a prescribed degree of stability as

described in Secs. III and IV. The following parameters were used: $\gamma = 0.005$, $R = 0.001C^*C$, $\Lambda = I$, $Q_c = 10BB^*$, and $W_c = 1$. The R matrix was chosen to minimize shear in the cost functional (46), the Q_c matrix was originally chosen to recover robustness properties using loop transfer recovery techniques,⁹ γ was chosen by trial and error to decrease settling time without increasing control energy, and W_c and Λ were chosen using trial and error. The gain of the integral controller was chosen as $K_I = 0.07$.

Figures 5 and 6 show the shear output and blowing/suction input signal for the closed-loop system (validation model plus

Table 1 Models used in LQG controller design

Model name	Order
Validation	252
Reduced-order	140
Low-order	8

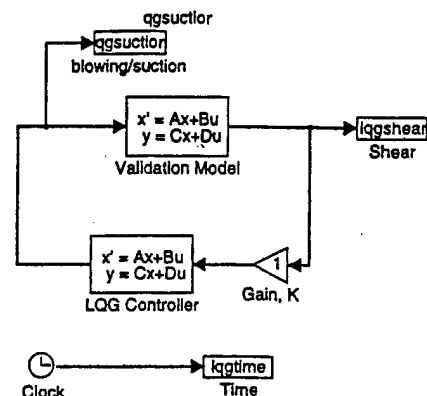


Fig. 4 LQG control loop for validation model plant and LQG controller.

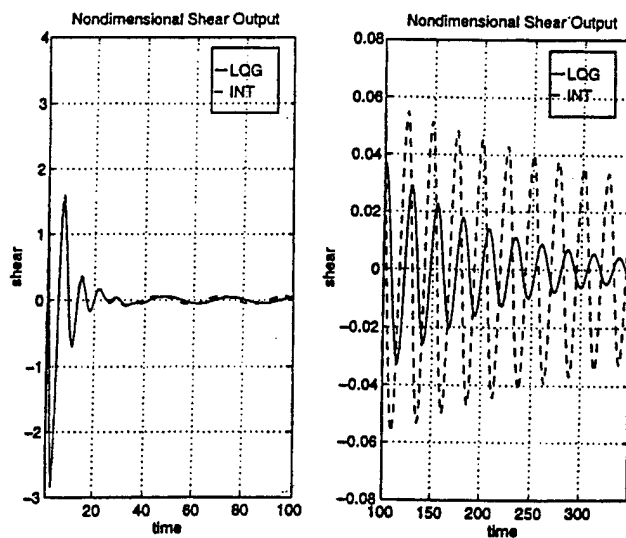
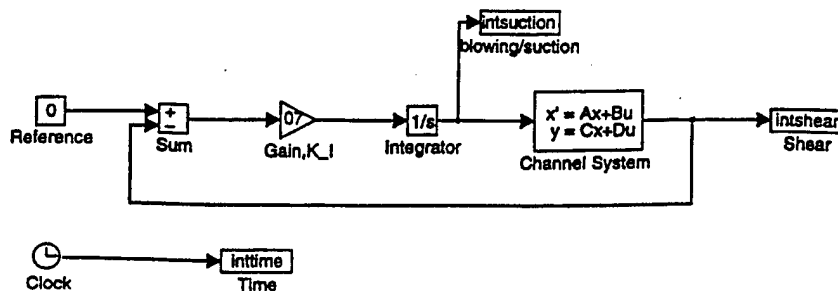


Fig. 5 Shear at output of closed-loop system: ---, Integral control method, and —, reduced-order LQG control method.



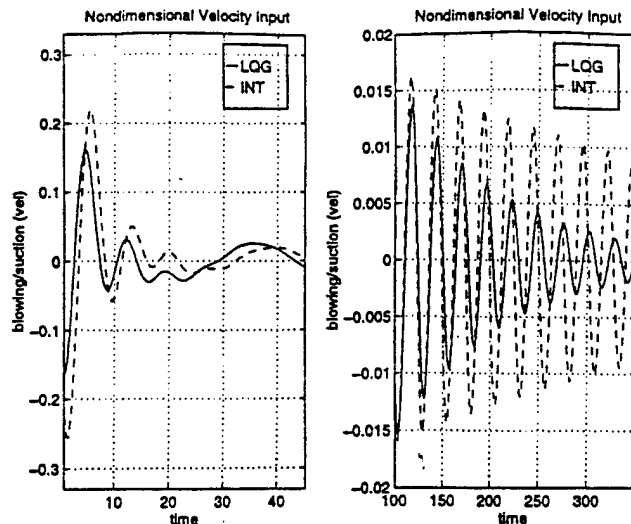


Fig. 6 Blowing and suction control input: ---, input from integral control method, and —, input from reduced-order LQG control method.

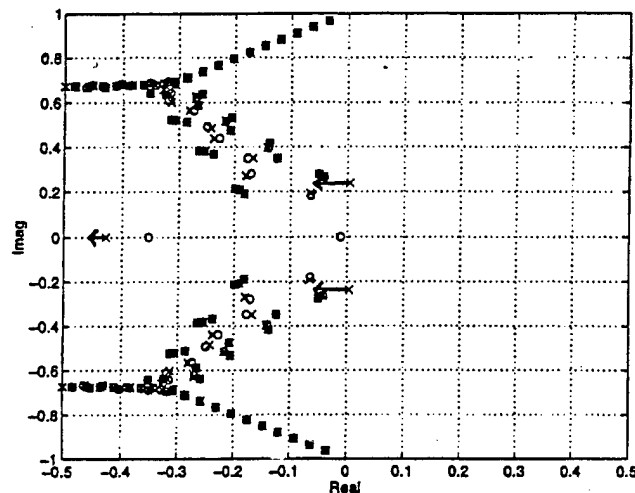


Fig. 7 Root locus of optimal controller synthesized using reduced-order model in series with validation model plant for gain K varying from 0 to 4.

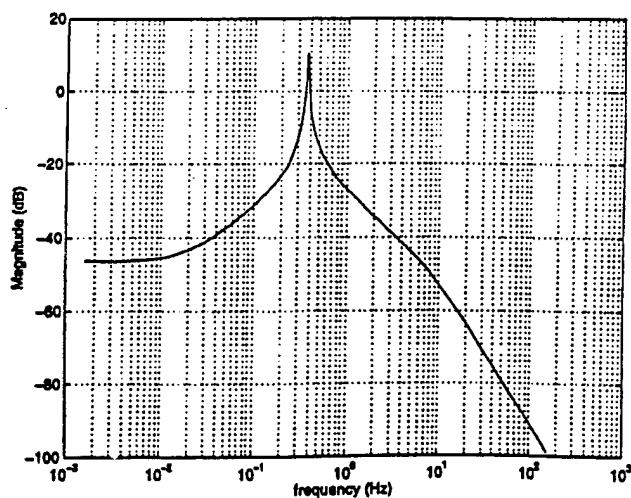


Fig. 8 Open-loop response magnitude for series connection of LQG controller (using reduced-order model) and validation model.

controller) for the same plant initial condition [ones (252, 1) in MATLAB]. Clearly, using the LQG controller, the channel system has a much shorter settling time. More significantly, this reduced settling time is accompanied by lower control energy. Indeed, for the LQG case, $E_{LQG} = 0.5809$, whereas for the integral controller case, $E_{INT} = 0.8178$. Note that, because all values are nondimensional, it is the comparison of energies that is important, not the actual numbers. Similar results were obtained for other initial conditions, as well as disturbance inputs.

In analyzing the resulting control system, consider Fig. 4. The optimal control is defined at $K = 1$ with a properly designed LQG controller. Note that many poles in the validation model are either uncontrollable or unobservable as shown by pole/zero cancellations (Fig. 2). These poles cannot be moved. We concentrate on moving only the observable/controllable poles. Figure 7 shows the root locus of the controller/estimator, designed using the reduced-order model (order 140), in series with the validation model (order 252), for gain values K varying from 0 to 4. Poles of the closed-loop system achieve the goal of being to the left of $s = -0.005$ with gain $K = 1$. Consequently, settling time is reduced. Finally, Fig. 8 shows the magnitude response for the open-loop series connection of the LQG controller (using the reduced-order model) and the validation model. Note that the loop gain rolls off at higher frequencies.

VII. Control Design Using Low-Order Models

Although we achieved our goal in Sec. VI, we designed our LQG controller with a high dimensional plant model (order 140). This might lead to numerical problems if the design was attempted with a

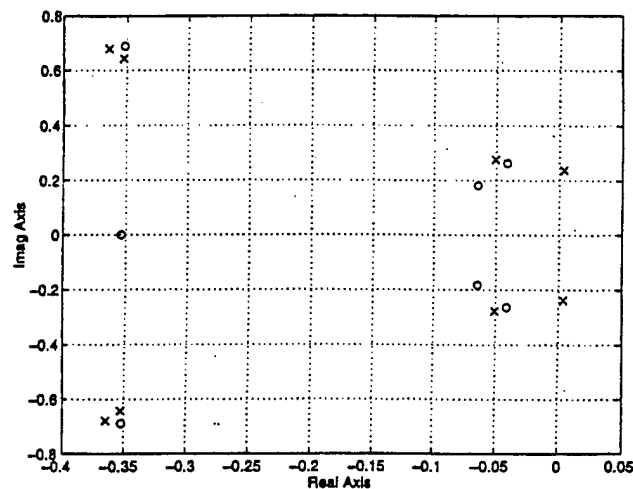


Fig. 9 Pole (x)/zero (o) configuration of low-order model.

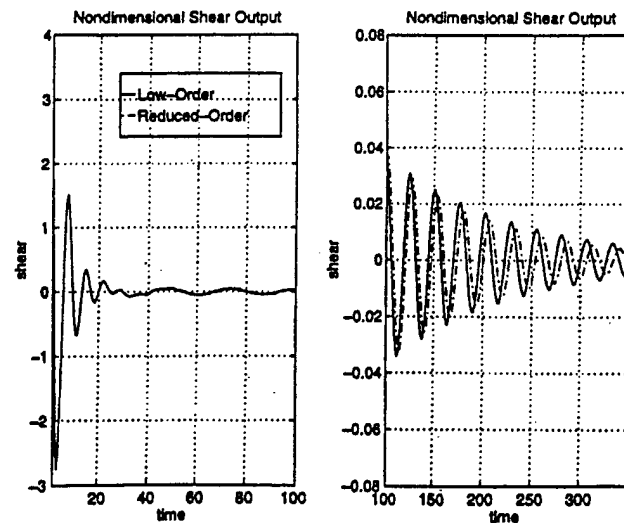


Fig. 10 Shear at output of closed-loop system: ---, using reduced-order LQG controller, and —, using low-order LQG controller.

new model that contained several wave numbers as the model would be even larger. As a result, we would like to develop a design that uses an extremely low-order model. Consider the model shown in Fig. 9 (low-order model). This model contains eight poles and seven zeros.

An LQG controller is designed using only the low-order model. The parameters for the design are the same as in Sec. VI. Figure 10 shows the closed-loop output response of the validation model (order 252) and the controller obtained from the low-order model (Fig. 9). An almost identical settling time is achieved compared with the controller using the reduced-order model (order 140). Also, the control energy is only slightly increased to $E_{\text{low-order}} = 0.6131$. Using this design, we have reduced the order of the LQG controller from 140 to 8, while maintaining performance.

VIII. Conclusion

Linear stabilization of plane, Poiseuille flow using linear quadratic Gaussian optimal control theory has been examined. The infinite dimensional nature of the problem poses challenges for finite dimensional control. Distributed actuation and/or sensing methods, as well as loop gain roll-off, can be used to address the inherent unmodeled dynamics of finite dimensional models of infinite dimensional systems. Using linear quadratic Gaussian methods, we achieved significantly higher dissipation rates, while using lower control energy, than those reported in integral compensator control schemes. We showed linear quadratic Gaussian designs that used both a high-order and an extremely low-order plant model for control synthesis. The low-order controller produced results essentially equivalent to the high-order controller. In this paper, we have examined linear quadratic Gaussian control methods. Other control approaches exist that are based on worst-case design.¹⁰ The methods discussed in this paper were aimed at reducing settling time and control energy. However, additional criteria such as limiting transient growth will be important in preserving the integrity of a linear model of channel flow and preventing transition of laminar channel flow to turbulent channel flow.

Acknowledgments

The work described in this paper was performed partially at the Jet Propulsion Laboratory, California Institute of Technology, under a contract with NASA, and partially at the University of California, Los Angeles, sponsored by Air Force Office of Scientific Research University Research Initiative Grant F496920-97-1-0276 and NASA Dryden Grant NCC2-374-PR41.

References

- ¹Hu, H. H., and Bau, H. H., "Feedback Control to Delay or Advance Linear Loss of Stability in Planar Poiseuille Flow," *Proceedings of the Royal Society of London, A*, Vol. 447, No. 1, 1994, pp. 299-312.
- ²Joshi, S. S., Speyer, J. L., and Kim, J., "A Systems Theory Approach to the Feedback Stabilization of Infinitesimal and Finite-Amplitude Disturbances in Plane Poiseuille Flow," *Journal of Fluid Mechanics*, Vol. 331, Feb. 1997, pp. 157-184.
- ³Joshi, S. S., Speyer, J. L., and Kim, J., "Feedback Stabilization of Plane Poiseuille Flow," *Proceedings of the Conference on Decision and Control* (New Orleans, LA), Inst. of Electrical and Electronics Engineers, New York, 1995, pp. 921-927.
- ⁴Joshi, S. S., "A Systems Theory Approach to the Control of Plane Poiseuille Flow," Ph.D. Dissertation, Dept. of Electrical Engineering, Univ. of California, Los Angeles, CA, March 1996.
- ⁵Anderson, B. O., and Moore, J. B., *Optimal Control: Linear Quadratic Methods*, Prentice-Hall, Englewood Cliffs, NJ, 1990, pp. 110-115.
- ⁶Sesak, J. R., Likins, P., and Coradetti, T., "Flexible Spacecraft Control by Modal Error Sensitivity Suppression," *Journal of Aeronautical Science*, Vol. 27, No. 2, 1979, pp. 131-156.
- ⁷Doyle, J., and Stein, G., "Multivariable Feedback Design: Concepts for a Classical/Modern Synthesis," *IEEE Transactions on Automatic Control*, Vol. AC-26, No. 1, 1981, pp. 4-16.
- ⁸Grace, A., Laub, A. J., Little, J. N., and Thompson, C. M., *Control System Toolbox: For use with MATLAB*, MathWorks, Natick, MA, 1992, pp. 2-102, 115, 116.
- ⁹Doyle, J., and Stein, G., "Robustness with Observers," *IEEE Transactions on Automatic Control*, Vol. AC-24, No. 4, 1979, pp. 607-611.
- ¹⁰Rhee, I., and Speyer, J. L., "A Game Theoretic Approach to a Finite-Disturbance Attenuation Problem," *IEEE Transactions on Automatic Control*, Vol. 36, No. 9, 1991, pp. 1021-1032.

Skin-friction Drag Reduction *Via* Robust Reduced-order Linear Feedback Control

L. CORTELEZZI ^{a, b, *}, K. H. LEE ^a, J. KIM ^a and J. L. SPEYER ^a

^a *Department of Mechanical and Aerospace Engineering, University of California, Los Angeles, California 90095-1597, USA;*

^b *Department of Mathematics, University of California, Los Angeles, California 90095-1555, USA*

A successful application of a linear controller to a two-dimensional channel flow is presented. An optimal and robust reduced-order linear feedback controller is derived by using multi-variable linear-quadratic-Gaussian synthesis, or, in modern term, \mathcal{H}_2 synthesis, combined with model reduction techniques. This controller based on a reduced-model of the linearized Navier–Stokes equations is applied to suppress finite-amplitude near-wall disturbances in a channel flow at $Re = 1500$. The controller efficiently reduced near-wall disturbances obtaining a substantial drag reduction and eventually the flow is relaminarized.

Keywords: Robust feedback flow control, model reduction, shear flows, skin-friction, drag reduction

1. INTRODUCTION

Wide attention has been given to the problem of reducing wall-shear stresses generated by near-wall turbulence, or, in other words, to the problem of reducing drag produced by skin friction. “The skin friction constitutes about 50%, 90%, and 100% of the total drag on commercial aircraft, underwater vehicles, and pipelines, respectively” [1]. Consequently, important economic and environmental benefits will spring from the successful and reliable control of near-wall turbulence.

In the recent years, boundary layer control has been attempted by several investigators with some success [1–24]. However, controllers able to

analyze distributed measurements and coordinate distributed actuators are regarded by the fluid mechanics community as essential for achieving better results. Tools for designing this class of controllers have been developed by the control community over the past two decades [25, 26]. Very little has been done to exploit these tools in connection with the control of boundary layers [27–29] because of the belief that linear controllers are not suited for controlling a nonlinear phenomenon, like wall turbulence.

Recently, Cortelezzi and Speyer [30] used multi-input-multi-output (MIMO) linear quadratic Gaussian (LQG) synthesis, or, in modern terms, \mathcal{H}_2 synthesis, combined with model reduction

* Corresponding author. Tel.: (310) 206-2732, Fax: (310) 206-6673, e-mail: crtltz@math.ucla.edu

techniques for designing an optimal and robust linear feedback controller able to suppress wall-disturbances leading to transitions in a two-dimensional laminar channel flow. The present paper shows that the controller derived by Cortelezzi and Speyer, based on a reduced-model of the linearized Navier–Stokes equations, can be successfully applied to the control of skin-friction drag in a two-dimensional channel flow. This is an essential intermediate step toward the derivation and application of this class of controllers to three-dimensional boundary layers.

The intermediate step of controlling skin-friction drag in a two-dimensional channel flow will perhaps disappoint some readers because of the fundamental differences between two and three-dimensional turbulent channel flows. Turbulence is essentially a three-dimensional phenomenon. Consequently, results obtained by controlling skin-friction drag in two-dimensional cannot be readily extrapolated to the three-dimensional case. However, the derivation and testing of optimal and robust reduced-order linear feedback controllers in a two-dimensional environment has been very valuable for understanding the potentiality of MIMO LQG, \mathcal{H}_2 , synthesis and model reduction in relation to boundary layer control problems.

In Section 2, we formulate the problem in terms of Navier–Stokes equations and we provide details about the numerical scheme used to integrate them. In Section 3, we derive the state space equations from the linearized Navier–Stokes equations. In Section 4, we reduce the order of the state space equations and derive an optimal and robust reduce-order controller by using LQG, \mathcal{H}_2 synthesis. In Section 5 we apply the controller to a turbulent channel flow at $Re = 1500$ and discuss its performance. Conclusions will close the article.

2. MATHEMATICAL FORMULATION

We consider the turbulent flow of an incompressible fluid in a two-dimensional periodic channel

of length Lh and height $2h$, see Figure 1. This problem is governed by the Navier–Stokes and continuity equations

$$\begin{aligned} \frac{\partial u}{\partial t} + u \frac{\partial u}{\partial x} + v \frac{\partial u}{\partial y} &= -\frac{\partial p}{\partial x} + \frac{1}{Re} \Delta u, \\ \frac{\partial v}{\partial t} + u \frac{\partial v}{\partial x} + v \frac{\partial v}{\partial y} &= -\frac{\partial p}{\partial y} + \frac{1}{Re} \Delta v, \end{aligned} \quad (1)$$

$$\frac{\partial u}{\partial x} + \frac{\partial v}{\partial y} = 0 \quad (2)$$

where Δ is the two-dimensional Laplacian. We made the problem dimensionless by using h as characteristic length and h/U_c as characteristic time, where U_c is the velocity at the center of the channel. The Reynolds number is $Re = U_c h/\nu$.

We apply blowing and suction at the bottom wall to suppress near-wall turbulence within the bottom boundary layer. To simplify the problem the actuators are assumed uniformly distributed along the bottom wall. Near-wall turbulence within the top boundary layer is left free to evolve. The corresponding boundary conditions are

$$\begin{aligned} u(x, \pm 1, t) &= v(x, 1, t) = 0, \\ v(x, -1, t) &= v_w(x, t). \end{aligned} \quad (3)$$

The control function v_w prescribes the amount of blowing and suction at the wall. In the next section, we will impose that the amount of fluid removed equals the amount of fluid injected.

We measure the gradient of the streamwise velocity at given points $x = x_i$ to detect and measure near-wall turbulence within the bottom

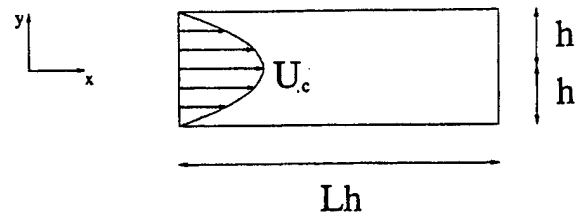


FIGURE 1 Flow geometry.

boundary layer. In other words, we measure the first term of the wall-shear stress, $\tau_{yx} = Re^{-1}(\partial u / \partial y + \partial v / \partial x)|_{y=-1}$, i.e.,

$$z(x_i, t) = \frac{\partial u}{\partial y} \Big|_{x=x_i, y=-1} \quad (4)$$

Note that the second term of the wall-shear stress is known when the actuators operate while is zero in the uncontrolled case.

Time dependent incompressible Navier-Stokes equations (1)–(3) with the appropriate initial condition are integrated numerically using a semi-implicit fractional step method. The second-order implicit Crank-Nicolson is used for the viscous terms and the nonlinear convective terms are advanced using a 3rd-order low-storage Runge-Kutta scheme.

A staggered grid is used in the computation. All spatial derivatives are discretized with a 4th-order compact finite-difference scheme. A uniform grid is used in the streamwise direction, while a nonuniform grid corresponding to Chebyshev collocation points is used in the wall-normal direction. We simulate turbulent channel flows on a computational domain of $4\pi \times 2$ with a resolution of 512×64 . Detailed description of the numerical methods used to simulate the flow under investigation are given in Ref. [31].

3. DERIVATION OF THE STATE-SPACE EQUATIONS

In this section we outline the derivation of the state-space equations [30]. To derive the state-space equations we first linearize Eq. (1) with respect to the laminar velocity field $U(y) = (y^2 - 1)$, see Figure 1. To identically satisfy continuity, the linearized Navier-Stokes equations are written in terms of the stream-function ψ

$$\left(\frac{\partial}{\partial t} + U \frac{\partial}{\partial x} \right) \Delta \psi - \frac{d^2 U}{dy^2} \frac{\partial \psi}{\partial x} = \frac{1}{Re} \Delta \Delta \psi, \quad (5)$$

and corresponding boundary conditions are

$$\begin{aligned} \frac{\partial \psi}{\partial x} \Big|_{y=-1} &= -v_w(x, t), \\ \frac{\partial \psi}{\partial y} \Big|_{y=\pm 1} &= \psi(x, 1, t) = 0. \end{aligned} \quad (6)$$

The measurement Eq. (4) becomes

$$z(x_i, t) = \frac{\partial^2 \psi}{\partial y^2} \Big|_{y=-1} \quad (7)$$

The design of a controller for the LQG (\mathcal{H}_2) problem is contingent on the definition of an optimal performance index, or cost function. A cost function should be constructed with the intent of simultaneously minimizing near-wall turbulence and the cost of the controller. It is crucial to minimize the cost of the controller because the energy available to drive the controller is limited in any engineering application. Furthermore, the system could be driven away from the region where the linear model is valid by large control action. Because of the high correlation between near-wall disturbances and wall-shear stress, we choose the following cost function:

$$J = \lim_{T \rightarrow \infty} \int_0^T \int_{-1}^1 \left[\left(\frac{\partial^2 \psi}{\partial y^2} \right)^2 + \left(\frac{\partial^2 \psi}{\partial x^2} \right)^2 \right]_{y=-1} dx dt. \quad (8)$$

The integrand represents the cost of the wall-shear stress being different from zero. Moreover, the second term of the integrand implicitly accounts for the cost of implementing the control itself.

To reduce (5)–(7) to a set of first-order ordinary differential equations, we make a few transformations as shown in Ref. [30]. Taking advantage of the linearity of the problem, we assume that the stream-function ψ is the sum by two parts: a modified stream-function ϕ which satisfies to the forced Eq. (5) with homogeneous boundary condition, and a function χ which satisfies to the non-homogeneous boundary conditions forming a forcing function to (5). Subsequently, flow quan-

ties are spectrally decomposed by using circular functions in the streamwise direction and Chebyshev polynomials in the vertical direction. We expand ϕ and χ as follows:

$$\phi(x, y, t) = \sum_{n=1}^N \sum_{m=0}^M [a_{nm}(t) \cos(\alpha_n x) + b_{nm}(t) \sin(\alpha_n x)] C_m(y), \quad (9)$$

$$\chi(x, y, t) = \sum_{n=1}^N [p_n(t) \cos(\alpha_n x) + q_n(t) \sin(\alpha_n x)] D(y). \quad (10)$$

where $\alpha_n = 2\pi n/L$. Functions C_m and D are combinations of Chebyshev polynomials constructed to satisfy the boundary conditions, *i.e.*,

$$\begin{aligned} C_m(y = \pm 1) &= \frac{dC_m}{dy} \Big|_{y=\pm 1} = 0, \\ D(y = -1) &= 1, \\ D(y = 1) &= \frac{dD}{dy} \Big|_{y=\pm 1} = 0. \end{aligned} \quad (11)$$

We also expand the measurement function z as follows:

$$z(x, t) = \sum_{n=1}^N [c_n(t) \cos(\alpha_n x) + d_n(t) \sin(\alpha_n x)]. \quad (12)$$

We substitute expansions (9), (10), and (12) into the evolution and measurement Eqs. (5)–(7) and use Galerkin's projection to obtain a set of ordinary differential equations. These equations are cast by matrix transformations into the following state-space equations:

$$\frac{dx}{dt} = Ax + Bu, \quad z = Cx + Du, \quad (13)$$

with initial conditions $x(0) = x_0$. The vectors x , u and z are the internal state vector, the control vector, and the measurement vector, respectively. The dynamics of the Poiseuille flow, actuators and sensors, are contained into the matrices A , B , and C , respectively, while the direct coupling between

sensors are actuators is contained into the matrix D . Note that this coupling would be eliminated if actuators dynamics could be explicitly imposed. The cost function (8) becomes

$$J = \lim_{t_f \rightarrow \infty} \int_t^{t_f} [z^T z + u^T W^T W u] dt, \quad (14)$$

where the superscript T denotes transpose. The matrix W is generated by spectral decomposition of the last term in the cost function (8).

The main advantage of this formulation is the decoupling of the problem with respect to the wave number where all matrices in (13) and (14) are block diagonal. Consequently, the state-space system (13) is equivalent to N state-space subsystems, one for each wave number. The state-space equations for a given wave number r are

$$\frac{dx_r}{dt} = A_r x_r + B_r u_r, \quad z_r = C_r x_r + D_r u_r, \quad (15)$$

with initial condition $x_r(0) = x_{r0}$. The structure of vectors x_r , u_r , z_r is the following: $x_r = [a_{r0}, \dots, a_{rM}, b_{r0}, \dots, b_{rM}]^T$, $u_r = [p_r, q_r]^T$, $z_r = [c_r, d_r]^T$. The cost function (14) also decouples with respect to the wave number. It is the sum of N optimal performance indexes J_r . The cost function for a given wave number r is defined as follows

$$J_r = \lim_{t_f \rightarrow \infty} \int_t^{t_f} [z_r^T z_r + u_r^T W_r^T W_r u_r] dt. \quad (16)$$

Consequently, the design of an optimal and robust controller for the system (13) with (14) has been reduced to the independent design of N optimal and robust controllers, one for each wave number, for the sub-systems (15) with (16).

The reader is referred to Ref. [30] for a detailed derivation of the state-space equations.

4. MODEL REDUCTION AND CONTROLLER DESIGN

The size of the controller is a crucial parameter in engineering applications because of the amount of

hardware and computer power necessary to compute a real-time control law. Since a controller based on the full system would have $2N(M+1)$ states, where $N = 32$ and $M = 64$ is considered a simple case in literature, it is crucial to reduce the order of the controller. A low-order controller for the present problem can be derived in two steps [30]: First by constructing a lower order model of (15), and subsequently, by designing an optimal and robust controller for the reduced-order model.

In order to obtain a lower order model for each wave number, we transform each state-space subsystem (15) into Jordan Canonical form. This transformation decouples the modes of each subsystem, in other word it reduces the subsystem matrices to a block diagonal form. From the transformed B_r and C_r matrices the states that are equally well controllable and observable are determined. The matrices \hat{A}_r , \hat{B}_r , \hat{C}_r , D_r that describe the dynamics of the reduced-order internal state-space subsystem are obtained from the matrices in Jordan Canonical form by removing rows and columns corresponding to poorly controllable or observable states. Hat denotes the quantities associated with the reduced-order model.

Although a rigorous mathematical framework for the designs of disturbance attenuation (\mathcal{H}_∞) linear controllers is provided by the control synthesis theory in [25,26], for this initial study LQG (\mathcal{H}_2) synthesis is quite adequate. In general, the design of an optimal and robust linear feedback controller for the LQG (\mathcal{H}_2) problem is divided in two parts: linear-quadratic regulator (LQR) and minimum variance estimator (Kalman-Bucy filter). The LQR design provides an optimal control law in terms of the internal state vector by minimizing a cost function. The internal state vector is essential to implement the control law but, in general, it is not a physical quantity directly measurable. The internal state vector is reconstructed from the measurement vector z_r by the estimator. Since we have assumed no statistics, the power spectral densities required for the

minimum variance estimator are chosen as design parameters in order to keep the eigenvalues of the estimator at the same order of magnitude as the eigenvalues of the controller. In particular, the power spectral density of the process noise is chosen so that the resulting loop transfer matrix approximates the loop transfer matrix of the LQR which has significant robustness properties [32, 33]. In this study the LQG (\mathcal{H}_2) design of an optimal and robust controller for each reduced-order state space subsystem (15) can be carried out in parallel. The final result of the LQG (\mathcal{H}_2) is summarized by the following equations:

$$u_r = -\hat{K}_r \hat{x}_r, \quad (17)$$

$$\frac{d\hat{x}_r}{dt} = \hat{A}_r \hat{x}_r + \hat{B}_r u_r + \hat{L}_r [z_r - \hat{C}_r \hat{x}_r - D_r u_r], \quad (18)$$

with initial conditions $\hat{x}_r(0) = 0$. Equation (17) is the control law. It predicts the optimal blowing and suction at the bottom wall by processing the estimated reduced-order internal state vector \hat{x}_r with the gains matrix \hat{K}_r . The gains matrix \hat{K}_r is obtained by minimizing the following optimal performance index:

$$\hat{J}_r = \lim_{t_f \rightarrow \infty} \int_0^{t_f} [\hat{z}_r^T \hat{z}_r + u_r^T W_r^T W_r u_r] dt, \quad (19)$$

where $\hat{z}_r = \hat{C}_r \hat{x}_r - D_r u_r$. Although Eq. (18) is the minimum variance estimator in a statistical sense, this filter is essentially an observer that reconstructs from the measurements an estimate of the reduced-order internal state vector. However, when the estimator is eventually implemented in a system where the measurements and process dynamics are corrupted by noise, the Gaussian white noise assumption will be used to develop the filter gains. The initial condition $\hat{x}_r(0) = 0$ implies that the estimator starts with no information about \hat{x}_r .

Note that the numerical integration of the estimator (18), the computation of the control law (17), and fast direct and inverse Fourier trans-

forms can be programmed in a computer routine suited for parallel computing [30]. Subsequently, this routine can be embedded in any Navier–Stokes solver for the control of simulated turbulent channel flows as shown in the next section.

5. RESULTS

We designed a controller for two-dimensional Poiseuille flow in a periodic channel of length $L = 4\pi$ at $Re = 1500$. We used a grid resolution of $N = 32$ and $M = 60$, consequently, the order of the full system is 3904. Using the model reduction technique previously described, we created 32 reduced models and derived 32 controllers of order 12, one for each state space subsystem (15). Controllers operate in parallel [30]. The combined order of the controllers for all 32 wave numbers is 384, it represents a dramatic reduction, about 90%, with respect to the order of the full system.

This controller is tested on a two-dimensional turbulent channel flow at $Re = 1500$. Since there are no unstable modes at $Re = 1500$, we use a combination of channel and wall modes to create a worse scenario initial perturbation velocity field [34]. The maximum *rms* value of the initial perturbation velocity field is $u_{rms} = 0.3$, i.e., 30% of the centerline velocity of the undisturbed laminar flow. We construct the initial velocity field by superimposing a perturbation velocity field onto the laminar flow. The corresponding initial vorticity field produces pockets of positive and negative vorticity distributed along the center and walls of the channel. Although the initial disturbances in the two-dimensional channel flow will eventually decay, they permit testing the capability of the controller in suppressing near-wall turbulence that can increase drag and trigger boundary layer eruptions and flow separations in turbulent boundary layers. Note that this initial condition includes nonlinear effects that are not included in the linear model and also stimulates modes that are not included in the reduced-order model, and consequently, cannot be directly controlled.

Figure 2 presents a comparison of the vorticity field in the controlled and uncontrolled cases at time $t = 2$ and 4. Figure 2 also presents the amplitude of blowing and suction applied to the bottom wall of the channel. In the uncontrolled case, at time $t = 2$, two large pockets of negative and positive vorticity can be recognized on the left along the bottom wall, while minor vortical structures populate the remaining part of the boundary layer. At time $t = 4$, the interaction of the two pockets of vorticity with the rest of the flow generates an eruption of fluid toward the center of the channel. A large negative vortex entrains some of the positive vorticity from the wall increasing the separation. A similar process takes place on a smaller scale further downstream. Flow separation also occurs at the top boundary layer; a large eruption can be recognised on the left and two smaller eruptions further downstream.

In the controlled case, at time $t = 2$, the vorticity field near the bottom wall is strongly modified by the action of the controller, see Figure 2. Pockets of high positive vorticity have been removed while pockets of high negative vorticity have been lifted away from the wall. Only low negative vorticity can be recognized within the bottom boundary layer. The plot of v_w shows that the controller tends to inject fluid underneath pockets of negative vorticity while it tends to remove fluids in correspondence with pockets of positive vorticity. At time $t = 4$, the action of the controller can be more easily interpreted. The controller breaks the pockets of negative vorticity that have been lifted up into smaller vortical structure. These structures are made rolling along the bottom wall by injecting and removing fluid from the rear and the front of each vortical structure. Note that at time $t = 2$ the controller affects only the flow near to the bottom wall leaving most of the vorticity field unaffected. At time $t = 4$, however, the controller action has penetrated further toward the center of the channel because of the viscous and nonlinear effects.

Figure 3 presents a comparison of the vorticity field in the controlled and uncontrolled cases at

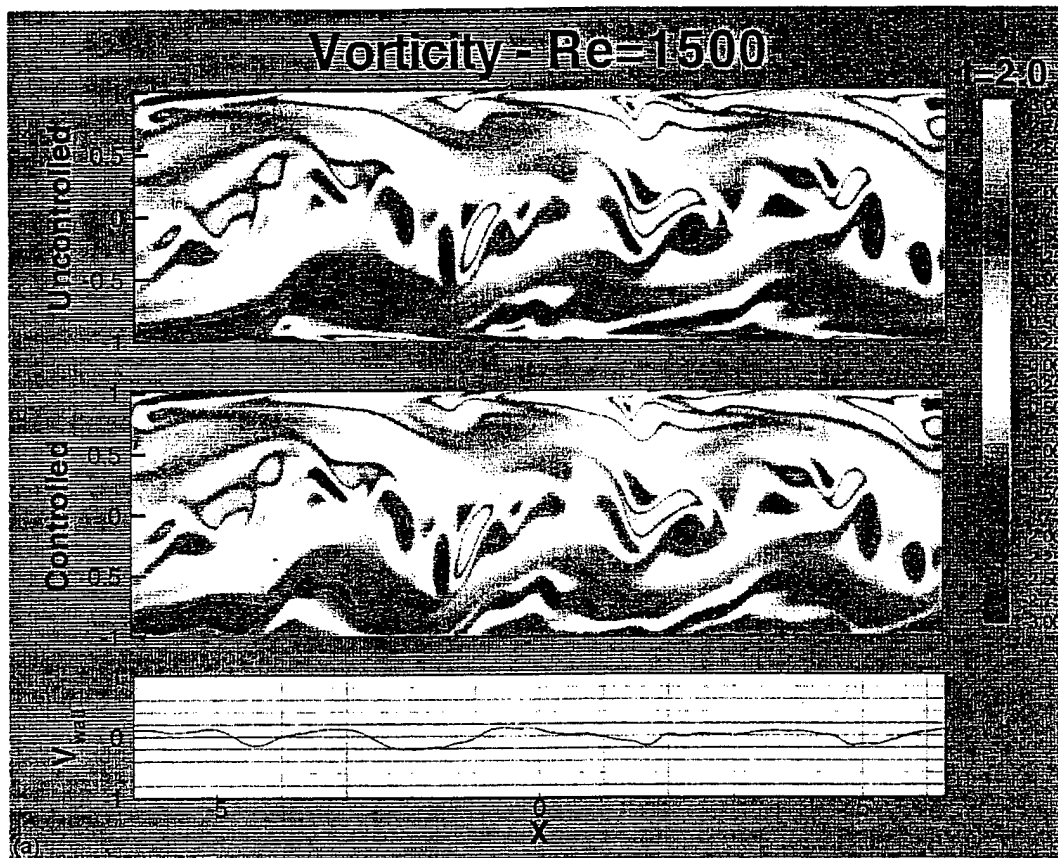


FIGURE 2 Vorticity field for the uncontrolled and controlled case and amplitude of v_w at time $t = 2$ (a) and 4 (b). (See Color Plate I at the end of this issue.)

time $t = 12$ and 14. Figure 3 also presents the amplitude of blowing and suction applied to the bottom wall of the channel. The uncontrolled case shows the evolution of a major eruption along the bottom wall that affects nearly half of the bottom boundary layer as well as part of the top boundary layer. In particular, the pairing process of two large negative vortical structures interacts with a pocket of positive vorticity on the bottom wall. The vortex pairing entrains parts of the positive vorticity enhancing the separation of the flow. In the controlled case almost the entire vorticity field has been strongly modified by the controller, high values of vorticity are confined to the top boundary layer. Near to the bottom wall three negative vortical structures are kept rolling by the controller action although there is no significant

vorticity along the wall. As in the previous figure, the controller injects and removes fluid from the rear and the front of each vortical structure. In this figure it is easy to see that v_w changes sign at the streamwise locations corresponding with the center of the vortical structures. The action of the controller has also reduced the interaction between top and bottom boundary layers resulting in a mild attenuation of the near-wall turbulence at the top wall.

Figure 4 presents a comparison of the vorticity field in the controlled and uncontrolled cases at time $t = 50$. Figure 4 also presents the amplitude of blowing and suction applied to the bottom wall of the channel. The uncontrolled case is dominated by the least stable modes, while all the other modes have been subdued by viscosity. Although the flow

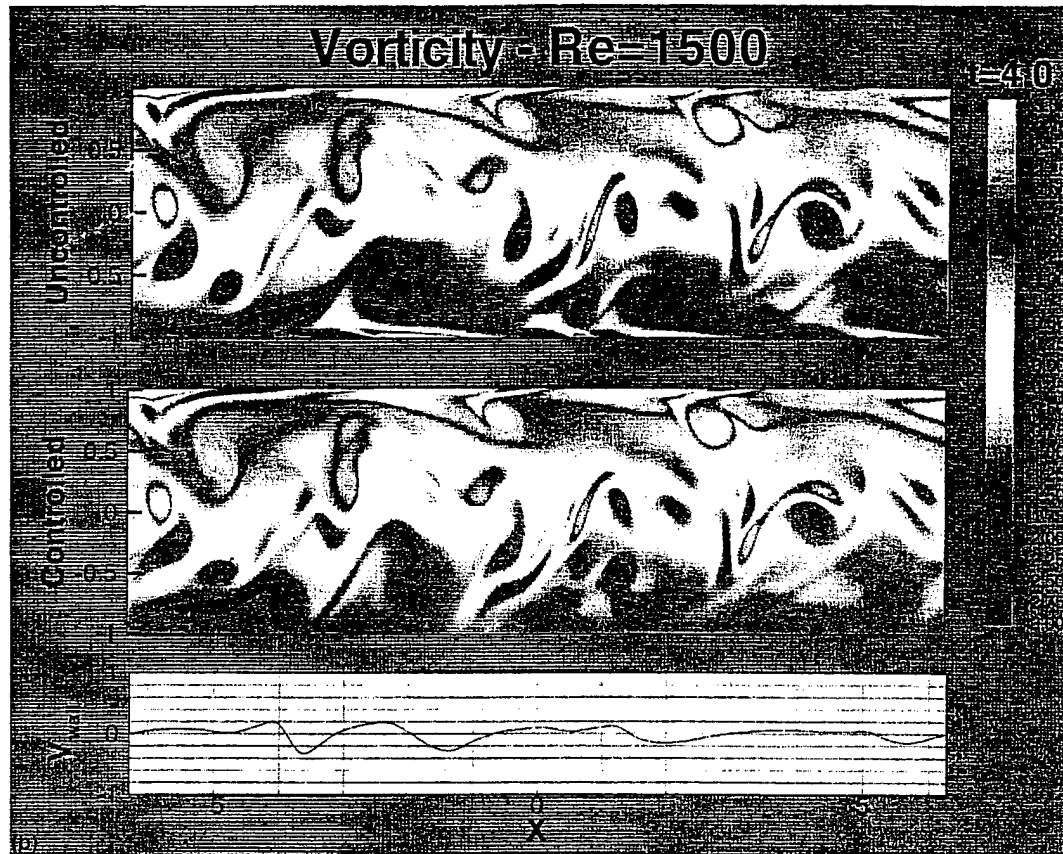


FIGURE 2 (Continued). (See Color Plate II at the end of this issue.)

is slowly relaxing toward the laminar regime, the top and bottom boundary layers are still showing sign of flow separation. In the controlled case the flow has been nearly relaminarized over the entire computational domain. Correspondingly, blowing and suction at the bottom wall is nearly zero.

Figure 5 shows the spatial and temporal evolution of the wall-shear stresses in the uncontrolled case. The wall-shear stresses present a rich structure because of the near-wall turbulence generated by the initial condition. However, viscous effects eventually reduce the amplitude of the wall-shear stresses over time; turbulence in fact cannot sustain itself in a two-dimensional channel flow at $Re = 1500$.

Figure 6 presents the spatial and temporal evolution of the wall-shear stresses and blowing

and suction in the controlled case. The controllers reduce the initial wall-shear stresses in the first few time steps although the estimators (18) start with no information about the reduced-order internal state vector. Subsequently, the amplitude of blowing suction rises to suppress the effects of near-wall turbulence. Eventually, blowing and suction decreases as the near-wall turbulence subdues. Controlled wall-shear stresses show some waviness due to poorly controllable low wave number modes and some ripples at wave numbers higher than 32. Ripples quickly disappears after few time units, while low wave numbers waviness persists for longer time. By the end of the computation, $t = 50$, all the perturbations of the wall-shear stresses have been suppressed and flow has been nearly relaminarized, see Figure 4. The

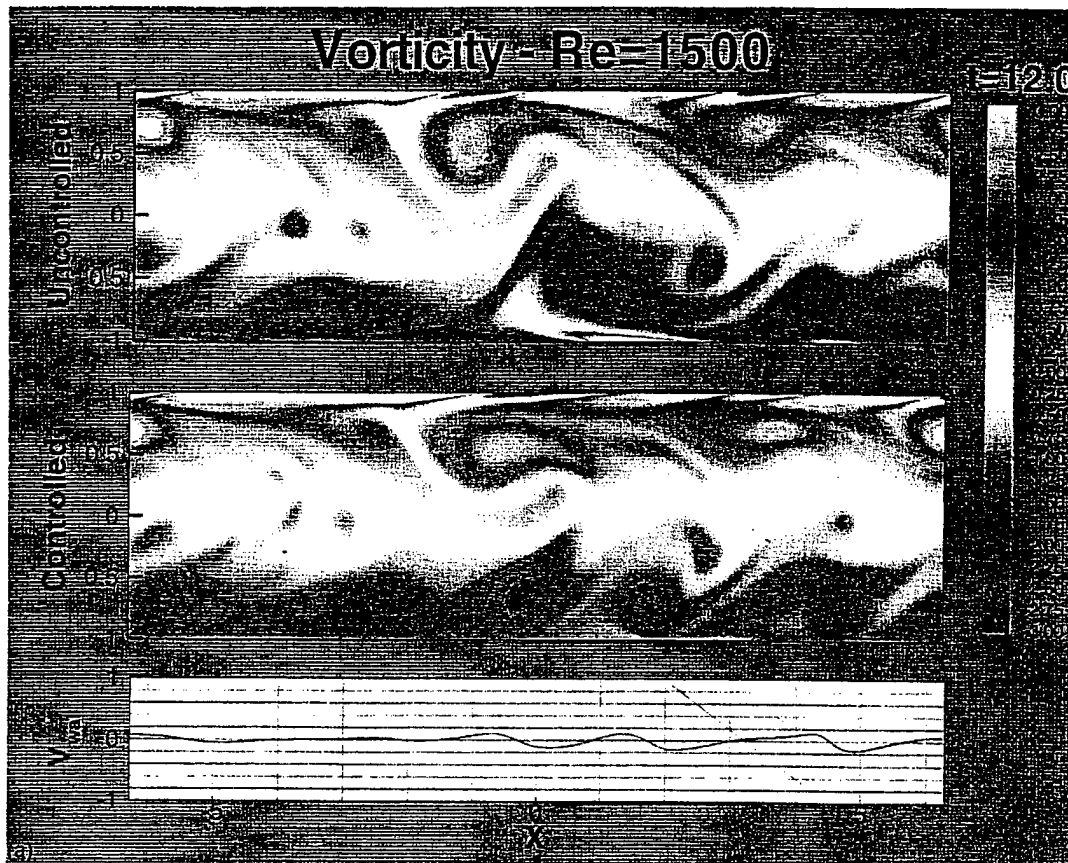


FIGURE 3 Vorticity field for the uncontrolled and controlled case and amplitude of v_w at time $t = 12$ (a) and 14 (b). (See Color Plate III at the end of this issue.)

wall-shear stresses have a nearly constant value 1.62. This value indicates that the average velocity profile near the bottom wall generates about 20% less drag than the parabolic profile. However, this more efficient profile will eventually relax to the parabolic profile due to the viscous effects.

Figures 2–6 indicates the successful performance of the 32 robust reduced-order linear controllers operating in parallel. It is not clear that it is necessary to control disturbances for all 32 wave numbers since disturbances correspondingly to high wave numbers are very quickly damped. Consequently there is hope for further reducing the size of the controller. Any further reduction of the size of the controller increases the potential of using the controller in engineering applications. To investigate this issue we ran the

same simulation presented in Figures 2–6 with only 16 robust reduced-order controllers operating in parallel. The combined order of the controllers for 16 wave numbers is 192, a substantial reduction, 50%, with respect to the previous reduced-order controller, and about 95%, with respect to the order of the full system.

Figure 7 presents the spatial and temporal evolution of the wall-shear stresses in the controlled case when only the controllers corresponding to the 16 lowest wave numbers are operating. During the first few time steps, when the turbulence structures span over all the wave numbers, this partially controlled case presents some noticeable differences with respect to the fully controlled case (Fig. 6). The controller compensates for its inability of controlling high wave numbers by

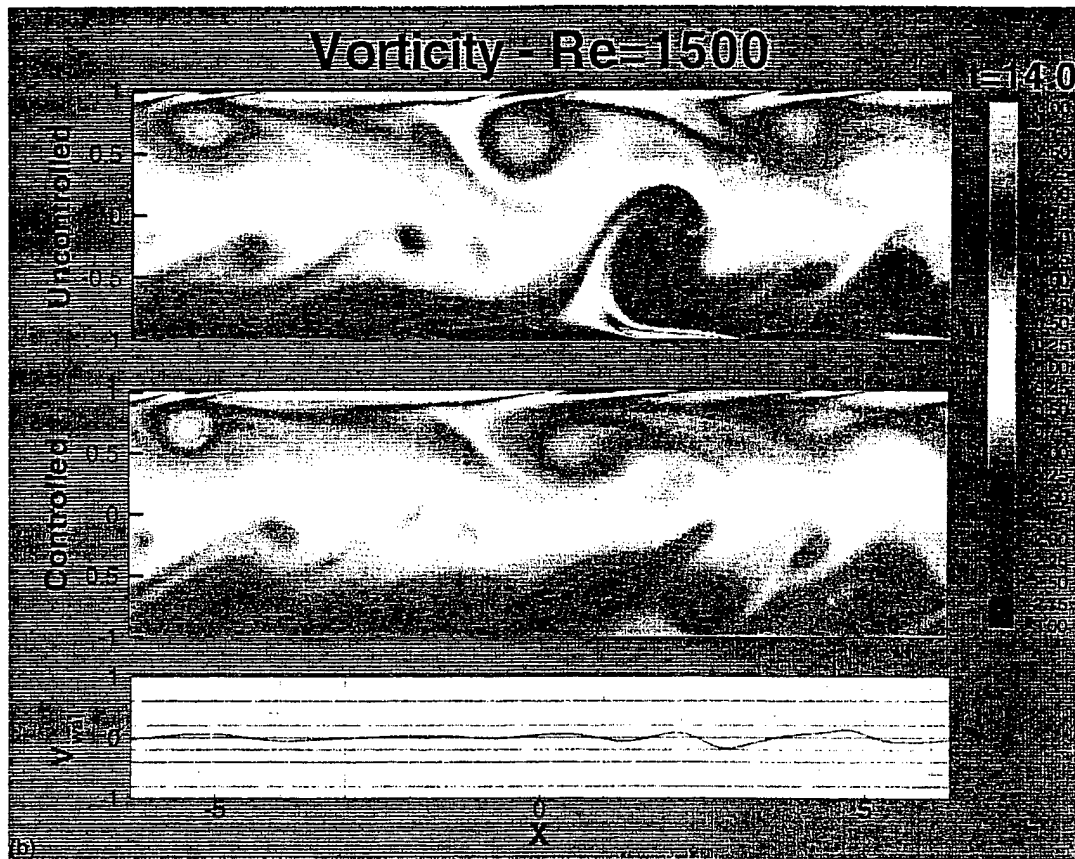


FIGURE 3 (Continued). (See Color Plate IV at the end of this issue.)

increasing the amplitude of blowing and suction at low wave numbers. Consequently, wall-shear stresses show some spikes corresponding to high wave number near-wall turbulence. However, beside these events the wall-shear stresses retain the same trend as in the fully controlled case. At later times, $t > 10$, the wall-shear stresses and blowing and suction at the wall present a trend very similar to the fully controlled case. The wall-shear stresses show some low amplitude waviness at wave numbers higher than 16. Blowing and suction at the wall present a slightly higher amplitude and deformation with respect to the fully controlled case. Nevertheless, the overall effect of the 16 wave numbers controller is a dramatic reduction of the wall-shear stresses and a almost complete relaminarization of the entire flow.

Drag reduction is the dominant reason driving the effort of controlling near-wall turbulence. To estimate the performance of the controller, we compute the drag by integrating the wall-shear stresses along the bottom wall of the channel. Figure 8 compares the drag in the uncontrolled, laminar, fully controlled and partially controlled cases. The drag for the laminar case is exact and equals 2. In the uncontrolled and controlled cases the drag is initially 2 because the initial velocity field has been constructed by superimposing a zero-mean perturbation velocity field onto the laminar flow. In the uncontrolled case, the drag drops below the laminar value during the transient period. Subsequently, drag increases above the laminar value and with some fluctuation reaches its maximum value 2.46 around $t = 25$. In the last half

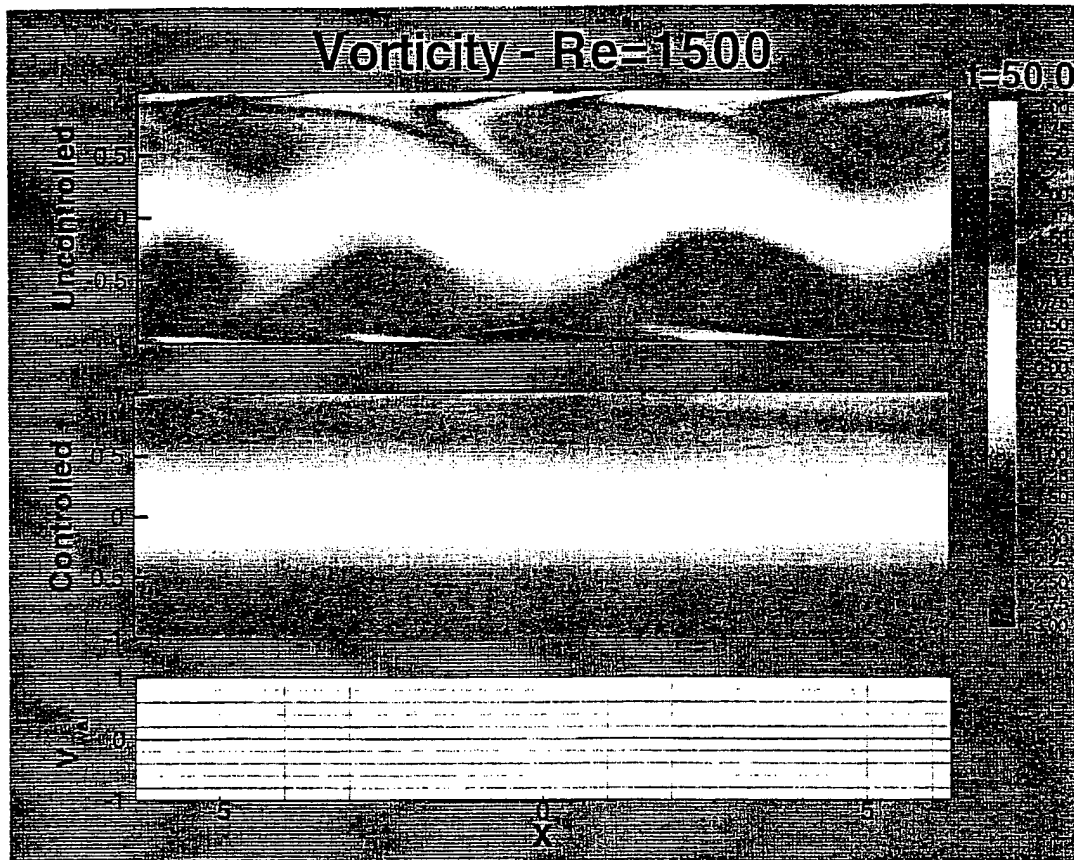


FIGURE 4 Vorticity field for the uncontrolled and controlled case and amplitude of v_w at time $t = 50$. (See Color Plate V at the end of this issue.)

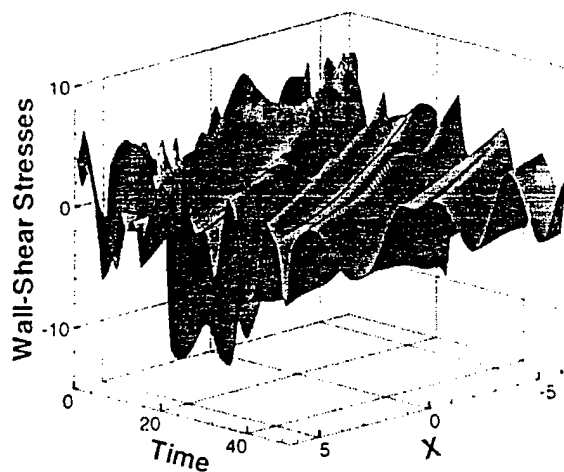
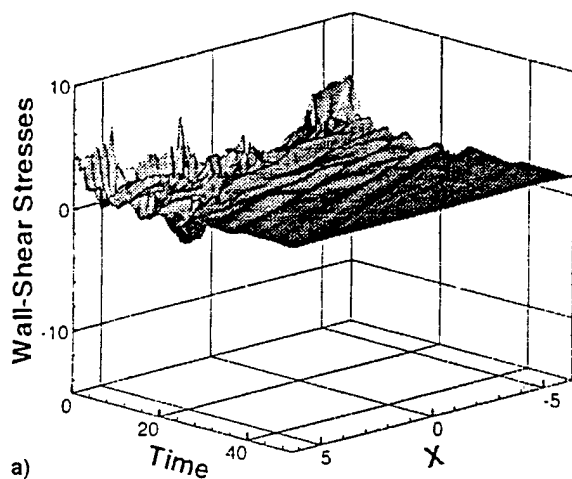
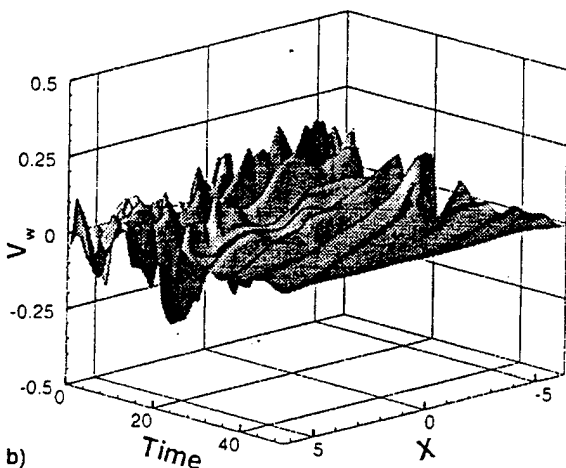


FIGURE 5 Time evolution of the wall-shear stresses along the bottom wall of the channel in the uncontrolled case.

of the simulation the drag decreases toward the laminar value because turbulence is subdued by viscosity, since turbulence cannot sustain itself in a two-dimensional channel flow at this Reynolds number. In the fully controlled case, the drag presents some large fluctuation below the laminar value during the first few time units at the onset of the turbulent flow. The amplitude of the fluctuations reduces with time while the value of the drag stays at about half of the laminar value. In the later part of the simulation the drag slowly increases while the flow is nearly relaminarized. The drag in the partially controlled case is remarkably similar to the fully controlled case. This results substantiates the notion that it is not necessary to control all the wave numbers.



a)

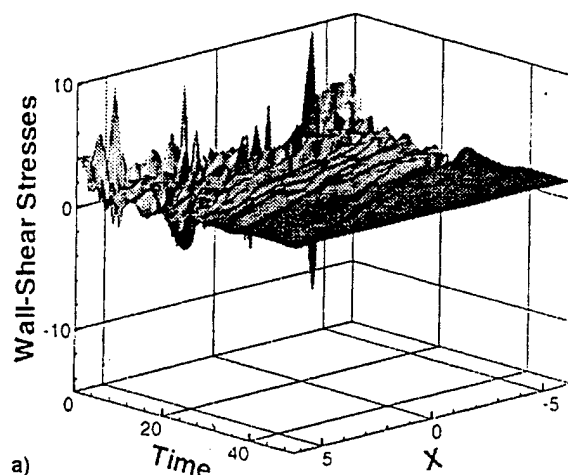


b)

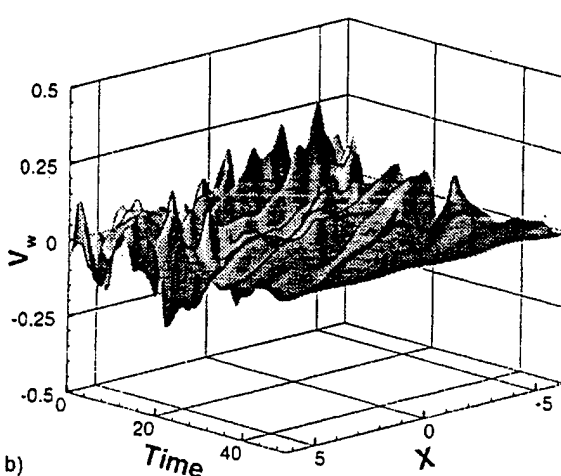
FIGURE 6 Time evolution of the wall-shear stresses (a) and blowing and suction (b) along the bottom wall of the channel with all the controllers operating.

6. CONCLUSIONS

In this article we presented a successful application of robust reduced-order linear feedback control to a two-dimensional channel flow whose initial condition consist of finite-amplitude disturbances. A controller based on a reduced-model of the linearized Navier–Stokes equation, *i.e.*, 10% of the order of the full size system, was designed by using LQG (\mathcal{H}_2) synthesis. This controller was programmed in a computer routine whose input



a)



b)

FIGURE 7 Time evolution of the wall-shear stresses (a) and blowing and suction (b) along the bottom wall of the channel with the controllers operating only on wave numbers 1 through 16.

measurements are the gradients of the streamwise velocity component and whose output controls are the blowing and suction at the wall. This routine, suited for parallel computing, was embedded in a direct numerical simulation of the Navier–Stokes equations. As a case study, we applied the controller to the bottom wall of a two-dimensional turbulent periodic channel flow at $Re = 1500$. The controller drastically reduced near-wall turbulence preventing boundary layer eruptions and flow separations and eventually relaminarized

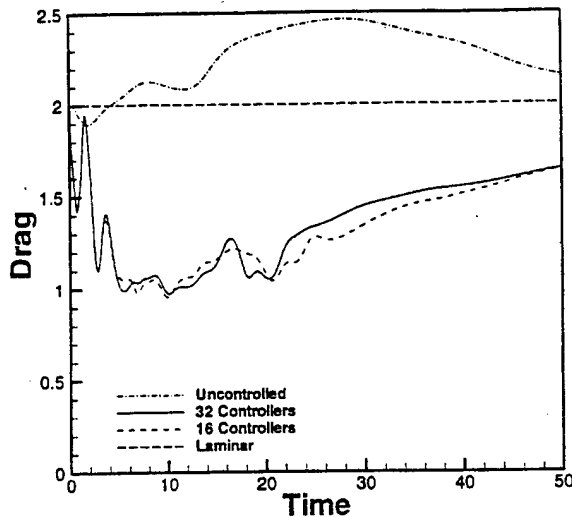


FIGURE 8 Comparison of the total drag measured at the bottom wall of the channel: laminar flow, uncontrolled turbulent flow, fully and partially controlled turbulent flow.

almost the entire flow. A dramatic drag reduction was obtained, up to 50% with respect to the laminar flow and up to 60% with respect to the turbulent flow. Extensions of LQG (\mathcal{H}_2) design and applications of \mathcal{H}_∞ design [25, 26] to three-dimensional channel flows and three-dimensional Blasius boundary layers are in progress.

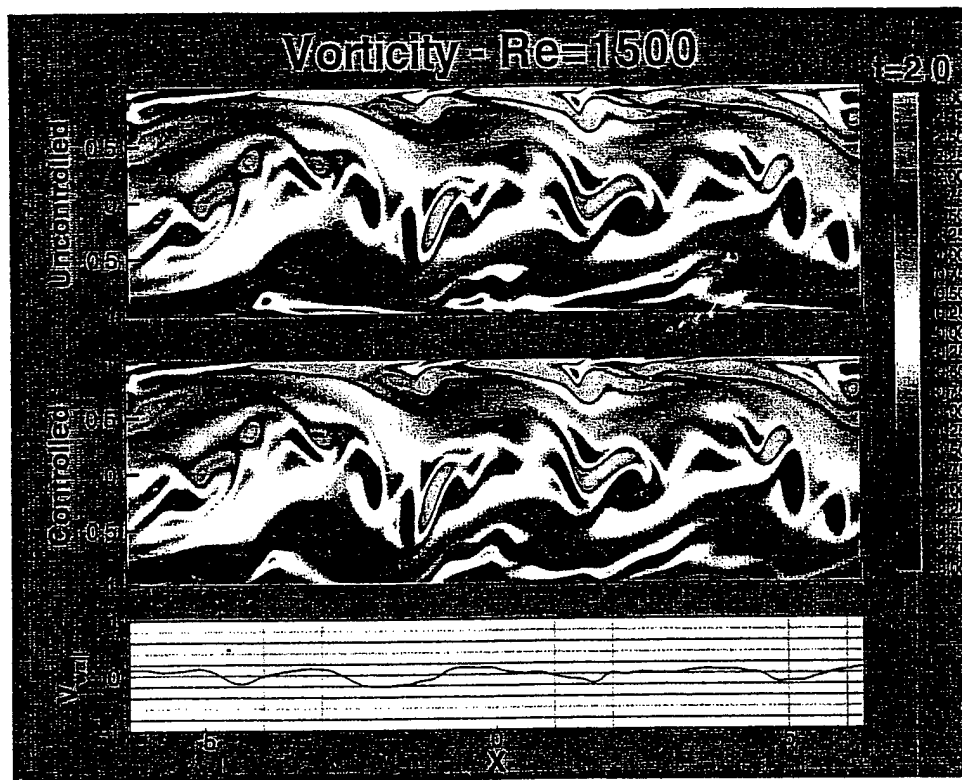
Acknowledgements

The authors thank Dr. J. Burns, Dr. S. Joshi, Dr. R. E. Kelly and Dr. R. T. Mcloskey for the enlightening discussions. This work is supported by AFOSR Grant F49620-97-1-0276 and by NASA Grant NCC 2-374 Pr 41.

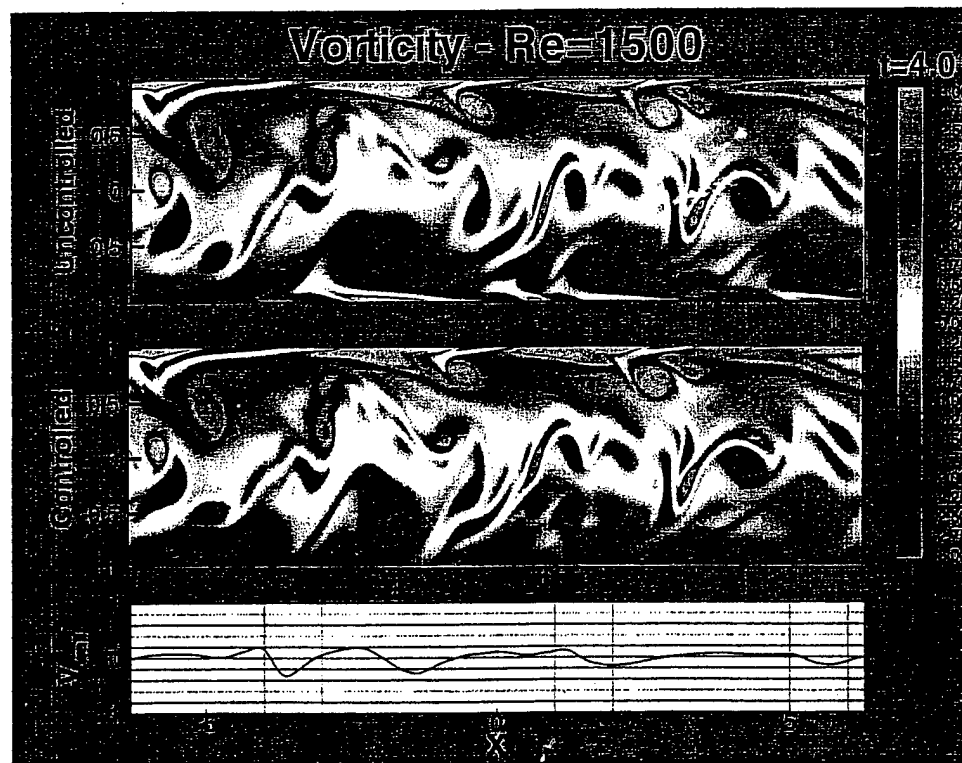
References

- [1] Gad-el-Hak, M. (1994). Interactive control of turbulent boundary layers - A futuristic overview, *AIAA Journal*, 32(9), 1753.
- [2] Modi, V. J. (1997). Moving surface boundary-layer control: A review, *Journal of Fluids and Structures*, 11(6), 627-663.
- [3] Reed, H. L., Saric, W. S. and Arnal, D. (1996). Linear stability theory applied to boundary layers, *Annu. Rev. Fluid Mech.*, 28, 389.
- [4] Barnwell, R. W. and Hussaini, M. Y. (1992). "Natural laminar flow and laminar flow control" (Springer-Verlag, New York).
- [5] Koumoutsakos, P. (1997). Active control of vortex-wall interactions, *Physics of Fluids*, 9(12), 3808-3816.
- [6] Rathnasingham, R. and Breuer, K. S. (1997). System identification and control of a turbulent boundary layer, *Physics of Fluids*, 9(7), 1867-1869.
- [7] Lee, C., Kim, J., Babcock, D. and Goodman, R. (1997). Application of neural networks to turbulence control for drag reduction, *Physics of Fluids*, 9(6), 1740-1747.
- [8] Crawford, C. H. and Karniadakis, G. E. (1997). Reynolds stress analysis of EMHD-controlled wall turbulence. 1. Streamwise forcing, *Physics of Fluids*, 9(3), 788-806.
- [9] Kato, T., Fukunishi, Y. and Kobayashi, R. (1997). Artificial control of the three-dimensionalization process of T-S waves in boundary-layer transition, *JSME International Journal Series B-Fluids and Thermal Engineering*, 40(4), 536-541.
- [10] Singh, S. N. and Bandyopadhyay, P. R. (1997). Linear feedback control of boundary layer using electromagnetic microtiles, *Journal of Fluids Engineering-Transactions of the ASME*, 119(4), 852-858.
- [11] Nelson, P. A., Wright, M. C. M. and Rioual, J. L. (1997). Automatic control of laminar boundary-layer transition, *AIAA Journal*, 35(1), 85-90.
- [12] Carlson, H. A. and Lumley, J. L. (1996). Active control in the turbulent wall layer of a minimal flow unit, *Journal of Fluid Mechanics*, 329, 341-371.
- [13] Farrell, B. F. and Ioannou, P. J. (1996). Turbulence suppression by active control, *Physics of Fluids*, 8(5), 1257-1268.
- [14] Joslin, R. D., Eriebacher, G. and Hussaini, M. V. (1996). Active control of instabilities in laminar boundary layers - overview and concept validation, *Journal of Fluids Engineering-Transactions of the ASME*, 118(3), 494-497.
- [15] Lee, T., Fisher, M. and Schwarz, W. H. (1995). Investigation of the effects of a compliant surface on boundary-layer stability, *Journal of Fluid Mechanics*, 288, 37-58.
- [16] Choi, H., Moin, P. and Kim, J. (1994). Active turbulence control for drag reduction in wall-bounded flows, *Journal of Fluid Mechanics*, 262, 75-110.
- [17] Hackenberg, P., Rioual, J. L., Tutty, O. R. and Nelson, P. A. (1995). The automatic control of boundary-layer transition - experiments and computation, *Applied Scientific Research*, 54(4), 293-311.
- [18] Rist, U. and Fasel, H. (1995). Direct numerical simulation of controlled transition in a flat-plate boundary layer, *Journal of Fluid Mechanics*, 298, 211-248.
- [19] Hubbard, S. and Riley, N. (1995). Boundary-layer control by heat and mass transfer, *International Journal of Heat and Mass Transfer*, 38(17), 3209-3217.
- [20] Joslin, R. D., Nicolaides, R. A., Eriebacher, G., Hussaini, M. Y. and others (1995). Active control of boundary-layer instabilities - use of sensors and spectral controller, *AIAA Journal*, 33(8), 1521-1523.
- [21] Modi, V. J., Stihl, S. and Yokomizo, T. (1995). Drag reduction of trucks through boundary-layer control, *Journal of Wind Engineering and Industrial Aerodynamics*, 54, 583-594.
- [22] Jimenez, J. (1994). On the structure and control of near wall turbulence, *Physics of Fluids*, 6(2), 944-953.

- [23] Elrefaee, M. M. (1994). Boundary layer control of separated flow over circular cylinders – a bemparapetric study, *Engineering Analysis with Boundary Elements*, **14**(3), 239–254.
- [24] Kwong, A. H. M. and Dowling, A. P. (1994). Active boundary-layer control in diffusers, *AIAA Journal*, **32**(12), 2409–2414.
- [25] Shou, K., Doyle, J. C. and Glover, K. (1996). Robust and optimal control (Prentice Hall).
- [26] Rhee, I. and Speyer, J. L. (1996). A game theoretic approach to a finite-time disturbance attenuation problem, *IEEE Trans. Automatic Control*, **36**(9), 1021.
- [27] Joshi, S. S., Speyer, J. L. and Kim, J. (1997). A systems theory approach to the feedback stabilization of infinitesimal and finite-amplitude disturbances in plane Poiseuille flow, *J. Fluid Mech.*, **332**, 157.
- [28] Joshi, S. S., Speyer, J. L. and Kim, J., Modelling and control of two dimensional Poiseuille flow, *Proc. 34th Conference on Decision and Control*, New Orleans, Louisiana, December 1995, p. 921.
- [29] Hu, H. H. and Bau, H. H. (1994). Feedback control to delay or advance linear loss of stability in planar Poiseuille flow, *Proc. Royal Soc. of London A*, **447**(1930), 299.
- [30] Cortelezzi, L. and Speyer, J. L., Robust reduced-order controller of laminar boundary layer transitions, *Phys. Rev. E*, **58**(2), to appear.
- [31] Lee, K.-H., Doctoral dissertation, in preparation.
- [32] Doyle, J. C. and Stein, G. (1981). Multivariable feedback design: Concepts for a classical/modern synthesis, *IEEE Trans. Automatic and Control*, **AC-26**(2).
- [33] Thak, M. and Speyer, J. L. (1987). Modeling and parameter variations on asymptotic LQG synthesis, *IEEE Trans. Automatic and Control*, **AC-32**(9).
- [34] Farrell, B. F. (1988). Optimal excitation of perturbations in viscous shear flows, *Phys. Fluids*, **31**(8), 2093.



COLOR PLATE I (See L. Cortelezzi *et al.*, page 85).

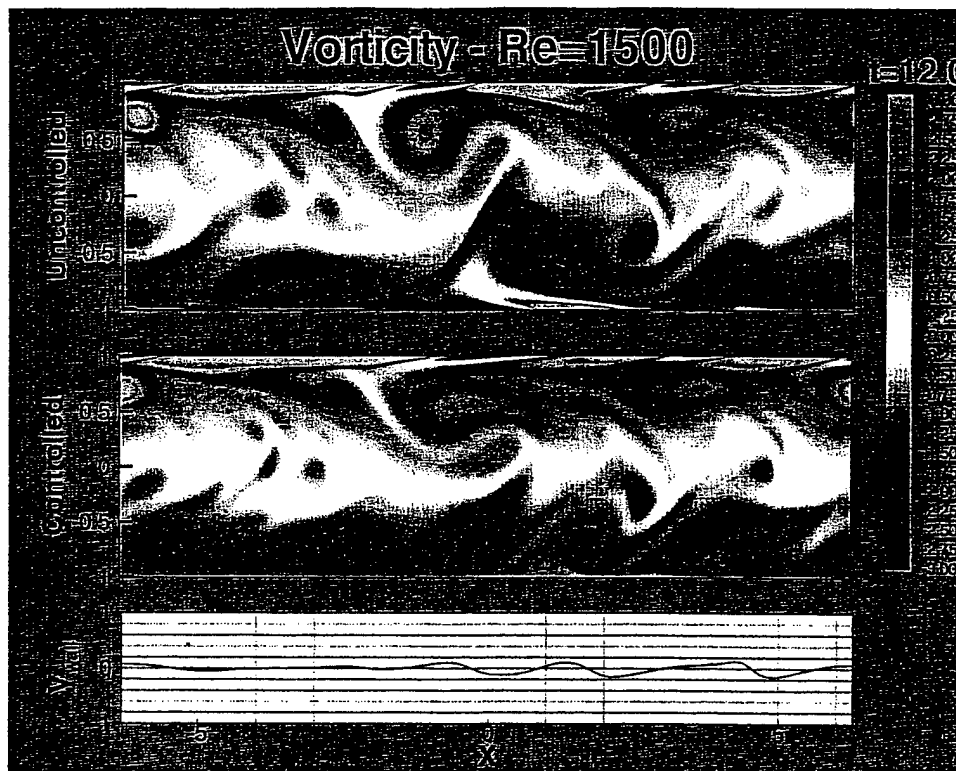


COLOR PLATE II (See L. Cortelezzi *et al.*, page 86).

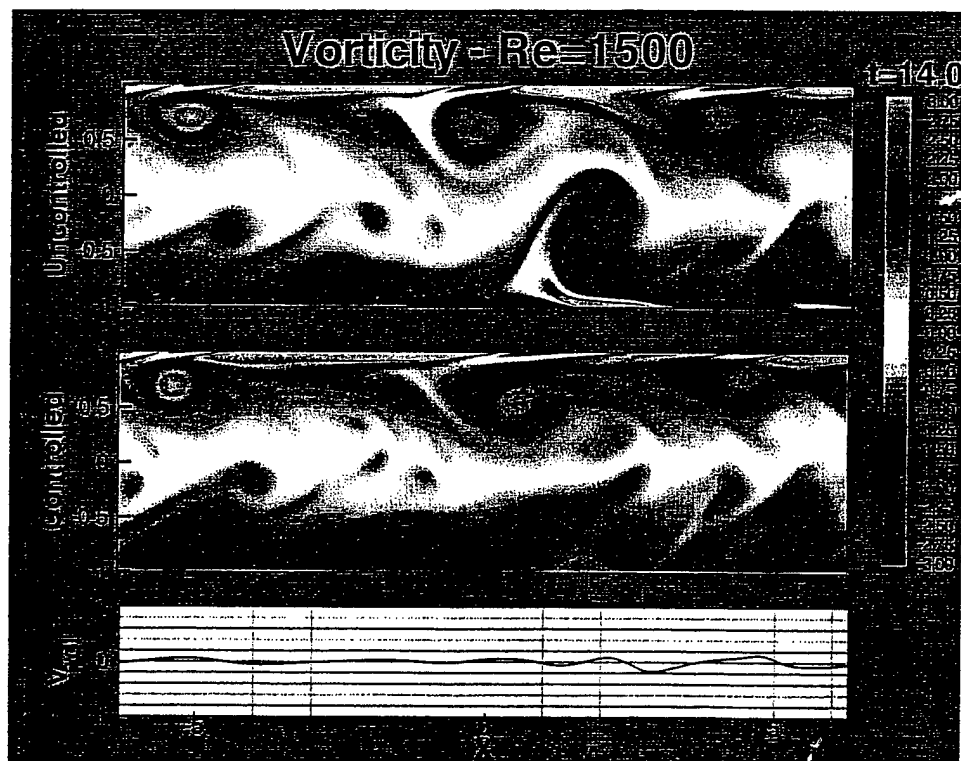
APPENDIX C

Skin-Friction Drag Reduction via Robust Reduced-Order Linear Feedback Control

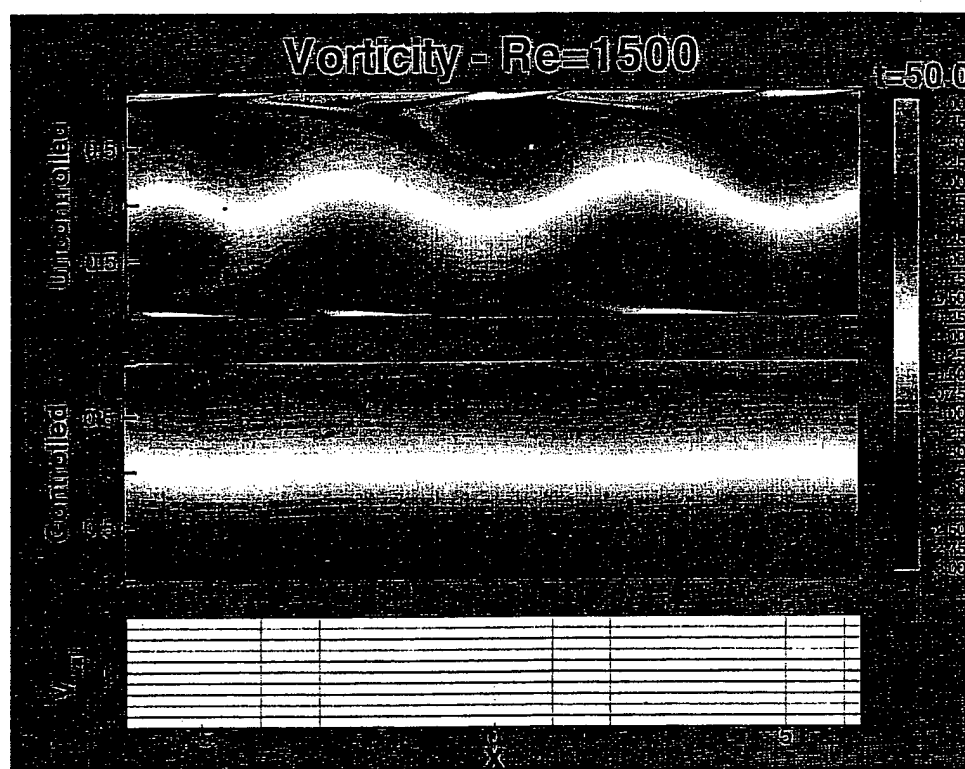
L. Cortelezzi, K.H. Lee, J. Kim, J.L. Speyer



COLOR PLATE III (See L. Cortelezzi *et al.*, page 87).



COLOR PLATE IV (See L. Cortelezzi *et al.*, page 88).



COLOR PLATE V (See L. Cortelezzi *et al.*, page 89).

APPENDIX D

Robust Reduced-Order control of Turbulent Channel Flows via Distributed Sensors and Actuators

L. Cortelezzi, J.L. Speyer, K.H. Lee, J. Kim

Robust Reduced-Order Control of Turbulent Channel Flows Via Distributed Sensors and Actuators

by L. CORTELEZZI,^{1,2,3} J.L. SPEYER², K.H. LEE² and J. KIM,²

² Department of Mechanical and Aerospace Engineering
University of California, Los Angeles, California 90095-1597

³ Department of Mechanical Engineering
McGill University, Montreal, Canada H3A-2K6

Abstract

Robust reduced-order feedback control of near-wall turbulence in a channel flow is investigated. Wall-transpiration is the means for suppressing near-wall disturbances. Measurements of wall-shear stress to be fed back to the controller are provided by sensors distributed along the wall of the channel. A quadratic cost function is composed of the wall-shear stress and the control effort. Linear-quadratic-Gaussian/loop-transfer-recovery synthesis, and model reduction techniques are used to derive robust feedback controllers from the linearized two-dimensional Navier-Stokes equations. Controllers' performance is first tested on a numerical simulation of infinitesimal three-dimensional disturbances in the presence of finite-amplitude two-dimensional perturbations. Controllers' performance is subsequently tested on a direct numerical simulation of a fully developed turbulent channel flow. Preliminary controllers' performance for the nonlinear flow was surprisingly good, suggesting that the linear system can be used as a basis for developing controllers for near-wall turbulence.

1 Introduction

The reduction of drag produced by skin friction, or, in other words, the reduction of wall-shear stresses generated by near-wall turbulence have received wide attention. "The skin friction constitutes about 50%, 90%, and 100% of the total drag on commercial aircraft, underwater vehicles, and pipelines, respectively" [1]. Two are the near-wall flows of interest: boundary layers that transition from laminar to turbulent regime and boundary layers that are inherently turbulent. Correspondingly, efforts of reducing skin friction fall in two broad categories: transition inhibition and turbulence suppression. References [1-3] are recent reviews summarizing achievements and open questions in boundary

¹Corresponding author: Telephone (310) 206-2732, Facsimile (310) 206-6673, E-mail: cortl@math.ucla.edu

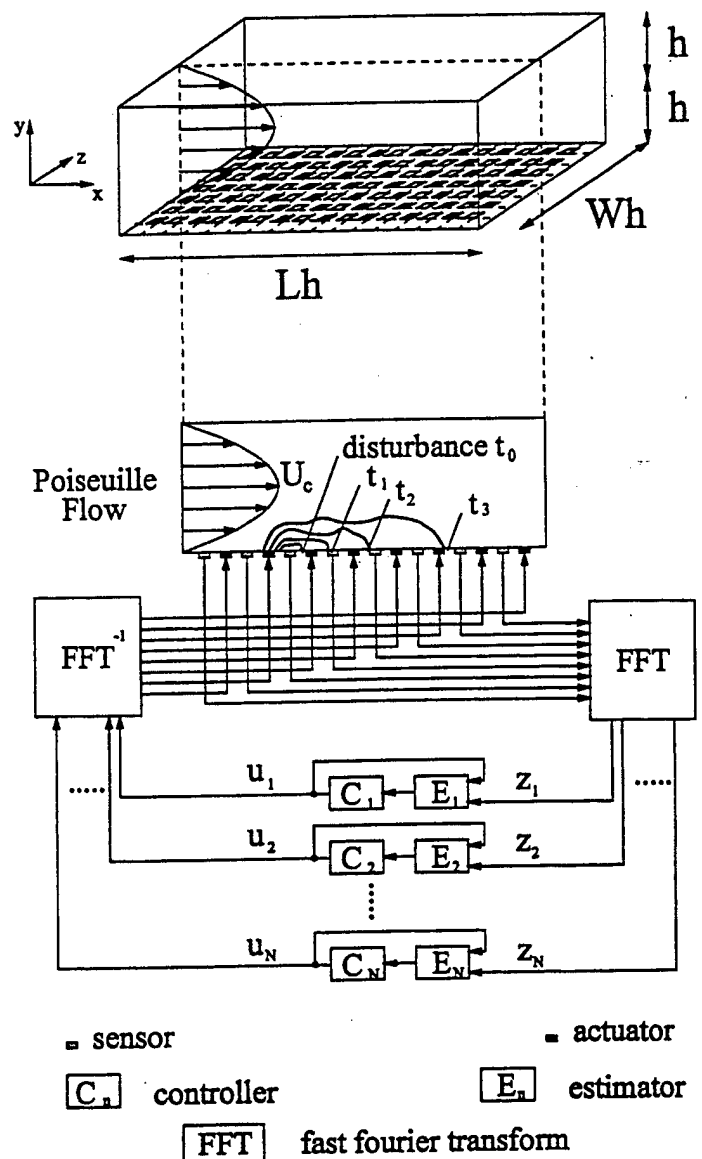


Figure 1: Controller architecture.

layer control.

Boundary layer control has been attempted with some success. It is becoming widely accepted that even better results could be obtained by using controllers able to analyze distributed measurements and coordinate distributed actuators. However, very little has been done except for Refs. [4-7] to exploit the tools recently developed in the control community [8], [9]. In particular, linear-quadratic-Gaussian (LQG) design, or, in modern terms, \mathcal{H}_2 design, combined with model reduction techniques for multi-inputs-multi-outputs (MIMO) systems has been introduced in fluid mechanics by Cortezzi and Speyer [10].

Recently, Cortezzi and Speyer [10] used multi-input-multi-output (MIMO) linear-quadratic-Gaussian (LQG)/loop-transfer-recovery (LTR) synthesis [11], combined with model reduction techniques for designing an optimal and robust linear feedback controller able to suppress wall-disturbances leading to transitions in a two-dimensional laminar channel flow. The present paper shows that the controller derived by Cortezzi and Speyer, based on a reduced-model of the linearized two-dimensional Navier-Stokes equations, can be applied to the control of skin-friction drag in a fully developed three-dimensional turbulent channel flow.

In Section 2, we formulate the problem in terms of the three-dimensional Navier-Stokes equations and we provide details about the numerical scheme used to integrate them. In Section 3, we provide some motivation for the approximate structure of the controller. Furthermore, we derive the state space equations from the linearized two-dimensional Navier-Stokes equations. In Section 4, we reduce the order of the state space equations and derive a robust reduce-order controller by using LQG/LTR synthesis. In Section 5 we apply the controller based on the two-dimensional linearized Navier-Stokes equations to a three-dimensional transitional channel flow at $Re = 1500$ and to a fully turbulent channel flow at $Re = 1700$ and discuss its performance. Conclusions will close the article.

2 Mathematical Formulation

We consider the flow of an incompressible fluid in a three-dimensional periodic channel of length Lh , width Wh , and height $2h$, see Figure 1. This problem is governed by the Navier-Stokes and continuity equations

$$\begin{aligned} u_t + uu_x + vv_y + ww_z &= -p_x + Re^{-1} \Delta u, \\ v_t + uv_x + vv_y + wv_z &= -p_y + Re^{-1} \Delta v, \end{aligned} \quad (1)$$

$$w_t + uw_x + vw_y + ww_z = -p_z + Re^{-1} \Delta w,$$

$$u_x + v_y + w_z = 0. \quad (2)$$

We made the problem dimensionless by using h as characteristic length and h/U_c as characteristic time, where U_c is the velocity at the center of the channel. The Reynolds number is $Re = U_c h / \nu$.

We apply blowing and suction at the walls of the channel to suppress near-wall disturbances within the boundary layer. To simplify the problem the actuators are assumed continuously distributed along the walls. The corresponding boundary conditions are

$$\begin{aligned} u(x, \pm 1, z, t) &= w(x, \pm 1, z, t) = 0, \\ v(x, \pm 1, z, t) &= v_{\pm w}(x, z, t). \end{aligned} \quad (3)$$

The control functions $v_{\pm w}$ prescribe the amount of blowing and suction at the walls.

We measure the gradient of the streamwise velocity along the walls at given points (x_i, z_j) to detect and measure near-wall disturbances within the boundary layer. In other words, we measure

$$z(x_i, z_j, t) = u_y|_{x=x_i, z=z_j, y=\pm 1}. \quad (4)$$

Time dependent incompressible Navier-Stokes equations (1)-(3) with the appropriate initial condition are integrated numerically by using a spectral code with computational domain $(4\pi, 2, 4\pi/3)$ and a grid resolution of $(32, 65, 32)$ in the (x, y, z) directions, respectively.

3 Derivation of the State-Space Equations

The challenge of the present study is to reduce the size of the controller. The controller based on the full system would have $> 10^5$ states, when the Navier-Stokes equations are written in the vertical-velocity-vertical-vorticity (v, ω_y) form, and spectrally decomposed with 32 Fourier modes in the streamwise and spanwise directions and 65 Chebyshev polynomials in the vertical direction. A controller with hundreds of thousands of states is of no interest in engineering applications because of the amount of hardware and computer power necessary to compute a real-time control law. Consequently, it is crucial to reduce the order of the controller.

Figure 1 presents the architecture of the controller tested in this study. In order to reduce the order of the controller we slice the channel with 32 xy -planes equally spaced in the z -direction. Since the gap between planes is small with respect to the spanwise dimension of the channel and there is no mean flow in the spanwise direction, we assume that the flow in a xy -plane is nearly two-dimensional. We apply the controller derived by Cortezzi and Speyer [10] from the linearized two-dimensional Navier-Stokes equation to each plane. This controller has successfully reduced skin-friction drag generated by near-wall finite-amplitude disturbances in a two-dimensional channel flow at $Re = 1500$ [12].

In this section we outline the derivation of the state-space equations in a given xy -plane [10]. In Section 5 blowing and suction is applied to the bottom wall only in the case of a transitional flow while is applied to both walls in the case of a fully developed turbulent flow. Consequently, to simplify the exposition we derive the state space equations assuming that blowing and suction is applied only at the bottom wall. The application of blowing and suction to both walls is a trivial extension of this case.

We consider two-dimensional incompressible Poiseuille flow in a periodic channel of length Lh and height $2h$. The undisturbed velocity field has a parabolic profile with centerline velocity U_c , see Figure 1. We linearize two-dimensional Navier-Stokes equations about the parabolic profile and we rewrite them in terms of the perturbation stream-function ψ

$$(\partial_t + U\partial_x) \Delta \psi - U''\psi_x = Re^{-1} \Delta \Delta \psi, \quad (5)$$

to identically satisfy continuity.

To suppress perturbations evolving within the bottom boundary layer we apply blowing and suction at the bottom wall (see Figure 1). For simplicity we assume that the actuators are continuously distributed. Perturbations in the top boundary layer are left free to evolve. The corresponding boundary conditions are

$$\psi_x|_{y=-1} = -v_w(x, t), \quad \psi_y|_{y=\pm 1} = \psi|_{y=1} = 0, \quad (6)$$

where the control function v_w prescribes the amount of blowing and suction at the bottom wall. We impose that the mass of fluid injected equals the mass of fluid removed.

To detect and measure the near-wall disturbances, we measure the gradient of the streamwise velocity component at given points $x = x_i$ along the bottom wall (see Figure 1)

$$z(x_i, t) = \psi_{yy}|_{y=-1}. \quad (7)$$

In other words, we measure the first term of the wall-shear stress, $\tau_{yx} = Re^{-1}(\psi_{yy} - \psi_{xx})|_{y=-1}$. The second term of the wall-shear stress is zero in the uncontrolled case and is known in the controlled case.

We define an optimal performance index J , or cost function, to design a controller for the LQG (\mathcal{H}_2) problem. Since we are interested in suppressing wall-shear stress, we define

$$J = \lim_{t_f \rightarrow \infty} \int_{t_f}^{t_f} \int_0^L (\psi_{yy}^2 + \psi_{xx}^2)|_{y=-1} dx dt. \quad (8)$$

The integrand represents the cost of the wall-shear stress being different from zero. Moreover, the integrand implicitly accounts for the cost of implementing

the control itself. There are two reasons to minimize the cost of the controller: In any engineering application the energy available to drive the controller is limited; and a large control action may drive the system away from the region where the linear model is valid.

To reduce (5)-(7) to a set of first-order ordinary differential equations, we make a few transformations. We write the stream-function as $\psi = \phi + \chi$ to embed the actuator into the evolution equation and to make the boundary conditions homogeneous. Substituting $\psi = \phi + \chi$ into equation (5), we obtain a forced equation for the Poiseuille flow

$$(\partial_t + U\partial_x) \Delta \phi - U''\phi_x = Re^{-1} \Delta \Delta \phi - (\partial_t + U\partial_x) \Delta \chi + U''\chi_x + Re^{-1} \Delta \Delta \chi, \quad (9)$$

with homogeneous boundary conditions $\phi|_{y=\pm 1} = \phi_y|_{y=\pm 1} = 0$. The forcing function χ satisfies the non-homogeneous boundary conditions (6), i.e., $\chi_x|_{y=-1} = -v_w(x, t)$, $\chi|_{y=1} = \chi_y|_{y=\pm 1} = 0$. We also substitute $\psi = \phi + \chi$ into equations (7) and (8). The measurement equation (7) becomes

$$z(x_i, t) = (\phi_{yy} + \chi_{yy})|_{x=x_i, y=-1}, \quad (10)$$

while the cost function (8) takes the following form

$$J = \lim_{t_f \rightarrow \infty} \int_{t_f}^{t_f} \int_0^L [(\phi_{yy} + \chi_{yy})^2 + \chi_{xx}^2]|_{y=-1} dx dt. \quad (11)$$

Subsequently, flow quantities are spectrally decomposed by using circular functions in the streamwise direction and Chebyshev polynomials in the vertical direction. We expand ϕ and χ as follows:

$$\phi = \sum_{n=1}^N \sum_{m=0}^M [a_{nm}(t) \cos(\alpha_n x) + b_{nm}(t) \sin(\alpha_n x)] C_m(y), \quad (12)$$

$$\chi = \sum_{n=1}^N [p_n(t) \cos(\alpha_n x) + q_n(t) \sin(\alpha_n x)] D(y), \quad (13)$$

where $\alpha_n = 2\pi n/L$. Functions C_m and D are combinations of Chebyshev polynomials constructed to satisfy the boundary conditions, i.e., $C_m(\pm 1) = C'_m(\pm 1) = D(1) = D'(\pm 1) = 0$ and $D(-1) = 1$. We also expand the measurement function z as follows:

$$z = \sum_{n=1}^N [c_n(t) \cos(\alpha_n x) + d_n(t) \sin(\alpha_n x)]. \quad (14)$$

Substituting expansions (12), (13) and (14) into equations (9) and (10) and using Galerkin's projection, we obtain

$$\frac{dy}{dt} = A y + B_1 u + B_2 \frac{du}{dt}, \quad z = C y + D_3 u. \quad (15)$$

To transform the above equations into standard state-space form, we define a new vector $x = y + B_2 u$, and two new matrices $B = B_1 + A B_2$, $D = D_3 + C B_2$. Finally, we obtain the state-space equations

$$\frac{dx}{dt} = A x + B u, \quad z = C x + D u, \quad (16)$$

with initial condition $x(0) = x_0$; where x is the internal state vector, u is the control vector and z is the measurement vector. Matrices A , B , C contain the dynamics of the Poiseuille flow, actuators and sensors, respectively. Matrix D contains the coupling between sensors and actuators. The cost function (11) becomes

$$J = \lim_{t_f \rightarrow \infty} \int_t^{t_f} [z^* z + u^* W^* W u] dt, \quad (17)$$

where the superscript * denotes transpose. The matrix W is obtained by spectrally decomposing the last term in the cost function (11).

The advantage of the present formulation is that the whole problem decouples with respect to the wave number. All matrices in (16) and (17) are block diagonal. The block diagonal structure of the matrix A was first recognized in Ref. [5]. The above state-space system is consequently equivalent to N state-space sub-systems, one for each wave number. For a given wave number r the state-space equations are

$$\frac{dx_r}{dt} = A_r x_r + B_r u_r, \quad z_r = C_r x_r + D_r u_r, \quad (18)$$

with initial condition $x_r(0) = x_{r0}$. Vectors x_r , u_r , z_r have the following structure: $x_r = [a'_{r0}, \dots, a'_{rM}, b'_{r0}, \dots, b'_{rM}]^*$, $u_r = [p_r, q_r]^*$, $z_r = [c_r, d_r]^*$, where ' indicates the Fourier coefficients that have been affected by the transformation. The cost function also decouples with respect to the wave number and we obtain N optimal performance indexes. For a given wave number r the cost function is defined as follows

$$J_r = \lim_{t_f \rightarrow \infty} \int_t^{t_f} [z_r^* z_r + u_r^* W_r^* W_r u_r] dt. \quad (19)$$

Consequently, the design of a robust controller for the system (16) with (17) has been reduced to the independent design of N robust controllers, one for each wave number, for the sub-systems (18) with (19).

4 Model Reduction and Controller Design

In this section we take a further step toward model reduction. We derive a lower order two-dimensional controller in two steps: First we construct a lower order model of (18), and subsequently, we design a robust controller for the reduced-order model. To obtain a lower order model, we transform (18) into Jordan Canonical form. The matrices $\hat{A}_r, \hat{B}_r, \hat{C}_r, D_r$ that describe the dynamics of the reduced-order model are

obtained from the matrices in Jordan Canonical form by retaining rows and columns corresponding to equally well controllable or observable states. Hat denotes the quantities associated with the reduced-order model.

Although a rigorous mathematical framework for the design of disturbance attenuation (\mathcal{H}_∞) linear controllers is provided by the control synthesis theory in Refs. [8] and [9], for this initial study LQG (\mathcal{H}_2) synthesis is quite adequate. In general, the design of a robust linear feedback controller for the LQG (\mathcal{H}_2) problem is divided in two parts: linear-quadratic-regulator (LQR) and minimum variance estimator (Kalman-Bucy filter). The LQR design provides an optimal control law in terms of the internal state vector by minimizing a cost function. The internal state vector is essential to implement the control law but, in general, it is not a physical quantity directly measurable, but reconstructed from the measurement vector z_r by the estimator. The result of the LQG (\mathcal{H}_2) design of a robust controller based on the reduced-order model of (18) is summarized by the following equations:

$$u_r = -\hat{K}_r \hat{x}_r, \quad (20)$$

$$\frac{d\hat{x}_r}{dt} = \hat{A}_r \hat{x}_r + \hat{B}_r u_r + \hat{L}_r [z_r - \hat{C}_r \hat{x}_r - D_r u_r], \quad (21)$$

with initial conditions $\hat{x}_r(0) = 0$. Equation (20) is the control law. The gains matrix \hat{K}_r is obtained by minimizing the following optimal performance index:

$$\hat{J}_r = \lim_{t_f \rightarrow \infty} \int_t^{t_f} [\hat{z}_r^* \hat{z}_r + u_r^* W_r^* W_r u_r] dt, \quad (22)$$

where $\hat{z}_r = \hat{C}_r \hat{x}_r + D_r u_r$. Equation (21) is the minimum variance estimator. The matrix \hat{L}_r is obtained by minimizing the variance of the estimated state vector \hat{x}_r with respect to the internal state vector \hat{x}_r assuming that the reduced-model of (18) is affected by additive Gaussian white noise. Since we have assumed no statistics, the power spectral densities required for the minimum variance estimator are chosen as design parameters in order to keep the eigenvalues of the estimator at the same order of magnitude as the eigenvalues of the controller. In particular, the spectral density for process noise is chosen as $\rho \hat{B}_r \hat{B}_r^*$, where the parameter ρ is increased to obtain the desired loop transfer recovery of the full state LQR problem [11]. In this study the LQG (\mathcal{H}_2) design of a robust controller for each reduced-order state space subsystem (18) can be carried out in parallel.

Figure 1 links with simplicity the mathematical formulation to its computational implementation by summarizing in a block diagram the control strategy described above. The controller can be programmed in a computer routine whose input is a matrix containing the gradients of the streamwise velocity component

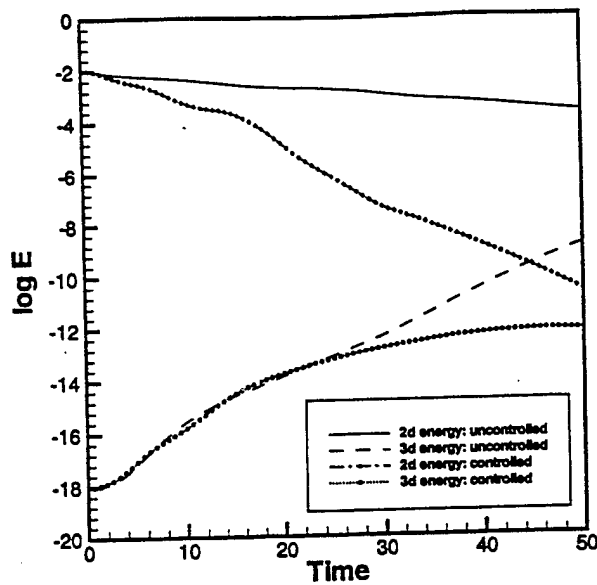


Figure 2: Comparison of the time evolution of the energy of a two-dimensional finite amplitude disturbance and of a three-dimensional infinitesimal disturbance at $Re = 1500$ in the controlled and uncontrolled cases.

and whose output is a matrix containing the blowing and suction at the wall. Each column of the measurements matrix contains the gradients of the streamwise velocity component in a given xy-plane. Each column is processed in parallel by a fast Fourier transform (FFT) and converted into z_r 's. Each pair of estimator (21) and control (20) blocks is integrated in time by, for example, a third-order low-storage Runge-Kutta scheme. Parallel computation produces u_r 's. An inverse FFT converts u_r 's into the columns of the matrix containing the blowing and suction at the wall. This routine can be embedded in any Navier-Stokes solver able to handle time-dependent boundary conditions for the control of three-dimensional channel flows.

Figure 1 also provides the basic architecture for the potential implementation of the present controller in practical engineering applications. The gradients of the streamwise velocity component can be measured by micro-electro-mechanical-systems (MEMS) hot film sensors [13]. For each xy-plane, analog to digital converters (A/D) and digital signal processors (DSP) convert the measured gradients into z_r 's. Each pair of estimator (21) and control (20) blocks is replaced by a microprocessor, and a parallel computation produces u_r 's. A DSP and a digital to analog converter (D/A) produce the actuating signal in each xy-plane. Finally, MEMS technology will provide the necessary hardware to implement the actuating signal at the wall of the channel. Note that a variety of actuators can mimic small amplitude blowing and suction at the wall:

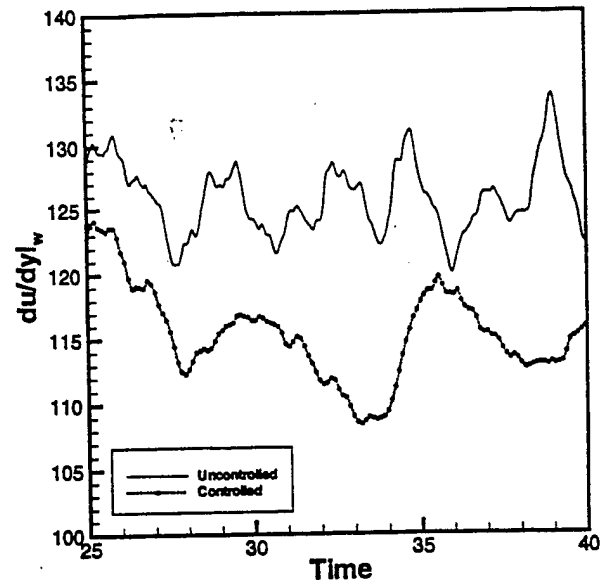


Figure 3: Comparison of the time evolution of the skin-friction drag in a fully developed turbulent channel flow at $Re = 1700$ in the controlled and uncontrolled cases.

porous walls, micro pumps, deformable walls and thermal actuators [13].

5 Results

We designed a controller for two-dimensional Poiseuille flow in a periodic channel of length $L = 4\pi$ at $Re = 1500$ [10]. We used a grid resolution of $N = 32$ and $M = 65$. A controller is applied to each xy-plane, consequently, the order of the full system is $32 \times 3904 = 124928$. Using the model reduction technique previously described, we created 32 reduced models and derived 32 controllers of order 12, one for each state space subsystem (18). Controllers operate in parallel. The combined order of the controllers for all 32 wave numbers is $32 \times 384 = 12288$, it represents a dramatic reduction, about 90%, with respect to the order of the full system.

Figure 2 shows a comparison of the time evolution of the energy of a two-dimensional finite amplitude disturbance and of a three-dimensional infinitesimal disturbance at $Re = 1500$ in the controlled and uncontrolled cases. In the uncontrolled case at this Reynolds number, two-dimensional disturbance wave-number, and initial energy level, we see the two-dimensional disturbance decaying slowly. On the other hand, the three-dimensional disturbance is seen to gain energy rapidly. Orszag and Patera [14] showed that the two-dimensional instability acts as a mediator for transfer of energy from the mean two-dimensional flow to the three-dimensional disturbances which may cause

transition to turbulence. In the controlled case we apply blowing and suction only at the bottom wall, while near-wall disturbances within the top boundary layer are left free to evolve. The attenuation of the finite-amplitude two-dimensional disturbance is dramatically increased. As a consequence, the infinitesimal three-dimensional disturbance is also stabilized and the mechanism responsible for transition to turbulence is inhibited.

Figure 3 shows a comparison of the time evolution of the averaged skin-friction drag measured at the walls in the controlled and uncontrolled cases at $Re = 1700$. In both cases, the fully developed turbulent channel flow is left free to evolve up to time $t = 25$ to ensure that the statistics are correct. In the uncontrolled case the averaged drag oscillates stochastically around a mean value of 125.8. In the controlled case blowing and suction is applied to top and bottom walls. All 64 controllers operate in parallel, 2 controllers for each xy-plane. Only the 4 lowest wave-numbers are controlled. In this case the order of the controller is $64 \times 48 = 3072$, it represents a dramatic reduction, about 99%, with respect to the order of the full system $64 \times 3904 = 249856$. The controlled averaged drag drops as soon as the blowing and suction is applied at the wall. The drag reduction is further improved along the simulation, it oscillates around a mean value of 114.1. The averaged drag reduction is about 10%. This preliminary result is very encouraging and justifies the current efforts for deriving improved low order controllers.

6 Conclusions

In this article we presented a successful application of robust reduced-order linear feedback control based on a two-dimensional design to a three-dimensional channel flow in the transitional and fully turbulent regimes. A controller based on a reduced-model of the linearized Navier-Stokes equations, i.e. 10% of the order of the full size system, was designed by using LQG (H_2)/LTR synthesis. This controller was programmed in a computer routine whose input measurements are the gradients of the streamwise velocity component and whose output controls are the blowing and suction at the wall. This routine, suited for parallel computing, was embedded in a direct numerical simulation of the Navier-Stokes equations. First, we applied the controller to the bottom wall of a three-dimensional transitional periodic channel flow at $Re = 1500$. The controller attenuated dramatically the finite-amplitude two-dimensional disturbance, and consequently stabilized the three-dimensional infinitesimal disturbance and inhibited the mechanism responsible for transition to turbulence. Subsequently, we applied the controller at both wall of a fully developed channel flow at $Re = 1700$. Only the 4 lowest wave-numbers are controlled, reducing the order of the controller to about

1% of order of the full size system. Preliminary result showed a drag reduction of about 10% with respect to the uncontrolled turbulent flow. Extensions of LQG (H_2)/LTR design by using three-dimensional channel flow models are in progress.

The authors thank Dr. S. Joshi, and Dr. R.T. MCloskey for the enlightening discussions. This work is supported by AFOSR Grant F49620-97-1-0276 and by NASA Grant NCC 2-374 Pr 41.

References

- [1] M. Gad-el-Hak, "Interactive control of turbulent boundary layers - A futuristic overview", *AIAA Journal*, **32**, (9), 1753 (1994).
- [2] V.J. Modi, "Moving surface boundary-layer control: A review", *Journal of Fluids and Structures*, **11**, (6), 627 (1997).
- [3] H.L. Reed, W.S. Saric and D. Arnal, "Linear stability theory applied to boundary layers", *Annu. Rev. Fluid Mech.*, **28**, 389 (1996).
- [4] S.S. Joshi, J.L. Speyer and J. Kim, Proc. 34th Conference on Decision and Control, New Orleans, Louisiana, December 1995, p. 921.
- [5] S.S. Joshi, J.L. Speyer and J. Kim, "A systems theory approach to the feedback stabilization of infinitesimal and finite-amplitude disturbances in plane Poiseuille flow", *J. Fluid Mech.*, **332**, 157 (1997).
- [6] S.N. Singh and P.R. Bandyopadhyay, "Linear feedback control of boundary layer using electromagnetic microtiles", *J. Fluids Eng. - Trans. ASME*, **119**, (4), 852 (1997).
- [7] T.R. Bewley and S. Liu, "Optimal and robust control and estimation of linear paths to transition", *J. Fluid Mech.*, **365**, 305, (1998).
- [8] K. Zhou, J.C. Doyle and K. Glover, "*Robust and optimal control*", (Prentice Hall, 1996).
- [9] I. Rhee and J.L. Speyer, "A game theoretic approach to a finite-time disturbance attenuation problem", *IEEE Trans. Automatic Control*, **36**, (9), 1021 (1991).
- [10] L. Cortelezzi and J.L. Speyer, "Robust reduced-order controller of laminar boundary layer transitions", *Phys. Rev. E*, **58**, (2), 1906 (1998).
- [11] J.C. Doyle and G. Stein, "Multivariable feedback design: Concepts for a classical/modern synthesis", *IEEE Trans. Automatic Control*, **AC-26**, (2), (1981).
- [12] L. Cortelezzi, K.H. Lee, J. Kim and J.L. Speyer, "Skin-friction drag reduction via robust reduced-order linear feedback control", *Int. J. Comp. Fluid Dyn.*, **11**, to appear.
- [13] C.M. Ho and Y.C. Tai, "Micro-electro-mechanical-systems (MEMS) and fluid flows", *J. Fluids Eng. - Trans. ASME*, **118**, 437 (1996).
- [14] S.A. Orszag and A.T. Patera, "Secondary instability of wall-bounded shear flows", *J. Fluid Mech.* **128**, 689 (1983).

APPENDIX E

Application of Robust Reduced-Order Controller to Turbulent Flows for Drag Reduction

K.H. Lee, L. Cortelezzi, J. Kim, J.L. Speyer

Application of robust reduced-order controller to turbulent flows for drag reduction

Keun H. Lee, Luca Cortelezzi*, John Kim[†] and Jason Speyer

Department of Mechanical & Aerospace Engineering,

University of California,

Los Angeles, California 90095

*Present address: Department of Mechanical Engineering, McGill University, Canada; Electronic
mail:crtlz@ametista.mecheng.mcgill.ca

[†]Corresponding author: Telephone: (310) 825-4393; Fax:(310) 206-4830; Electronic mail:
jkim@seas.ucla.edu

Abstract

A robust reduced-order linear feedback controller is designed and applied to turbulent channel flow for drag reduction. From the linearized two-dimensional Navier-Stokes equations a distributed robust feedback controller, which produces blowing/suction at the wall based on the measured turbulent streamwise wall-shear stress, is derived using model reduction techniques and linear-quadratic-Gaussian/loop-transfer-recovery control synthesis. The quadratic cost criterion used for synthesis is composed of the streamwise wall-shear stress, which includes the control effort of blowing/suction. This distributed two-dimensional controller developed from a linear system theory is shown to reduce the skin-friction by 10% in direct numerical simulations of a low-Reynolds number turbulent nonlinear channel flow. Spanwise shear-stress variation, not captured by the distributed two-dimensional controller, is suppressed by augmentation of a simple spanwise ad hoc control scheme. This augmented three-dimensional controller, which requires only the turbulent streamwise velocity gradient, results in further reduction in the skin-friction drag. It is shown that the input power requirement is significantly less than the power saved by reduced drag. Other turbulence characteristics affected by these controllers are also discussed.

1 Introduction

Much attention has been paid to the drag reduction in turbulent boundary layers. Skin friction drag constitutes approximately 50%, 90%, and 100% of the total drag on commercial aircraft, underwater vehicles, and pipelines, respectively.¹ The decrease of skin-friction, therefore, entails a substantial saving of operational cost for commercial aircraft and submarines. Recent reviews¹⁻³ summarize achievements and open questions in boundary layer control.

With the notion that near-wall streamwise vortices are responsible for high skin-friction in turbulent boundary layers, Choi *et al.*⁴ manipulated the near-wall turbulence by applying various wall actuations. They achieved a 20% skin-friction reduction in a turbulent channel flow by applying a wall transpiration equal and opposite to the wall-normal velocity component measured at $y^+ = 10$. This control is shown to effectively make the streamwise vortices weaker. However, it is not easily implementable since it is difficult to place sensors inside the flow field. Other attempts at weakening the near-wall streamwise vortices have been made by imposing spanwise oscillation of the wall⁵ and using external body force.⁶ These methods, however, require a large amount of input energy. Reduction in skin-friction must be accompanied with the required input energy much less than the energy saved by the reduction.

A systematic approach, not relying on physical intuition, has been tried in the past. A suboptimal control, which determines the optimal control input by minimizing the cost functional for a short time interval, was successfully applied to the stochastic Burger's equation.⁷ Bewley and Moin⁸ extended the suboptimal control to a turbulent channel flow.

This method, however, requires information about the whole flow field and excessive computation, so that it is impossible or at best extremely difficult to implement. It is necessary to develop a control scheme that utilizes easily-measurable quantities.

Lee *et al.*⁹ developed a neural network control algorithm that approximates the correlation between the wall-shear stresses and the wall actuation and then predicts the optimal wall actuation to produce the minimum value of skin-friction. They also produced a simple control scheme from this neural network control, which determines the actuation as the sum of the weighted spanwise wall-shear stress, $\frac{\partial w}{\partial y}|_w$. Recently, Koumoutsakos¹⁰ reported a substantial drag reduction obtained by applying a feedback control scheme based on the measurement and manipulation of the wall vorticity flux. Furthermore, he showed that the strength of unsteady mass transpiration actuators can be derived explicitly by inverting a system of equations.

Other systematic controls^{11–14,17,19–20} have been developed by exploiting the tools recently developed in the control community.^{15–16} Joshi *et al.*^{11–13} and Bewley and Liu¹⁴ developed an integral feedback controller, a Linear Quadratic (LQ) controller, and an \mathcal{H}_∞ controller (worst case controller) to successfully stabilize unstable disturbances in transitional flow. In particular, Cortezzi and Speyer¹⁷ introduced the multi-input-multi-output (MIMO) linear-quadratic-Gaussian (LQG)/loop-transfer-recovery (LTR) synthesis,¹⁸ combined with model reduction techniques, for designing an optimal and robust linear feedback controller. This controller successfully suppressed near-wall disturbances, thus preventing transition in two-dimensional laminar channel flows. This robust reduced-order controller¹⁹ was applied to two-dimensional nonlinear transitional flows, illustrating that the controller designed from the linear model works surprisingly well in nonlinear flows.

The purpose of the present study is to develop a realistic robust optimal controller that systematically determines the wall actuation, in the form of blowing and suction at the wall, relying only on measured streamwise velocity gradient to reduce skin-friction in a fully developed turbulent channel flow. A dynamic representation of the flow field is required for controller design. Due to the complexity and nonlinearity of the Navier-Stokes equations, it is difficult to derive model-based controllers. Therefore, the linearized Navier-Stokes equations for Poiseuille flow are used as an approximation of the flow field and form the basis of system modelling. A robust reduced-order controller has been designed based on this model and applied to linear and nonlinear transitional flows.^{17,19–20} Encouraged by these results, in this paper we apply this distributed two-dimensional controller to a direct numerical simulation of turbulent channel flow at a low Reynolds number. We then augment our two-dimensional distributed controller by including an ad hoc control scheme to attenuate the residual disturbances in the spanwise direction.

In Section 2, we formulate the problem in terms of the three-dimensional Navier-Stokes equations and provide details about the numerical scheme used to integrate them. In Section 3, we provide the motivation behind the approximate structure of the controller. Furthermore, we derive the state-space equations from the linearized two-dimensional Navier-Stokes equations. In Section 4, we reduce the order of the state-space equations and derive a robust reduced-order two-dimensional controller by using LQG/LTR synthesis. In Section 5, we construct and apply the distributed two-dimensional controller based on the linearized Navier-Stokes equations to a fully developed turbulent channel flow at $Re_\tau = 100$, where Re_τ is the Reynolds number based on the wall-shear velocity, u_τ , and the half-channel height, h . In Section 6, this distributed two-dimensional controller augmented with a simple ad

hoc control scheme is applied to the same flow. In Section 7, we present some statistics associated with the controlled flows followed by conclusions in Section 8.

In this paper, we use (u, v, w) to represent the velocity components in the streamwise (x) , wall-normal (y) , and spanwise (z) directions, respectively.

2 Mathematical Formulation

We consider the unsteady incompressible flow in a channel with half-height h and centerline velocity U_c . Non-dimensionalized by U_c and h , the governing equations are given by the Navier-Stokes and continuity equations,

$$\begin{aligned} u_t + uu_x + vv_x + ww_x &= -p_x + Re^{-1}\Delta u, \\ v_t + uv_x + vv_y + ww_y &= -p_y + Re^{-1}\Delta v, \end{aligned} \tag{1}$$

$$\begin{aligned} w_t + uw_x + vw_y + ww_z &= -p_z + Re^{-1}\Delta w, \\ u_x + v_y + w_z &= 0, \end{aligned} \tag{2}$$

where $\Delta \equiv \partial^2/\partial x^2 + \partial^2/\partial y^2 + \partial^2/\partial z^2$ and $Re = \frac{U_c h}{\nu}$ is the Reynolds number.

We apply blowing and suction at the top and bottom walls of the channel to suppress near-wall turbulence within the boundary layer. The corresponding boundary conditions are

$$\begin{aligned} u(x, y = \pm 1, z, t) &= w(x, y = \pm 1, z, t) = 0, \\ v(x, y = \pm 1, z, t) &= v_{\pm w}(x, z, t). \end{aligned} \tag{3}$$

The control functions $v_{\pm w}$ prescribe the amount of blowing and suction at the top and bottom walls.

We measure the gradient of the streamwise velocity along the walls at given points (x_i, z_j) to detect near-wall disturbances within the boundary layer. In other words, we measure

$$z(x_i, z_j, t) = u_y|_{x=x_i, z=z_j, y=\pm 1}. \quad (4)$$

Time-dependent incompressible Navier-Stokes equations (1)-(3) with the appropriate initial condition are integrated numerically by using a spectral code with a computational domain of $(4\pi, 2, \frac{4\pi}{3})$ and a grid resolution of (32,65,32) in the (x, y, z) directions. The numerical technique used in this study is essentially the same as that of Kim *et al.*²¹ except that the time advancement for the nonlinear terms is a third-order Runge-Kutta (RK3) method. The second-order accurate Crank-Nicolson (CN) method is used for the linear terms.

3 Derivation of the State-Space Equations

One of the goals in the present study is to reduce the size of the controller. The controller based on the full system would have $> 10^5$ states when the Navier-Stokes equations are written in the wall-normal velocity and wall-normal vorticity (v, ω_y) form with 32 Fourier modes in the streamwise and spanwise directions and 65 Chebyshev modes in the wall-normal direction. A controller with hundreds of thousands of states is of no practical interest in engineering applications because of the amount of hardware and computer power necessary to compute a real-time control law. Consequently, it is crucial to reduce the order of the controller.

Figure 1 presents the architecture of the controller tested in this study. In order to reduce the order of the controller, we slice the channel with 32 xy -planes equally spaced in the z -direction. We then construct the distributed two-dimensional controller by applying

the two-dimensional controller developed from the linearized two-dimensional Navier-Stokes equation¹⁷ to each plane. The two-dimensional controller has been shown to reduce the skin-friction drag caused by finite amplitude disturbances in a two-dimensional channel flow at $Re = 1500$.¹⁹

In this section we outline the derivation of the state-space equations in a given xy -plane.^{17,19} The wall transpiration is applied to both top and bottom walls in a fully developed turbulent channel flow. For simplicity, though, we derive the state-space equations assuming that blowing and suction is applied only at the bottom wall. The application of blowing and suction to both walls is a trivial extension.

We consider two-dimensional incompressible Poiseuille flow in a periodic channel of streamwise length, L_x , and channel height, 2. The undisturbed velocity field has a parabolic profile with centerline velocity U_c . We linearize the two-dimensional Navier-Stokes equations about the parabolic profile and rewrite them in terms of the perturbation stream-function, ψ ,

$$(\partial_t + U\partial_x)\Delta\psi - U''\psi_x = Re^{-1}\Delta\Delta\psi, \quad (5)$$

to eliminate the continuity equation.

To suppress perturbations evolving within the bottom boundary layer, we apply blowing and suction at the bottom wall (see Fig. 1). For simplicity, we assume that the actuators are continuously distributed. The corresponding boundary conditions are

$$\psi_x|_{y=-1} = -v_w(x, t), \quad \psi_y|_{y=\pm 1} = \psi|_{y=1} = 0, \quad (6)$$

where the control function v_w prescribes the amount of blowing and suction at the bottom wall. We impose the wall transpiration of zero net mass-flux.

To detect the near-wall disturbances, we measure the gradient of the streamwise disturbance velocity at given points $x = x_i$ along the bottom wall (see Fig. 1)

$$z(x_i, t) = \psi_{yy}|_{y=-1}. \quad (7)$$

In other words, we measure the first term of the disturbance wall-shear stress, $\tau_{yx} = Re^{-1}(\psi_{yy} - \psi_{xx})|_{y=-1}$. The second term of the wall-shear stress is zero in the uncontrolled case and is known in the controlled case.

We define a performance index \mathcal{J} , or cost criterion, to design a controller for the LQG (\mathcal{H}_2) problem. Since we are interested in suppressing the disturbance wall-shear stress, τ_{yx} , we define

$$\mathcal{J} = \lim_{t_f \rightarrow \infty} \int_t^{t_f} \int_0^L (\psi_{yy}^2 + \psi_{xx}^2)|_{y=-1} dx dt. \quad (8)$$

The integrand represents the cost of the disturbance wall-shear stress, τ_{yx} , being different from zero. Moreover, the integrand implicitly accounts for the cost of implementing the control itself. There are two reasons to minimize the cost of the control. In any engineering application the energy available to drive the controller is limited, and a large control action may drive the system away from the region where the linear model is valid.

To convert Eqs. (5-7) to a set of first-order ordinary differential equations, we make a few transformations. We write the stream-function as $\psi = \phi + \chi$ to embed the actuator into the evolution equation and to make the boundary conditions homogeneous. Substituting $\psi = \phi + \chi$ into Eq. (5), we obtain a forced equation for the Poiseuille flow:

$$(\partial_t + U\partial_x)\Delta\phi - U''\phi_x = Re^{-1}\Delta\Delta\phi - (\partial_t + U\partial_x)\Delta\chi + U''\chi_x + Re^{-1}\Delta\Delta\chi, \quad (9)$$

with homogeneous boundary conditions $\phi|_{y=\pm 1} = \phi_y|_{y=\pm 1} = 0$. The forcing function χ

satisfies the nonhomogeneous boundary conditions, Eq. (6), i.e., $\chi_x|_{y=-1} = -v_w(x, t)$, $\chi_x|_{y=1} = \chi_y|_{y=\pm 1} = 0$. We also substitute $\psi = \phi + \chi$ into Eqs. (7-8). The measurement equation (7) becomes

$$z(x_i, t) = (\phi_{yy} + \chi_{xx})|_{x=x_i, y=-1}, \quad (10)$$

while the cost criterion, Eq. (8), takes the following form

$$\mathcal{J} = \lim_{t_f \rightarrow \infty} \int_t^{t_f} \int_0^L [(\phi_{yy} + \chi_{yy})^2 + \chi_{xx}^2]_{y=-1} dx dt. \quad (11)$$

Subsequently, flow quantities are spectrally decomposed by using periodic functions in the streamwise direction and Chebyshev polynomials in the wall-normal direction. We expand ϕ and χ as

$$\phi = \sum_{n=1}^N \sum_{m=0}^M [a_{nm}(t) \cos(\alpha_n x) + b_{nm}(t) \sin(\alpha_n x)] C_m(y), \quad (12)$$

$$\chi = \sum_{n=1}^N [p_n(t) \cos(\alpha_n x) + q_n(t) \sin(\alpha_n x)] D(y), \quad (13)$$

where $\alpha_n = 2\pi n/L_x$. Functions C_m and $D(y)$ are combinations of Chebyshev polynomials constructed to satisfy the boundary conditions, i.e., $C_m(\pm 1) = C'_m(\pm 1) = D(1) = D'(\pm 1) = 0$ and $D(-1) = 1$. We also expand the measurement function z as follows:

$$z = \sum_{n=1}^N [c_n(t) \cos(\alpha_n x) + d_n(t) \sin(\alpha_n x)]. \quad (14)$$

Substituting the expansions, Eqs. (12-14), into Eqs. (9-10), and applying Galerkin projection, we obtain the system and measurement equations from Eqs. (9) and (10), respectively,

$$\frac{dy}{dt} = \mathbf{A}y + \mathbf{B}_1 \mathbf{u} + \mathbf{B}_2 \frac{d\mathbf{u}}{dt}, \quad z = \mathbf{C}y + \mathbf{D}_3 \mathbf{u}, \quad (15)$$

where $y = [a_{10}, \dots, a_{1M}, b_{10}, \dots, b_{1M}, \dots, a_{N0}, \dots, a_{NM}, b_{N0}, \dots, b_{NM}]^T$ and $\mathbf{u} = [p_1, q_1, \dots, p_N, q_N]^T$.

Note that matrices are obtained from the orthogonality of periodic functions and Chebyshev polynomials.²²

To transform the above equations into a standard state-space form, we define a new vector $\mathbf{x} = \mathbf{y} + \mathbf{B}_2 \mathbf{u}$, and two new matrices, $\mathbf{B} = \mathbf{B}_1 + \mathbf{A} \mathbf{B}_2$ and $\mathbf{D} = \mathbf{D}_3 + \mathbf{C} \mathbf{B}_2$. Finally, we obtain the state-space equations

$$\frac{d\mathbf{x}}{dt} = \mathbf{A} \mathbf{x} + \mathbf{B} \mathbf{u}, \quad \mathbf{z} = \mathbf{C} \mathbf{x} + \mathbf{D} \mathbf{u}, \quad (16)$$

with the initial condition $\mathbf{x}(0) = \mathbf{x}_0$, where \mathbf{x} is the internal state vector, \mathbf{u} is the control vector, and \mathbf{z} is the measurement vector. Matrices \mathbf{A} , \mathbf{B} , \mathbf{C} contain the dynamics of the Poiseuille flow, actuators and sensors, respectively. Matrix \mathbf{D} contains the coupling between sensors and actuators. The cost criterion, Eq. (11), becomes

$$\mathcal{J} = \lim_{t_f \rightarrow \infty} \int_t^{t_f} [\mathbf{z}^T \mathbf{z} + \mathbf{u}^T \mathbf{W}^T \mathbf{W} \mathbf{u}] dt, \quad (17)$$

where the superscript T denotes a transposed quantity. The matrix \mathbf{W} is obtained by spectrally decomposing the last term in the cost criterion, Eq. (11).

The advantage of the present formulation is that the whole problem decouples with respect to the wavenumber when Eqs. (16-17) are transformed into Fourier space in the streamwise direction. All matrices in Eqs. (16-17) are block diagonal. The block diagonal structure of the matrix \mathbf{A} was first recognized by Joshi *et al.*¹² The above state-space system is consequently equivalent to N state-space sub-systems, one for each wavenumber. For a given wavenumber, α , the state-space equations are

$$\frac{d\mathbf{x}_\alpha}{dt} = \mathbf{A}_\alpha \mathbf{x}_\alpha + \mathbf{B}_\alpha \mathbf{u}_\alpha, \quad \mathbf{z}_\alpha = \mathbf{C}_\alpha \mathbf{x}_\alpha + \mathbf{D}_\alpha \mathbf{u}_\alpha, \quad (18)$$

with the initial condition $\mathbf{x}_\alpha(0) = \mathbf{x}_{\alpha 0}$. Vectors \mathbf{x}_α , \mathbf{u}_α , \mathbf{z}_α have the following structures:

$\mathbf{x}_\alpha = [\check{a}_{\alpha 0}, \dots, \check{a}_{\alpha M}, \check{b}_{\alpha 0}, \dots, \check{b}_{\alpha M}]^T$, $\mathbf{u}_\alpha = [p_\alpha, q_\alpha]^T$, $\mathbf{z}_\alpha = [c_\alpha, d_\alpha]^T$, where $\check{\cdot}$ indicates the Fourier

coefficients that have been affected by the transformation. The cost criterion also decouples with respect to the wavenumber, and we obtain N performance indexes. For a given wavenumber, α , the cost criterion is defined as

$$\mathcal{J}_\alpha = \lim_{t_f \rightarrow \infty} \int_t^{t_f} [\mathbf{z}_\alpha^T \mathbf{z}_\alpha + \mathbf{u}_\alpha^T \mathbf{W}_\alpha^T \mathbf{W}_\alpha \mathbf{u}_\alpha] dt. \quad (19)$$

Consequently, the design of a robust two-dimensional controller for the system, Eq. (16), with a specified cost criterion, Eq. (17), has been reduced to the independent design of N robust single-wavenumber controllers for the sub-systems, Eq. (18), along with Eq. (19).

4 Model Reduction and Controller Design

In this section we derive a lower order two-dimensional controller in two steps.¹⁷ First, we construct a lower order model of Eq. (18), and subsequently, design a robust single-wavenumber controller for the reduced-order model. To obtain a lower order model, we transform Eq. (18) into a Jordan canonical form. The matrices $\hat{\mathbf{A}}_\alpha, \hat{\mathbf{B}}_\alpha, \hat{\mathbf{C}}_\alpha, \mathbf{D}_\alpha$ that describe the dynamics of the reduced-order model are obtained from the matrices, $\mathbf{A}_\alpha, \mathbf{B}_\alpha, \mathbf{C}_\alpha, \mathbf{D}_\alpha$ in the Jordan canonical form by retaining rows and columns corresponding to equally well controllable and observable states. The hat denotes the quantities associated with the reduced-order model.

Although a rigorous mathematical framework for the design of disturbance attenuation (\mathcal{H}_∞) linear controllers is provided by the control synthesis theory,¹⁵⁻¹⁶ for this initial study LQG(\mathcal{H}_2) synthesis is quite sufficient. In general, the design of a linear feedback controller for the LQG(\mathcal{H}_2) problem is divided into two parts: linear-quadratic-regulator (LQR) and minimum variance estimator (Kalman-Bucy filter). The LQR design provides an optimal control law in terms of the internal state vector by minimizing a quadratic performance

index. The internal state vector is essential to predict the optimal control input. However, it is very difficult or impossible, in general, to directly obtain this internal state vector. Therefore, it should be reconstructed from the measurement vector \mathbf{z}_α by an estimator. The result of the LQG(\mathcal{H}_2) design of a single-wavenumber controller based on the reduced-order model of Eq. (18) is summarized by the following equations:

$$\mathbf{u}_\alpha = -\hat{\mathbf{K}}_\alpha \tilde{\mathbf{x}}_\alpha, \quad (20)$$

$$\frac{d\tilde{\mathbf{x}}_\alpha}{dt} = \hat{\mathbf{A}}_\alpha \tilde{\mathbf{x}}_\alpha + \hat{\mathbf{B}}_\alpha \mathbf{u}_\alpha + \hat{\mathbf{L}}_\alpha [\mathbf{z}_\alpha - \hat{\mathbf{C}}_\alpha \tilde{\mathbf{x}}_\alpha - \mathbf{D}_\alpha \mathbf{u}_\alpha], \quad (21)$$

with initial conditions $\tilde{\mathbf{x}}_\alpha(0) = \mathbf{0}$, where $\tilde{\mathbf{x}}_\alpha$ is the estimated reduced-order internal state vector. Equation (20) is the control law. The gains matrix $\hat{\mathbf{K}}_\alpha$ is obtained by minimizing the following optimal performance index:

$$\hat{\mathcal{J}} = \lim_{t_f \rightarrow \infty} \int_t^{t_f} [\hat{\mathbf{z}}_\alpha^T \hat{\mathbf{z}}_\alpha + \mathbf{u}_\alpha^T \mathbf{W}_\alpha^T \mathbf{W}_\alpha \mathbf{u}_\alpha] dt, \quad (22)$$

where $\hat{\mathbf{z}}_\alpha = \hat{\mathbf{C}}_\alpha \hat{\mathbf{x}}_\alpha + \mathbf{D}_\alpha \mathbf{u}_\alpha$ and $\hat{\mathbf{x}}_\alpha$ is the reduced-order internal state. Equation (21) is the minimum variance estimator. The matrix $\hat{\mathbf{L}}_\alpha$ is obtained by minimizing the variance of the error between the estimated reduced-order internal state and the reduced-order internal state vectors assuming that the reduced-model of Eq. (18) is affected by additive Gaussian white noise. Since we have assumed no statistics, the power spectral densities required for the minimum variance estimator are chosen as design parameters in order to keep the eigenvalues of the estimator at the same order of magnitude as the eigenvalues of the controller. In particular, the spectral density for process noise is chosen as $\rho \hat{\mathbf{B}}_\alpha \hat{\mathbf{B}}_\alpha^T$, where the parameter ρ is increased to recover approximately the loop transfer matrix of the full state LQR problem.¹⁸ In this study the LQG(\mathcal{H}_2) design of robust single-wavenumber controller

for each reduced-order state-space sub-system, Eq. (18), can be carried out independently and computed in parallel.

Figure 1 links the mathematical formulation to its computational implementation by summarizing in a block diagram the control strategy described above. The two-dimensional distributed controller can be programmed in a computer routine whose input is a matrix containing the gradients of the streamwise velocity component and whose output is a matrix containing the blowing and suction at the wall. Each column of the measurement matrices contains the gradients of the streamwise velocity component in a given xy -plane. Each column is processed in parallel by a fast Fourier transform (FFT) and converted into z_α 's. Each single-wavenumber controller, Eqs. (20-21), is integrated in time by, for example, a third-order low-storage Runge-Kutta scheme. The u_α 's are computed in parallel. An inverse FFT converts u_α 's into the columns of the matrix containing the blowing and suction at the wall. This routine can be embedded in any Navier-Stokes solver able to handle time-dependent boundary conditions for the control of three-dimensional channel flows.

Figure 1 also provides the basic architecture for the potential implementation of the present distributed two-dimensional controller in practical engineering applications. For instance, the gradients of the streamwise velocity component can be measured by micro-electro-mechanical-systems (MEMS) hot-film sensors.²³ For each xy -plane, analog-to-digital converters (A/D) and digital signal processors (DSP) convert the measured gradients into z_α 's. Each single-wavenumber controller, Eqs. (20-21), is replaced by a microprocessor, and a parallel computation produces u_α 's. A DSP and a digital-to-analog converter (D/A) produce the actuating signal in each xy -plane. A variety of actuators, such as synthetic jets, micro-bubble actuators, and thermal actuators, can mimic small amplitude blowing

and suction at the wall.²³

5 Performance of a Two-dimensional Controller

We designed a distributed two-dimensional controller in two steps. First, we designed reduced-order controllers for two-dimensional Poiseuille flow in a periodic channel of stream-wise length $L_x = 4\pi$ at $Re = 5000$, which has the same mean wall-shear stress as turbulent channel flow at $Re_\tau = 100$. Subsequently, we fine-tuned single-wavenumber reduced-order controllers in order to minimize the magnitude of the Fourier coefficients of the wall-shear stresses in turbulent channel flow at $Re_\tau = 100$. We used $N = 32$ and $M = 60$ in this linear model flow. Controllers operate at both top and bottom walls in parallel. If the two-dimensional controllers without model reduction were applied at each z -plane, then the order of the ensemble of controllers would be $64 \times 3904 = 249856$. Using the model reduction technique previously described, we designed eight single-wavenumber controllers of order 12, corresponding to the eight lowest wavenumbers. Since we use the eight lowest single-wavenumber controllers in our simulation, the combined order of the controllers is $64 \times 96 = 6144$. It represents a state-space reduction of about 97.5%, with respect to the full-order system.

Figure 2 shows the time history of the drag in the uncontrolled and controlled flows. Drag is measured by the mean value of the wall-shear stresses averaged over each top and bottom wall. This two-dimensional control yields about a 10% drag reduction. Choi *et al.*⁴ reported that the in-phase u -control measured at $y^+ = 10$ also gives a 10% drag reduction. This in-phase streamwise velocity at the wall causes a similar effect, $\frac{du'}{dy}|_w \simeq 0$, which is the

to-be-minimized target of our cost criterion in our two-dimensional controller. Note that this observed drag reduction is a by-product since our controller is designed to suppress the fluctuations of the streamwise wall-shear stress, not the mean wall-shear stress. Note also the sudden drop in the drag as soon as the controller is switched on at $t = 25$. This transient phenomena is also observed in other studies.⁸⁻⁹

Figure 3 compares the magnitude of Fourier coefficients of the wall-shear stresses in the controlled and uncontrolled flows. The wall-shear stresses are measured at the bottom wall at a given spanwise location. Figures 3(a) and (b) show the comparisons corresponding to wavenumbers $k_x = 0.5$ and $k_x = 1.0$, respectively. Both figures show an order-of-magnitude reduction between the controlled and uncontrolled cases. The magnitude of the Fourier coefficients of wall-shear stress decreases very quickly as soon as the controller is activated at $t = 25$. These results indicate that our distributed two-dimensional linear robust reduced-order controller suppresses disturbance wall-shear stress surprisingly well even in a fully developed turbulent flow. The high wavenumber components of the wall-shear stress in Fig. 3(c) do not show any reduction since only the lowest eight single-wavenumber controllers (up to $k_x = 4.0$) are used in the control of flow. Examinations of other spanwise locations show similar results.

Contours of the disturbance wall-shear stresses at the bottom wall in the controlled and uncontrolled flows at $t = 30$ are shown in Fig. 4. Contours for the uncontrolled flow show the usual elongated regions of low- and high-shear stress. Note that contours for the controlled flow show the dramatic effect of the distributed two-dimensional controller. The long streaky wall-shear stress region spans almost the entire streamwise direction, indicating that the low wavenumber components are completely suppressed, which is consistent with Fig. 3. The

remaining spanwise variations, i.e., the alternating regions of high- and low-shear stress, are due to the fact that the two-dimensional controllers distributed along the streamwise direction are operated independently from one z -plane to another.

The above results demonstrate that our distributed two-dimensional controller designed from the linear model works surprisingly well in suppressing near-wall disturbances in the fully developed turbulent flow. Reduction of fluctuating wall-shear stress led to drag reduction. However, this distributed two-dimensional controller has a limited impact on the total drag since it cannot control the spanwise variation of the wall-shear stress. In the next section an augmentation to the distributed two-dimensional controller is presented and implemented.

6 An Augmented Three-dimensional Controller

In the previous section, successful control of fully developed turbulent channel flow has been obtained by applying a distributed two-dimensional controller. However, it has been observed that this controller does not take into account the spanwise variations of fluid motion. An augmentation to the distributed two-dimensional controller that accommodates the three-dimensional characteristics of a fully developed turbulent flow is developed in this section.

A simple ad hoc control augmentation scheme is introduced in an attempt to capture the remaining spanwise variations of the controlled flow. This additional control, which generates blowing/suction to attenuate the spanwise variation of the wall-shear stress, is

given as follows:

$$v_{ad}(z) = C \left(\left. \frac{\partial u}{\partial y} \right|_w^{(x,z)} - \left. \frac{\partial u}{\partial y} \right|_w^x \right), \quad (23)$$

where $\left. \frac{\partial u}{\partial y} \right|_w^{(x,z)}$ and $\left. \frac{\partial u}{\partial y} \right|_w^x$ are the streamwise velocity gradients averaged over the xz -plane and the x direction, respectively, and C is a constant to be adjusted for the best performance. The subscript ad indicates the ad hoc control, and v_{ad} is a function of only z . Therefore, the new control input is defined by

$$v_w(x, z) = v_{ad} + v_{2d}, \quad (24)$$

where v_{2d} is the actuation velocity generated by the distributed two-dimensional controller used in the previous section.

Using the distributed two-dimensional controller augmented with this ad hoc control scheme, the control of the fully developed turbulent flow with $Re_\tau = 100$ increased drag reduction to about 17% as shown in Fig. 5. As before, the turbulent flow is left free to evolve without any wall actuation until $t = 25$. As soon as the controller is activated at $t = 25$, the drag drops sharply within a very small time period. The constant, C , in Eq. (23) is adjusted such that the root-mean-square (rms) value of the actuation is maintained at $0.1u_\tau$, where u_τ is the wall-shear velocity for the uncontrolled flow. We have found empirically that C between $0.05u_\tau$ and $0.2u_\tau$ gives similar performance. Introduction of this simple control augmentation enhances the drag reduction, indicating that more sophisticated controllers which best take into account the three-dimensionality of turbulent flow may produce even more efficient suppression of skin-friction drag.

Figure 6 presents the comparison of contours of the disturbance wall-shear stresses at the bottom wall between the ad hoc controlled flow and the uncontrolled flow at $t = 30$.

Compared to Fig. 4, additional effort in the spanwise direction, v_{ad} , removes the pronounced peak-valley variation of the wall-shear stress which is observed in the controlled flow with the distributed two-dimensional controllers (see Fig. 4(b)). Note that the high wavenumber components of the wall-shear stress are persistently sustained because of the lowest eight single-wavenumber controllers adopted in the control of flow.

7 Turbulence Statistics

Some statistics of the flow field associated with the two controllers applied in this paper were examined to investigate the effect of the controllers on turbulence. All statistical quantities were averaged over a sufficiently long interval of time as well as over the planes parallel to the wall. An overbar indicates a statistical quantity, while a prime is used for a fluctuating quantity. For simplicity, the flows controlled by the distributed two-dimensional controller only and the distributed two-dimensional controller augmented with ad hoc control scheme are called "2D-controlled" and "ad hoc-controlled" flows, respectively.

The mean velocity profiles normalized by the actual wall-shear velocities are shown in Fig. 7 for three different channel flows. These profiles show the same trend shown in Choi *et al.*'s⁴ drag-reduced flow: the slope of the log-law for controlled flows remains the same while the mean velocity itself is shifted upward in the log-law region.

The root-mean-square values of turbulent velocity fluctuations are shown in Fig. 8 and compared to those of the uncontrolled flow. Note that all quantities in this figure are normalized by the wall-shear velocity of the uncontrolled flow. The controllers reduce the value of turbulent intensity significantly throughout the channel. In particular, the reduction of

these quantities in the ad hoc-controlled flow is greater than that in the 2D-controlled flow. The increase in v_{rms} very near the wall is due to the control input. A similar feature is also observed by Choi *et al.*⁴ and Lee *et al.*⁹ Both controllers mitigate the rms of spanwise velocity fluctuation throughout the channel compared to that in uncontrolled flow. However, the introduction of v_{ad} in Eq. (23) causes this value to increase very close to the wall, which leads to the buildup of additional streamwise vorticity at the wall.

The change of the Reynolds shear stress, $-\overline{u'v'}$, is plotted in Fig. 9. The total shear stress, $-\overline{u'v'} + (1/Re_\tau)\partial\bar{u}/\partial y$, where $Re_\tau = u_{\tau_w}h/\nu$ and u_{τ_w} is the wall-shear velocity for the uncontrolled flow, is shown in Fig. 9(a). The straight line of this total Reynolds stress indicates that the flow has reached a statistically steady state. The total shear stress is reduced by the controllers. The Reynolds shear stress is reduced throughout the channel. Note that the reduction for the ad hoc-controlled flow is greater throughout the channel, indicating the effect of the ad hoc controller is felt by the entire flow field.

Root-mean-square values of vorticity fluctuations for the controlled flows are compared with those for the uncontrolled flow in Fig. 10. All components of vorticity fluctuations are significantly reduced throughout the channel. Very close to the wall, the increase of streamwise vorticity in the ad hoc-controlled flow is due to the streamwise vorticity built at the wall by the three-dimensional nature of the ad hoc controller. The high streamwise vorticity at the wall slows the sweeping motion of high momentum fluid induced by the streamwise vorticity away from the wall, thus resulting in a significant reduction in skin-friction. A similar feature is also observed in Lee *et al.*⁹ Note that the streamwise vorticity at the wall for the 2D-controlled flow, however, is less than that for the uncontrolled flow. The reduction of ω_z is a direct consequence of the controller, which was designed to reduce

$\partial u' / \partial y|_w$. The reduction of ω_y also indicates that our controllers weaken the strength of near-wall streaks.

Figure 11 compares the streamwise vorticity fields in the uncontrolled and controlled flows. The strength of the near-wall streamwise vorticity for the controlled flows are greatly attenuated due to the wall transpiration produced by the controllers. The distributed two-dimensional controller augmented by the ad hoc control scheme is able to diminish the strength of the streamwise vorticity more substantially than the distributed two-dimensional controller alone. This has also been observed by Lee *et al.*⁹ While Lee *et al.*⁹ suppressed the streamwise vorticity field with the physical understanding that the control based on the weighted sum of $\partial w / \partial y|_w$ can prevent the physical eruption at wall, the present distributed two-dimensional controller attenuates the streamwise vorticity strength by minimizing the streamwise disturbance wall-shear stress systematically. These results further support the notion⁴ that a successful attenuation of the near-wall streamwise vortices results in a significant reduction in skin-friction drag.

8 Conclusions

A reduced-order linear feedback control based on a distributed two-dimensional controller design is applied to a turbulent channel flow. A controller based on a reduced-model of the linearized Navier-Stokes equations for a laminar Poiseuille flow was designed by using LQG (\mathcal{H}_2)/LTR synthesis. This controller was implemented using input measurements that are the gradients of the streamwise disturbance velocity and output controls that are the blowing and suction at the wall. This procedure, suited for parallel computing, was embedded in a

direct numerical simulation of the Navier-Stokes equations.

First, we applied the distributed two-dimensional controller to both walls of a turbulent channel flow at $Re_\tau = 100$. Eight single-wavenumber controllers corresponding to eight lowest wavenumbers, reducing the order of the controller about 2.5% of the order of the full size system, are applied to attain a skin-friction reduction of 10% with respect to the uncontrolled turbulent flow. Next, a simple ad hoc augmented control scheme of the distributed two-dimensional controller is introduced to capture the three-dimensionality of turbulent flow. The control of fully developed turbulent flow by the distributed two-dimensional controller augmented by the ad hoc control scheme produces a 17% reduction in skin-friction drag. Motivated by this result, we are currently developing controllers to more efficiently account for the three-dimensionality of turbulent flow.

This study is carried out at low Reynolds number. Whether our controller, based on the reduced-order linear model, would work in other turbulent flows, should be drawn from real experiments or simulations at high Reynolds number. However, we expect that it should work equally well for high Reynolds number flow since our controller, derived from LQG/LTR synthesis, recovers the robustness of LQR, whose characteristics has been partially tested over the different Reynolds number flows.²²

The statistics of controlled and uncontrolled flows are compared. The mean velocity profile is shifted upward in the log-region, a typical characteristics of drag-reduced flow. Velocity and vorticity fluctuations as well as Reynolds shear stress are significantly reduced due to the blowing/suction generated by controller. However, major change is confined to the wall-region. Instantaneous flow fields show that the distributed two-dimensional controller attenuates and modifies the streaky structure of the boundary layer. Streaks are observed

to span the entire streamwise direction with velocity variations in the spanwise direction. These variations are substantially reduced by the augmented controller.

The three-dimensional aspect of the distributed two-dimensional controller by the augmentation of the ad hoc control further reduced the skin-friction drag. This three-dimensional controller produces secondary streamwise vorticity at the wall, which slows the sweeping motions of high-momentum fluid induced by the streamwise vorticity away from the wall. This induced retarding of the primary streamwise vorticity leads to additional drag reduction, which was also observed in Choi *et al.*⁴

Regarding the scaling factor C in Eq. (23), we found an optimal value of C which yields the blowing/suction of $0.1u_\tau$. With this optimal C , the augmented controller generates wall transpiration with an rms value of about $0.12u_\tau$. The required power input per unit area to the system, $p_w v_w + 0.5\rho v_w^3 \approx 0.1\rho u_\tau^3$, is significantly less than the power saved from the drag reduction, $\Delta C_f / C_f \dot{\tau}_w U_c \approx 3.2\rho u_\tau^3$, where p_w , ρ , C_f , τ_w and U_c are the wall pressure, density, skin-friction coefficient, averaged wall-shear stress, and the centerline velocity, respectively.

Extensions of LQG (\mathcal{H}_2)/LTR design by using three-dimensional channel flow models are in progress.²⁴⁻²⁵

Acknowledgements: We thank Dr. S. Joshi and Prof. R.T. McCloskey for the enlightening discussions. We also thank Ms. V. Ryder and Mr. Sungmoon Kang for their careful proofreading. This work is supported by AFOSR Grant F49620-97-1-0276 and by NASA Grant NCC 2-374 Pr 41.

References

- [1] M. Gad-el-Hak "Interactive control of turbulent boundary layers - A futuristic overview," *AIAA Journal*, **32**(9), 1753 (1994).
- [2] V.J. Modi "Moving surface boundary-layer control: A review," *Fluids and Structures*, **11**(6), 627 (1997).
- [3] H.L. Reed, W.S. Saric and D. Arnal "Linear stability theory applied to boundary layers," *Annu. Rev. Fluid Mech.*, **28**, 389 (1996).
- [4] H. Choi, P. Moin, and J. Kim "Active turbulence control for drag reduction in wall-bounded flows," *J. Fluid Mech.*, **262**, 75 (1994).
- [5] R. Akhavan, W.J. Jung, and N. Mangiavacchi "Turbulence control in wall-bounded flows by spanwise oscillations," *Appl. Sci. Res.*, **51**, 299 (1993).
- [6] T. Berger, C. Lee, J. Kim, and J. Lim "Turbulent Boundary Layer Control Utilizing the Lorentz Force," Accepted for publication in *Physics of Fluids*.
- [7] H. Choi, R. Temam, P. Moin, and J. Kim "Feedback control for unsteady flow and its application to the stochastic Burgers equation," *J. Fluid Mech.*, **253**, 509 (1993).
- [8] T. Bewley and P. Moin "Optimal control of turbulent channel flow," *ASME Conference*, ASME DE-Vol. 75 (1994).
- [9] C. Lee, J. Kim, D. Babcock, and R. Goodman "Application of neural networks to turbulence control for drag reduction," *Phys. Fluids*, **9**(6), 1740 (1997).

- [10] P. Koumoutsakos "Vorticity flux control for a turbulent channel flow," *Phys. Fluids*, **11**(2), 248 (1999).
- [11] S. Joshi, J.L. Speyer, and J. Kim *Proc. 34th Conference on Decision and Control*, New Orleans, Louisiana, December 1995.
- [12] S. Joshi, J.L. Speyer, and J. Kim "A systems theory approach to the feedback stabilization of infinitesimal and finite-amplitude disturbances in plane Poiseuille flow," *J. Fluid Mech.*, **332**, 157 (1997).
- [13] S. Joshi, J.L. Speyer, and J. Kim "Finite Dimensional Optimal Control of Poiseuille Flow," *J. Guidance, Control, and Dynamics*, **22**(2), March-April 1999.
- [14] T. Bewley and S. Liu "Optimal and robust control and estimation of linear paths to transition," *J. Fluid Mech.*, **365**, 305 (1998).
- [15] K. Zhou, J.C. Doyle, and K. Glover Robust and optimal control, Prentice Hall, 1996.
- [16] I. Rhee and J.L. Speyer "A game theoretic approach to a finite time disturbance attenuation problem," *IEEE Trans., Automatic Control*, **36**(9), 1021 (1991).
- [17] L. Cortelezzi and J.L. Speyer "Robust reduced-order controller of laminar boundary layer transitions," *Phys. Rev. E*, **58**(2), 1906 (1998).
- [18] J.C. Doyle and G. Stein "Multivariable feedback design: Concepts for a classical/modern synthesis," *IEEE Trans. Automatic Control*, **AC-26**(2), (1981).

- [19] L. Cortelezzi, K.H. Lee, J. Kim and J.L. Speyer "Skin-friction drag reduction via robust reduced-order linear feedback control," *Int. J. Comp. Fluid Dyn.*, **11**(1-2), 79 (1998).
- [20] L. Cortelezzi, K.H. Lee, J.L. Speyer, J. Kim "Robust reduced-order control of turbulent channel flows via distributed sensors and actuators," *37th Conference on Decision and Control*, Seattle, Washington, December 1998.
- [21] J. Kim, P. Moin, and R. Moser "Turbulence statistics in fully-developed channel flow at low Reynolds number," *J. Fluid Mech.*, **177**, 133 (1987).
- [22] Keun H. Lee "A System Theory Approach to Control of Transitional and Turbulent Flows," Ph.D. dissertation, Dept. of Mechanical Eng. Univ. of California, Los Angeles, CA, September 1999.
- [23] C.M. Ho and Y.C. Tai "Microelectro-mechanical-systems (MEMS) and fluid flows," *J. Fluids Eng. - Trans. ASME*, **118**, 437 (1996).
- [24] S.M. Kang, V. Ryder, L. Cortelezzi and J.L. Speyer, "State-Space Formulation and Control Design for Three-Dimensional Channel Flows," *1999 American Control Conference*, San Diego, California, June 2-4, 1999.
- [25] S.M. Kang, L. Cortelezzi and J.L. Speyer, "Performance of a Linear Controller for Laminar Boundary Layer Transition in Three Dimensional Channel Flow," *38th Conference on Decision and Control*, Phoenix, Arizona, Dec 7-10, 1999.

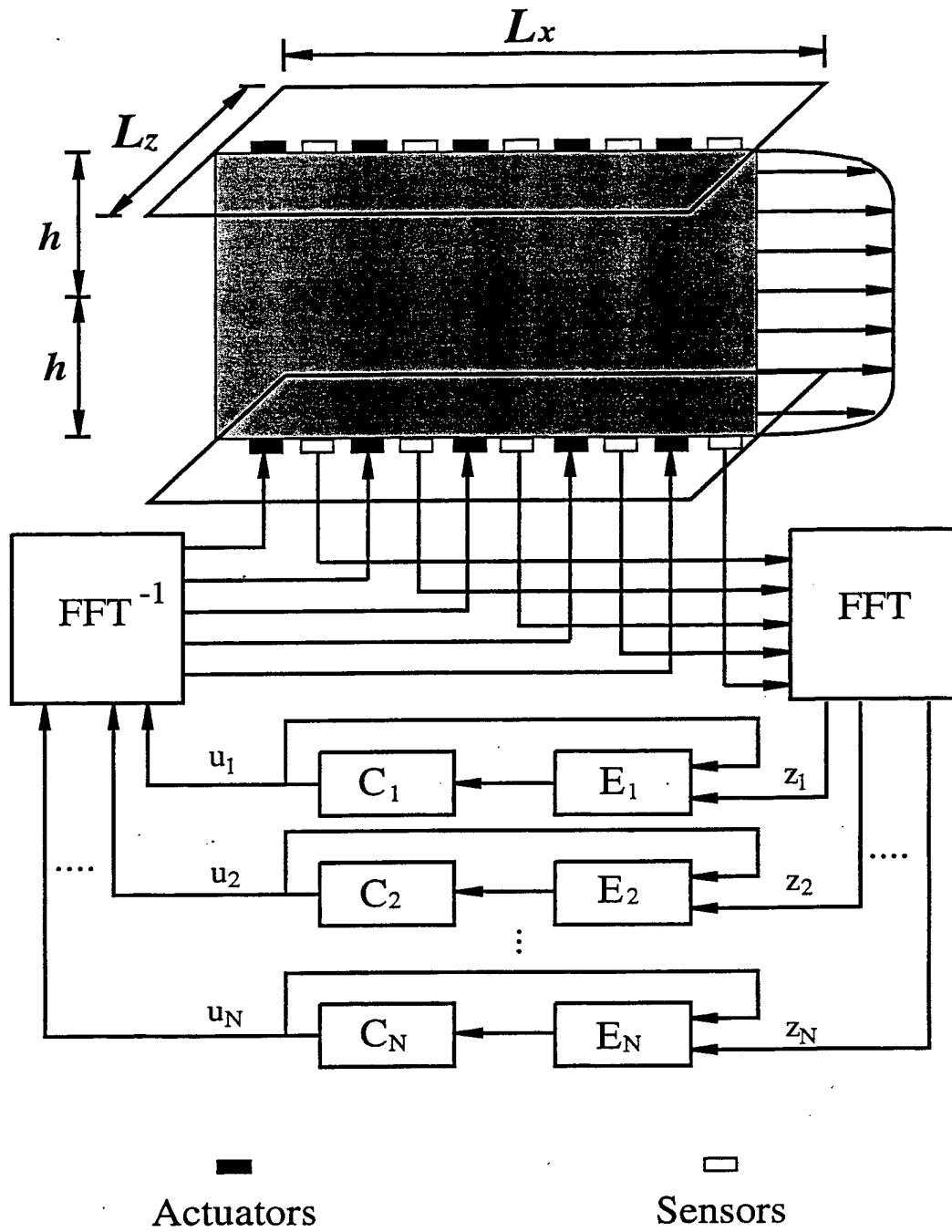


Figure 1: Schematic representation of turbulent channel flow equipped with sensors and actuators distributed in the streamwise direction in each z -plane.

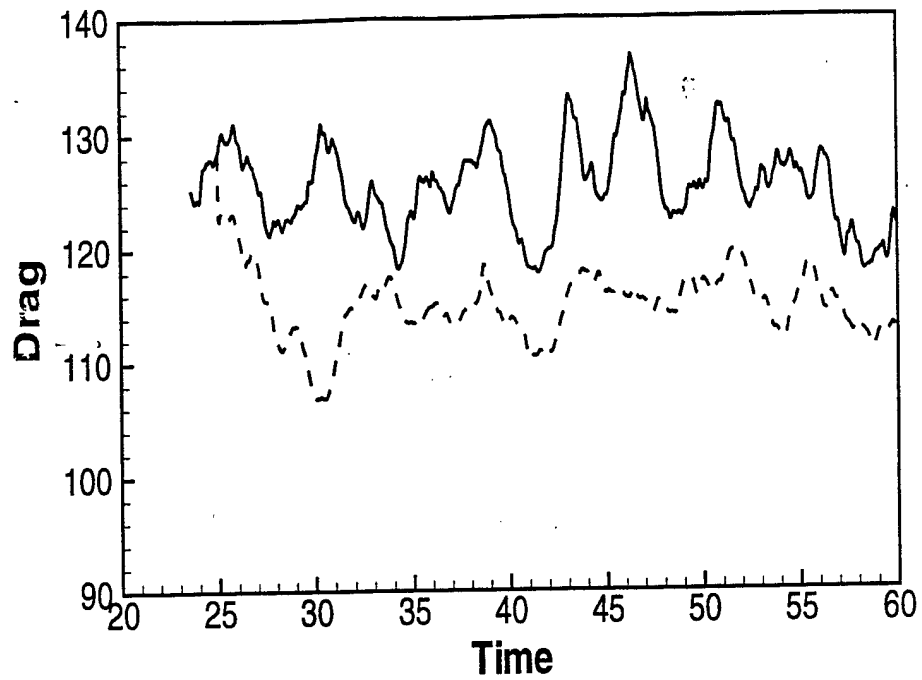


Figure 2: Time history of the drag for the controlled and uncontrolled flows: ---- , controlled flow; — , uncontrolled flow.

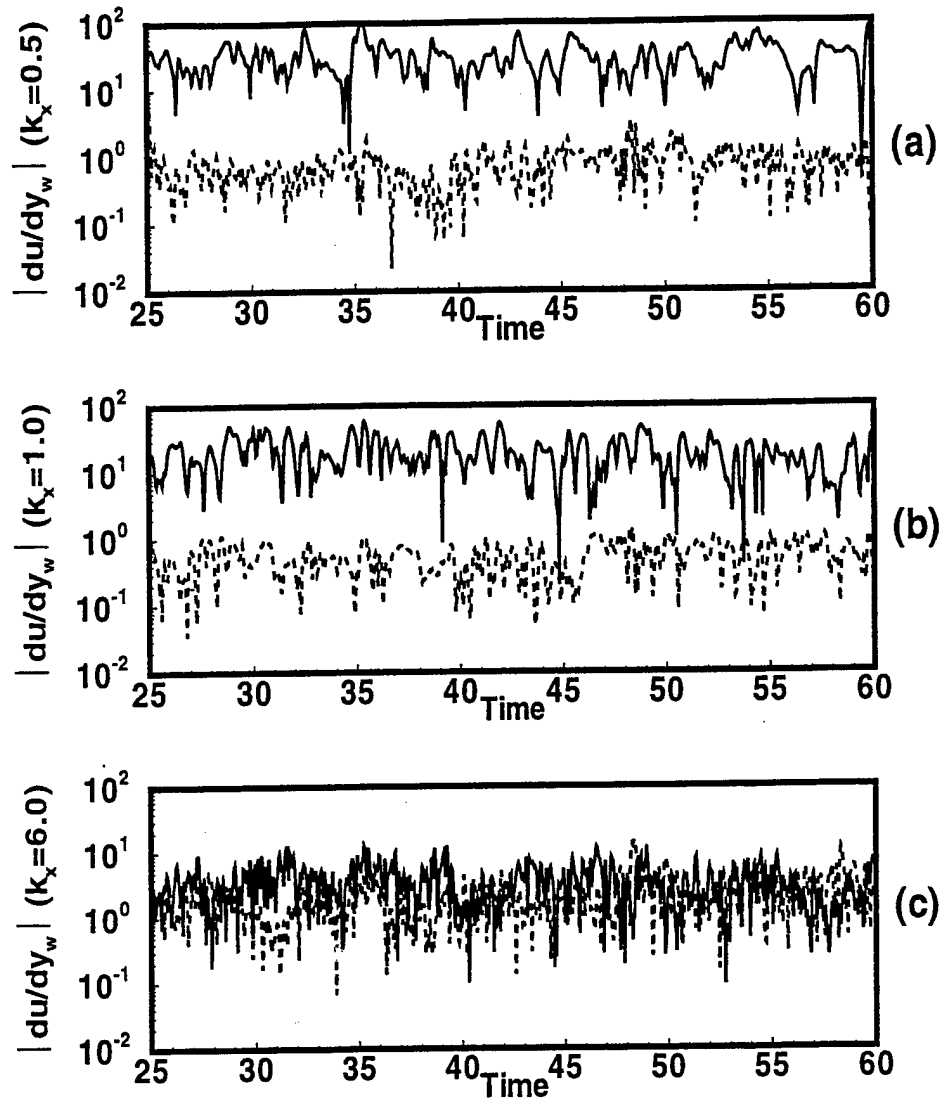


Figure 3: Time history of the magnitude of the Fourier coefficients of the wall-shear stresses measured at the bottom wall at a given spanwise location for the controlled and uncontrolled flows: — , uncontrolled flow; ---- , controlled flow. (a) $k_x = 0.5$, (b) $k_x = 1.0$, and (c) $k_x = 6.0$.

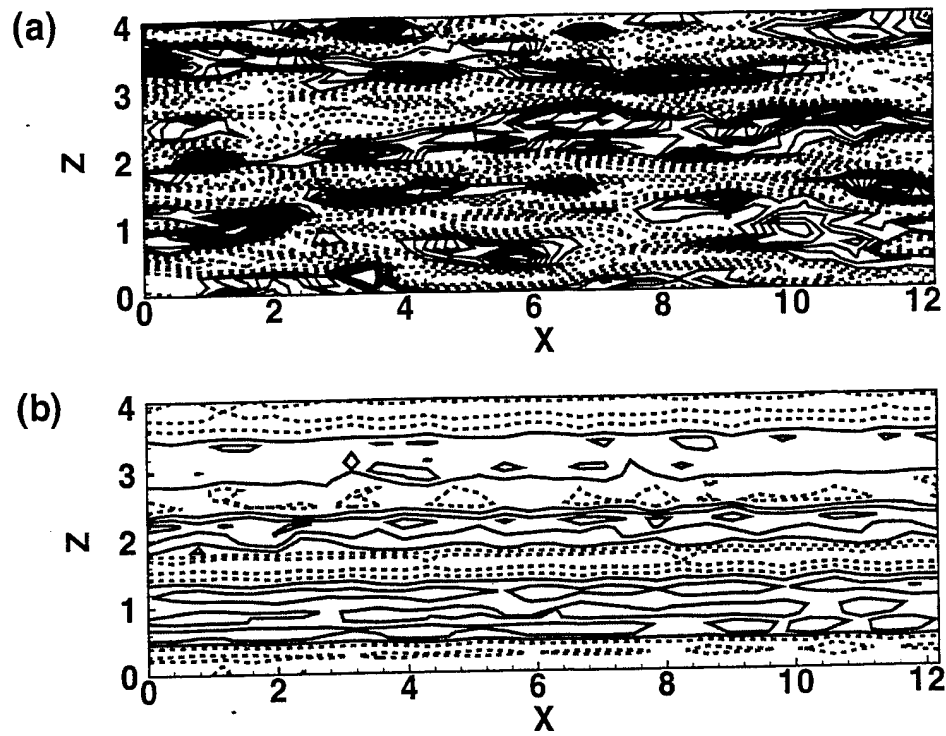


Figure 4: Contours of disturbance wall-shear stresses at the bottom wall at $t = 30$: (a) uncontrolled flow; (b) 2D-controlled flow. Negative contours are dashed.

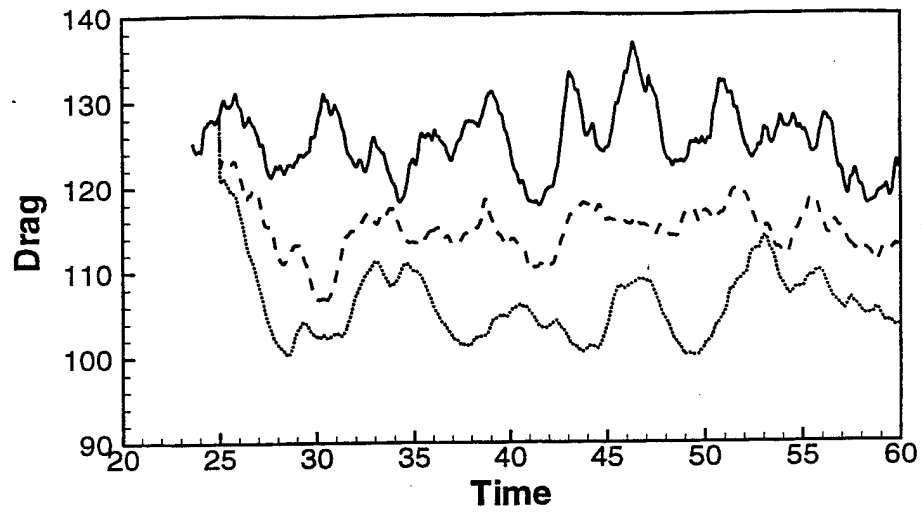


Figure 5: Time history of the drag for the controlled and uncontrolled flows: — , uncontrolled flow; ---- , 2D-controlled flow; , ad hoc-controlled flow.

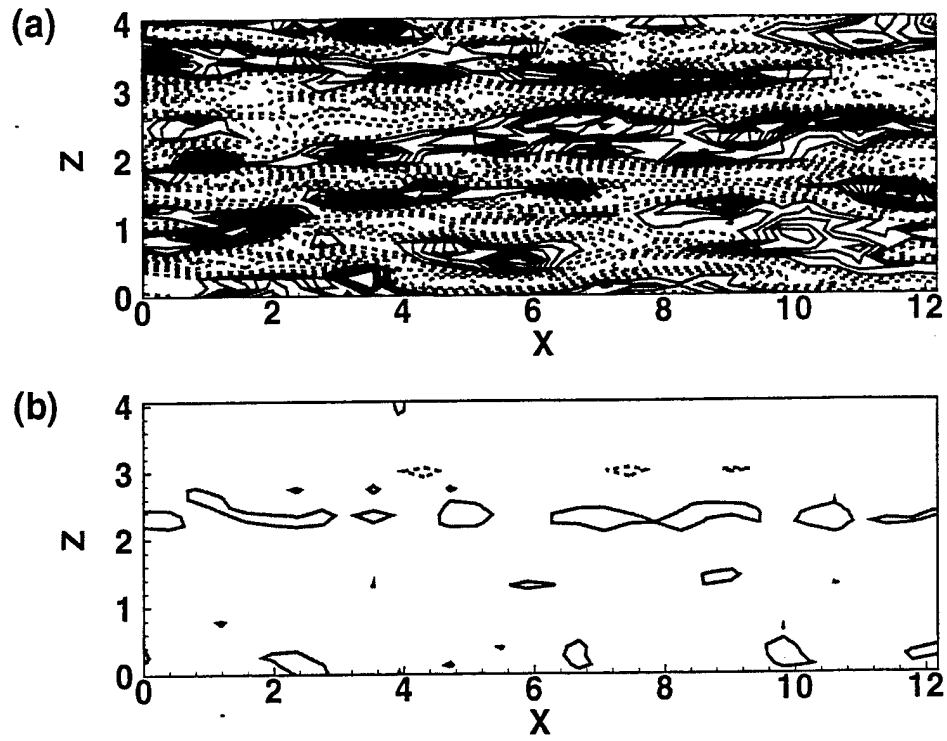


Figure 6: Contours of disturbance wall-shear stresses at the bottom wall at $t = 30$: (a) uncontrolled flow; (b) ad hoc-controlled flow. Negative contours are dashed.

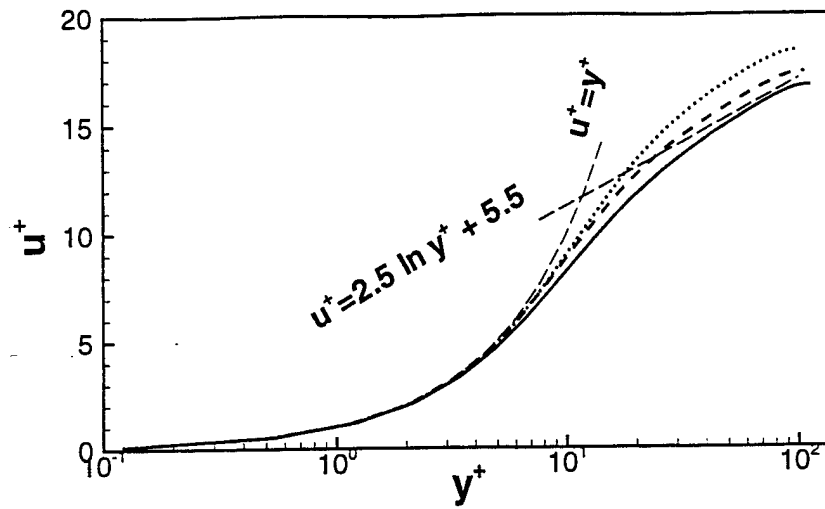


Figure 7: Mean-velocity profiles: , ad hoc-controlled flow; ---- , 2D-controlled flow; ——— , uncontrolled flow.

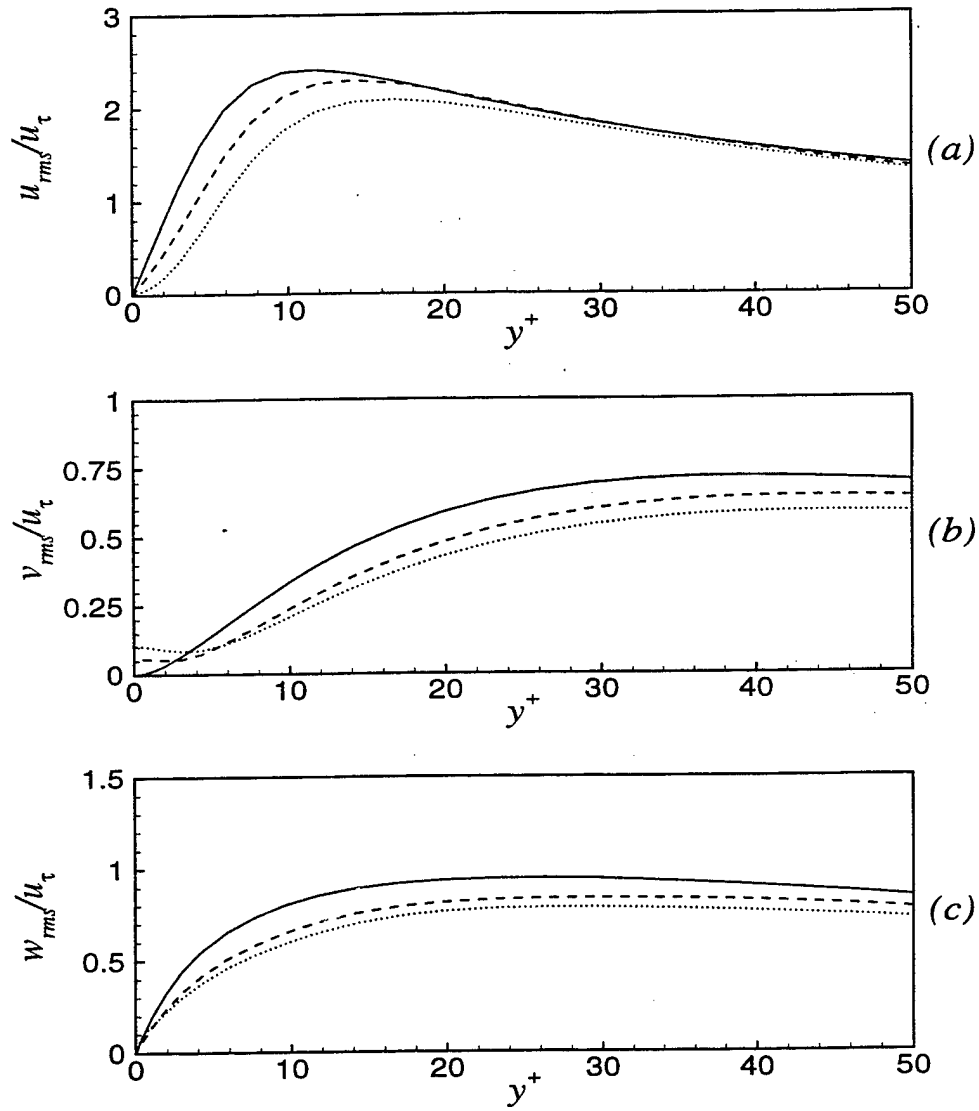


Figure 8: Root-mean-square values of turbulent velocity fluctuations normalized by the wall-shear velocity, u_τ for the uncontrolled flow: — , uncontrolled flow; ---- , 2D-controlled flow; , ad hoc-controlled flow.

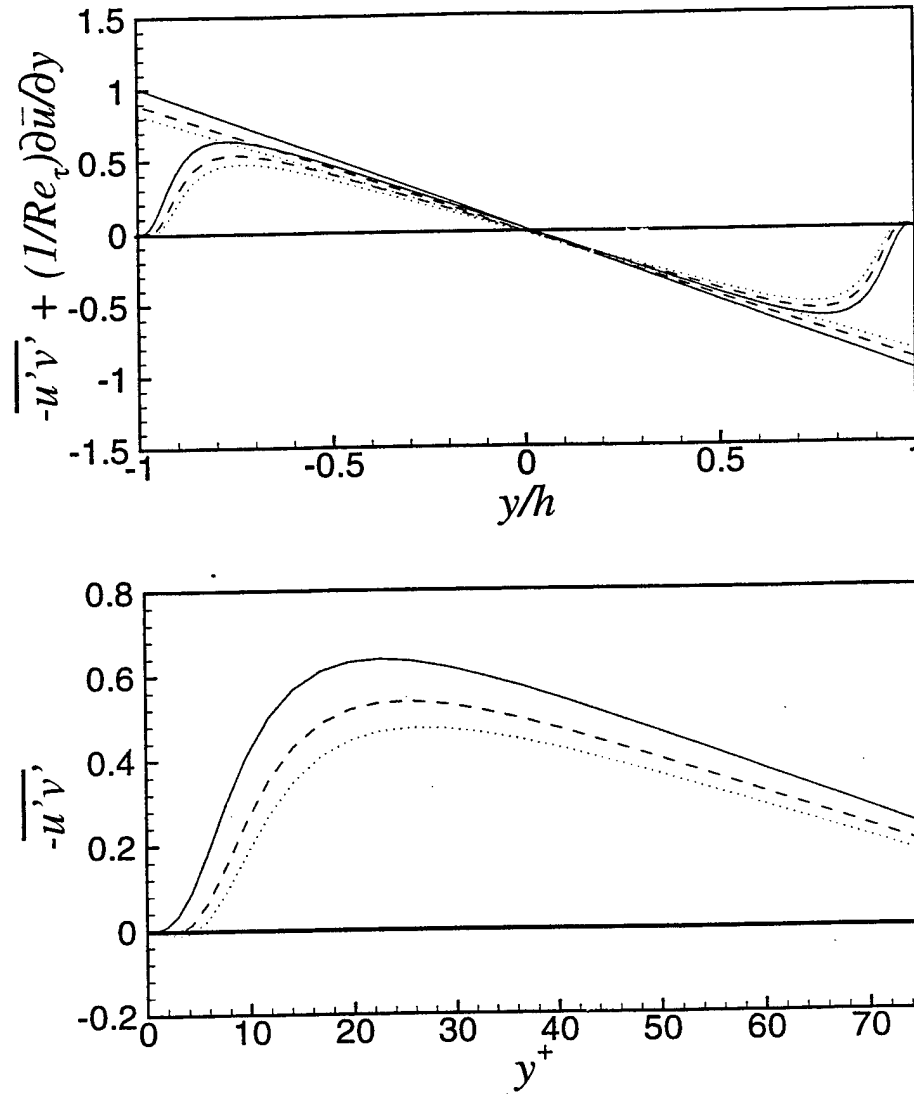


Figure 9: Comparison of Reynolds shear stress ($-\overline{u'v'}$) and total shear stress ($-\overline{u'v'} + (1/Re_\tau)\partial\bar{u}/\partial y$) between the ad hoc controlled and uncontrolled flows: —, uncontrolled flow; ----, 2D-controlled flow; ·····, ad hoc-controlled flow. Physical coordinate (a) and wall coordinate (b).

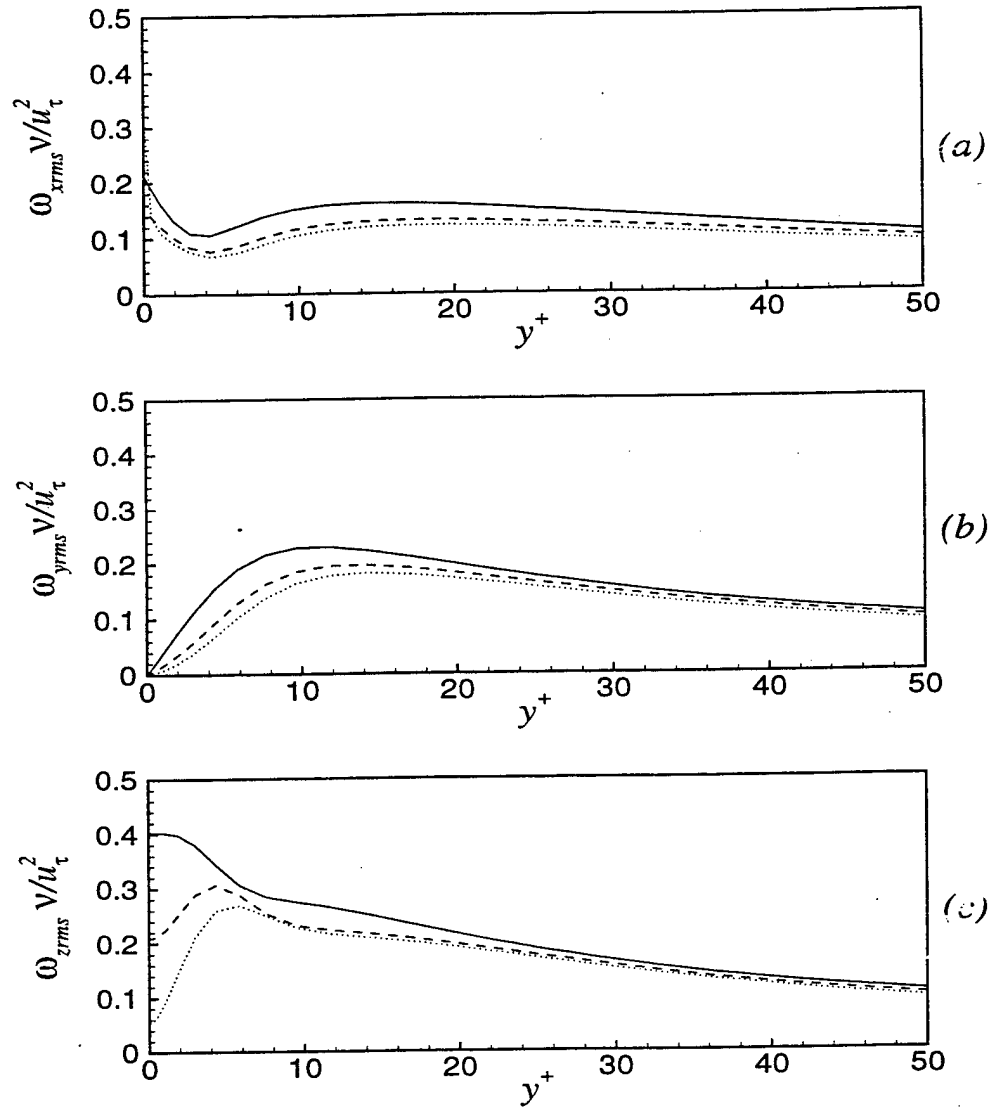


Figure 10: Root-mean-square values of vorticity fluctuations normalized by the wall-shear velocity in wall coordinates: — , uncontrolled flow; ---- , 2D-controlled flow; , ad hoc-controlled flow.

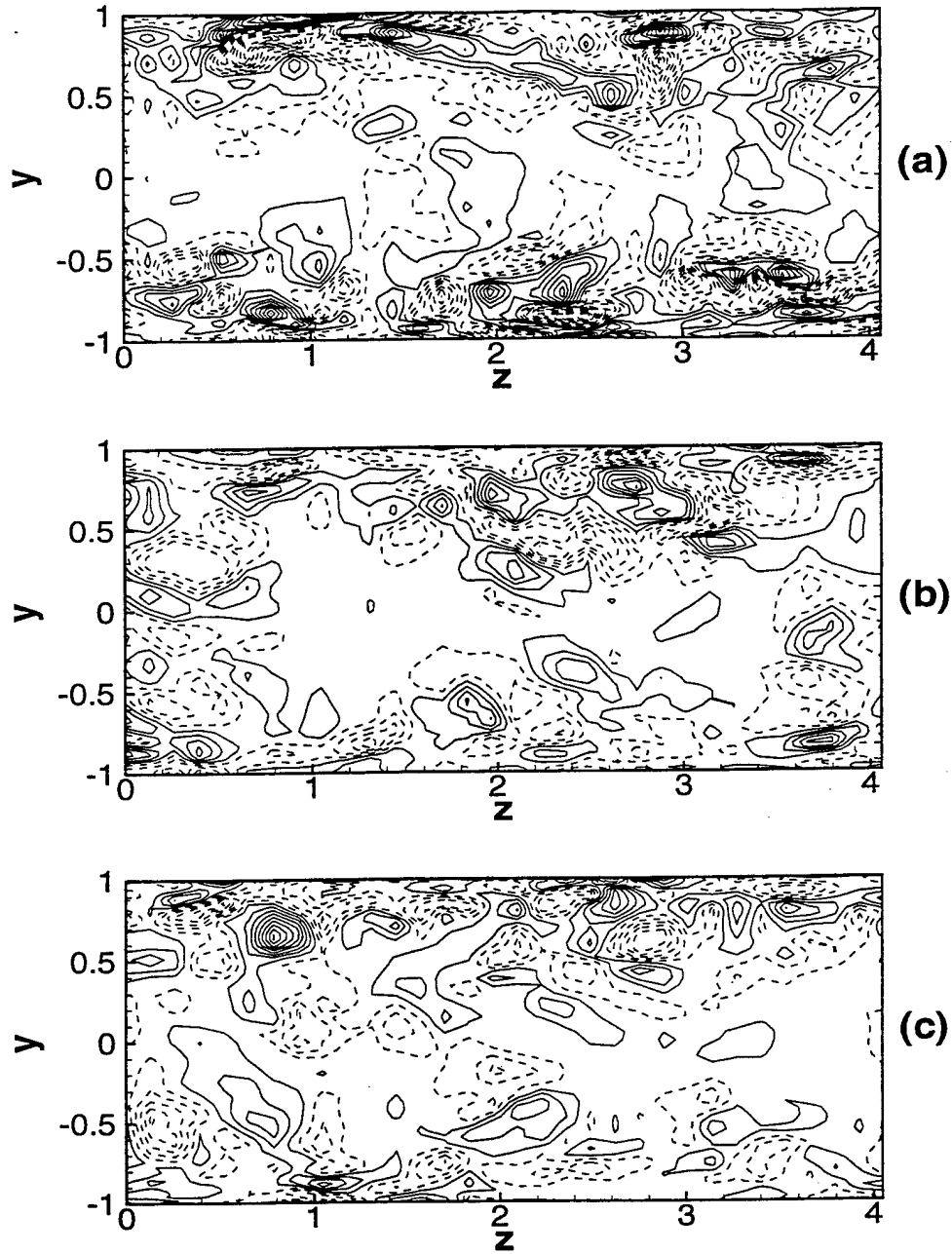


Figure 11: Comparison of streamwise vorticity contours in a yz -plane between controlled and uncontrolled flows: (a) uncontrolled flow; (b) 2D-controlled flow; (c) ad hoc-controlled flow. Negative contours are dashed.

APPENDIX F

State-Space Formulation and Controller Design for a Three-Dimensional Channel Flow

S.M. Kang, V. Ryder, L. Cortelezzi, J.L. Speyer

discuss its performance. Section 6 closes the article with some conclusions.

2 Mathematical Formulation

We consider the flow of an incompressible fluid in a three-dimensional periodic channel of length $L_x h$, width $L_z h$, and height $2h$ as shown in Figure 1. It has a steady Poiseuille velocity profile in the streamwise direction. The evolution of the perturbation velocities in such a flow is governed by the linearized Navier-Stokes equations:

$$\begin{aligned} \left(\frac{\partial}{\partial t} + U \frac{\partial}{\partial x} \right) u + U'v &= -\frac{\partial p}{\partial x} + \frac{1}{Re} \nabla^2 u, \\ \left(\frac{\partial}{\partial t} + U \frac{\partial}{\partial x} \right) v &= -\frac{\partial p}{\partial y} + \frac{1}{Re} \nabla^2 v, \\ \left(\frac{\partial}{\partial t} + U \frac{\partial}{\partial x} \right) w &= -\frac{\partial p}{\partial z} + \frac{1}{Re} \nabla^2 w, \end{aligned} \quad (1)$$

and the continuity equation:

$$\frac{\partial u}{\partial x} + \frac{\partial v}{\partial y} + \frac{\partial w}{\partial z} = 0, \quad (2)$$

where u , v , and w are the perturbation velocities in the x , y , and z directions respectively. We make the problem dimensionless by using h as the characteristic length and h/U_c as the characteristic time. U_c represents the maximum mean flow at the center of the Poiseuille profile. The Reynolds number is $Re = U_c h / \nu$. The governing equations (1) can be reduced to two equations dependent only on the vertical components of the perturbation velocity and vorticity, ω_y (e.g. Ref [7]):

$$\left(\frac{\partial}{\partial t} + U \frac{\partial}{\partial x} \right) \nabla^2 v - \frac{d^2 U}{dy^2} \frac{\partial v}{\partial x} = \frac{1}{Re} \nabla^2 \nabla^2 v, \quad (3)$$

$$\left(\frac{\partial}{\partial t} + U \frac{\partial}{\partial x} \right) \omega_y - \frac{1}{Re} \nabla^2 \omega_y = -\frac{dU}{dy} \frac{\partial v}{\partial z}. \quad (4)$$

Blowing and suction is applied at the bottom wall to suppress the near-wall disturbances. For simplicity, we assume that the actuators are uniformly distributed. The corresponding boundary conditions are:

$$\begin{aligned} v|_{y=\pm 1} &= \frac{\partial v}{\partial y} \Big|_{y=\pm 1} = \omega_y|_{y=\pm 1} = 0, \\ v|_{y=-1} &= v_w, \end{aligned} \quad (5)$$

where the control function v_w represents the amount of blowing and suction. With the linearity assumed for the problem, v can be seen as the sum of two parts: a \hat{v} which satisfies the homogeneous boundary conditions and a χ which satisfies the non-homogeneous boundary conditions. Thus we have that:

$$v = \hat{v} + \chi, \quad (6)$$

$$\hat{v}|_{y=\pm 1} = \frac{\partial \hat{v}}{\partial y} \Big|_{y=\pm 1} = \omega_y|_{y=\pm 1} = \frac{\partial \chi}{\partial y} \Big|_{y=\pm 1} = 0, \quad (7)$$

$$\chi|_{y=1} = 0, \quad \chi|_{y=-1} = v_w.$$

Substituting the above into equations (3) and (4), χ can be seen as the input, or control function.

To determine the deviation of the boundary layer from the laminar regime, we measure the gradients of the streamwise and spanwise velocity components at points (x_i, z_j) along the bottom wall. For the current study, we assume that the sensors are distributed in a way that provides an accurate measurement of the gradients. Thus, the sensor output is defined as:

$$\begin{aligned} z_u(x_i, z_j, t) &= \frac{\partial u}{\partial y} \Big|_{x=x_i, y=-1, z=z_j}, \\ z_w(x_i, z_j, t) &= \frac{\partial w}{\partial y} \Big|_{x=x_i, y=-1, z=z_j}. \end{aligned} \quad (8)$$

In other words, we measure the first terms of the wall-shear stresses, $\tau_{yx} = Re^{-1}(\partial u / \partial y + \partial v / \partial x)|_{y=-1}$ and $\tau_{yz} = Re^{-1}(\partial w / \partial y + \partial v / \partial z)|_{y=-1}$, respectively. Now, u and w need to be defined in terms of v and ω_y . As noted by Butler and Farrell [7]:

$$\begin{aligned} \left(\frac{\partial^2}{\partial x^2} + \frac{\partial^2}{\partial z^2} \right) u &= \frac{\partial \omega_y}{\partial z} - \frac{\partial^2 v}{\partial x \partial y}, \\ \left(\frac{\partial^2}{\partial x^2} + \frac{\partial^2}{\partial z^2} \right) w &= -\frac{\partial \omega_y}{\partial x} - \frac{\partial^2 v}{\partial z \partial y}. \end{aligned} \quad (9)$$

Once discretized as described in Section 3, we find that u and w can be directly defined in terms of \hat{v} , χ , and ω_y .

Finally, we define a cost function, J , to use in LQG synthesis. Since our objective is to suppress wall-shear stresses, we define:

$$J = \lim_{t_f \rightarrow \infty} \int_{t_i}^{t_f} \int_{L_x} \int_{L_z} \left[\frac{(\frac{\partial u}{\partial y})^2 + (\frac{\partial w}{\partial y})^2}{+(\frac{\partial v}{\partial x})^2 + (\frac{\partial v}{\partial z})^2} \right] dz dx dt. \quad (10)$$

The integrand represents the cost of the wall-shear stresses being different from zero which includes the cost of implementing the control. We have two primary reasons for restricting the controller gain: In any engineering application, there are physical limits to the control effort the actuators may be able to supply; and a large control action may drive the system away from the region where the linear model is valid.

3 Derivation of the State-Space Equations

In order to apply linear control techniques, the governing equations need to be put into state space form. Following the framework presented in Ref [8], we use complex Fourier series to discretize the relevant flow properties and then apply Galerkin's method to obtain the desired state space vectors and equations.

The two flow properties, \hat{v} and ω_y , and the input func-

tion, χ , are spectrally decomposed by Fourier expansions: tion (10) becomes:

$$\hat{v} = \frac{1}{2} \sum_{n,m,l} \left(a_{nml}(t) e^{(i\alpha_n x + i\beta_m z)} \right) \Gamma_l(y), \quad (11)$$

$$\omega_y = \frac{1}{2} \sum_{n,m,l} \left(b_{nml}(t) e^{(i\alpha_n x + i\beta_m z)} \right) \Upsilon_l(y), \quad (12)$$

$$\chi = \frac{1}{2} \sum_{n,m} \left(p_{nm}(t) e^{(i\alpha_n x + i\beta_m z)} \right) \Xi(y). \quad (13)$$

where the summation subscripts are defined as follows: the streamwise wave number $n = -N/2, \dots, -1, 1, \dots, N/2$, the spanwise wave number $m = -M/2, \dots, -1, 1, \dots, M/2$, and the Chebyshev polynomial index $l = 0, \dots, L$. For both the streamwise and spanwise expansions, the 0 wave number is omitted since it represents the mean perturbation values, which are set to zero. $\alpha_n = \frac{2\pi n}{L_x}$ is the streamwise wave number, and $\beta_m = \frac{2\pi m}{L_z}$ is the spanwise wave number. The $\Gamma_l(y)$ and $\Upsilon_l(y)$ are combinations of Chebyshev polynomials chosen to satisfy the boundary conditions: $\Gamma_l(\pm y) = \Gamma'_l(\pm y) = \Upsilon_l(\pm y) = 0$. $\Xi(y)$ is a function constructed to satisfy the boundary conditions: $\Xi(-1) = 1$ and $\Xi(1) = \Xi'(\pm 1) = 0$ of the input function.

The measurements are similarly expanded:

$$\begin{aligned} \frac{\partial u}{\partial y} &= \frac{1}{2} \sum_{n,m} \left(a_{nm}^u(t) e^{(i\alpha_n x + i\beta_m z)} \right), \\ \frac{\partial w}{\partial y} &= \frac{1}{2} \sum_{n,m} \left(a_{nm}^w(t) e^{(i\alpha_n x + i\beta_m z)} \right). \end{aligned} \quad (14)$$

Consequently, the $(\partial^2/\partial x^2 + \partial^2/\partial z^2)$ operator of equations (9) becomes $(\alpha_n^2 + \beta_m^2)$. This allows for the coefficients $a_{nm}^u(t)$ and $a_{nm}^w(t)$ to be defined directly in terms of the coefficients $a_{nml}(t)$, $b_{nml}(t)$, and $p_{nm}(t)$ of equations (11) - (13).

To construct the state space equations, we substitute (11) - (14) into equations (3), (4), (6), (8), and (9). Then by Galerkin's method, the coefficients are collected into first-order dynamic system and measurement equations. Stacking both the real and imaginary parts of the coefficients as elements of the state, input, and output vectors, equations (3) and (4) can be represented as:

$$A_1 \frac{d\bar{y}}{dt} = A_2 \bar{y} + B_1 \bar{u} + B_2 \frac{d\bar{u}}{dt}, \quad \bar{z} = C\bar{y} + D_3 \bar{u}. \quad (15)$$

These equations are then transformed into standard state-space form by making some substitutions: $\bar{x} = \bar{y} - A_1^{-1} B_2 \bar{u}$, $B = A_1^{-1} B_1 + A_2 A_1^{-1} B_2$, and $D = D_3 + C A_1^{-1} B_2$. Thus, \bar{x} becomes the internal state, \bar{u} the control vector, and \bar{z} the measurement vector to produce:

$$\frac{d\bar{x}}{dt} = A\bar{x} + B\bar{u}, \quad \bar{z} = C\bar{x} + D\bar{u}. \quad (16)$$

with initial condition $\bar{x}(0) = \bar{x}_0$. Similarly, the cost func-

$$J = \lim_{t_f \rightarrow \infty} \int_{t_i}^{t_f} [\bar{z}^* \bar{z} + \bar{u}^* W^* W \bar{u}] dt, \quad (17)$$

where the superscript * denotes the transpose.

Cast into state-space form, the full system decouples with respect to pairs of wave numbers (n, m) where $n = 1, \dots, N/2$ and $m = -M/2, \dots, -1, 1, \dots, M/2$. All the matrices in (16) and (17) are block diagonal consistent with the two dimensional block diagonal structure found in Refs [4, 5, 8]. The above system (16) is equivalent to 2NM state-space sub-systems, one for each wave number pair. For a given pair of wave numbers nm , the state space system is:

$$\begin{aligned} \frac{d\bar{x}_{nm}}{dt} &= A\bar{x}_{nm} + B\bar{u}_{nm}, \\ \bar{z}_{nm} &= C\bar{x}_{nm} + D\bar{u}_{nm}, \end{aligned} \quad (18)$$

with initial condition $\bar{x}_{nm}(0) = \bar{x}_{nm0}$. Vectors \bar{x}_{nm} , \bar{u}_{nm} , and \bar{z}_{nm} have the following structure: $\bar{x}_{nm} = [a_{nm0}^R, \dots, a_{nmL}^R, a_{nm0}^I, \dots, a_{nmL}^I, b_{nm0}^R, \dots, b_{nmL}^R, b_{nm0}^I, \dots, b_{nmL}^I]^T$, $\bar{u}_{nm} = [p_{nm}^R, p_{nm}^I]^T$, $\bar{z}_{nm} = [a_{nm}^u, a_{nm}^w]^T$, where R and I indicate the real and imaginary values of the coefficient and $'$ indicates that the coefficients have been modified by the matrix substitutions that produced equation (16).

The cost function also decouples into a sum of 2NM performance indices. The performance index for one wave number pair, nm , is:

$$J = \lim_{t_f \rightarrow \infty} \int_{t_i}^{t_f} [R \bar{z}_{nm}^* \bar{z}_{nm} + \bar{u}_{nm}^* W_{nm}^* W_{nm} \bar{u}_{nm}] dt, \quad (19)$$

where R is a scalar value. Consequently, the design of a robust controller for the system (16) and (17) has been reduced to the design of 2NM independent robust controllers, one for each pair of wave numbers. In each subsystem (18) and (19), the control vector has only 2 elements and the measurement vector 4.

Taking a closer look at the A matrix of (16), we see that it can be partitioned into four blocks, each of size $(L+1) \times (L+1)$. Block A_{12} (upper right corner) is identically zero, while A_{11} produces the Orr-Sommerfeld modes and A_{22} produces the Squire modes. The Coupling operator, A_{21} has been shown to produce significant energy amplification for certain wave numbers [7].

4 Model Reduction and Controller Design

A challenge of this study is to reduce the size of the controller. A controller based on the full system derived from equations (3) and (4) with $N = 32$, $M = 32$, and $L = 65$ would have more than 10^5 states. A controller with hundreds of thousands of states is of no interest in engineering applications because of the amount of hardware and

computing power necessary for real-time control. Consequently, it is crucial to reduce the order of the controller. We derive a lower order controller in two steps. First, we construct a lower order model of (18), and then, we design a robust controller for the reduced-order model.

To lower the order of the model, we first transform the system (18) into Jordan Canonical form. We find the minimal realization of the system by eliminating all states associated with the unobservable and uncontrollable modes. The less observable and less controllable modes are then removed to obtain a reduced-order system. The matrices \hat{A}_{nm} , \hat{B}_{nm} , \hat{C}_{nm} , D_{nm} and vector \hat{x}_{nm} represent the reduced-order model.

Although a rigorous mathematical framework for the design of disturbance attenuation (\mathcal{H}_∞) linear controllers is provided by control synthesis theory in Refs [9,10], for the current study LQG (\mathcal{H}_2) synthesis is adequate. The controller design is divided into two parts: linear-quadratic-regulator (LQR) and minimum variance estimator (Kalman-Bucy filter). The LQR design provides an optimal control law in terms of the internal state vector by minimizing a cost function. However, since the internal state vector is not directly measurable, it is reconstructed from the measurement vector by an estimator. The result of the LQG (\mathcal{H}_2) design based on the reduced-order model of the wave number pair sub-system (18) is summarized as:

$$\tilde{u} = -\hat{K}_{nm} \tilde{x}_{nm}, \quad (20)$$

$$\begin{aligned} \frac{d\tilde{x}_{nm}}{dt} &= \hat{A}_{nm}\tilde{x}_{nm} + \hat{B}_{nm}\tilde{u}_{nm} \\ &+ \hat{L}_{nm} [\tilde{z}_{nm} - \hat{C}_{nm}\tilde{x}_{nm} - D_{nm}\tilde{u}_{nm}], \end{aligned} \quad (21)$$

with initial conditions $\tilde{x}_{nm}(0) = \tilde{0}$. Equation (20) is the control law. The gain matrix \hat{K}_{nm} is obtained by minimizing the performance index (19). Equation (21) is the minimum variance estimator. The matrix \hat{L}_{nm} is the Kalman Filter gain assigning some value for the power spectral densities of the process and measurement noises. Since we have assumed no statistics, the power spectral densities are chosen as design parameters in order to keep the eigenvalues of the estimator at the same order of magnitude as the eigenvalues of the controller. In particular, the spectral density for process noise is chosen as $\rho\hat{B}_{nm}\hat{B}_{nm}^*$, where the parameter ρ is increased to obtain the desired loop transfer recovery of the full state LQR problem [6]. However, to move the eigenvalues to the left, an experimental weighting is also used [11].

Figure 1 shows how this mathematical formulation can be implemented either as a computational simulation or a mechanical system. The controller can be programmed in a computer routine whose input are matrices containing the gradients of u and w and whose output is a matrix containing the blowing and suction at the wall. The sensor matrix is processed by a two dimensional fast Fourier Transform (FFT) algorithm and converted into \tilde{z}_{nm} 's,

which are inputs to the compensator. Parallel computations produces the \tilde{u}_{nm} 's, and an inverse FFT process converts the \tilde{u}_{nm} into the columns of the matrix containing the blowing and suction at the wall. This routine can be embedded in any Navier-Stokes solver able to handle time-dependent boundary conditions for the control of three-dimensional channel flows.

5 Results

We designed a controller for a single wave number pair decomposition of three-dimensional Poiseuille flow in a periodic channel of length $L_x = 4\pi$ and width $L_z = 4\pi/3$ at $Re = 10,000$. We considered only the wave numbers $n = 1$ (streamwise wave number) and $m = 1$ (spanwise wave number) with 125 Chebyshev polynomials ($L = 124$). Consequently, the full system (16) and the wave number pair sub-system (18) are identical. Even so, the order of the system is 500×500 . Also, the system as described above produces no unstable eigenvalues. Therefore, our objective was to develop a controller that moves the least stable pole of the minimal realization to the left without making the closed loop system unstable.

Using the model reduction method described in Section 4, a reduced system containing 30 states was found. For this case, all states associated with poles with real parts less than -1.4 were eliminated because, compared to the poles near the imaginary axis, these poles decay much faster and are probably not important for the design of the controller. Additionally, several double poles from the Squire modes had to be handled manually. Single zeros lie on top of these poles which caused the automatic reduction scheme to eliminate both poles as unobservable and uncontrollable. Consequently, one of the two poles had to be added back in manually.

Although the reduced-order system was derived with methods that were not entirely systematic, the frequency response of the reduced system matches the full state (minus the resolution error) fairly well (see Figure 2). Thus,

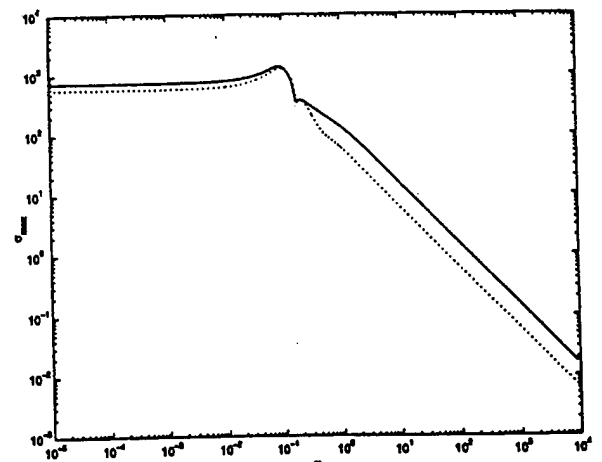


Figure 2: Maximum singular values for full (solid) and reduced (dotted) state systems.

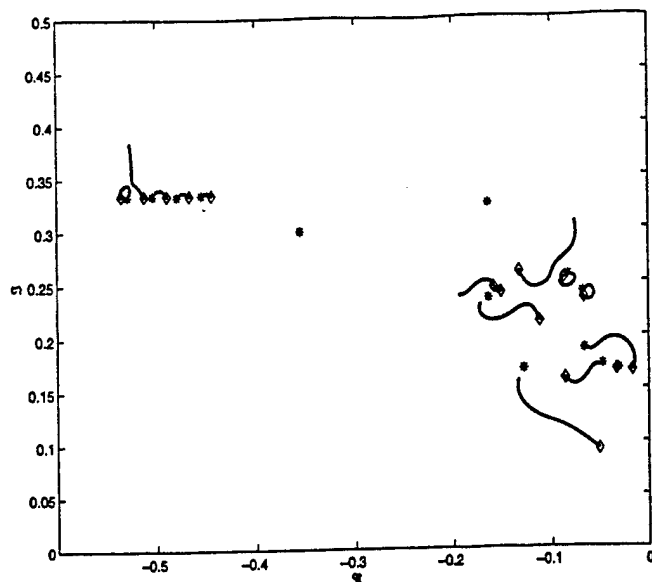


Figure 3: Reduced plant (diamond) & compensator (star).
the compensator was designed on this reduced-order system.

Figure 3 is the pole structure of the closed loop, reduced-order system, showing how the poles progress as the compensator gain is increased from zero to 1. Figure 4 similarly shows the pole structure of the full state system with the compensator. These figures demonstrate very clearly the effectiveness of the reduced-order controller. The controller was designed using a reduced-order system of only 30 states, which represents a dramatic decrease from the full 500 states. Even so, the controller is capable of suppressing the least stable pole of the minimal realization. Although these results are preliminary, they are very encouraging.

6 Conclusions

This article presents the successful application of reduced-order linear feedback control on a three-dimensional flow. A controller based on a model reduced from 500 to 30 states was designed using LQG synthesis. Although the analysis is limited to a single wave number pair decomposition of the flow, the controller demonstrates that it can increase the decay rate of the least stable mode (Figure 4).

These are preliminary but very encouraging results. Currently, we are investigating the possibility of further reducing the state and developing controllers for several wave number pairs. Since the system is decoupled for wave number pairs, these controllers will be developed and applied in parallel, making the control of multiple wave number pairs relatively simple. Ultimately, multi-wave pair controllers will be tested on fully non-linear simulations.

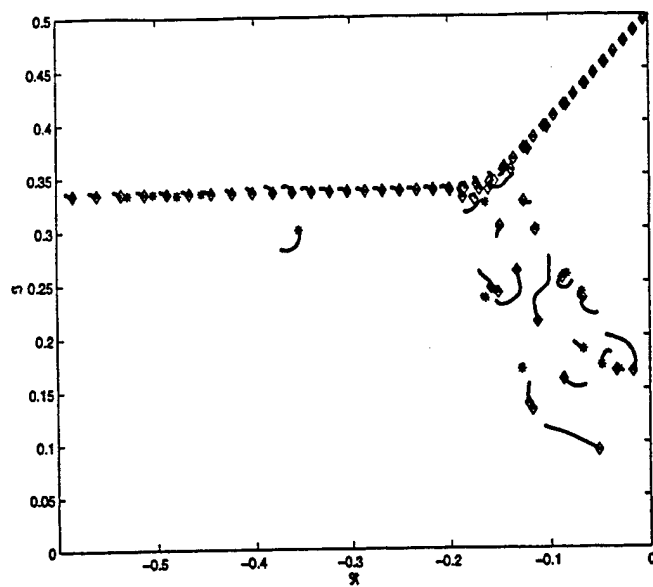


Figure 4: Full plant (diamond) & compensator (star).

References

- [1] M. Gad-el-Hak, "Interactive control of turbulent boundary layers - A futuristic overview", *AIAA Journal*, 32, (9), 1753 (1994).
- [2] V.J. Modi, "Moving surface boundary-layer control: A review", *Journal of Fluids and Structures*, 11, (6), 627 (1997).
- [3] H.L. Reed, W.S. Saric and D. Arnal, "Linear stability theory applied to boundary layers", *Annu. Rev. Fluid Mech.*, 28, 389 (1996).
- [4] L. Cortelezzi and J.L. Speyer, "Robust reduced-order controller of laminar boundary layer transitions", *Phys. Rev. E*, 58, (2), 1906 (1998).
- [5] L. Cortelezzi, J.L. Speyer, K.H. Lee and J. Kim, "Robust Reduced-Order Control of Turbulent Channel Flows Via Distributed Sensors and Actuators", 37th Conference on Decision and Control, Tampa, Florida, December 1998.
- [6] J.C. Doyle and G. Stein, "Multivariable feedback design: Concepts for a classical/modern synthesis", *IEEE Trans. Automatic Control*, AC-26, (2), (1981).
- [7] K.M. Butler and B.F. Farrell, "Three-dimensional Optimal Perturbations in Viscous Shear Flow", *Physics of Fluids A*, 4, (8), 1637 (1992).
- [8] S.S. Joshi, J.L. Speyer and J. Kim, "A systems theory approach to the feedback stabilization of infinitesimal and finite-amplitude disturbances in plane Poiseuille flow", *J. Fluid Mech.*, 332, 157 (1997).
- [9] K. Zhou, J.C. Doyle and K. Glover, "Robust and optimal control", (Prentice Hall, 1996).
- [10] I. Rhee and J.L. Speyer, "A game theoretic approach to a finite-time disturbance attenuation problem", *IEEE Trans. Automatic Control*, 36, (9), 1021 (1991).
- [11] B.O. Anderson and J.B. Moore, *Optimal Control: Linear Quadratic Methods*, Prentice-Hall, 1990.

APPENDIX G

Robust Feedback Control of Rayleigh Bénard Convection
A.C. Or, L. Cortelezzi, J.L. Speyer

Robust Feedback Control of Rayleigh-Bénard Convection

A.C. Or,¹ L. Cortelezzi,² and J.L. Speyer,¹

¹Department of Mechanical & Aerospace Engineering,
University of California, Los Angeles, CA 90095-1597

²Department of Mechanical Engineering,
McGill University, Montreal, Canada H3A-2K6

November 18, 2000

Abstract

We investigate the application of linear-quadratic-Gaussian (LQG) feedback control, or, in modern terms, \mathcal{H}_2 control, to the stabilization of the no-motion state against the onset of Rayleigh-Bénard convection in an infinite layer of Boussinesq fluid. We use two sensing and actuating methods: the planar sensor model (Tang and Bau 1993, 1994), and the shadowgraph model (Howle, 1997a). By extending the planar sensor model to the multi-sensor case, it is shown that a LQG controller is capable of stabilizing the no-motion state up to 14.5 times the critical Rayleigh number. We characterize the robustness of the controller with respect to parameter uncertainties, unmodelled dynamics. Results indicate that the LQG controller provides robust performances even at high Rayleigh numbers.

1 Introduction

When a layer of fluid at rest is heated from below, fluid motions will develop into well organized convection patterns if the temperature difference across the layer is sufficiently large (Cross and Hohenberg, 1993). For certain industrial applications, developing a temperature gradient across the fluid layer is unavoidable but at the same time preventing convective fluid motions is desirable. Some examples involving undesirable effects of convection are material processing, solidification, semiconductor melts, welding, evaporative coating and crystal growth. Our aim is to use robust modern control methodologies to inhibit the onset of convection while permitting a large thermal gradient across the layer of fluid.

The idea of stabilizing the fluid layer against the onset of cellular motions has been advanced by Tang and Bau (1993,1994,1998a,b) and Howle (1997a,b,c,2000). Tang and Bau assumed that the temperature field can be measured continuously on a horizontal plane in x, y and t (see Fig. 1). The measurements are then used to control the temperature at the lower wall, in order to cancel the thermal disturbances in the fluid that drive the overturning motions. Howle (1997a) investigated a similar control problem, except in his case the measurements consist of shadowgraph images of the fluid. The shadowgraph images capture the horizontal distribution of the vertical-mean temperature. Moreover, in Howle's model, heat-flux rather than temperature is prescribed at the lower wall. Both types of sensor and actuator models will be considered in this study using a more sophisticated form of control synthesis.

Based on proportional feedback control, the results of Tang and Bau and Howle show that both sensor models exhibit a maximal achievable stable value of Rayleigh number Ra , beyond which this simple controller is ineffective for stabilization. For the planar-sensor model Tang and Bau (1993,1994) showed that the controller can inhibit convection up to a maximum of

about 3.8 times Ra_{c0} at $Pr = 7$, where $Ra_{c0} = 1707.76$ is the uncontrolled critical value. This value is Pr -dependent. Furthermore, the authors (Tang and Bau, 1994) considered a velocity actuator which inhibits convection up to 10 times the critical Rayleigh number. For the shadowgraph sensor model this maximum is about 3.13 times $Ra_{c0} = 1295.78$. In Section 4 the differences in performance between the two sensor models using only the thermal actuators, and the limitations of the proportional feedback control will be discussed.

The degree of stabilization can be improved significantly by using synthesis methods for multiple-input/multiple-output systems which produce dynamic compensators. However, in this study a distributed single-input/multiple-output strategy will be considered, since normal modes of different wavenumbers decouple and each normal mode can be controlled individually.

One of such synthesis methods is known as the linear-quadratic-Gaussian (LQG) control (Bryson and Ho, 1969), or, in modern terms, \mathcal{H}_2 control. Other methods such as \mathcal{H}_∞ synthesis (Rhee and Speyer, 1991) could also be applied, but we suspect with similar results. The LQG approach allows us to consider a nominal design Rayleigh number (Ra^*) significantly higher than that considered in the previous studies. For values of Ra sufficiently near Ra^* , stabilization with the LQG controller appears always to be achievable. Moreover, for Ra^* below a certain threshold, the complete range of Ra up to a critical value can be stabilized. In this study, we show that the system can be stabilized up to $Ra = 14.8Ra_{c0}$. In this range the first even and odd modes of convection can become unstable. However, these two modes are damped by the LQG controller. The higher modes are naturally damped within this range of Ra . Our aim is to ensure stability over the entire range of Ra up to a maximum critical Rayleigh number, without the formation of isolated

unstable regions within this range. This requires the determination of the value of Ra^* to produce this maximum critical Rayleigh number.

Unlike the proportional control method, the LQG synthesis method requires some elaboration. This synthesis method consists of two steps: (i) a reconstruction of the internal states of the plant based on the measured information, and (ii) a regulation of the plant states in order to drive the estimated perturbations to a zero level. To accomplish these two steps, the LQG controller is formed by a Kalman filter and an optimal regulator in cascade.

The LQG synthesis method has recently been used in the study of drag reduction in channel flow by Joshi et al. (1999) and by Cortelezzi and Speyer (1998) based on Joshi et al. (1997) who first introduced the system theoretic approach. Cortelezzi and Speyer (1998) presented a framework suited for practical implementations and demonstrated the performance of the design in numerical simulations. Following this framework, our investigations focus on a robust stability analysis of the closed-loop system as applied to Rayleigh-Bénard convection. Design parameters of the filter and regulator are carefully chosen to enhance the robustness of the stabilization. Several integrated design aspects are discussed.

This study intends to provide a design of controllers for future experiments. The design goal is to maximize the stability range of Rayleigh number. This implies designing controllers at the highest possible design value Ra^* , without causing an unstable, isolated region to form below Ra^* . Since the controllers are implemented at each wavenumber and only Ra is being varied, one form of robustness being demonstrated is the robustness of the system with respect to variations in Ra away from Ra^* . Another form of robustness is concerned with uncertainties in the system apart from the mismatch in Ra . For example, uncertainties due to nonlinearities or unmodelled dynamics. **The objective of this paper is to produce a robust design based on classical relative stability measures of gain and phase**

margins that accommodates to a degree unmodelled dynamics and nonlinearities. Nonlinear simulation is required to validate the design. We will show that the gain and phase margins depends crucially on the number of sensors used. More measurements implies better knowledge about the internal states of the system. In this study we are interested in determining the minimum number of sensor planes, as well as their locations, for achieving a reasonable degree of robustness. From a theoretical point of view, the planar sensor model appears to be more effective and accurate than the shadowgraph sensor model, mainly because a multiple planar sensor configuration can be readily incorporated. As the results will show, increasing the number of sensors, i.e., the measured information about the internal states, is crucial for achieving the desirable robustness.

We now proceed to Section 2 to derive the standard state-space equations for both sensor models. In Section 3, we review the theory of the LQG optimal control synthesis. In Section 4, the results are discussed and in Section 5, we conclude the paper.

2 State-Space Formulation

In this Section, we derive the state-space equations. Following the framework presented by Cortezzi and Speyer (1998), we start from the governing equations and subsequently transform them into a set of ordinary differential equations expressed in state space form. This procedure includes a transformation of variables, a spectral decomposition of the resulting equations and expressing these equations in the standard state-space form.

2.1 Governing Equations

We consider an infinite layer of Boussinesq fluid heated from below, which is parallel to the xy -plane and bounded by non-permeable walls at $z = \pm d/2$ (see Fig. 1). Our aim is to com-

pare the performance of the LQG controller with the performance of the proportional feedback control method based on two known models. Therefore, in our formulation the boundary conditions used in these two models will be preserved. For both models, the upper wall is assumed to be infinitely conductive at constant temperature T_1^* . For the planar sensor model (Tang and Bau, 1993,1994,1998,1998b) temperature is measured on an interior plane (see Fig.1, $T^*(z)$ denotes the basic state). These measurements are used to modify the constant lower wall temperature T_2^* with the actuator temperature $\theta_c^*(x, y, t)$. For the shadowgraph sensor model (Howle, 1997a, 1997b) measurements of the vertical-mean temperature distribution are obtained in the form of a shadowgraph. These measurements are used to modify the constant heat flux Q^* at the lower wall with the actuator heat flux $q_c^*(x, y, t)$. Different actuators are used to allow direct comparisons between the performances of the LQG controllers with the proportional controllers used in the original models.

We scale length, time, velocity, pressure relative to the hydrostatic pressure, and temperature, respectively, by d , d^2/κ , κ/d , $\rho\nu\kappa/d^2$ and $(T_2^* - T_1^*)$ or Q^*d/K depending on the model chosen, where ρ , κ , ν and K are, respectively, density, thermal diffusivity, kinematic viscosity and thermal conductivity of the fluid. The linear stability equations for the vertical perturbation velocity $w(x, y, z, t)$ and perturbation temperature $\theta(x, y, z, t)$ are

$$(Pr^{-1}\partial_t - \nabla^2)\nabla^2 w = Ra\nabla_{\perp}^2 \theta, \quad (1)$$

$$(\partial_t - \nabla^2)\theta = w, \quad (2)$$

where $\nabla_{\perp}^2 = \nabla^2 - \partial_{zz}$ (e.g. Chandrasekhar, 1961). The Prandtl number is $Pr = \nu/\kappa$. The Rayleigh number for the planar and shadowgraph cases are defined, respectively, as $Ra = \alpha g(T_2^* - T_1^*)d^3/\nu\kappa$ and $Ra = \alpha gQ^*d^4/K\nu\kappa$, where α is the coefficient of volume expansion and g is the gravitational acceleration.

The boundary conditions on velocity are

$$w(x, y, \pm 1/2, t) = \partial_z w(x, y, \pm 1/2, t) = 0. \quad (3)$$

As for the thermal boundary conditions, the upper wall is considered isothermal so that the perturbation temperature must satisfy

$$\theta(x, y, 1/2, t) = 0. \quad (4)$$

Based on the planar and shadowgraph sensor models (Tang and Bau, 1993, 1994, Howle, 1997a), we apply a continuous time-dependent control temperature along the lower wall for the planar sensor case,

$$\theta(x, y, -1/2, t) = \theta_c(x, y, t), \quad (5)$$

while for the shadowgraph model we apply a continuous time-dependent heat flux q_c instead,

$$\partial_z \theta(x, y, -1/2, t) = q_c(x, y, t). \quad (6)$$

The planar sensor model measures the temperature distribution at a number I of xy -planes located at $z = z_s^{(i)} \in [-1/2, 1/2]$, where $i = 1, 2, \dots, I$. The measurement equations are

$$\theta_s^{(i)}(x, y, t) = \theta(x, y, z_s^{(i)}, t), \quad i = 1, 2, \dots, I, \quad (7)$$

where $z_s^{(i)}$ is the z -coordinate of the i^{th} sensor plane. The shadowgraph model measures the average density over the whole layer, ρ_s , which is expressed in terms of temperature by

$$\rho_s(x, y, t) = \int_{-1/2}^{1/2} \nabla_{\perp}^2 \theta(x, y, z, t) dz, \quad (8)$$

where ρ_s is the measurement function in density. We refer readers to Howle (1997a) for the derivations of this integral expression.

2.2 Transformation of Dependent Variables and Cost Criterion

We transform the perturbation temperature so that equations (1)-(8) have homogeneous thermal boundary conditions. The perturbation velocity remains unchanged. With the perturbation temperature as $\theta \equiv \phi + \xi$, we obtain for both sensor models

$$(Pr^{-1}\partial_t - \nabla^2)\nabla^2 w - Ra\nabla_{\perp}^2 \phi = Ra\nabla_{\perp}^2 \xi, \quad (9)$$

$$(\partial_t - \nabla^2)\phi - w = -(\partial_t - \nabla^2)\xi, \quad (10)$$

subject to the boundary conditions

$$w(x, y, \pm 1/2, t) = \partial_z w(x, y, \pm 1/2, t) = \phi(x, y, 1/2, t) = 0. \quad (11)$$

Furthermore, for the planar sensor model ϕ must satisfy the boundary condition

$$\phi(x, y, -1/2, t) = 0, \quad (12)$$

while for the shadowgraph sensor model ϕ must satisfy the boundary condition

$$\partial_z \phi(x, y, -1/2, t) = 0. \quad (13)$$

The forcing function ξ satisfies a non-homogeneous boundary condition at the lower wall and a homogeneous boundary condition at the upper wall. For the planar case these conditions are

$$\xi(x, y, -1/2, t) = \theta_c(x, y, t), \quad \xi(x, y, 1/2, t) = 0, \quad (14)$$

and for the shadowgraph case we have instead

$$\partial_z \xi(x, y, -1/2, t) = q_c(x, y, t), \quad \xi(x, y, 1/2, t) = 0. \quad (15)$$

The two set of measurement equations in terms of the new variables for the planar and shadowgraph cases become

$$\theta_s^{(i)}(x, y, t) = \phi(x, y, z_s^{(i)}, t) + \xi(x, y, z_s^{(i)}, t), \quad i = 1, 2, \dots, I, \quad (16)$$

and

$$\rho_s(x, y, t) = \int_{-1/2}^{1/2} \nabla_{\perp}^2 (\phi(x, y, z, t) + \xi(x, y, z, t)) dz . \quad (17)$$

Note that the sensors could be located at discrete points in the $x - y$ plane, but to be consistent with Tang and Bau (1993,1994) we have considered continuously distributed sensors. Furthermore, Tang and Bau's experiment (1998a) using discrete sensors and actuators show consistency with their theoretical work using continuously distributed sensors and actuators. Finally, we introduce the cost criterion. Our goal is to design a controller able to drive the measured perturbation temperature to zero, without using unnecessarily large control action hopefully resulting in little saturation of the actuators. Thus, the performance index includes weighting on the control. We consider a layer of fluid with large aspect ratios L_x and L_y with periodic boundary conditions (see Fig. 1), assuming that the influence of the lateral boundary conditions in a finite layer of fluid is negligible. The LQG controller is determined by finding the control action which minimize the cost criterion. For the planar sensor model we define the cost criterion as

$$\mathcal{J} = \int_t^T \left\{ \int_0^{L_x} \int_0^{L_y} \left[\sum_{i=1}^I (\theta_s^{(i)})^2 + \gamma \theta_c^2 \right] dx dy \right\} d\tau , \quad (18)$$

and for the shadowgraph sensor model it is

$$\mathcal{J} = \int_t^T \left\{ \int_0^{L_x} \int_0^{L_y} \int_t^T (\rho_s^2 + \gamma q_c^2) dx dy \right\} d\tau . \quad (19)$$

2.3 Modal Decomposition

A periodic boundary condition permits us to perform a Fourier decomposition in the horizontal coordinates. The vertical dependence of the flow field and thermal field is constrained by the upper and lower wall boundary conditions. The vertical dependence will be decomposed

separately in Section 2.4. We describe an infinitesimal three-dimensional disturbance to the no-motion state. Consequently, we have a double sum of the Fourier normal modes for the disturbances:

$$\begin{aligned} w(x, y, z, t) &= \sum_{m=1}^M \sum_{n=1}^N \left\{ \frac{1}{2} [W_{r,mn}(z, t) + i W_{i,mn}(z, t)] e^{i(mk_x x + nk_y y)} + c.c. \right\}, \\ \phi(x, y, z, t) &= \sum_{m=1}^M \sum_{n=1}^N \left\{ \frac{1}{2} [\Phi_{r,mn}(z, t) + i \Phi_{i,mn}(z, t)] e^{i(mk_x x + nk_y y)} + c.c. \right\}, \\ \xi(x, y, z, t) &= \sum_{m=1}^M \sum_{n=1}^N \left\{ \frac{1}{2} [\Xi_{r,mn}(z, t) + i \Xi_{i,mn}(z, t)] e^{i(mk_x x + nk_y y)} + c.c. \right\}, \end{aligned} \quad (20)$$

where *c.c.* denotes the complex conjugate. The measurement and control functions are represented by

$$\begin{aligned} \theta_s^{(j)}(x, y, t) &= \sum_{m=1}^M \sum_{n=1}^N \left\{ \frac{1}{2} [\Theta_{sr,mn}^{(j)}(t) + i \Theta_{si,mn}^{(j)}(t)] e^{i(mk_x x + nk_y y)} + c.c. \right\}, \quad j = 1, \dots, I, \\ \rho_s(x, y, t) &= \sum_{m=1}^M \sum_{n=1}^N \left\{ \frac{1}{2} [R_{sr,mn}(t) + i R_{si,mn}(t)] e^{i(mk_x x + nk_y y)} + c.c. \right\}, \\ \theta_c(x, y, t) &= \sum_{m=1}^M \sum_{n=1}^N \left\{ \frac{1}{2} [\Theta_{cr,mn}(t) + i \Theta_{ci,mn}(t)] e^{i(mk_x x + nk_y y)} + c.c. \right\}, \\ q_c(x, y, t) &= \sum_{m=1}^M \sum_{n=1}^N \left\{ \frac{1}{2} [Q_{cr,mn}(t) + i Q_{ci,mn}(t)] e^{i(mk_x x + nk_y y)} + c.c. \right\}, \end{aligned} \quad (21)$$

where the subscripts *r* and *i* indicate real and imaginary parts, respectively. The two fundamental wavenumbers are $k_x = 2\pi/L_x$ and $k_y = 2\pi/L_y$. From the classical theory without control, a normal mode disturbance is unstable in the region above a neutral curve $Ra_0(k)$ (Chandrashekar, 1961), where Ra_0 is the Rayleigh number at neutral stability in the open-loop system and $k = \sqrt{k_x^2 + k_y^2}$ is the magnitude of the wavevector. We truncate the infinite series above to $M \times N$ horizontal modes, which span the unstable range. Since the basic equations depend only on the horizontal Laplacian ∇_{\perp}^2 , the wavenumbers appear only in even powers and can be described in terms of an internal parameter $k(m, n)$, where $k(m, n) = \sqrt{m^2 k_x^2 + n^2 k_y^2}$. We further substitute (20) and (21) into equations (9)-(17) and separate the real and imaginary parts. It should be remarked that the linear structure

includes all patterns at the onset. Certain realizable patterns, such as rolls and hexagons, will be selected when the nonlinear and symmetry-breaking effects are included in the model. The paper is focused on the stabilization of the no-motion state. Suppression of selected convection patterns and return to the no-motion state will be addressed by applying our LQG controller to a direct numerical simulation of convection.

Since the governing equations contain only even derivatives with respect to x or y , the real and imaginary parts of the dependent variables decouple and satisfy to the same set of equations. Furthermore, since the problem is linear, we can consider each normal mode separately. For simplicity of notation, we drop the indices of the Fourier coefficients, and define $W \equiv W_{r,mn} = W_{i,mn}$, $\Phi \equiv \Phi_{r,mn} = \Phi_{i,mn}$, $\Xi \equiv \Xi_{r,mn} = \Xi_{i,mn}$, $\Theta_c \equiv \Theta_{cr,mn} = \Theta_{ci,mn}$, $Q_c \equiv Q_{cr,mn} = Q_{ci,mn}$, $\Theta_s^{(i)} \equiv \Theta_{sr,mn}^{(i)} = \Theta_{si,mn}^{(i)}$ and $R_s \equiv R_{sr,mn} = R_{si,mn}$. The governing equations are reduced as followed:

$$[Pr^{-1}(\partial_z^2 - k^2)\partial_t - (\partial_z^2 - k^2)^2]W + Rak^2\Phi = -Rak^2\Xi, \quad (22)$$

$$[\partial_t - (\partial_z^2 - k^2)]\Phi - W = -[\partial_t - (\partial_z^2 - k^2)]\Xi. \quad (23)$$

The boundary conditions are homogeneous. For the planar case we have

$$W(\pm 1/2, t) = \partial_z W(\pm 1/2, t) = \Phi(\pm 1/2, t) = 0, \quad (24)$$

and for the shadowgraph sensor model we have instead

$$W(\pm 1/2, t) = \partial_z W(\pm 1/2, t) = \Phi(1/2, t) = 0, \quad \partial_z \Phi(-1/2, t) = 0. \quad (25)$$

The forcing function Ξ satisfies non-homogeneous boundary condition at the lower wall and homogeneous boundary condition at the upper wall. For the planar case the forcing function is given by

$$\Xi(-1/2, t) = \Theta_c(t), \quad \Xi(1/2, t) = 0, \quad (26)$$

and the corresponding measurement functions are

$$\Theta_s^{(i)}(t) = \Phi(z_s^{(i)}, t) + \Xi(z_s^{(i)}, t), \quad i = 1, 2, \dots, I. \quad (27)$$

For the shadowgraph sensor model, the forcing function Ξ is

$$\partial_z \Xi(-1/2, t) = Q_c(t), \quad \Xi(1/2, t) = 0, \quad (28)$$

and the corresponding measurement function is

$$R_s(t) = -k^2 \int_{-1/2}^{1/2} (\Phi(z, t) + \Xi(z, t)) dz. \quad (29)$$

In our approach, each distinct horizontal normal mode is controlled by a separate controller. Therefore, for the implementation $M \times N$ controllers are required. As a simple illustration for the analysis, consider an aspect ratio L_x/d and L_y/d equal to 20π . In this case, the only wavenumbers present are the fundamental wavenumber $k_f = 2\pi/L = 0.05$, and its harmonics. For Ra up to $15Ra_{c0}$, the wavenumbers from $k = k_f$ to $k = 12$ (equal to $240k_f$). These wavenumbers represent the ensemble of normal modes used to represent the convection field.

In a physical implementation of the planar sensor model, both the measurements and control action occur in physical space but the controllers operate in the Fourier space. Sensors and actuators are interfaced to the controllers by fast Fourier transforms (FFT). Figure 2(a) links with simplicity the mathematical formulation to its computational implementation by summarizing in a block diagram the control strategy described above. The controllers can be programmed in a computer routine whose inputs are the arrays containing the temperatures measured by the planar sensors and whose output is an array containing the temperatures to be applied at the bottom the wall. The temperature measurements obtained by the planar sensors are converted by a fast Fourier transform into a set of modal sensor variables. Each pair of estimator and control blocks is integrated in time. Parallel computation produces

the modal control variables. An inverse FFT converts the modal control variables into the actuating temperature at the bottom wall. This routine can be embedded in any Navier-Stokes solver able to handle time-dependent boundary conditions for the control of more realistic simulations of Rayleigh-Bénard convection.

Figure 2(a) also provides the basic architecture for the potential implementation of the present controller in an experiment and, eventually, in practical engineering applications. The temperature distribution at a given plane ($z_s^{(i)}$) ($i = 1, 2, \dots, I$) could be measured by a planar sensor constructed with an array of micro-electro-mechanical-systems (MEMS) diode sensors (see Tang and Bau, 1998a and 1998b). Analog to digital converters (A/D) and digital signal processors (DSP) would convert the measured temperatures $z_s^{(i)}$ into the modal sensor variables. Each pair of estimator and control blocks would be replaced by a microprocessor, and a parallel computation produces the modal control variables. A DSP and a digital to analog converter (D/A) would produce the actuating signal. Finally, an array of MEMS heaters would provide the temperature distribution at the bottom wall (Tang and Bau, 1998a,b).

2.4 State Space Representation of Temporal Dynamics

In this subsection, we consider a numerical procedure to represent the vertical dependence of the velocity and thermal field. We consider the Galerkin approach (Gottlieb and Orszag, 1981) for the representation of the vertical dependence of the normal modes. The beam functions $\{\varphi_m\}$ are used as the basis functions for W which has to satisfy four boundary conditions. On the other hand the sinusoidal functions $\{\beta_m\}$ are used as basis functions for Φ which only has to satisfy two boundary conditions. In our numerical computations, we truncate the infinite set to the first N_z terms for both W and Θ . We use the same truncation number for both

fields mainly for numerical convenience.

In general the Chebyshev polynomials have good convergence properties. However, in our application individual polynomial does not satisfy the homogeneous boundary conditions. In contrast, individual beam functions do satisfy the homogeneous boundary conditions naturally and they converge reasonably fast for our stability analysis. Also, since we have transformed the thermal boundary condition at the lower wall to a homogeneous form, our results are not affected by Gibb's phenomenon.

The Fourier coefficients for the vertical velocity $W(z, t)$ is expanded as follows:

$$W(z, t) = \sum_{m=1}^{N_z} A_m(t) \varphi_m(z) = \sum_{m=1}^{N_z} A_m(t) \left[\frac{\sinh(a_m z + im\pi/2)}{\sinh(a_m + im\pi/2)} - \frac{\sin(a_m z + m\pi/2)}{\sin(a_m + m\pi/2)} \right]. \quad (30)$$

Since the thermal boundary conditions for the planar sensor model and shadowgraph sensor model are different, the sinusoidal basis functions $\{\beta_m\}$ are different for the two cases. For the planar sensor model we let

$$\Phi(z, t) = \sum_{m=1}^{N_z} B_m(t) \beta_m(z) = \sum_{m=1}^{N_z} B_m(t) \sqrt{2} \sin[m\pi(z + 1/2)], \quad (31)$$

and for the shadowgraph sensor model we have instead

$$\Phi(z, t) = \sum_{m=1}^{N_z} B_m(t) \beta_m(z) = \sum_{m=1}^{N_z} B_m(t) \sqrt{2} \sin[(m - 1/2)\pi(z - 1/2)]. \quad (32)$$

A convenient choice for Ξ which satisfies the appropriate boundary conditions of the planar sensor case is

$$\Xi(z, t) = (1/2 - z) \Theta_c(t), \quad (33)$$

and which satisfies the boundary conditions of the shadowgraph sensor case is

$$\Xi(z, t) = (z - 1/2) Q_c(t). \quad (34)$$

For the planar case, we now substitute (30), (31) and (33) into Eqs. (22) and (23), and perform the Galerkin projection. The following equations are obtained:

$$Pr^{-1} \sum_{m=1}^{N_z} \langle \varphi_j, (\partial_z^2 - k^2) \varphi_m \rangle \dot{A}_m = \sum_{m=1}^{N_z} \langle \varphi_j, (\partial_z^2 - k^2)^2 \varphi_m \rangle A_m \quad (35)$$

$$-k^2 Ra \sum_{m=1}^{N_z} \langle \varphi_j, \beta_m \rangle B_m - k^2 Ra \langle \varphi_j, (1/2 - z) \rangle \Theta_c ,$$

$$\dot{B}_m = \sum_{m=1}^{N_z} \langle \beta_j, (\partial_z^2 - k^2) \beta_m \rangle B_m + \sum_{m=1}^{N_z} \langle \beta_j, \varphi_m \rangle A_m \quad (36)$$

$$- \langle \beta_j, (1/2 - z) \rangle \dot{\Theta}_c + \langle \beta_j, (\partial_z^2 - k^2)(1/2 - z) \rangle \Theta_c ,$$

where the index j runs from 1 to N_z and the inner product \langle , \rangle denotes integration over $z \in [-1/2, 1/2]$. The corresponding equations for the shadowgraph model can be obtained from Eqs.(35,36) by replacing Θ_c by Q_c and $(1/2 - z)$ by $(z - 1/2)$. Therefore the shadowgraph model equations will not be presented explicitly.

After substituting (31) and (33) into Eq. (27), we obtain I measurement equations for the planar case,

$$\Theta_s^{(i)}(t) = \sum_{m=1}^{N_z} B_m(t) \beta_m(z_s^{(i)}) + (1/2 - z_s^{(i)}) \Theta_c, \quad i = 1, 2, \dots, I . \quad (37)$$

For the shadowgraph case, upon substitution of Eqs. (32) and (34) into Eq. (29), we have a single measurement equation

$$R_s(t) = \sum_{m=1}^{N_z} B_m(t) \int_{-1/2}^{1/2} (-k^2) \beta_m(z) dz + Q_c \int_{-1/2}^{1/2} (-k^2)(z - 1/2) dz . \quad (38)$$

As a final step, we construct a state vector \mathbf{X} by arranging the coefficients A_m and B_m as follows

$$\mathbf{X} \equiv [A_1, A_2, \dots, A_{N_z}, B_1, B_2, \dots, B_{N_z}]', \quad (39)$$

where superscript $'$ denotes transpose. Equations (35) and (36) can be rewritten in state space form as

$$\dot{\mathbf{X}} = \mathbf{A}\mathbf{X} + \mathbf{B}_1\Theta_c + \mathbf{B}_2\dot{\Theta}_c , \quad (40)$$

while the measurement equation (37) can be re-written as

$$\Theta_s = CX + D_3\Theta_c . \quad (41)$$

In order to cast the matrix equation in a standard state-space form we can either choose Θ_c or its time derivative as the control action variable. Here we define $u = \Theta_c$. The term $\dot{\Theta}_c$ can be eliminated from Eq.(40) by defining a new state vector $x = X - B_2\Theta_c$. Upon transformation, the state-space equations can be written as

$$\dot{x} = Ax + Bu , \quad (42)$$

$$z = Cx + Du , \quad (43)$$

where $B = B_1 + AB_2$, $D = D_3 + CB_2$, $u = \Theta_c$ and $z = \Theta_s$. Matrices A , B , and C contain the dynamics of the plant, actuators, and sensors, respectively. Matrix D contains the direct coupling between sensors and actuators.

The cost function of each wavenumber can be minimized individually, because of the orthogonality between pairs of Fourier modes. From Eqs.(18,19), following the normal decomposition, the cost function in state-space form for wavenumber k is

$$\mathcal{J}(k) = \int_t^T (z'z + \gamma u'u) d\tau . \quad (44)$$

In Section 4, we allow z to be a vector but restrict u to a scalar quantity u .

3 Optimal Control Theory

In this section we describe the basic theory of the LQG control (Bryson and Ho, 1969), or, in modern terms, \mathcal{H}_2 control. A brief review will be given in a self-contained manner to provide the necessary governing equations for the closed-loop stability analysis.

The LQG problem is formulated as a stochastic optimal control problem described by equations

$$\dot{\mathbf{x}} = \mathbf{A}\mathbf{x} + \mathbf{B}\mathbf{u} + \mathbf{\Gamma}\mathbf{w} , \quad (45)$$

$$\mathbf{z} = \mathbf{C}\mathbf{x} + \mathbf{D}\mathbf{u} + \mathbf{v} , \quad (46)$$

where $\mathbf{\Gamma}$ is an input matrix, \mathbf{w} and \mathbf{v} are both white noise processes with zero means and auto-correlation functions

$$E[\mathbf{w}(t)\mathbf{w}'(\tau)] = \mathbf{W}\delta(t - \tau) , \quad E[\mathbf{v}(t)\mathbf{v}'(\tau)] = \mathbf{V}\delta(t - \tau) , \quad (47)$$

where $E[\cdot]$ is the expectation operator averaging over all underlying random variables and $\delta(t - \tau)$ is the delta function. Note that \mathbf{W} and \mathbf{V} , the power spectral densities, will be chosen here as design parameters to enhance system performance. In our case $\mathbf{\Gamma}$ will be taken as \mathbf{B} , implying that the disturbances, in a manner similar to the control, enter the system dynamics at the wall.

The LQG controller is determined by finding the control action $\mathbf{u}(Z_t)$, where $Z_t = \{z(\tau); 0 \leq \tau \leq t\}$ is the measurement history, which minimizes the cost criterion

$$J = \lim_{T \rightarrow \infty} \frac{1}{T - t} E \left[\int_t^T (\mathbf{x}'\mathbf{Q}\mathbf{x} + 2\mathbf{x}'\mathbf{N}\mathbf{u} + \mathbf{u}'\mathbf{R}\mathbf{u}) d\tau \right] \quad (48)$$

subject to the stochastic dynamic system model equations (45) and (46). The division by $(T - t)$ ensures that the cost criterion remains finite in the presence of uncertainties in the infinite-time problem ($T \rightarrow \infty$). Note Eq.(48) can include Eq.(44) where

$$J = \lim_{T \rightarrow \infty} \frac{1}{T - t} E[\mathcal{J}(k)] . \quad (49)$$

Note that even though the time interval is infinite, time response is still measured by the eigenvalues of the closed-loop system. We consider the infinite-time problem with a time-invariant dynamics system because the controller gains become constants. For \mathbf{Q} and \mathbf{N}

chosen to be consistent with the cost criterion Eq.(44) (see Eq.(62)), the cost criterion will remain positive definite (see Bryson and Ho (1969) for necessary and sufficient conditions for optimality with general Q and N).

By nesting the conditional expectation with respect to Z_t within the unconditional expectation of Eq.(48), i.e., $E[J(k)] = E[E[J(k)/Z_t]]$ where $E[\cdot/Z_t]$ denotes the expectation (\cdot) conditioned on Z_t , the cost criterion can be written as

$$J = \lim_{T \rightarrow \infty} \frac{1}{T-t} E \left[\int_t^T [\hat{x}' Q \hat{x} + 2\hat{x}' N u + u' R u + tr(P)] d\tau \right] . \quad (50)$$

where $\hat{x} = E[x/Z_t]$ is the conditional mean estimate of the state x . The term $tr(P)$ is the trace of the error variance matrix which naturally occurs as a result of taking the conditional expectation into the integrand of the cost criterion. This cost criterion is now minimized subject to the estimation equations discussed below. Note that P does not depend on the control (see Eq.(53) below) and therefore, does not enter into the optimization process.

The solution to the regulator problem (Bryson and Ho, 1969) is a compensator composed of a state reconstruction process, known here as a filter (in the no noise case it is known as an observer) in cascade with a controller (see Fig. 2(b)). The state estimate (conditional mean) is called the Kalman filter, and is governed by

$$\dot{\hat{x}} = A^* \hat{x} + B^* u + K_f \nu , \quad \nu = z - \hat{z} = C^*(x - \hat{x}) + v , \quad (51)$$

where the matrices with asterisk superscripts correspond to the nominal point (k^*, Ra^*) . The Kalman gain matrix K_f , constructed to trade the accuracy of the new measurements against the accuracy of the state propagated from the system dynamics, is given by

$$K_f = P C^{*'} V^{-1} , \quad (52)$$

where P is the error variance in the statistical problem. In the infinite-time stationary formulation, the error variance P is the solution to the algebraic Riccati equation (ARE),

$$A^*P + PA^{*'} + \Gamma W \Gamma' - PC^{*'}V^{-1}C^*P = 0. \quad (53)$$

If the system is (A^*, C^*) observable and (A^*, Γ) controllable, then P is positive definite. Under these assumptions, it can be shown that the difference between the internal state x and the estimated state \hat{x} , i.e., the error

$$e = x - \hat{x}, \quad (54)$$

goes to zero as time goes to infinity. In other words, the evolution equation

$$\dot{e} = A_f e + K_f \nu + \Gamma w, \quad (55)$$

is stable, i.e., all the eigenvalues of the matrix

$$A_f = A^* - K_f C^* \quad (56)$$

have negative real part.

Minimizing the infinite-time cost function J , Eq.(50) subject to Eq.(51) yields the following control law,

$$u = -K_c \hat{x}, \quad (57)$$

where

$$K_c = R^{-1}(B^{*'}S + N'), \quad (58)$$

and S is the solution of the algebraic Riccati equation (ARE)

$$A^{*'}S + SA^* + Q - (SB^* + N)R^{-1}(B^{*'}S + N') = 0. \quad (59)$$

It should be remarked that the control gain matrix K_c is determined from functions only of the known dynamic coefficients (A^*, B^*) and weightings in the cost criterion (Q, R) , and

not the statistics of the input (V, W) . Consequently, K_c is determined from a performance index as (48), independent of the stochastic inputs. If (A^*, B^*) is controllable and $(A^*, Q^{1/2})$ observable, then the loop coefficient matrix

$$A_c = A^* - K_c B^* \quad (60)$$

is stable. The controllable and observable conditions can be weakened to stabilizable and detectable (Kwakernaak and Sivan, 1972).

When we combine the estimator and the regulator together, the dynamic system composed of the controlled process and filter becomes

$$\begin{pmatrix} \dot{e} \\ \dot{\hat{x}} \end{pmatrix} = \begin{bmatrix} A_f & 0 \\ K_f C^* & A_c \end{bmatrix} \begin{pmatrix} e \\ \hat{x} \end{pmatrix} + \begin{pmatrix} K_f v + \Gamma w \\ K_f v \end{pmatrix}. \quad (61)$$

Note that any choice of two between e , \hat{x} and x produce the same dynamics because they are algebraically related by Eq.(54). Under the above controllability and observability assumptions, A_f and A_c have only stable eigenvalues if optimal gains K_f and K_c of Eqs. (56,60) are used. Other schemes such as \mathcal{H}_∞ could be proposed (Rhee and Speyer, 1991), but from experience these schemes seem to produce only secondary modifications in the system performance over our LQG controller.

The infinite-time stationary formulation will be used in our study. The LQG control loop is shown in the block diagram of Fig. 2(b). Note that the cost function (44) can be expressed in the standard form (48), if we let

$$Q = C^{*'} C^*, \quad N = C^{*'} D^*, \quad R = (\gamma + D^{*'} D^*). \quad (62)$$

Since the power spectral density is not known, for simplicity of the design we consider V and W to be of the form $V = \alpha I$ and $W = \beta I$ where α and β are scalar and I is a unity matrix. Only the ratio of α with β is important.

The process noise spectral density β and the weighting γ in the cost function are considered design parameters. The case where $\gamma \rightarrow 0$ corresponds to unlimited control authority of the full-state feedback controller. The choice $\Gamma = B^*$ allows for loop-transfer recovery (Doyle and Stein, 1979). Loop-transfer recovery of the LQG controller to full-state feedback guarantees that robust performance occurs when the process noise goes to infinity, i.e., $\beta \rightarrow \infty$, provided there exists no nonminimal-phase zero in the plant. In our case, there are nonminimal-phase zeros, but a partial recovery is still shown to be possible (Turan et al. 1994).

As we have noted in Section 2, the analysis will be based on a single normal-mode model because the normal modes decouple. Although only one controller is needed at (Ra^*, k^*) , it is implemented **for different k^* over a range of wavenumbers**. The design point is determined so that when the controller is implemented, no unstable region appears below the neutral curve. Although the plant has multiple outputs, the system can be analyzed in terms of robustness as a single-input/single-output (SISO) system by breaking the loop at the plant input (see Fig. 2(b)). We denote the output u of the controller with u_o and the input u to the plant with u_i . The open-loop system of equations formed by breaking the loop at the input to the plant is

$$\dot{x}_a = A_a x_a + B_a u_i, \quad u_o = C_a x_a + D_a u_i \quad (63)$$

where the augmented state composed of the plant and compensator in cascade is $x_a = [x', \hat{x}]'$.

The coefficient matrices are given by

$$A_a = \begin{bmatrix} A & 0 \\ K_f C & (A^* - B^* K_c - K_f C^* + K_f D^* K_c) \end{bmatrix}, \quad B_a = \begin{bmatrix} B \\ K_f D \end{bmatrix}, \quad (64)$$

$$C_a = [0, -K_c], \quad D_a = 0.$$

The evolution equation for the closed-loop feedback system is

$$\begin{pmatrix} \dot{\mathbf{x}} \\ \dot{\hat{\mathbf{x}}} \end{pmatrix} = \begin{bmatrix} \mathbf{A} & -\mathbf{K}\mathbf{B}\mathbf{K}_c \\ \mathbf{K}_f\mathbf{C} & (\mathbf{A}^* - \mathbf{K}_f\mathbf{C}^* - \mathbf{B}^*\mathbf{K}_c + \mathbf{K}_f(\mathbf{D}^* - \mathbf{K}\mathbf{D})\mathbf{K}_c) \end{bmatrix} \begin{pmatrix} \mathbf{x} \\ \hat{\mathbf{x}} \end{pmatrix} \quad (65)$$

where $u_i = \mathbf{K}u_0$. In the above equation, matrices with an asterisk superscript correspond to the design parameters k^* and Ra^* . Note that in the particular case when the plant operates at nominal design condition, i.e, $k = k^*$, $Ra = Ra^*$ and $K = 1$, the closed-loop poles will correspond to the ensemble of eigenvalues of \mathbf{A}_f and of \mathbf{A}_c . In other words, Eq. (65) reduces to Eq.(61) and the filter poles and regulator poles decouple. One can show this from the following transformation,

$$\begin{pmatrix} \mathbf{x} \\ \hat{\mathbf{x}} \end{pmatrix} = \begin{bmatrix} \mathbf{I} & \mathbf{I} \\ \mathbf{0} & \mathbf{I} \end{bmatrix} \begin{pmatrix} \mathbf{e} \\ \hat{\mathbf{x}} \end{pmatrix} \quad (66)$$

where \mathbf{I} is an identity matrix.

In general, the plant does not operate at the nominal design condition. Consequently, there is a mismatch between the parameters (k^*, Ra^*) used to design the controller and the operating parameters (k, Ra) . Our analysis uses two methods to characterize the robustness of the stabilized system: neutral curves and gain and phase margins. In the first method, we select the nominal points (k^*, Ra^*) and construct the region of stability of the dynamics system (65) as Ra and k vary with $K = 1$. The boundary of this region is where the real part of the least stable closed-loop pole of Eq.(65) becomes zero. This boundary curve in the $k - Ra$ plane is called the neutral curve. We identify the minimum of Ra with respect to wavenumber on the neutral curve, so that the range of Ra from zero to this minimum, along with the whole range of wavenumber is stable. By robustness we mean constructing the largest range of Ra from zero up to this minimum.

The second method used to estimate robustness is the classical gain and phase margins approach. This approach allows us to characterize robustness with respect to more general

uncertainties, such as unmodelled dynamics. To obtain the gain and phase margins, we consider an error model $K = |K|e^{i\phi}$ (see Fig. 2(b)), with the plant operating at the nominal parameters $k = k^*$ and $Ra = Ra^*$. The shift of $|K|$ and ϕ from these nominal values ($|K| = 1$, $\phi = 0$) to where the system becomes unstable are essentially the gain and phase margins, respectively. Their values can be determined from accompanying Nyquist plots. The gain and phase margins are defined explicitly in Section 4.2.1 where these values indicate the amount of gain and phase change that the system can tolerate due to uncertainties in the system dynamics.

4 Results

In this paper, we consider the condition of $Pr = 7$ which enables us to compare our numerical results with those of Tang and Bau (1994, 1998b) and Howle (1997a). In their experiments, however, Howle (1997b, 1997c) used a high- Pr fluid ($Pr \approx 200$) whereas in Tang and Bau (1998a) the Pr value of their testing fluid was not given. It should be noted that while the stability properties in the uncontrolled case is independent of Pr , they are Pr dependent in the controlled case.

Our numerical results have been obtained using $N_z = 26$ (see Section 2.4) which appears to be adequate for our stability analysis. For example, consider the closed-loop eigenvalue problem of Eq. (65) with controller design values $Ra^* = 14.8Ra_{c0}$ and $k^* = 3.15$ and the system evaluated at $k = 5.5$ and $Ra = 14.52$ which lies on the neutral curve (see Fig. 8(d)), the norm of eigenvector (square root of the mean-square sum of entries) of the neutral eigenvalue of the coefficient matrix of Eq.(65) appears well converged. When $N_z = 26$ is increased to 52, this norm changes only by less than 0.7%.

4.1 Proportional Feedback Control

For convection in a layer of fluid bounded by rigid walls with prescribed temperatures, it is well known that the critical Rayleigh number $Ra_{c0} = 1707.76$ occurs at wavenumber $k_{c0} = 3.117$ (Chandrasekhar, 1961). Instead, when heat flux is prescribed at the lower wall, the critical value $Ra_{c0} \approx 1295.78$ occurs at $k_c = 2.552$.

In the case of proportional feedback control, the control law is $u = -K_p z$, where K_p is a constant proportional gain. We consider the planar sensor model to illustrate the effects of feedback control upon stability, and the results are shown in Fig. 3(a). In this figure three neutral curves are shown, each curve consists of a heavy and a thin solid line, representing a monotonic mode and an oscillatory mode of convection, respectively. The oscillatory mode corresponds to a complex conjugate pair of eigenvalues. The three curves correspond to three sensor locations: $z_s = 0$ at the mid-plane and $z_s = \pm 0.1$. The offset with respect to the mid-plane is 10% of the thickness of the fluid layer and gives a substantial shift in stability properties. The unstable and stable regions are separated by a neutral curve and are identified by the letters "U" and "S", respectively. In each case the maximum Ra achievable corresponds to the crossing point, between the heavy and thin line.

For $z_s = 0.0$, the monotonic mode is the lowest even mode of convection since the first odd mode is unobservable. In fact, in this case the sensor plane coincides with the node of the first odd mode. As K_p increases beyond the crossing point the critical Ra decreases. With this in mind, a pole-zero map and a root locus diagram are helpful to understand the stability behavior. Figure 3(b) shows the open loop poles (\times) and zeros (\circ) and Fig. 3(c) the corresponding root locus diagram. For a given Ra , as K_p increases from zero the unstable pole moves to the left while a stable pole moves to the right. Subsequently, the two poles coalesce. After coalescence a pair of complex conjugate poles (corresponding to the oscillatory

mode) break off the real axis. The break-away point (where the coalescence occurs) moves to the right as Ra increases. The crossing point in Fig. 3(a) corresponds to the coalescence at the origin in Fig. 3(c). As Ra increases and keeping K_p constant, the closed loop poles move to the right.

From the root locus of Fig. 3(c), the results of Fig. 3(a) can be interpreted as follows. For Ra above the crossing point, the system is unstable for any gain K_p . For Ra below the crossing point, there exists a finite range of gain K_p in which the system is stable. The lower end point of the range corresponds to the minimal value of K_p required in order to move the monotonic pole to left-half s -plane. The upper end point of the range corresponds to the maximal value of K_p that can be used before the pair of complex conjugate modes become unstable.

The stability diagram for the shadowgraph sensor model can be found in Howle's paper (1997a). In this case there are no unstable complex conjugate modes. As K_p increases to ∞ , the critical Ra increases monotonically to about 3.13 times Ra_{c0} .

4.2 LQG (\mathcal{H}_2) Control

The limitation in the performance of proportional feedback control provides the motivation for developing LQG controllers. We will apply the LQG synthesis method to both planar sensor and shadowgraph sensor models. We first seek to reduce the number of design parameters in our analysis. For a given set of physical parameters we examine the closed-loop eigenvalues and observe that for a stable system the real part of the least stable eigenvalue has its largest magnitude when $\gamma \rightarrow 0$ and $\beta \rightarrow \infty$. Since the observed improvements become less significant for $\gamma < 0.1$ and $\beta > 100$, we let $\gamma = 0.1$ and $\beta = 100$.

4.2.1 Planar Sensor Model

(i) One-Sensor Control

The one-sensor model is especially convenient for understanding the closed-loop stability properties of the system. Once the qualitative properties of this case are understood, the performance of the controller will be improved by adding additional sensors.

Figures 4(a)-4(f) show the neutral stability diagram in the (k, Ra) plane for a controller designed at the nominal values k^* and Ra^* . The nominal point (k^*, Ra^*) is indicated by a solid circle in the figures. The thin line and heavy line curves correspond to the neutrally stable oscillatory and monotonic modes, respectively. In Figs. 4(a)-4(b) the sensor plane is located at $z_s = 0.15$. We use a larger sensor displacement with respect to the mid-plane than the one used for the proportional feedback control to dramatize the effect on the neutral curve. Figure 4(a) shows the neutral curves for a controller designed at nominal point $Ra^* = 5Ra_{c0}$ and $k^* = 5.3$. The neutral curves have two minima, and the value $k^* = 5.3$ has been chosen to make the minima nearly the same. The controller stabilizes the system for any $Ra < Ra^*$. To characterize the stability of the controlled system with respect to Ra^* , we re-design the controller for $Ra^* = 6Ra_{c0}$ while maintaining k^* fixed. Figure 4(b) shows a dramatic change in the neutral curve, the banana-shaped branch moves downward giving rise to an unstable region below Ra^* .

To further characterize the stability of the controlled system with respect to the location of the sensor, we move the sensor plane at $z_s = -0.15$. We design a controller for $k^* = 5.3$, as before, and $Ra^* = 5Ra_{c0}$ (Fig. 4(c)) and $Ra^* = 7Ra_{c0}$ (Fig. 4(d)). Figures 4(c)-4(d) show similar stability characteristics as those in Figs. 4(a)-4(b). However, the two branches of the neutral stability curves switch role. The left branch now represents the monotonic onset while the right branch represents the oscillatory onset.

The role switch in relation to the location of the sensor plane deserves a closer examination. We consider a smaller perturbation of the sensor location with respect to the mid-plane. Figure 4(e) shows the stability limits for three very close sensor locations. At $z_s = 0.000$ (solid lines), the neutral curve is composed of an oscillatory segment on the left and a monotonic segment on the right. At $z_s = 0.005$ (dashed-dotted lines), the monotonic segment of the neutral curve retreats rightward while the oscillatory segment predominates the range. At $z_s = -0.005$ (dashed lines), the opposite effect occurs, the oscillatory segment of the neutral curve retreats to the left. These results are consistent with the results presented in Figs. 4(a)-4(d). Since significant distortions and shifts of the stability limits have occurred within a very small perturbation of z_s , sensitivity to sensor location becomes an important factor for the practical implementation of the sensors. As subsequent results will show, this type of sensitivity is no longer present if three sensors are incorporated.

In order to show that the lower unstable region will become much larger with further increase of Ra^* , we design a controller at the nominal values $Ra^* = 10Ra_{c0}$ and $k^* = 5.3$ and place the sensor plane at $z_s = 0.15$ for an illustration. Fig. 4(f) shows a thin island of stability in the unstable region. This stable region is bounded by two neutral curves which coalesce on the right and intersect on the left. Figures 4(a)-4(f) reveal the occurrence of an unstable region at $Ra < Ra^*$ which severely restricts the achievable degree of stabilization.

The results of proportional feedback control has demonstrated the significance of the sensor location at $z_s = 0$. This location gives the maximum range of stabilization even for the LQG controller. We observe that Ra^* can be raised to $10Ra_{c0}$ at properly chosen values of k^* (see Figs. 5(a)-5(c)) without inducing a large lower unstable region, if the sensor is placed at the mid-plane. At this Ra^* , the system is stable up to the critical Ra of the first odd mode ($Ra_c \approx 10.31Ra_{c0}$ and $k_c = 5.36$, see Chandrasekhar, 1961), since the first odd mode

is not stabilizable because it is unobservable. Hence, there is no reason to place Ra^* above $10.31Ra_{c0}$. Below this value, however, the critical point of the neutral curve lies to the right of the nominal point if k^* is sufficiently small, or to the left of the nominal point if k^* is sufficiently large. For this case, we can use two nominal points to lift the overall neutral curve to coincide with the neutral curve of the first odd mode.

Consider $Ra^* = 10Ra_{c0}$, just below the Ra_c of the first odd mode. We choose the two nominal k^* on both sides of $k_c = 5.36$. The values at $k^* = 4$ and 6 (marked by solid circles) produce small dips in the unstable region and are reasonable to be used as nominal points. Figures 5(a)-5(c) illustrate how the stability limit is determined by the principle of superposition. The nominal point at $k^* = 4$ in Fig. 5(a) corresponds to unstable region delimited by the heavy solid lines which has a minimum $Ra \approx 8.4Ra_{c0}$. For $k < 5.9$, the stability limit corresponds to the neutral curve of the first odd mode. Similarly, in Fig. 5(b) the second nominal point at $k^* = 6$ corresponds to the an unstable region delimited by the thin and heavy solid lines which has a minimum at about $9.5Ra_{c0}$. The thin line curve corresponds to an oscillatory onset. The solid line curve coincides with a segment of the neutral curve of the odd mode. If both nominal points are used for the controllers, then the overall stability limit coincide with the neutral curve of the first odd mode upon superposition. The controllers designed at the first nominal point $k^* = 4$ operate over the band $0 < k < k_c \approx 5.36$, while the controller designed at $k^* = 6$ operates over the wavenumbers greater than k_c .

The result shows that the degree of stabilization is significantly higher than that achievable with the proportional control. Unfortunately, the one-sensor design is not sufficiently robust with respect to the location of the sensor plane. This problem is significant because a perfect sensor placement is not achievable in practice. To demonstrate the sensitivity, in Fig. 6(a) we consider a planar sensor at $z_{s1} = 0.01$, i.e., slightly off with respect to the mid-plane, and

re-design the controller for $Ra^* = 10Ra_{c0}$ and $k^* = 4$. Fig. 6(a) shows the presence of a thin stable region in the middle of the unstable region. This stable region is bounded from above by a neutral curve of an oscillatory mode (thin line) and below by a neutral curve of a monotonic mode (heavy solid line). The stable region exists for $k < 3$. As k increases it becomes a very narrow strip which eventually terminates at $k \approx 7.1$, similar to the behavior in Fig. 4(f). For comparison the neutral curve for the $z_s = 0$ case (thin dashed line) is also included in Fig. 6(a). Comparing Fig 6(a) to Fig. 5(c), we see a dramatic difference in stability properties due to a small shift of sensor location of 0.01. Fortunately, this sensitivity can be significantly reduced by introducing a second sensor located close to the mid-plane. Figure 6(b) shows the stability diagram when a second sensor included. This case will be discussed in the next subsection.

To characterize the robustness of the controlled system with respect to plant uncertainties we compute gain and phase margins at $Ra = Ra^*$ and $k = k^*$. In all the cases considered, the open-loop system has one unstable pole so that for closed-loop stability the Nyquist locus encircles (counter-clockwise) the point $(-1,0)$ once. Because of this property, in general there exists an upper and lower value to each gain and phase margin. The upper and lower gain margins are designed to measure how much the gain K can be decreased, or increased, before the system becomes unstable (Fig 2(b)). Likewise, the upper and lower phase margins are designed to measure how much the phase can be decreased, or increased, before the system becomes unstable. Accordingly, the lower and upper gain margins are defined as $20 \log_{10}(1/X_1)$ (dB) and $20 \log_{10}(X_2)$ (dB), respectively, where X_1 ($|X_1| < 1$) and X_2 ($|X_2| > 1$) are the smaller and larger x -distances of the two crossing points of the Nyquist locus with the x -axis. Since the angle is measured positive in counterclockwise direction, the lower phase margin is defined as $180 - \sin^{-1}(Y_1)$ degrees and the upper phase margin is defined

as $\sin^{-1}(Y_2) - 180$ degrees, where Y_1 (positive) and Y_2 (negative) are, respectively, the y-coordinates of the intersecting points between the Nyquist locus and the unit circle centered at origin.

For the one-sensor model, the gain and phase margins are too small. At $Ra = Ra^* = 10Ra_{c0}$, for example, the margins are typically about 0.5 dB and 4° . In engineering applications, margins below 3 dB and 10° are often considered marginal. Therefore, we conclude that as the system is stabilized for higher values of Ra , the magnitude of the gain increases, increasing the sensitivity, as indicated by the very small gain and phase margins. Sensitivity can be reduced by implementing multiple sensors, as indicated by the improved gain and phase margins (see next subsections).

(ii) Two-Sensor Control

To eliminate the lower unstable region shown in Fig. 6(a), we place two sensors on opposite sides of the mid-plane at $z_s = \pm 0.01$. It is crucial that both sensors are close to the mid-plane. Placement of one sensor or both away from the mid-plane will give rise to a lower unstable region.

In the two-sensor model we re-design the controller at the nominal condition used for the case shown in Fig. 6(a). The two-sensor model result is shown in Fig. 6(b), in which the same dashed curve as in Fig. 6(a) is included for comparison. We observe that the lower unstable region has disappeared. The neutral curve of the monotonic mode (heavy solid line) terminates at $k \approx 7.3$. Beyond this wavenumber the neutral curve of an oscillatory mode replaces the stability limit (thin solid line). If we allow z_s to tend to zero, then the solid curve in Fig. 6(b) will approach the dashed curve. The gap between the two curves indicates there is a trade-off between the large pole shifts due to the small sensor-plane offset, and the information gained

by adding one more sensor near to the mid-plane. The gain and phase margins increase by roughly 10% to 20% by adding the second sensor. However, the improvements are still too small to be considered acceptable.

Better gain and phase margins (over 100% increase) can be obtained with sensors placed further away from the mid-plane. The sensors located at about $z_s = \pm 0.25$ appear to give the best result. However, in this case a lower unstable region forms. The two-sensor model is still not suited for practical implementation. For this reason, we shall not devote more effort on analyzing this case. Instead, we proceed to the three-sensor model.

(iii) Three-Sensor Control

When three sensors are used, we can improve gain and phase margins by placing two outer sensors further away from the mid-plane without inducing any lower unstable region, provided that the remaining sensor is placed at the mid-plane. With two sensors placed significantly away from the mid-plane, it is observed that the sensor located at the mid-plane is no longer sensitive to a small offset. To determine the best sensor locations, we first observe that a lower unstable region always occurs when no sensor is placed at or very close to the mid-plane. With a mid-plane sensor in place, then by fixing one outer sensor and moving the other, it appears that the best locations are when the two outer sensors are at equal distance from the mid-plane. The best locations are determined in terms of the minimum of the real part of the least stable closed-loop pole. Hence, for our design, we let the three sensor locations be: $z_s^{(1)} = -z_s$, $z_s^{(2)} = 0$ and $z_s^{(3)} = z_s$.

In order to improve gain and phase margins, we consider the Nyquist plots for various values of z_s . In the subsequent results concerning the stability limit of the controlled system (see Fig. 8), a good nominal condition is found to be $k^* = 3.15$ and $Ra^* = 14.8$. For this

nominal condition, Fig. 7(a) shows the Nyquist curves for $z_s = 0.1$ (dotted), 0.2 (dashed) and 0.3 (solid). Figure 7(b) provides a magnified view of Fig. 7(a) near the point $(-1,0)$. The case $z_s = 0.3$ presents no lower phase margin but has an upper phase margin of about 20.5° . The upper and lower gain margins are about 3.3dB and 4.4dB, respectively. These values of gain and phase margins are quite satisfactory. A slight improvement of the margins is still possible by increasing z_s further, at the expense of increasing the real part of the least stable pole closer to zero, thus making the system less stable. Thus, $z_s = 0.3$ appears to be our best choice. It is desirable to see how changing the values of k^* and Ra^* will affect the gain and phase margins for $z_s = 0.3$. In Fig. 7(c) we compare the Nyquist curves for three different nominal conditions: $k^* = 3.15$ and $Ra^* = 14.8Ra_{c0}$ (solid), $k^* = 4.5$ and $Ra^* = 12.5Ra_{c0}$ (dashed) and $k^* = 6.5$ and $Ra^* = 15Ra_{c0}$ (dotted). This choice of nominal points is based on the subsequent analysis of the stability limit of the controlled system. As shown in the magnified view of Fig. 7(d), the upper phase margin and the upper and lower gain margins for the three nominal conditions are quite close, suggesting that these margins are not sensitive to the values of k^* and Ra^* . However, the lower phase margin decreases rapidly as k^* and Ra^* increase, as shown in the dotted line. The gain and phase margins for the design case (solid) are within values used in practice.

Now, we consider the stability limit of the controlled system. In order to understand how the choice of the nominal condition (k^*, Ra^*) affects stability, we present the results for each set of nominal condition in Figs. 8(a)-8(c). For each nominal point the stable region is delimited by the neutral curve. Our goal is to maximize the minimum of the neutral curve by appropriately choosing the nominal point. In Fig. 8(a) we consider $k^* = 3$ and $Ra^* = 15Ra_{c0}$. There is no unstable region to the left of this nominal point and the neutral curve to its right corresponds to an oscillatory mode. The neutral curve in Fig. 8(b) corresponds to $k^* = 4.5$

and $Ra^* = 12.5Ra_{c0}$. An unstable banana-shaped region (monotonic onset) is present on each side of the main unstable region. The minimum of the main unstable region is about $Ra \approx 14.5Ra_{c0}$. We have decreased Ra^* from $15Ra_{c0}$ to $12.5Ra_{c0}$ because at $Ra^* = 15Ra_{c0}$ (not shown) the two banana-shaped unstable regions have merged generating a vast lower unstable region. However, because of the formation of an unstable region on each side, this nominal point is not desirable. Figure 8(c) shows the neutral curve for the system controlled by controllers designed at nominal condition $k^* = 6.5$ and $Ra^* = 15Ra_{c0}$. The banana-shaped region on the left of the nominal point has disappeared, but the region on the right remains.

By considering additional nominal points to the right of the first nominal point it seems that there is no significant improvement in stability. In other words, when the nominal wavenumber k^* is larger than a certain value, the controllers become ineffective in stabilizing the entire region up to $Ra = Ra^*$, even though better local stabilization is always possible. Based on the results of Figs. 8(a)-8(c), it appears that nominal points to the right of the first point does not improve the situation. In fact, we have tried more cases involving different locations of the nominal points, but none seems to raise the minimum Ra of the unstable region. To achieve a maximum Ra for the stable range, we fine-tune the first nominal point and obtain $k^* = 3.15$ and $Ra^* = 14.8Ra_{c0}$. For this point the stability diagram is shown in Fig. 8(d). Stabilization up to $Ra \approx 14.5Ra_{c0}$ is achievable by using controllers designed at only one nominal point. The neutral curve is formed by an oscillatory mode (thin solid line) and a monotonic mode (heavy solid line). To illustrate the degree of stabilization with respect to the uncontrolled system, we include in the figure the neutral curve (dashed line) for the uncontrolled convection. Without feedback control, the region above the dashed curve is unstable to convection. Below the solid curves, however, the region is stabilized by the LQG control.

In Section 2, we described that in the practical implementation a controller is responsible for stabilizing an unstable normal mode whose wavenumber is indicated by a point on the k -axis in Fig. 8(d). Results suggest that we can use the design condition $k^* = 3.15$ and $Ra^* = 14.8Ra_{c0}$ for all controllers. Coincidentally, we note that the design wavenumber, $k^* \approx 3.15$, is quite close to the critical wavenumber of the uncontrolled convection, $k_{c0} \approx 3.12$.

We conclude the analysis of the planar sensor model by discussing the time response of the closed-loop system. Our design condition is at $k^* = 3.15$ and $Ra^* = 14.8Ra_{c0}$. For high operating values of Ra , if we turn on the controller at this design condition with no initialization of the estimator, the transient response of the controlled system induces a large actuator signal $u(t)$, which will produce actuator saturation in practical applications. Therefore, in practical applications, the operating Ra value should be achieved in increments of Ra , so that for each increment the estimator remains initialized. For example, consider a controller operating at $k = k_c \approx 5.5$. Assume that we have increased the operating Ra value gradually up to $Ra = 12Ra_{c0}$ so that the closed-loop system remains at the no-motion equilibrium. When approaching equilibrium, both the plant internal states and the estimator states tend to zero. As an example, we increase Ra from $Ra = 12Ra_{c0}$ by an increment of $2Ra_{c0}$ to the operating value $Ra = 14Ra_{c0}$. Figure 9 shows the transient time responses for this case. In particular, Fig. 9(a) shows the temperatures measured by the planar sensors as functions of time, while Fig. 9(b) shows the control action signal $u(t)$. The initial transient disappears and the system settles to a new no-motion equilibrium. If we use a smaller increment than $2Ra_{c0}$, an even better result can be expected in terms of smaller overshoot and a faster approach to equilibrium.

It is important to consider the parameters in a physical set up to see if the LQG controller can be applied to an experiment. We note that t is in the unit of diffusive time unit, d^2/κ .

For example, in the case of a layer of water of thickness of $d = 0.8$ cm, this unit is about 438 seconds. A mildly supercritical condition $Ra \approx 1800$ corresponds to $\Delta T^* = 0.14^\circ\text{C}$, while for $Ra = 14Ra_{c0}$, the basic temperature difference is about 1.86°C . Thus, the physical quantities are reasonably easy to achieve in practice.

Comparison between the stability achievable by the proportional feedback control (Tang and Bau, 1993, 1994 as well as our Fig. 3(a)) and the LQG control is possible only from a qualitative point of view. The neutral curve structure using the LQG control law system appears to be more complex, possibly due to the additional filter modes. An additional important difference is worth noting: For proportional feedback beyond a certain value of Ra , there is no stable region regardless of the gain K_p . The unstable mode can be either monotonic or oscillatory. For the LQG control, the unstable regions can occur above and below the design value Ra^* . A local stable region about Ra^* can always be maintained. In fact, an even higher stable value of Ra than $14.8Ra_{c0}$ can be achieved by gradually increasing the temperature gradient across the fluid layer.

4.2.2 Shadowgraph Sensor Model

We now turn to the shadowgraph sensor model. The maximum Ra achievable over the stable range for the proportional feedback control is about $3.13Ra_{c0}$. We attempt to increase the stable region using the LQG method. However, for this sensor model our results indicate a significantly weaker stabilization. We have first designed a controller for $Ra^* \approx 10Ra_{c0}$ but encountered a vast lower unstable region. The second convection mode, which is closest to the imaginary axis, is destabilized in the control process. As a result, we gradually decreased the nominal condition Ra^* , down to a value of $5Ra_{c0}$. The drop in performance in the critical

Rayleigh number with respect to the planar sensor model is probably due to the nature of the shadowgraph sensor, which only measures the averaged temperature of the fluid layer. Figure 10(a) shows the stability diagram when controllers designed at five nominal points are used. The nominal points have same Ra^* while k^* increases by a factor $\Delta k^* = 1$. The results show that, except for the first nominal point ($k^* = 1$), each nominal point is enclosed by a left and a right stability limit (thin line for oscillatory mode and heavy line for monotonic mode). The stable range of wavenumbers associated with each nominal point is typically small. Figure 10(a) reveals two depressed unstable regions that reach below $Ra = Ra^*$ (near $k = 2.4$ and $k = 3.4$). To demonstrate how these dips can be removed, we add two more nominal points, one is chosen at $k^* = 2.4$ and the other at $k^* = 3.3$, both with a slightly higher $Ra^* = 5.4Ra_{c0}$. The improved result is shown in Fig. 10(b), which indicates that the minimum Ra of the unstable region is now above $5Ra_{c0}$.

Unlike the planar sensor model, the minimum Ra of the neutral curve obtained by applying a controller designed at a single nominal point over the whole wavenumber range is not that much higher than the value obtained using proportional feedback control. There may be further improvements on the LQG controller to be made, but we will not attempt further design in this study.

5 Conclusion

We have investigated the LQG (\mathcal{H}_2) controller design for two sensor models (planar sensor model and shadowgraph sensor model) studied by previous authors (Tang and Bau, 1994; Howle, 1997a) using proportional controllers. **Based on our results for $Pr = 7$, we have shown that the robustness of the controlled system is improved in two aspects:** (i) the controller remains stable over a larger range of the parameter Ra , and (ii) the robustness of

the controller accommodates to a degree unmodelled dynamics and nonlinearities, as measured by gain and phase margins on the Nyquist diagram. It should be noted that although only one controller is needed to be designed at (k^*, Ra^*) , this controller is implemented at each wavenumber k to span over the entire range of unstable wavenumbers.

The number of sensors plays an important role in dramatically improving the robustness of the stabilization of the system operating at large Ra . Because multiple sensor planes can be easily incorporated into the planar sensor model, the performance of the planar sensor model is found to be superior to that of the shadowgraph sensor model, which only utilizes averaged temperature measurements. By using three planar sensors, it is possible to stabilize the no-motion state up to $Ra \approx 14.5Ra_{c0}$. The controller has 3 dB of gain margin and 20 degrees of phase margin at the design parameter values. Beyond this value of Ra , stabilization in the region near to a nominal point can still be achieved, but an unstable region forms for Ra below Ra^* . It should be noted that in our design procedure, we designed the controllers to span the whole range of unstable wavenumbers and at the same time demanded that the whole Ra range from zero up to $14.5Ra_{c0}$ be stable.

We have also shown that the transient responses incurred at the initial time can be reduced significantly by increasing Ra to its operating value in small increments. This technique allows us to initialize the estimator at each increment of Ra and consequently avoid controller saturations. Furthermore, by making incremental changes in Ra and using a controller designed to stabilize the system in a region about the design values, the value of the maximum value of Ra could be increased further, even though there will be unstable regions formed below stable regions in Ra .

So far, we have assumed that the order of the controller is equal to the order of the plant. In full numerical simulations and experiments, controller designs

based on reduced-order models are more practical for implementation (see, for example, Cortelezzi and Speyer, 1998, Armaou and Christofides, 2000). In our current model the actuation is assumed to be distributed continuously. In practice it will be discrete and implementation issues need to be addressed.

Acknowledgement

This research is supported by a grant from United States Air Force (Grant no. F49620-93-1-0332), and also by NASA Microgravity Physics Program (NAG3-1819) in the preliminary stage. We thank R.E. Kelly and R.T. M'Closkey for their encouragement and numerous stimulating discussions on the subject during the course of this study.

Figure Captions

Fig. 1: The geometric configuration.

Fig. 2: (a) Schematic for the physical implementation of the multi-wavenumber controller; (b) Block diagram of the control loop for a single wavenumber.

Fig. 3: (a) Neutral curves for the planar sensor model using the proportional feedback control. From bottom up, the three sets correspond to $z_s = -0.1, 0.0$ and 0.1 (heavy and thin lines indicate monotonic and oscillatory onset, respectively). (b) Pole-zero diagram of the plant for $k = 4.4$, $Ra = 3.5Ra_{c0}$ and (c) corresponding root loci for K_p varied between 0 and 2000.

Fig. 4: Stability diagrams for the planar sensor model with one sensor, using the LQG control. The nominal condition (k^*, Ra^*) is denoted by a solid circle. The heavy and thin lines correspond to the monotonic and oscillatory onsets, respectively. Panels 4(a)-4(b) and 4(f) are obtained for $z_s = 0.15$ and Panels 4(c)-4(d) for $z_s = -0.15$. All 4(a)-4(e) correspond to $Ra^* = 5Ra_{c0}$ and $k^* = 5.3$ but 4(f) corresponds to $Ra^* = 10Ra_{c0}$ and same k^* . Panel 4(e) shows the sensitivity about $z_s = 0.0$ with respect to z_s . Panel 4(f) shows a vast lower unstable region developed at a sufficiently high Ra^* .

Fig. 5: Stability diagrams for the planar sensor model with a single mid-plane sensor: (a) neutral curve for the nominal condition $k^* = 4$ and $Ra^* = 10Ra_{c0}$; (b) neutral curve for the nominal conditions $k^* = 6$ and $Ra^* = 10Ra_{c0}$; (c) the resulting neutral curve by incorporating the two sets of nominal conditions. This curve coincides with the neutral curve of the first odd mode of convection in the uncontrolled case.

Fig. 6: (a) Stability diagram for the one-sensor model with a small offset $z_s = 0.01$. Results show a vast lower unstable region below $Ra^* = 10Ra_{c0}$. The heavy (thin) solid line corresponds to a monotonic (oscillatory) onset. (b) Stability diagram for the two-sensor model, with a second sensor positioned at $z_s = -0.01$. As a result, the lower unstable region is eliminated.

Fig. 7: Nyquist plots for the three-sensor model: (a) Nyquist curves at nominal condition $k^* = 3.15$ and $Ra^* = 14.5Ra_{c0}$ and sensor locations are $z_s = 0.1$ (dashed), 0.2 (dotted) and 0.30 (solid); (b) magnified view of panel (a); (c) Nyquist curves for $z_s = 0.3$ and nominal conditions with $k^* = 3.15$ and $Ra^* = 14.5Ra_{c0}$ (solid), $k^* = 4.5$ and $Ra^* = 12.5Ra_{c0}$ (dashed) and $k^* = 6.5$ and $Ra^* = 15Ra_{c0}$ (dotted); (d) magnified view of panel (c).

Fig. 8: The stability diagrams for the three-sensor model with sensor planes located at $z_s = -0.3, 0.0$ and 0.3 , and nominal conditions at (a) $k^* = 3$ and $Ra^* = 15Ra_{c0}$, (b) $k^* = 4.5$ and $Ra^* = 12.5Ra_{c0}$, (c) $k^* = 6.5$ and $Ra^* = 15Ra_{c0}$. (d) $k^* = 3.15$ and $Ra^* = 14.8Ra_{c0}$ (the design conditions).

Fig. 9: The time response of (a) the three measurements and (b) the control action $u(t)$, in the three-sensor model with the nominal condition $k^* = 3.15$ and $Ra^* = 14.8Ra_{c0}$. The convection mode considered is at $Ra = 14Ra_{c0}$ and the least stable wavenumber about $k = 5.5$.

Fig. 10: (a) The stability diagram for the shadowgraph sensor model showing the stability limit corresponding to five equally spaced nominal points at $Ra^* = 5Ra_{c0}$; (b) An improved

design with two nominal points added. Stabilization for the entire range of wavenumbers up to $Ra^* = 5Ra_{c0}$ is achievable for this improved case.

References

- Armaou A. and Christofides, P.D., 2000 Feedback control of the Kuramoto-Sivashinsky equation, *Physica D*, **137**, 49-61.
- Bryson, A.E. and Y.C. Ho, 1969 *Applied Optimal Control*, Xerox, Waltham, Mass.
- Chandrasekhar, S., 1961 *Hydrodynamic and Hydromagnetic Stability*, Oxford Univ. Press.
- Cortelezzi, L. and Speyer, J.L., 1998 Robust reduced-order controller of laminar boundary layer transitions, *Phys. Rev. E*, **58**, 1906-1910.
- Cross, M.C. and Hohenberg, P.C., 1993 Pattern formation outside of equilibrium, *Rev. Mod. Phys.*, **65**, 851-1112.
- Doyle, J.C. and Stein, G., 1979 Robustness with observers, *IEEE Transactions on Automatic Control*, **AC-24**, 607-611.
- Gottlieb, D. and Orszag, S.A., 1981 *Numerical analysis of spectral methods: theory and applications*, SIAM, Philadelphia.
- Howle, L.E., 1997a Linear stability analysis of controlled Rayleigh-Bénard convection using shadowgraphic measurement, *Phys. Fluids*, **9**, 3111-3113.
- Howle, L.E., 1997b Control of Rayleigh-Bénard convection in a small aspect ratio container,

Int. J. Heat Mass Transfer, **40**, 817-822.

Howle, L.E., 1997c Active control of Rayleigh-Bénard convection, *Phy. Fluids*, **9**, 1861-1863.

Howle, L.E., 2000 The effect of boundary properties on controlled Rayleigh-Bénard convection, *J. Fluid Mech.*, **411**, 39-58.

Joshi, S.S., Speyer, J.L. and Kim, J., 1997 A systems theory approach to the feedback stabilization of infinitesimal and finite-amplitude disturbances in plane Poiseuille flow, *J. Fluid Mech.*, **332**, 157.

Joshi, S.S., Speyer, J.L. and Kim, J., 1999 Finite dimensional optimal control of Poiseuille flow, *J. Guidance, Control and Dynamics*, 1999, **22**, 340-348.

Kwakernaak, H. and Sivan, R., 1972 *Linear optimal control system*, John Wiley & Sons, Inc., 575 pp.

Rhee, I. and Speyer, J.L., A game theoretic approach to a finite-time disturbance attenuation problem, *IEEE Trans. Automat. Contr.*, **36**, 1021-1032.

Tang, J. and Bau, H.H., 1993 Stabilization of the no-motion state in Rayleigh-Bénard convection through the use of feedback control, *Phy. Rev. Letters*, **70**, 1795-1798.

Tang, J. and Bau, H.H., 1994 Stabilization of the no-motion state in the Rayleigh-Bénard

problem, *Proc. R. Soc. Lond. A*, **447**, 587-607.

Tang, J. and Bau, H.H., 1998a Experiments on the stabilization of the no-motion state of a fluid layer heated from below and cooled from above, *J. Fluid Mech.*, **363**, 153-171.

Tang, J. and Bau, H.H., 1998b Numerical investigation of the stabilization of the no-motion state of a fluid layer heated from below and cooled from above, *Phys. Fluids*, **10**, 1597.

Turan, L., Mingori, D.L. and Goodwin, G.C., 1994 Loop transfer recovery design using biased and unbiased controllers, *IEEE Trans. Automat. Contr.*, **39**, 601-605.

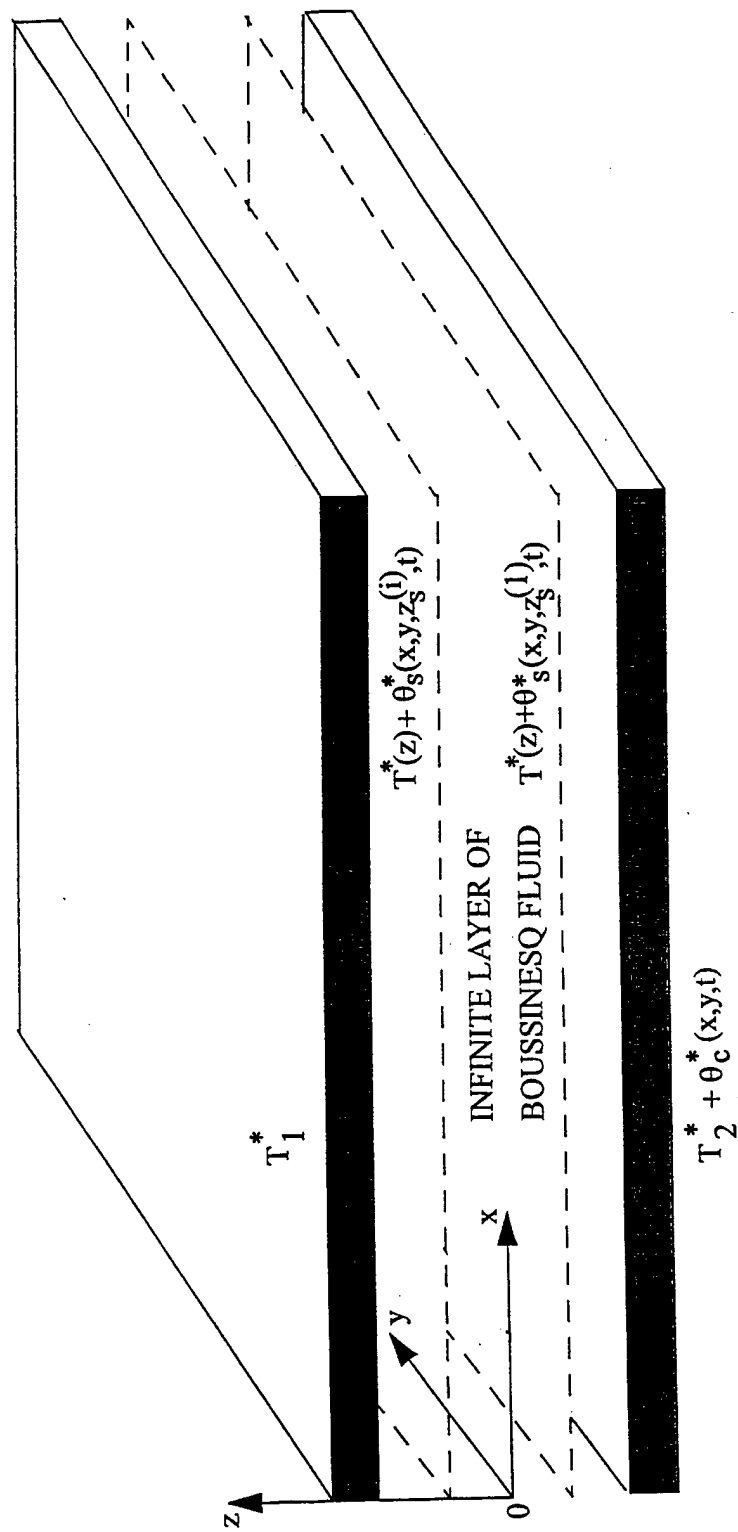
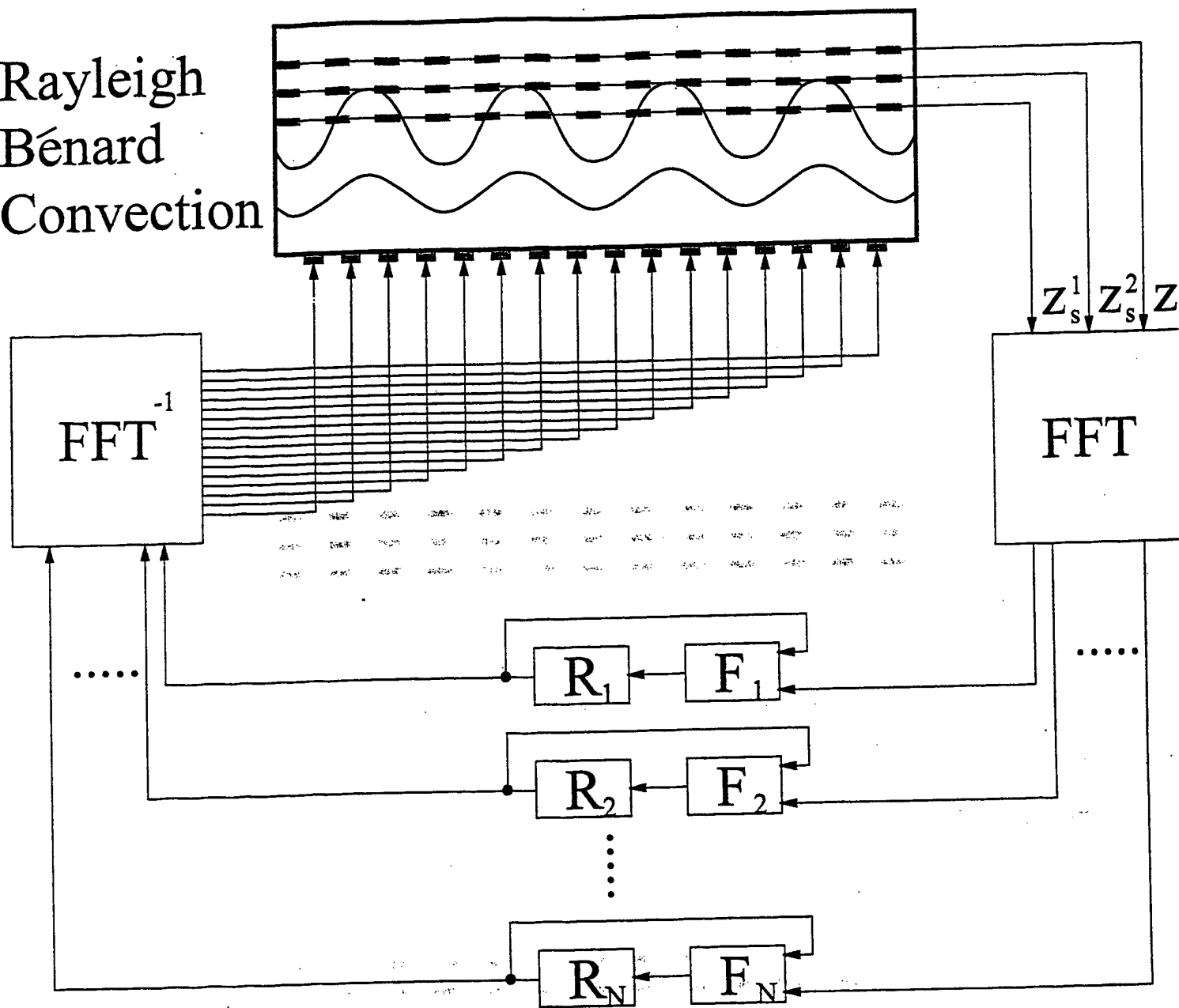


FIG. 1: PLANAR SENSOR MODEL

Rayleigh
Bénard
Convection



■ sensor

■ actuator

R_n regulator

F_n filter

FFT fast fourier transform

Figure 2(a)

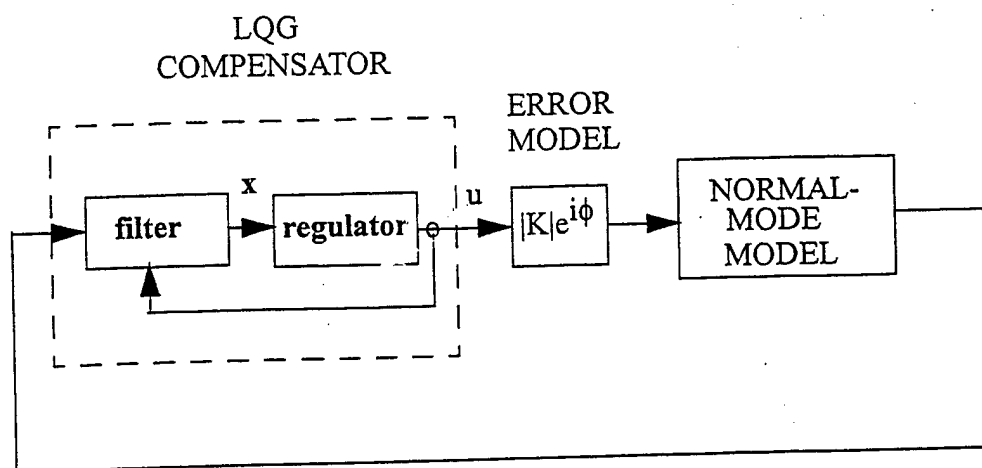


FIG. 2(b): Control Loop For a Single Wavenumber. $K=1$ Gives the LQG Control Loop.

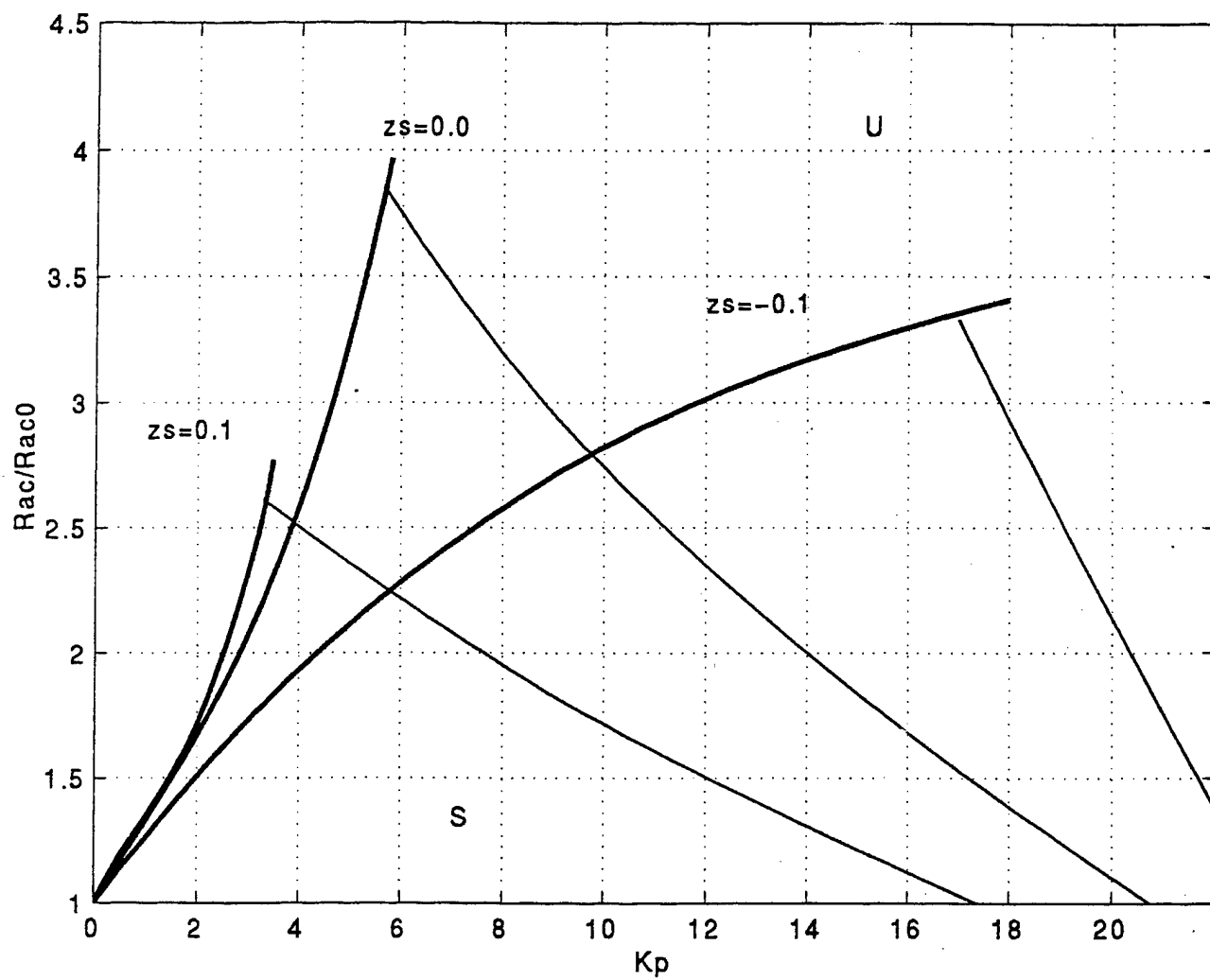
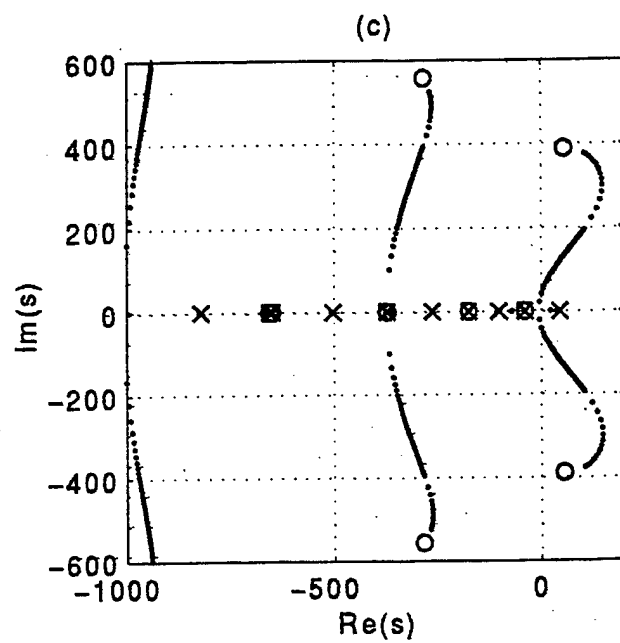
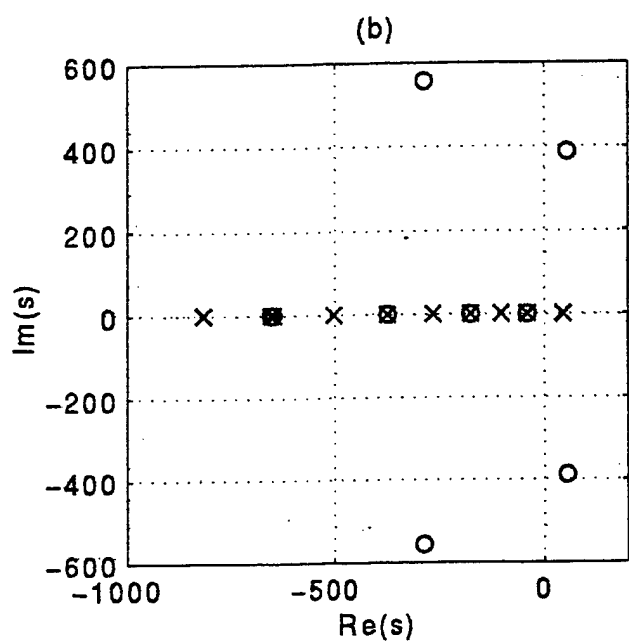
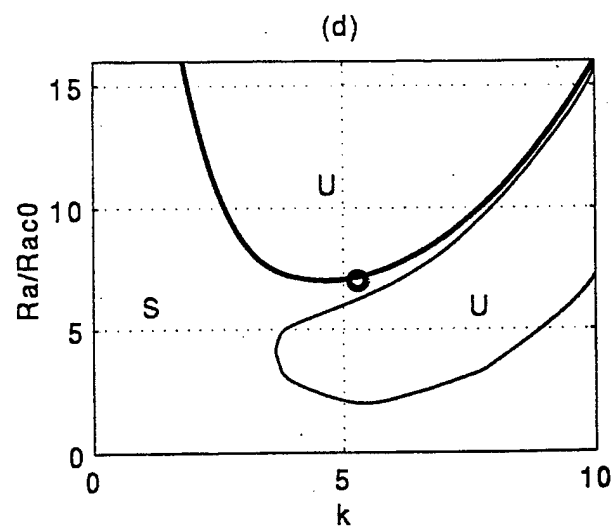
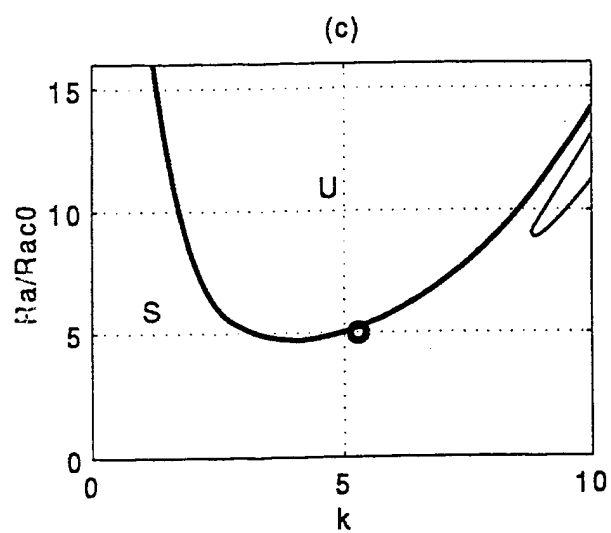
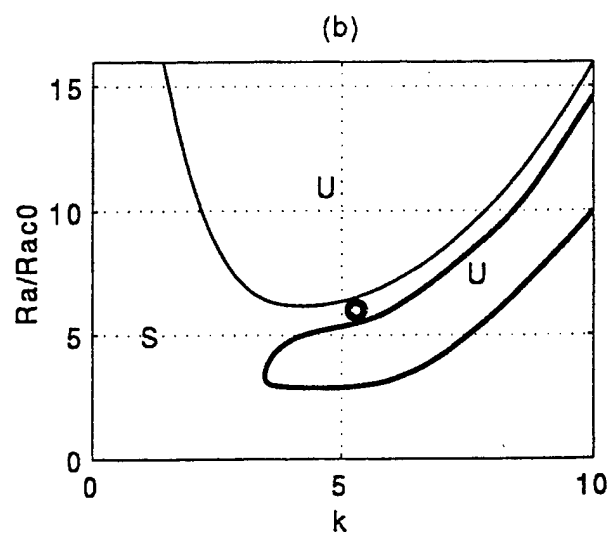
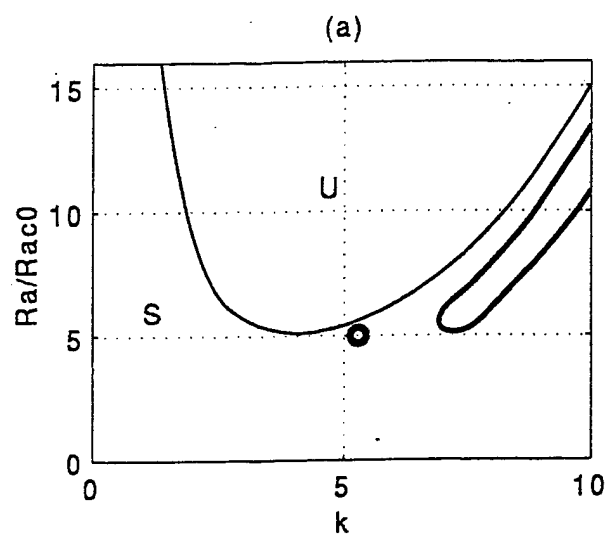


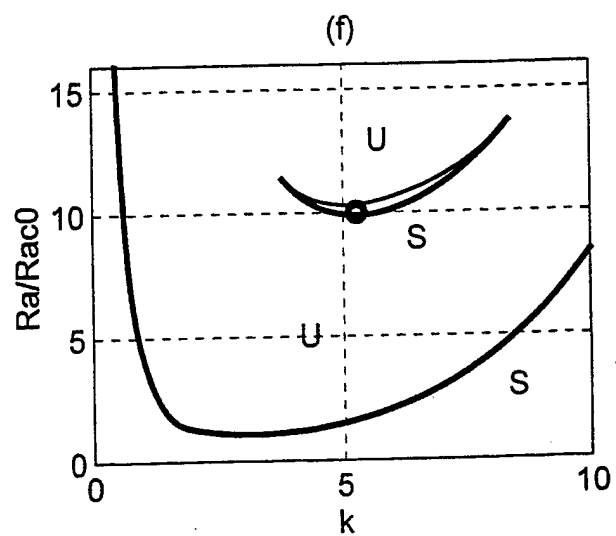
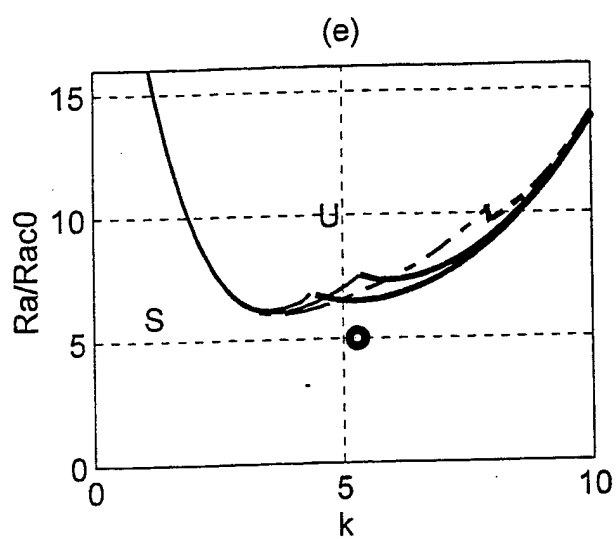
Figure 3(a)



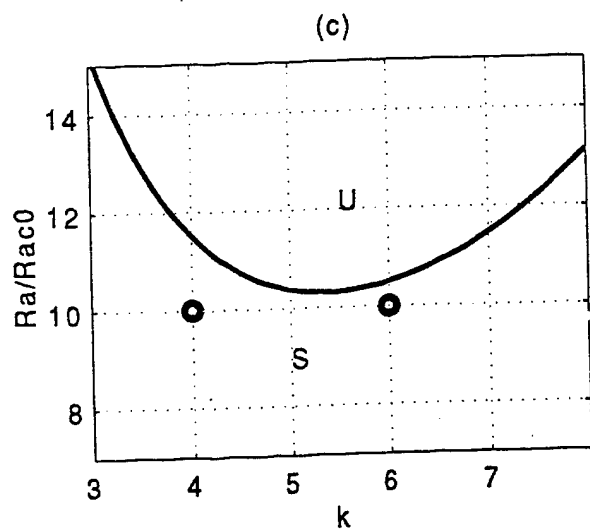
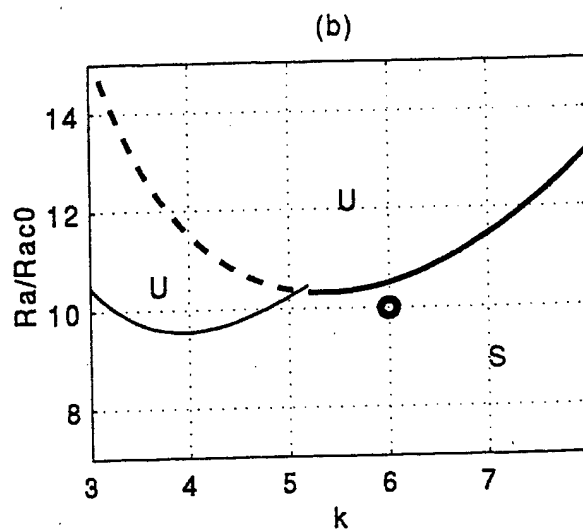
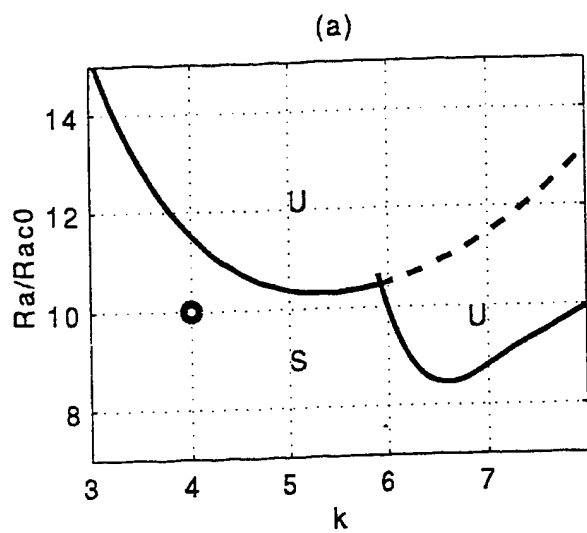
Figures 3(b)-3(c)



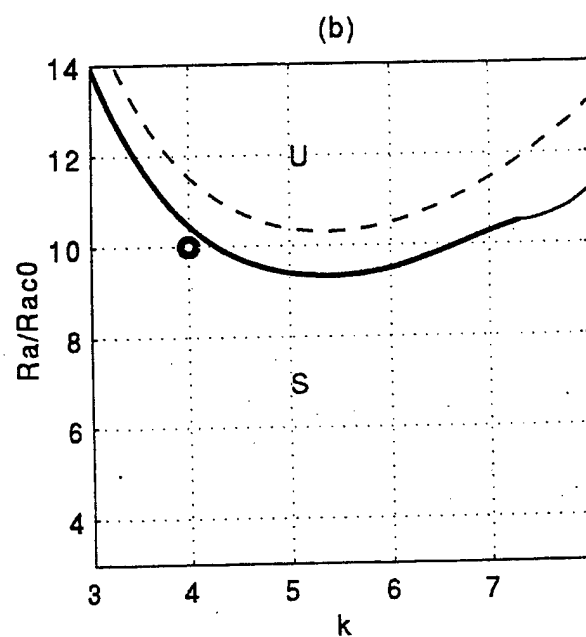
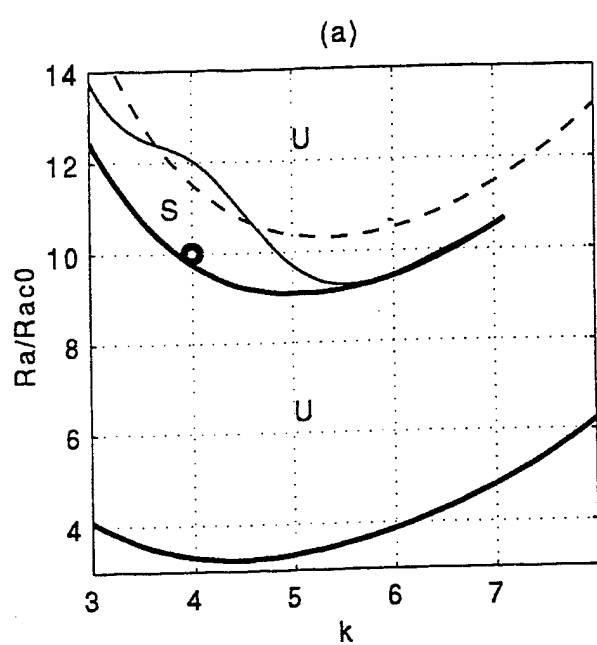
Figures 4(a)-4(d)



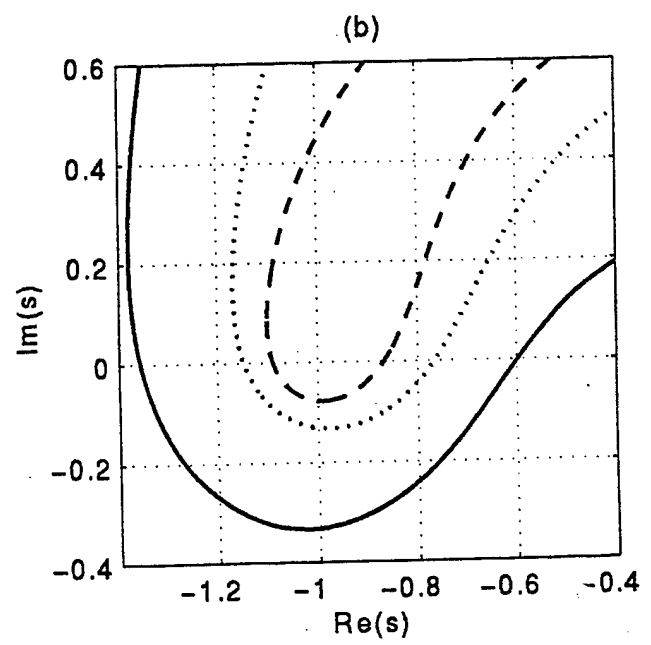
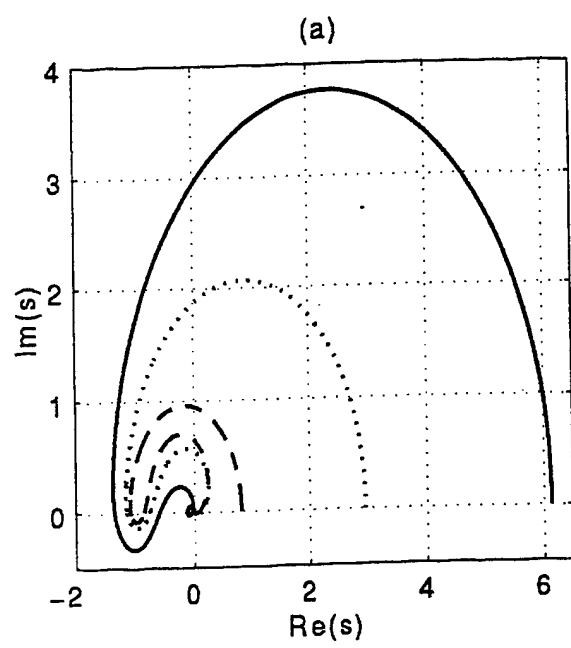
Figures 4(e)-4(f)



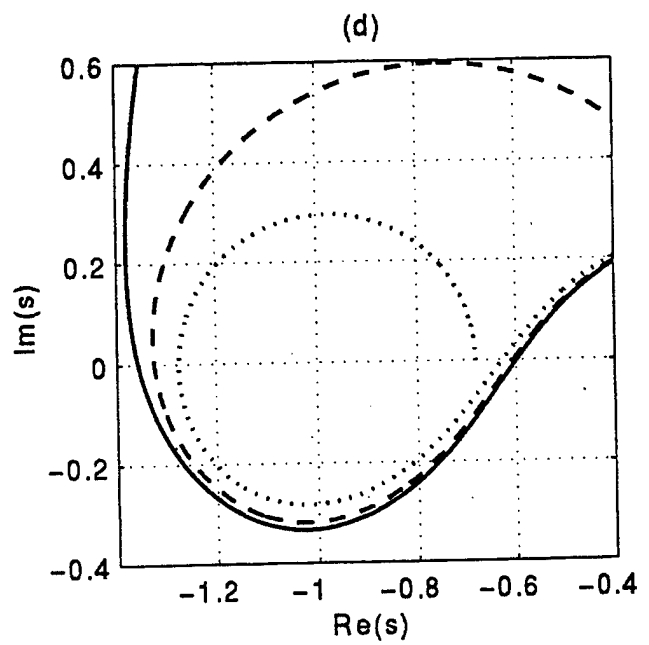
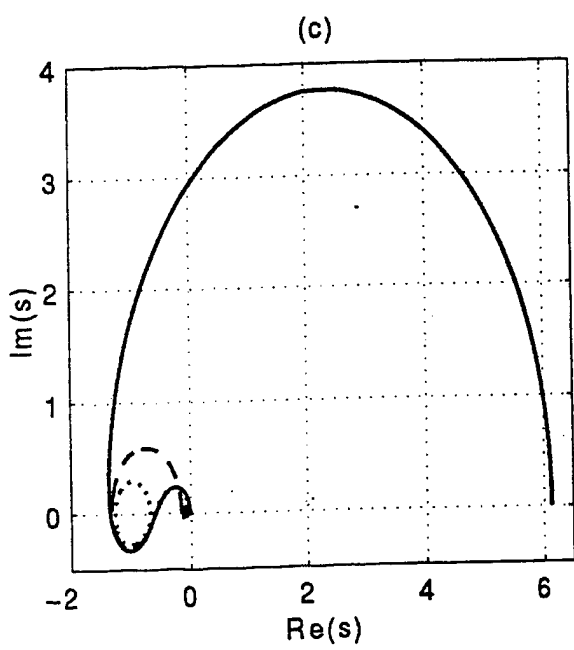
Figures 5(a)-5(c)



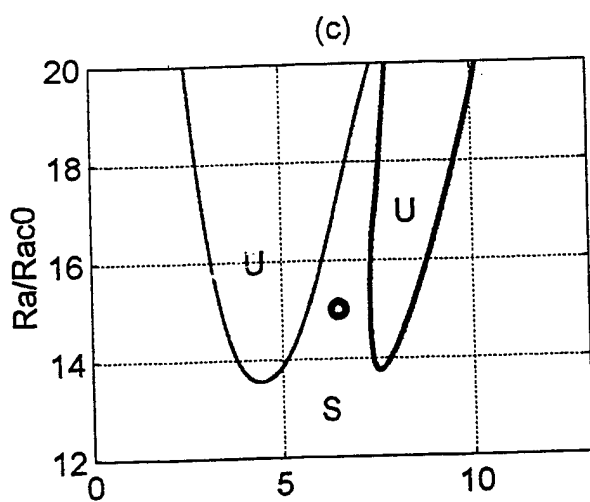
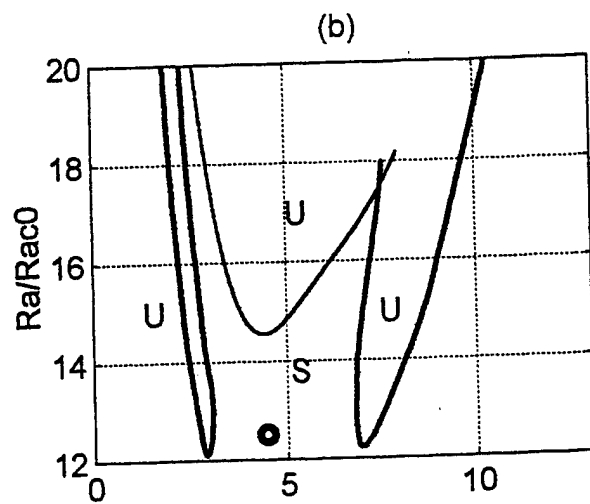
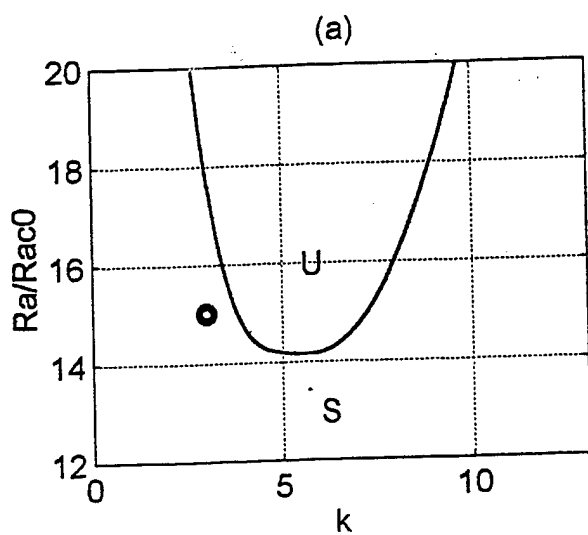
Figures 6(a)-6(b)



Figures 7(a)-7(b)



Figures 7(c)-7(d)



Figures 8(a)-8(c)

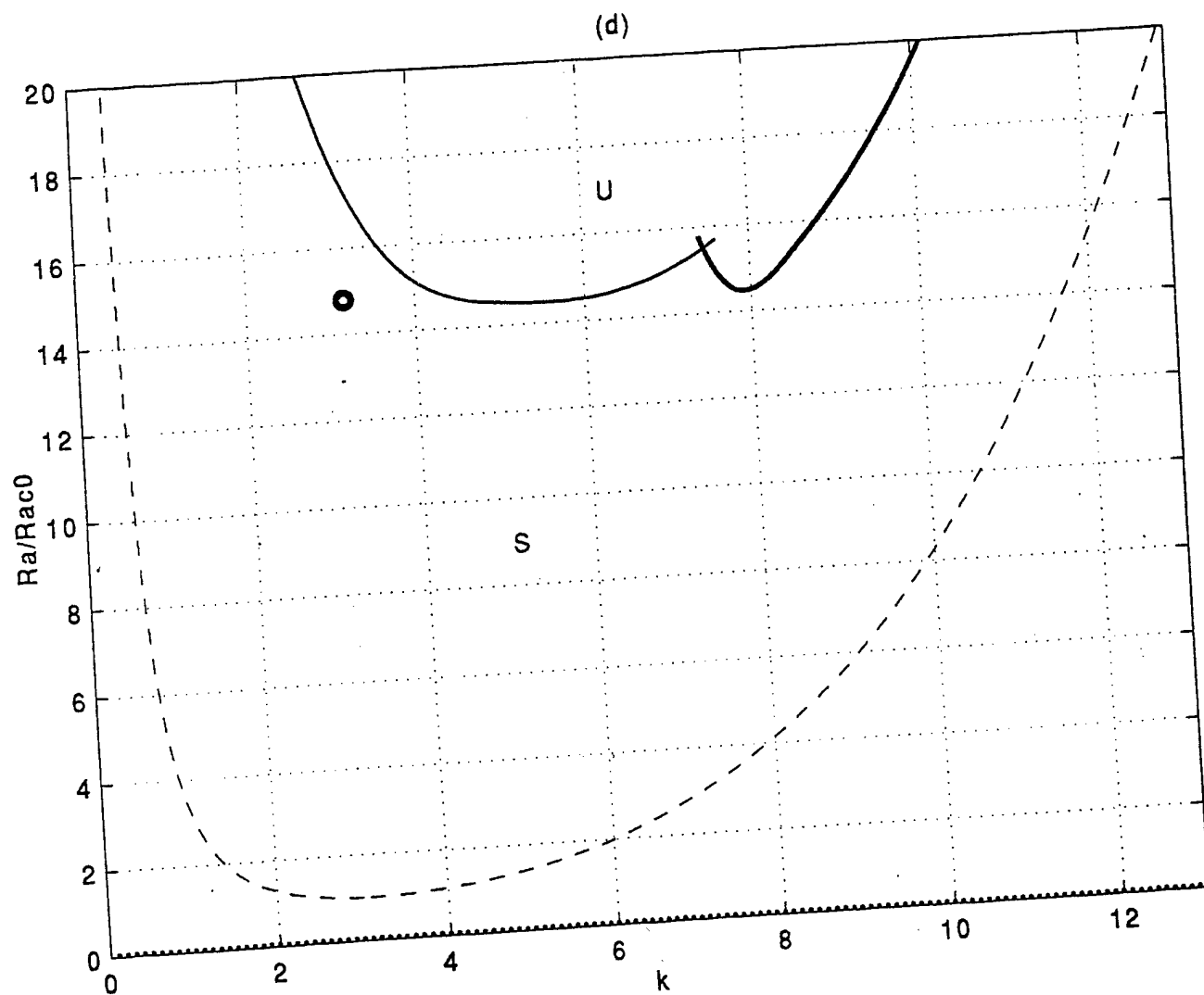
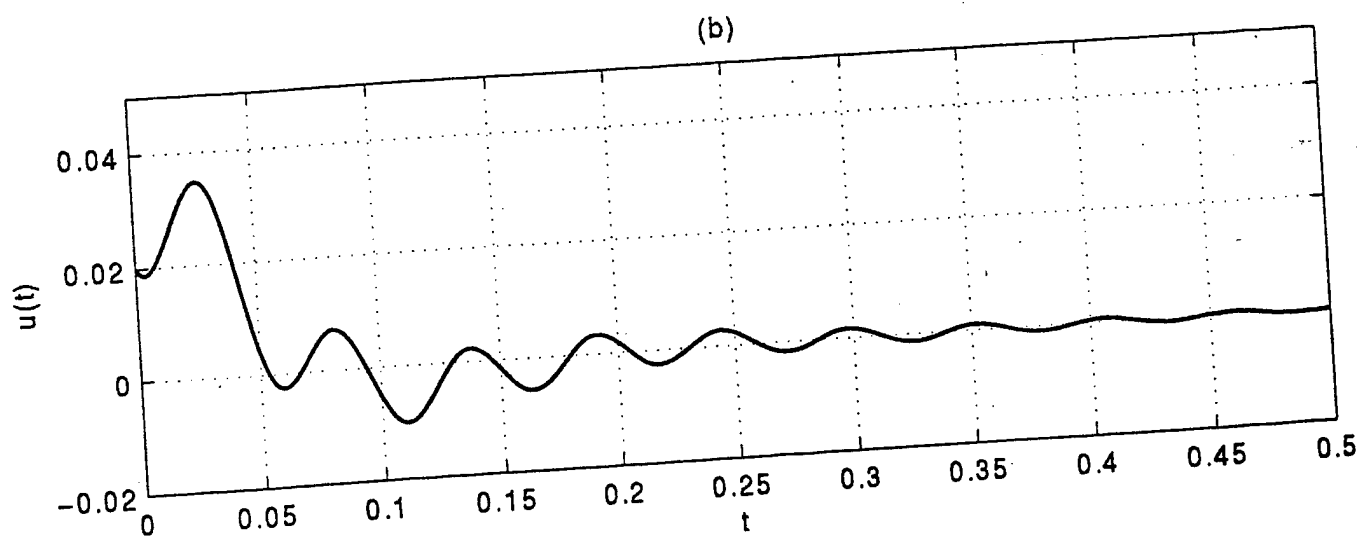
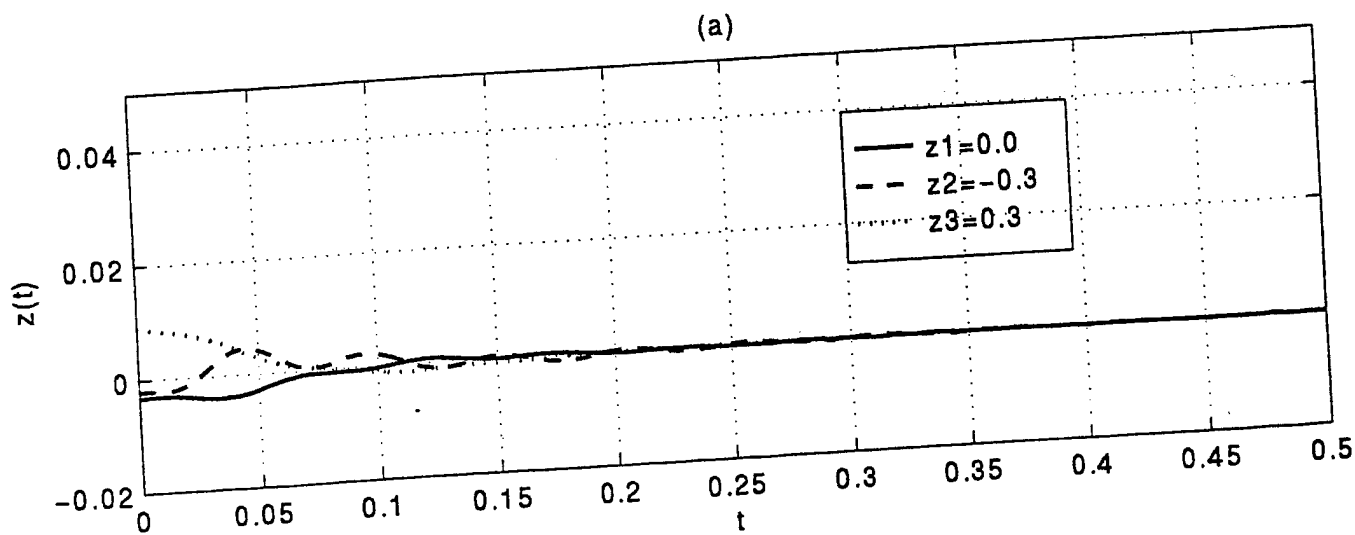
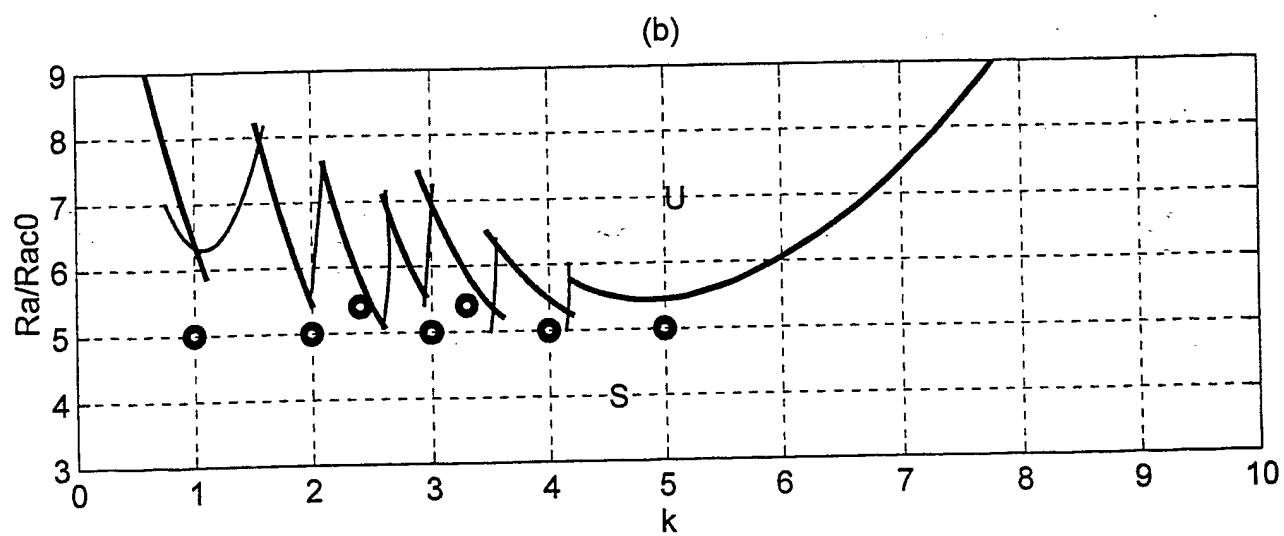
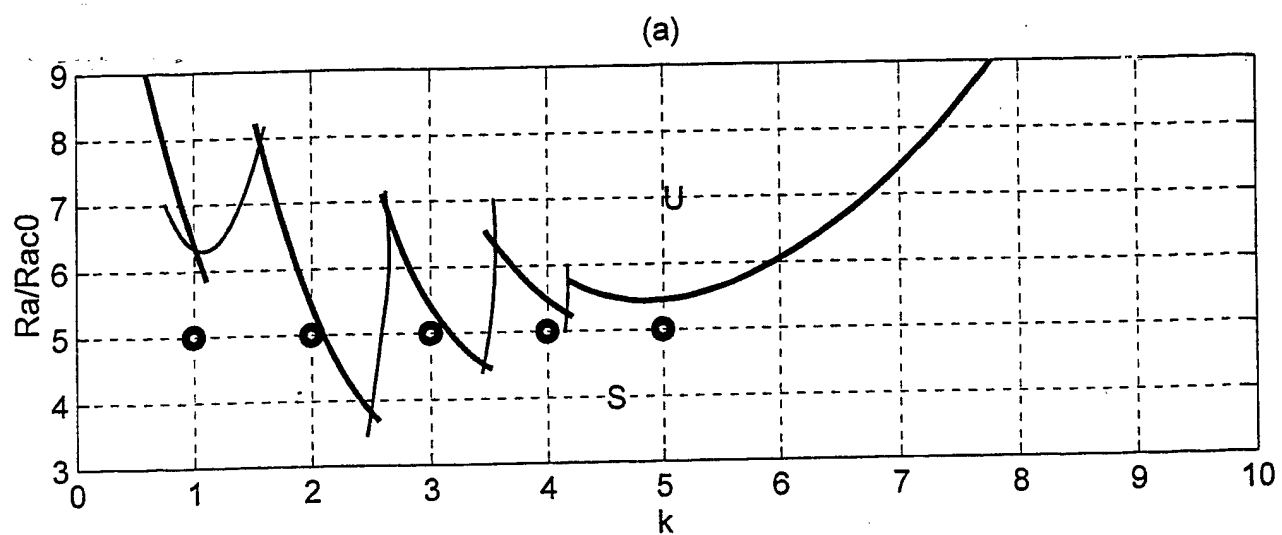


Figure 8(d)



Figures 9(a)-9(b)



Figures 10(a)-10(b)